Characterisation of Low Symmetry Liquid Crystal Structures

Warren D. Stevenson

Supervised by Prof. Goran Ungar and Dr. Xiangbing Zeng.

A thesis submitted for the degree of Doctor of Philosophy in the

Department of Materials Science and Engineering,

University of Sheffield.

June 2017

Acknowledgements

Project Aims

Over the last two decades a new liquid crystal phase known as the 'twist bend nematic' (N_{tb} phase) has become an increasingly prevalent subject of research. The focus of investigation has been the molecular level arrangement of the mesogens inside the phase. It was theorised that on average the mesogens follow a helicoidal director field with nano-scale pitch. Before the closing stages of this project, ambiguity of supporting experimental evidence led many to question the helical model and consider alternative structures. In earlier work the observed phase is sometimes referred to as the "N_x phase" [1-3] as a result of inconclusive experimental findings. The first aim of this project was therefore to investigate the molecular level structure of the experimentally observed N_{tb} phase and provide direct empirical evidence relating to: (i) phase chirality, (ii) the local intermolecular packing behaviour and (iii) the orientational order inside the phase. The importance of this research goal lay in progressing the fundamental understanding of the N_{tb} phase and finding methods that allow one to characterise the bulk phase.

The second research goal of this project was to characterise the unknown structure of an organic-semiconductor hybrid liquid crystal phase and in doing so, explain its unusual 'high absorption, low re-emission' properties at optical wavelengths. Self-assembly of such a phase may be of technological significance in photovoltaic applications, particularly solar cells, where re-emission of absorbed light is undesirable.

[1]   A. Hoffmann, A. G. Vanakaras, A. Kohlmeier, G. H. Mehl, D. J. Photinos, *Soft Matter*, 2015, **11**, 850.

[2]   V. P. Panov, M. Nagaraj, J. K. Vij, Yu. P. Panarin, A. Kohlmeier, M. G. Tamba, R. A. Lewis, G. H. Mehl, *Phys. Rev. Lett.*, 2010, **105**, 167801.

[3]   V. P. Panov, R. Balachandran, M. Nagaraj, J. K. Vij, M. G. Tamba, A. Kohlmeier, G. H. Mehl. *App. Phys. Lett.*, 2011, **99**, 261903.

Abstract

Chirality in the bulk N_{tb} phase was confirmed directly by resonant X-ray scattering of 'hard' X-rays in a selenium-labelled binary mixture of bent liquid crystal (LC) dimers. Furthermore the high orientation of the resonant Bragg spots, corresponding to the pitch length of a well aligned helix, enabled estimation of the coherent N_{tb} domain size. N_{tb} phase chirality was also confirmed by circular dichroism measurements in various pure LC dimer compounds. In addition to resonant Bragg spots, non-resonant broad peaks at larger scattering angles were observed. These are attributed to localised cybotactic layering of the mesogens, which was found to depend on spacer length and mesogen composition. To account for simultaneous observation of sharp and broad X-ray peaks, a new two component orientational order parameter was introduced, which can be deconvoluted if the conical angle is known or if near perfect helical order is achieved. Based on these findings, a more quantitative molecular level model of the N_{tb} phase was geometrically constructed. In order to follow the local director the dimers or polymer chains adopt an average conformation resembling a helix (helical segment in dimer case). The helical conformation was supported by the findings of polarised infrared spectroscopy in the N_{tb} phase of a main-chain LC copolyether. Experimental evidence suggests that the N_{tb} phase is very similar in both polymer and dimer sample types.

Throughout the project several banana phases in bent LC dimers were observed and characterised, some of which are new or previously misidentified. In the case of the misidentified phase, an alternative molecular level model was proposed based on polarisation splay of the molecules.

A LC self-assembling 3D array of dendron functionalised CdS quantum dots (QDs) was investigated by a variety of experimental techniques including grazing incidence X-ray scattering and fluorescence spectroscopy. The structure was found to possess very low cubic symmetry and represents the lowest symmetry QD array to date. The strange fluorescence quenching properties of the material were found to be dependent on the annealing temperature, hence the degree of positional order among QDs inside the array.

Contents

Chapter 1 – Structures of Liquid Crystal Mesophases

1.0 – Introduction

The discovery of liquid crystals is commonly accredited to Friedrich Reinitzer for his report in 1888 of multiple melting points within an ester of cholesterol [1,2]. He noticed that the solid sample melted into a cloudy liquid, which upon further heating became suddenly transparent. What he had at the time unknowingly observed was the temperature dependent phase sequence within a liquid crystal (LC) material. In modern times a LC material is generally defined as a substance that is able to reach thermodynamic equilibrium between the crystalline solid and the isotropic liquid states of matter [3,4]. As an intermediary, but independent state, LCs can simultaneously possess traits comparable to crystalline solids and isotropic liquids; for example the molecules may be highly mobile, but remain oriented in the same direction. Since their initial discovery a wide variety of LC phases, or "mesophases", have been discovered, each classified by the type of organisation exhibited by the composite molecules or polymer chains. Depending on the internal structure, LC materials may exhibit a variety of unique optical, electrical and mechanical properties, which have led to their inclusion in a diverse range of applications. Among the most prevalent is the liquid crystal display [5,6], which has become a staple in commercial technology.

1.1 – Liquid Crystal Mesogens

Mesogens are the chemical components of LC molecules (or polymers) that are responsible for the formation and organisational properties of mesophases. Mesophases can be divided into two main groups: thermotropic and lyotropic. In lyotropic systems the mesogens are typically amphiphilic i.e. they feature both hydrophobic and hydrophilic groups. Such molecules form LC phases only when an appropriate concentration is dissolved in another substance [7]. On the other hand, thermotropic phases do not require a solvent and are formed depending on the thermodynamic properties of the system. Mesomorphic behaviour is governed by temperature [8] and exhibited on heating from the crystal phase or cooling from the isotropic liquid phase. In this thesis we need only consider thermotropic systems.

Traditional thermotropic mesogens comprise a rigid assembly of aromatic rings in one of three approximate shapes: rod-like (calamitic), disc-like (discotic) or banana shaped (bent core), see Figure 1.0. These aromatic arrangements result in molecular anisotropy, i.e. molecules with differing dimensions. At temperatures above the crystal melting point, but below isotropisation, the increased mobility of the molecules permits Van der Waals forces [9] and interfacial surface effects [10] to align the unique axis (or axes) of the mesogens along a preferred direction. Orientational order among molecules reduces intermolecular potential, allowing the system to reside in a free energy minimum and reach thermodynamic equilibrium.
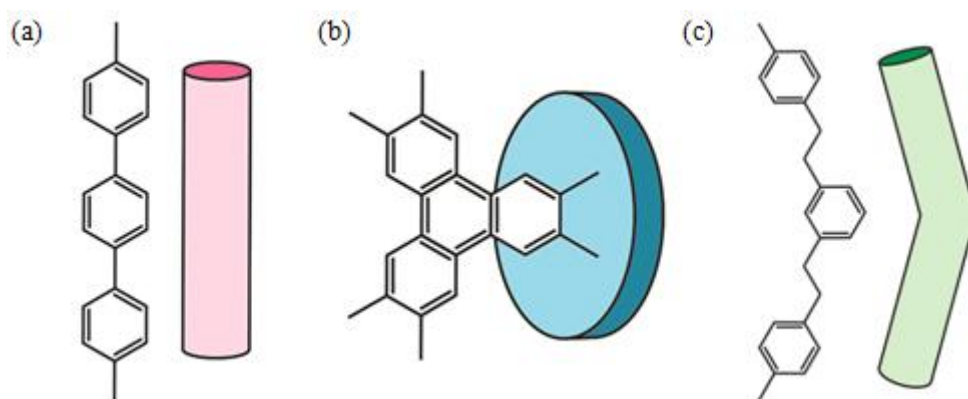
Figure 1.0 – Example aromatic arrangement in the three most common liquid crystal mesogen types. (a) Calamitic (b) Discotic and (c) Bent core.

The intrinsic anisotropy of mesogenic molecules means that physical properties such as the dipole moment are dependent on the axis in question. In the case of non-polar calamitic mesogens in an applied electric field, the induced charge separation is greatest along the length of the molecule. The long axis therefore possesses a larger electric dipole moment ($\mathbf{p}$), as explained by the general expression $\mathbf{p} = q_c \boldsymbol{r}$, where $\boldsymbol{r}$ is the vector charge separation and q_c is the net charge difference. The torque applied by the electric field may align the largest dipole moment parallel to the direction of the field [11]. Many mesogenic molecules can also be oriented by magnetic fields provided that a sufficient magnetic moment can be induced.

In regions of common molecular alignment (domains) the macroscopic properties such as the dielectric constant (ε_r) are also split into two components: one parallel to the average direction of the molecular long axes and the other perpendicular to it [12]. From

the relation for non-magnetic materials at optical wavelengths, $n = \sqrt{\varepsilon_r}$ [13], the same can be said for the components of refractive index. When polarised light is directed through an axial (birefringent) medium the light components oscillating parallel and perpendicular to the direction of alignment travel at different velocities, causing them to become out of phase as they exit the material. The resulting polarisation changes of the recombined light give rise to the vibrant optical textures commonly observed in mesophases when viewed between crossed polarisers [12].

1.2 – The Nematic Phase

The Nematic (N phase) is the simplest LC phase where the mesogenic molecules exhibit long range orientational order, but lack positional periodicity in all three dimensions [3,4,8]. The molecules prefer to orient with their longest axes approximately parallel as shown in Figure 1.1, which results in a uniaxial and cylindrically symmetric mesophase (point group $D_{\infty h}$). The average direction of molecular alignment is described by a dimensionless unit vector known as the director $\hat{\boldsymbol{n}}$. The director is approximately uniform within the local vicinity of a reference molecule, but may vary over the sample as a whole. The alignment direction is therefore a function of position described by the director field $\hat{\boldsymbol{n}}(\boldsymbol{r})$.
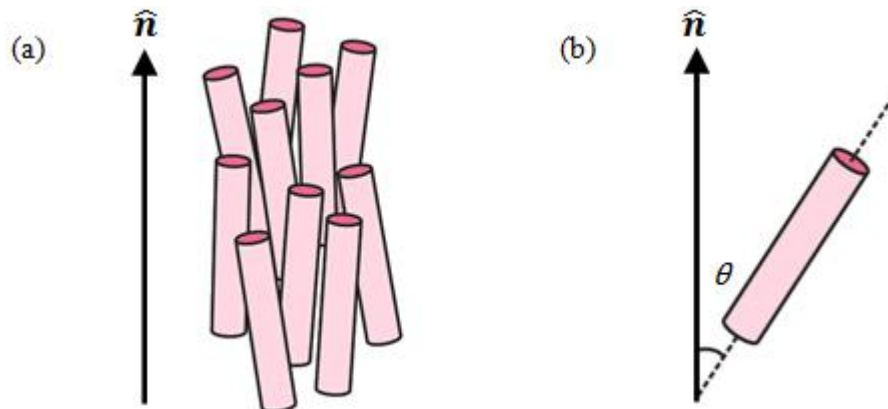
Figure 1.1 – (a) The arrangement of molecules in the uniaxial N phase. (b) A visual representation of the angular relationship between the director and the axis of an individual molecule.

The degree of organisation within the uniaxial N phase can be quantified by the orientational order parameter (S), which is ordinarily given as a symmetric second rank traceless tensor. However in the ideal case of cylindrical symmetry, the order parameter

is adequately described by the spatial average of the second Legendre polynomial in $\cos(\theta)$:

$$S = \langle P_2(\cos(\theta)) \rangle = \langle 3\cos^2(\theta) - 1 \rangle/2 \qquad (1.0)$$

Here θ is the angle between a molecule of reference and the local director. The orientational order parameter is equal to one when all the molecules are perfectly aligned with $\hat{\boldsymbol{n}}$ and decreases as the average value of θ increases. $S = 0$ when the molecules are randomly oriented as in the isotropic state.

1.3 – The Smectic Phase

In smectic LC phases the mesogens are aligned, but also confined to layers. Smectic phases therefore possess a minimum of 1D translational organisation in addition to orientational order [14,15]. There are several types of smectic mesophase with different in-layer molecular arrangements. The two most relevant phases are introduced below.

1.3.1 – Smectic A

In the Smectic A (SmA) phase the director runs perpendicular to the plane of the layers as shown in Figure 1.2. Within each layer the molecules have no long range side-to-side correlation, which results in cylindrical symmetry similar to the N phase. As the molecules are on average stood upright, the layer spacing is similar to the molecular length. The positional periodicity of molecules along the director means that the orientational order parameter (S) is insufficient to describe the organisation; instead De Gennes theory [16] employs a complex order parameter of the form $\Psi = |\Psi|exp(iq)$ to define a sinusoidal density wave along the direction of preferred alignment:

$$\rho(z) = \rho_0 \left[1 + |\Psi|\cos\left(\frac{2\pi}{d}z\right) \right] \qquad (1.1)$$

Here ρ_0 is the mean density, $|\Psi|$ is the wave amplitude, d is the inter-layer spacing and z represents position.

1.3.2 – Smectic C

The Smectic C (SmC) phase is very similar in its organisational properties to the SmA with the exception that the preferred alignment of the molecules is not perpendicular to the plane of the layers; instead the molecules are tilted with respect to the layer normal [14,15] (Figure 1.2). As the molecules are tilted, the layer spacing is smaller than the molecular length by a factor proportional to the cosine of the average tilting angle. The

order parameter can again be described as a density wave because the molecular centres are assumed unchanged by the tilt. Additional considerations are needed however, due to the fact that the direction of the density fluctuation is no longer parallel to the director.
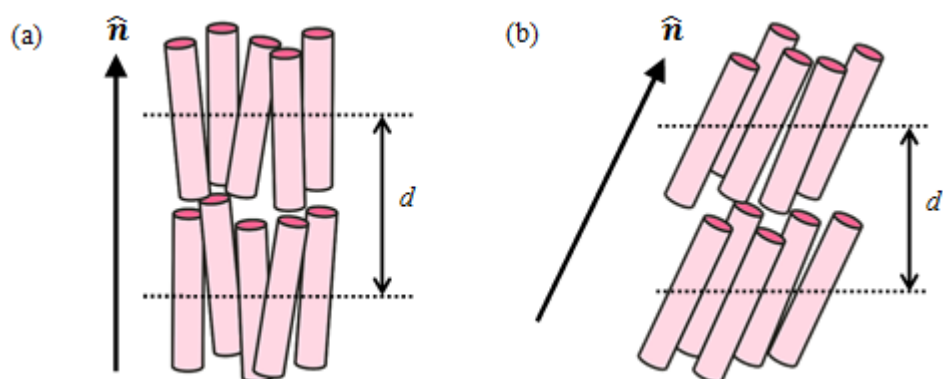
Figure 1.2 – The layered structure of the (a) SmA phase and (b) SmC phase.

1.4 – Chiral Mesophases

Chiral mesophases are formed by chiral molecules, i.e. molecules that lack a centre of symmetry and cannot be superimposed upon their mirror image. Chiral molecules come in both left and right handed varieties which are identical in chemical composition except for the direction of at least one bond in their make-up; chiral molecules are therefore 'enantiomorphic'. There are many chiral mesophases, most of which contain helical structures induced by the handed nature of the molecules within them. The handedness of the enantiomer determines the direction of the helical structure i.e. clockwise spiral or anticlockwise spiral. The chiral equivalent of a mesophase is typically denoted by an asterisk, for example N* (chiral nematic) and SmC* (chiral smectic C).

1.4.1 – Chiral Nematic

The chiral nematic (N* phase), also known as the cholesteric phase [8,17], was named after its initial discovery in derivatives of cholesterol. Similar to the non-chiral N phase there is no long range positional organisation between the mesogens, only local orientational order. Although there is no positional order the molecules form a helical structure in which the director periodically rotates about the helical axis [8,17]. The

rotating director field arises from the chiral bonds, which prevent the molecules from lying parallel to those stacked above and below. The helical axis is therefore perpendicular to the plane containing the long axes of the molecules. A visual representation of the cholesteric phase is provided in Figure 1.3, where the pitch (p) corresponds to the distance of one full rotation in the director field along the helix axis. However due to the equivalence of $\hat{\boldsymbol{n}}$ and $-\hat{\boldsymbol{n}}$, the structure effectively repeats in intervals of $p/2$.
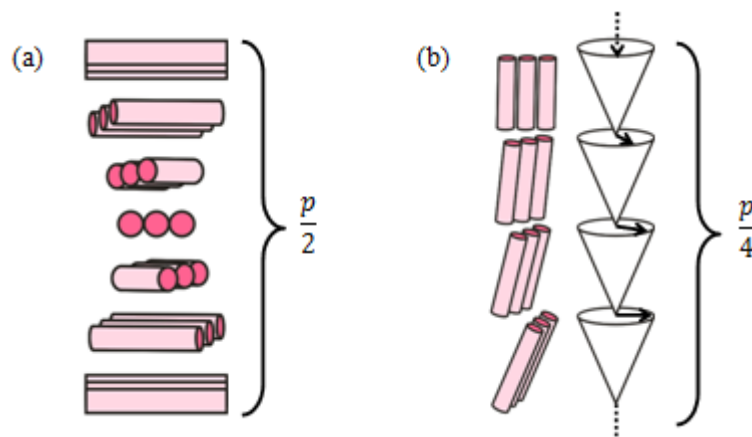
Figure 1.3 – (a) Diagrammatic representation of the N* phase. The molecules are not positionally ordered, but the director rotates on progression along the helical axis (vertical). (b) The SmC* phase, where the molecules are layered along the helical axis. The average tilting direction is rotated between successive layers. p indicates the helical pitch length i.e. the length of one full rotation.

1.4.2 – Smectic C*

The molecules in the SmC* phase are tilted in respect to the layer normal as previously explained for the standard SmC phase. However the chirality of the mesogens introduces a rotating tilt direction on progression from one layer to the next. The progressive rotation of the tilt direction creates a helical structure, where the helical axis runs parallel to the layer normal [17] (Figure 1.3). The combination of tilting and chirality has also been found to create spontaneous polarisation inside the layers, which enables the formation of several sub phases with ferroelectric [18,19], anti-ferroelectric [20,21] and ferrielectric [22,23] polar orderings.

1.5 – Mesophases of Banana Shaped Mesogens

In the preceding sub-sections the LC phases were described in the context of simple calamitic mesogens. However when the symmetry of the molecule is reduced i.e. the molecules possess more than one unique axis, the structures of the mesophases become more complicated. In the case of banana shaped mesogens, steric restrictions arising from the bent molecular shape enables the formation of exclusive liquid crystal phases sometimes referred to as "banana phases" [24].

The non-crystalline banana phases are lamellar much like traditional smectics, but require in-layer ordering of the bend direction to fill space efficiently. The combination of local polar ordering and tilting often result in ferroelectric or anti-ferroelectric switching properties such as those observed in the SmC* phase. Furthermore, the relationship between the tilting direction and the polarity of the molecular bend may also lead to spontaneous symmetry breaking inside the layers, despite the lack of intrinsic molecular chirality. In the mid 90's the banana phases were classified by the notation Bn, where n is the sequential number of discovery. The banana phases most relevant to later discussions are briefly introduced below.

1.5.1 – B1 Phase

The B1 structure is a frustrated smectic, where the layers are broken to form a columnar phase with a rectangular unit cell [25-27]. The three variations of the B1 structure are shown below in Figure 1.4d-f. The reversed direction of the molecular bend between successive columns means that the natural structures do not possess a net polarisation. However in the case of the $B1_{rev}$ and the $B1_{revtilt}$ phases, the polarity of the columns can be made constant by an applied electric field [25]. An applied electric field may also switch the tilting direction of the $B1_{revtilt}$ phase [25]. The B1 phases do not possess overall chirality; even in the tilted case the structure is racemic i.e. contains equal proportions of left and right handed columns, resulting in no overall chirality.
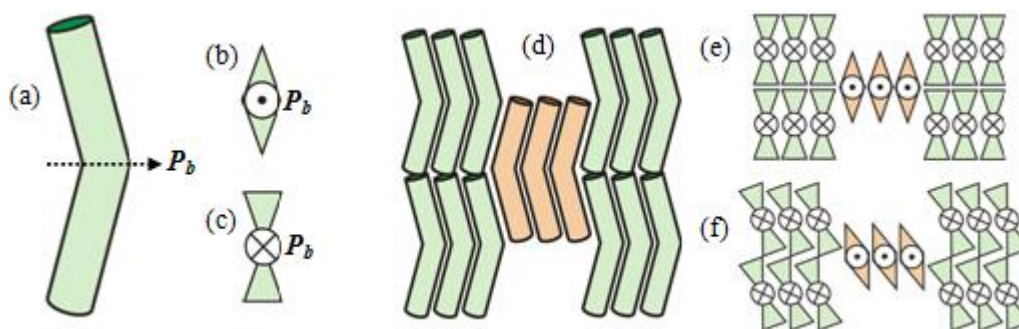
Figure 1.4 – Definition of the vector P_b describing the polar direction of the molecular bend. P_b could equivalently be defined in the opposite direction, but was selected here to coincide with the natural point of the molecule. (a) side view of the molecule and (b)/(c) view of the molecule anti-parallel/parallel to P_b, respectively. (d) The B1 phase, (e) the B1$_{rev}$ phase and (f) the B1$_{revtilt}$ phase. All three images show a single molecule slice of the respective structure in the xz plane. The y direction runs into the page.

1.5.2 – B2 Phase

The B2 structure is closely related to the calamitic SmC phase – the molecules reside in continuous layers and possess an average tilting angle in respect to the layer normal [28-30]. Unlike the simple calamitic case, there are four possible variations of B2 phase arsing from the interplay between bend polarity and the tilting direction. For this reason a newer notation SmC$_x$P$_y$ has been adopted to more accurately describe each of the four sub phases. The subscript x denotes the "clinicity" i.e. synclinic (S) or anticlinic (A), while the subscript y denotes the polarity of the phase i.e. ferroelectric (F) or anti-ferroelectric (A). Clinicity and the four B2 arrangements are explained diagrammatically in Figure 1.5a.

1.5.3 – B6 Phase

In the B6 phase the smectic layer height is less than or equal to half of the molecular length. This is because the molecules are intercalated [31-33], i.e. they are not confined to separate layers of their own and randomly interlock (see Figure 1.5b). There have been reports of both tilted (SmC-like) [32] and non-tilted (SmA-like) [33] versions of the B6 phase, but in either case there is no net polarity or chirality.
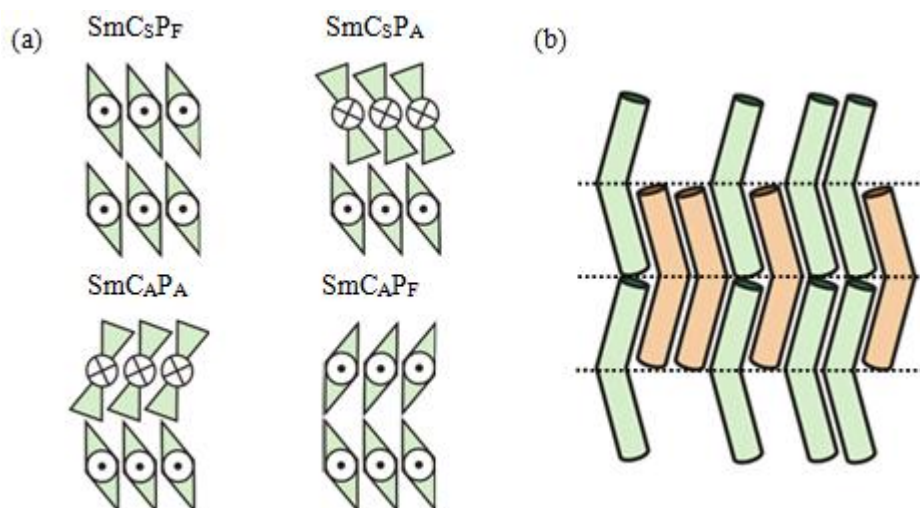
Figure 1.5 – (a) The four B2 structures. If the tilt direction of the molecules stays the same from one layer to the next, the arrangement is synclinic. If the tilt direction changes, the arrangement is anticlinic. The SmC_SP_F and the SmC_AP_A phases are chiral, whereas the remaining two are racemic. There are six B2 structures if enantiomorphs are included. (b) The layering structure of the B6 phase. The layer height is effectively half of the molecular length due to intercalation of mesogens. In the tilted B6, the tilt direction is into the plane of the page.

1.5.4 – B7 phase

The B7 phase has a similar structure to the B2; the molecules are confined to separate layers and are tilted. Unlike the B2 phase, the polarity of the molecular bend and the tilting direction alternate in the transverse direction i.e. inside the layers, rather than along the layer normal (see Figure 1.6). In this arrangement the structure is locally ferroelectric and chiral, however due to the reversing polarity and handedness, the phase is on average non-chiral and anti-ferroelectric. However in large electric fields the B7 has been known to undergo a field induced transition to the SmC_SP_F B2 phase.

In an experimental study by D. A. Coleman *et al* [34] it was shown that the discontinuous packing style of the B7 phase is made possible by layer undulation: the layer planes are wavy rather than flat. In the same study it was explained that the undulation wavelength must be coupled to periodic splay deformation of in-layer polar ordering. It was later proposed that modulated polarisation splay and the accompanying frustration may also account for the structures of the B1 phase and several other undulated SmCP (SmCPU) phases – some of which are yet to be experimentally observed [35]. The key principles of this theory are explained below.
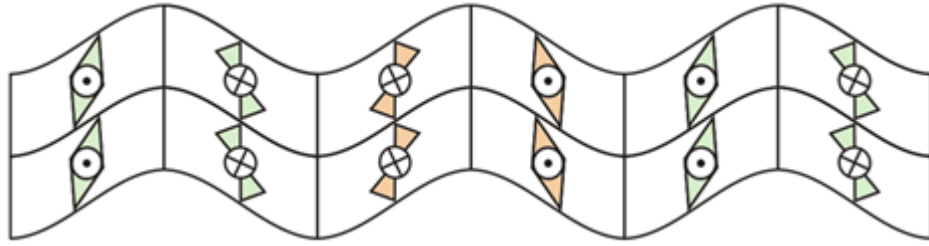
Figure 1.6 – A simplified diagram of the B7 layering structure. The handedness of the highly local structure (indicated by colour) periodically changes inside the layers, as does the polar direction of the molecular bend. The layers undulate in response to defects formed by polarisation splay. The splaying polarity of the molecules has not been shown here; only the tilt and polar direction of the central molecules in each section.

1.5.5 – Polarisation Splay Modulation

In fluid polar smectics such as the SmCP phases, the local preference of the bend polarisation field is to be non-uniform i.e. splayed such that $\nabla \cdot \boldsymbol{P_b} \neq 0$. To achieve local layer polarity (as observed in the B7 phase) the polarisation field must be non-symmetric, which cannot be achieved by splay of a single sign. The sign of $\nabla \cdot \boldsymbol{P_b}$ is therefore required to be spatially inhomogeneous and locally finite. This is possible only if the layers contain less ordered regions (defects) of the opposite splay sign. In the model proposed by D. A. Coleman *et al* [34,35], the defect regions arise periodically where stripes of the prevailing splay sign clash. The defects mediate the reorientation of the molecules from one stripe to the next, which results in a polarisation modulated structure (see Figure 1.7).
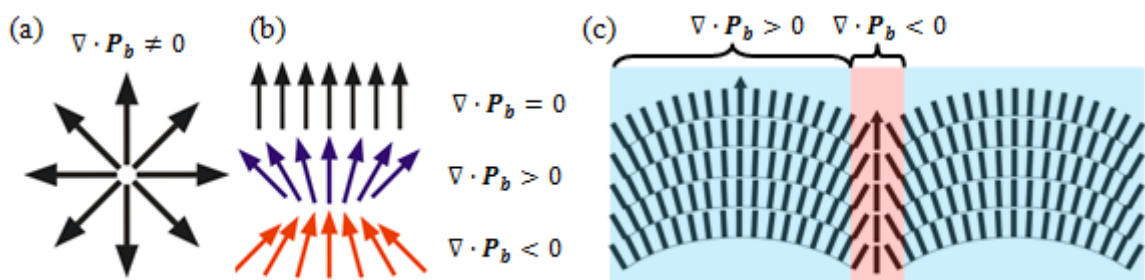
Figure 1.7 – (a) A symmetrically divergent polarisation field. Ferroelectricity requires non-symmetric polarisation as in (b). Steric interactions will encourage the molecules to splay locally i.e. discourage uniform polarisation. (c) Periodic polarisation stripes (blue) may be formed with homogeneous splay sign, as long as the defects (red), containing the opposite splay sign, are sufficiently low in energy.

The defect regions present a structurally different environment to that found towards the centre of the stripes, meaning that the molecules within them may possess a different polarisation density and tilting angle. The equilibrium layer height in the defect regions may therefore differ to that in the centre of the stripes, causing layer frustration. The structures of the previously described phases can then be explained by the way that the molecules choose to relieve this frustration. In the B7 phase the defects are accommodated by layer undulation; however in systems with less robust layering the defects may dislocate the structure, resulting in the B1 or B6 phases. In the B2 phase the splay defects are too energetically costly and are disfavoured. Instead the molecules choose to sacrifice the preferred local arrangement in favour of a globally frustrated structure with a uniform polarisation field ($\nabla \cdot \boldsymbol{P_b} = 0$).

The molecular arrangement inside polarisation splay stripes can be reconstructed by considering small bundles or 'blocks' of tilted molecules with locally splaying polarisation. The blocks are equal in width to the splay stripes and are consequentially undulated due to the defects at their edges. The enantiomorphic property of tilted polarisation splay can produce positive or negative undulation slopes as shown in Figure 1.8a. In the block centres the molecules must tilt in the direction that best follows the undulation curvature in order to minimise elastic energy. If the splay blocks are stacked together, four classes of undulated smectic (SmCPU) phases emerge with continuous or discontinuous layering styles (see Figure 1.8b). In such structures the molecular tilting direction may be preserved or reversed over the block boundaries. The structure is said to possess S/S' defects if the tilt direction is maintained or A/A' defects if switched. While it is not significant to later discussions, sub-phases with different chiral and polar arrangements may exist within each of the four classes. This is because there are several possible block combinations that achieve the same undulation pattern without changing the defect type.
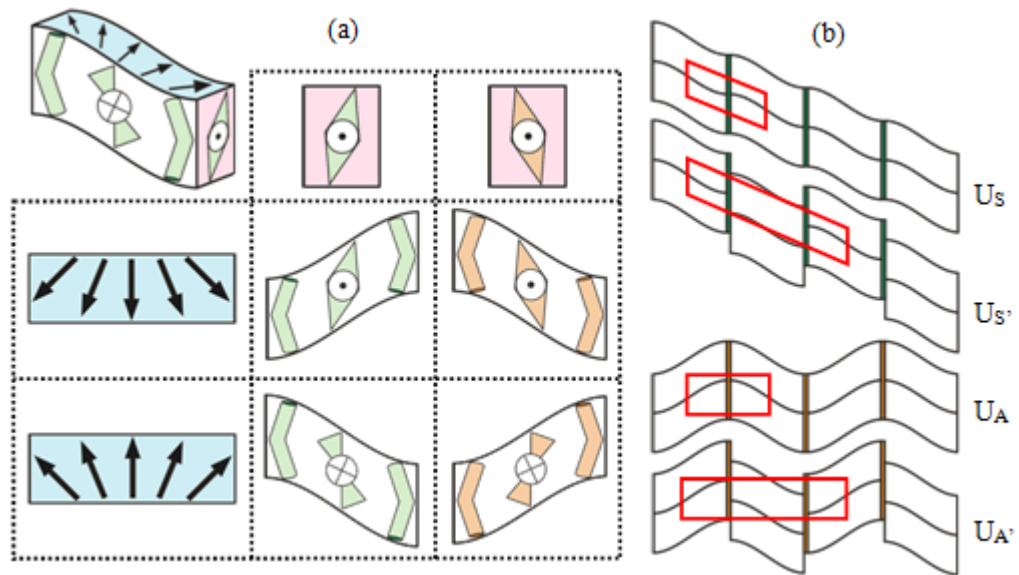
Figure 1.8 – (a) Tabulated derivation of the four possible polarisation splay blocks for bent core mesogens. Rows have the same polar direction, while columns have the same tilt direction in the indicated plane of the 3D example block (top left). (b) The four classes of SmCPU phase that can be created from the splay blocks and intervening defects (green/yellow). The structures are oblique or rectangular with either continuous or broken layering; the choice of structure depends on the defect strength. The $SmCPU_{A'}$ (bottom right) is yet to be experimentally observed [35].

1.6 – The Twist Bend Nematic (N_{tb}) Phase

It has been discussed how the bent shape of the molecules can create spontaneous polarity and symmetry breaking inside lamellar liquid crystal phases, but one may also expect the bent shape to perturb the molecular organisation inside the nematic phase. The transition from a uniaxial N phase to a second nematic phase with reduced symmetry was first proposed by Meyer in 1973 [36], although recent popularisation of the research topic is often associated with theoretical studies by Dozov [37] (2001) and Memmer [38] (2002). The modern theory explains that for systems of sufficiently bent molecules, the pathological elasticity associated with the molecular shape may induce spontaneous deformations of the local director field, resulting in one of two possible bend-modulated phases: The oscillating splay-bend nematic (N_{sb}) or the helical twist-bend nematic (N_{tb}). Inside both structures the molecules are said to retain liquid-like positional order, thereby preserving the nematic quality of the phase. Over the last two decades there has been a huge surge in effort to experimentally identify and characterise the proposed helical structure of the N_{tb} phase, making it one of the newest and most urgently studied liquid crystal research topics since "banana-mania" in the 1990's

[39,40]. In addition to widespread fundamental interest, the unique structure of the N_{tb} phase exhibits ultrafast electronic responses [41], which may one day revolutionise display and other FET based technologies. However, before further discussing the experimental properties of the N_{tb} phase, a brief overview of Dozov's theoretical framework [37] will be introduced, as it is the most frequently referenced model.

1.6.1 – Theory of the Spontaneously Bent Nematic Ground State

The free energy density in the bulk of a uniaxial N phase is minimised in the ideal case where the mesogens are oriented parallel, with alignment described by a uniform director field. In real systems, defects and other boundary conditions prevent perfect molecular alignment and disturb the uniformity of the director. The free energy of the N phase can therefore be written:

$$F_T = F_0 + F_d \qquad (1.2)$$

$$F_d = \frac{1}{2}[K_1 s^2 + K_2 t^2 + K_3 b^2] \qquad (1.3)$$

where F_T is the total free energy, F_0 is the free energy of the uniform state and F_d is the free energy contribution from elastic director distortions. In equation (1.3) K_n are the Frank elastic constants and $s = (\nabla \cdot \hat{\boldsymbol{n}})$, $t = \hat{\boldsymbol{n}} \cdot (\nabla \times \hat{\boldsymbol{n}})$ and $b = \hat{\boldsymbol{n}} \times (\nabla \times \hat{\boldsymbol{n}})$ respectively denote the three principle deformations: splay, twist and bend. Conventionally the Frank elastic constants are positive so that the presence of elastic deformation always increases the total free energy of the bulk phase. However there is no intrinsic symmetry reason that forbids one or more of the elastic constants to have a value ≤ 0. In the case of bent molecules it can be shown that $K_3 < 0$ may stabilise a nematic phase where the bulk free energy of the non-uniform state is equal to, or lower than that of the uniform state.

As mentioned above, the calamitic N phase is stabilised by making the angle between each mesogen as small as possible, giving the uniform state when $\theta = 0$ and the orientational order parameter $S = 1$ (Figure 1.9a). In an analogous N phase of achiral banana shaped or 'bow-like' mesogens, the director is uniform when the 'bow strings' are aligned parallel (Figure 1.9b). In this uniform state the molecular shape creates an angle, comparable to half the exterior bend angle ($\phi/2$), between neighbouring mesogenic segments. The exterior angle and the two segments of each molecule are defined in Figure 1.9c. By the same principle described for the N phase, a more

energetically favourable state would be one where the angle between segments is reduced closer to zero. This requires that the mesogens on average follow the curvature imposed by their neighbours and bend in the same direction locally. 'Close packing' of the banana shaped molecules therefore results in a non-uniform director field as shown in Figure 1.9d. This free energy minimum, featuring a non-uniform or "spontaneously bent" director field, arises mathematically with $K_3 < 0$.
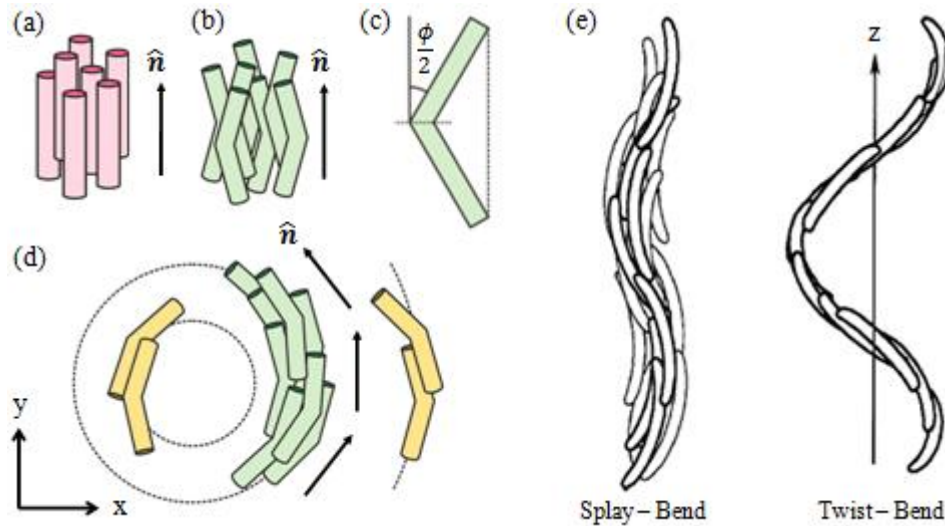
Figure 1.9 – (a) The perfect (idealised) N phase of calamitic mesogens with a uniform director field and $S = 1$. (b) An analogous uniform N phase of bent-core mesogens. (c) Definition of the 'bow-string', exterior half angle and the two 'segments' of each molecule. (d) A bent nematic phase of banana shaped mesogens. The bent director field allows each segment to align approximately parallel to those neighbouring, but only at a particular radius (green). Molecules at a smaller radius are not bent enough to follow the curvature, while molecules at a much larger radius are too bent (yellow). (e) Adapted from [37]. In order to avoid costly defects the bend direction must periodically change direction, producing the N_{sb}, or tilt out of the xy plane, giving the N_{tb} phase.

Geometrically, an exclusively bent state cannot fill space efficiently, i.e. a continuous bend leads to cylindrical curvature with an optimum radius (R_c) determined by the bending angle (Figure 1.9d). Molecules at a radius $< R_c$ are not bent enough to follow the curvature, while molecules at a radius $> R_c$ are too bent, and the average angle between neighbouring mesogenic segments must increase to follow the curvature. Defects are therefore created in the centre and at the edges of the cylinder, increasing the free energy density. This geometric problem can be avoided by periodically

alternating the bend direction or tilting a continuous curvature into the third dimension (out of the plane of the ring). These solutions respectively result in local splay or twist in the polarisation field of the molecular bend, giving rise to the two possible bent nematic ground states: N_{sb} or N_{tb} (Figure 1.9e). A chiral (N_{tb}) phase may therefore be preferential in a system of achiral banana shaped molecules with $K_3 < 0$. The lack of intrinsic molecular chirality should enable simultaneous formation of left and right handed helical domains. Due to broken polar symmetry, the phase should also exhibit electronic switching behaviour, as observed in the lamellar phases of banana shaped mesogens.

1.6.2 – Experimental Confirmation of the N_{tb} Phase

The first nematic-nematic phase transition was actually observed almost 10 years prior to Dozov's mathematical N_{tb} model in a system of main chain LC copolyethers [42,43]; however it has more recently been reported in flexible dimers [44-64] and rigid asymmetric molecules [65]. In all three sample types, the chemically linked mesogens were angled to one another to produce bent molecular/polymer chain conformations, in-line with the theoretical model. Under crossed polarisers the N_{tb} phase is recognised by either focal conic, block-like or rope-like optical textures; the rope-like texture is most frequently reported [44,45] and appears as a series of micron scale stripes on cooling from the N phase (Figure 1.10a). Electronic polarised optical microscopy (E-POM) studies have shown that the stripes may form two coexisting domain types, which can be distinguished by slightly uncrossing the polarisers [44] or by applying an electric field. In the latter case the two domains have been reported to switch in opposing directions (Figure 1.10b,c) and on a timescale consistent with a pitch length <10 nm [41]. The nano-scale pitch length was also supported by freeze fracture transmission electron microscopy (FF-TEM) [46,47] and atomic force microscopy (AFM) [48], which have shown ~8 nm periodicity on the surface of N_{tb} samples (Figures 1.10d and e). These findings support simultaneous presence of both left and right handed domains, as well as helical periodicity. Furthermore the switching behaviour is believed to arise from flexoelectrically driven electroclinicity [41], i.e. field-dependent polar tilting, which is also suggested in Dozov's model [37].
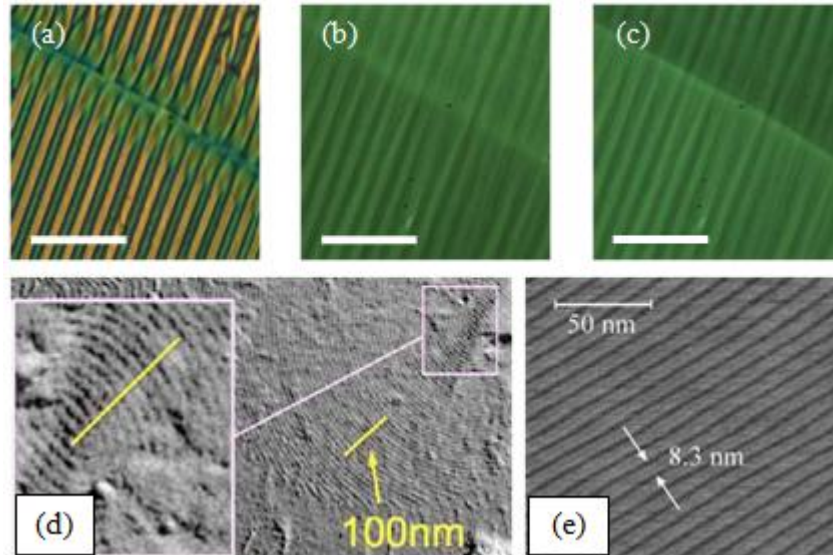
Figure 1.10 – (a-c) Adapted from reference [44]. (a) The rope-like optical texture of the N_{tb} phase with no field. The inverse domains can be identified after applying (b) +200V and (c) -200V across the cell gap. Scale bar = 50 μm. (d) Taken from reference [46]. FF-TEM image of the N_{tb} surface showing 8 nm periodicity. (e) Taken from reference [48]. AFM image of the crystal phase in the same sample as (d); the same periodicity can be identified.

Historically the above claims were widely debated. The stripe of the optical texture was shown to depend on the glass cell gap [45], indicating that the stripes are not thermodynamically stable and do not represent an intrinsic structural periodicity. In fact it was suggested [47] that the stripes represent undulation as a result of the Helfrich-Hurault effect [66,67] observed in smectics and short pitch N* phases. Moreover Panov *et al* [45] provided a similar explanation and pointed out that the texture is indicative of negative K_1 or K_2 (splay and saddle splay deformation), rather than $K_3 < 0$. It was also argued in the same AFM study mentioned above [48], that the periodicity observed on the N_{tb} surface closely resembles focal conic smectic ordering, suggestive of surface crystallisation (Figure 1.10e). Surface crystallisation is highly likely considering that the FF-TEM imaging was performed far below the temperature range of the N_{tb} phase. The electroclinic effect, common in smectic phases, also raised doubt because flexoelectricity is not a direct indicator of chirality and appears as a result polar coupling to splay and bend director deformations; it may therefore be observed in the N phase [68].

Due to the ambiguity of topological characterisation methods, several studies of the bulk phase were conducted, although many of these were also found to be inconclusive. Nuclear magnetic resonance (NMR) studies by Beguin *et al* [49], reported observation of chirality in the N_{tb} phase, evidenced by peak splitting on transition from the N phase. However in a consequent and more complex study by Hoffman *et al* [50], it was explained that the nano-scale helicoidal model of the N_{tb} phase was not directly evidenced by these findings and that the splitting could arise from chiral conformations of the flexible molecules. Raman spectroscopy studies were also performed [51], although this method is only sensitive to chemical bond orientations. Conventional X-ray diffraction experiments confirmed the absence of quasi-long range ordering associated with smectic phases, but also failed to provide solid evidence in support of the helical N_{tb} model [47,52]. In earlier work the lower temperature nematic is often referred to as the 'N_x phase' [44,45,50] due to the lack of conclusive experimental evidence and uncertainty surrounding the N_{tb} classification. However, during the closing stages of this project (May 2016), Zhu *et al* [53] reported the first direct and unambiguous identification of the bulk N_{tb} phase using resonant X-ray diffraction at the carbon absorption edge. Resonant peaks were observed in a flexible dimer compound known as 'CB7CB', corresponding to a temperature dependant helical pitch length of 8-10 nm (Figure 1.11) [53].
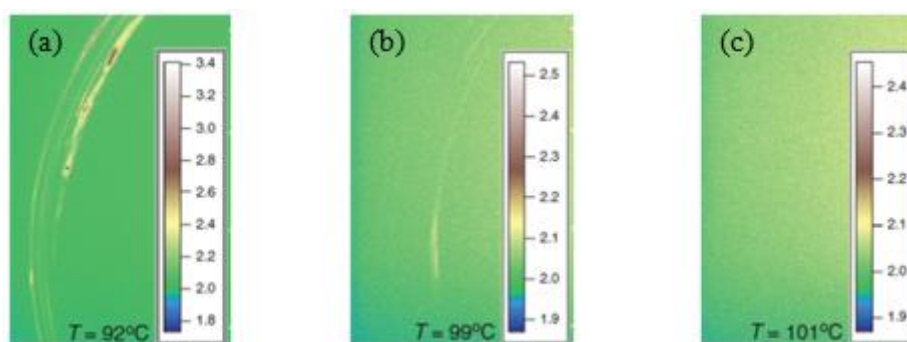
Figure 1.11 – (a-c) Taken from reference [53]. Carbon resonant X-ray diffractograms showing the progressive loss of resonant intensity on transition from the N_{tb} to the N phase. (a) N_{tb} phase, (b) N-N_{tb} boundary and (c) N phase. The resonant intensity arises from a helical pitch length.

Although the existence of the N_{tb} phase has now been experimentally confirmed, previous work offers very little insight into its structure beyond affirming the existence of phase chirality and measurement of the pitch length. Understanding the molecular-level packing inside the helix is of prime importance, as are finding analytical methods that allow one to quantify the extent of orientational and positional organisation in the N_{tb} phase.

1.7 – Self Organisation of Liquid Crystal – Nano-particle Arrays

Ordered superlattices of metallic and semiconductor nano-particles (NPs) are a topic of massive technological interest due to their exotic electromagnetic properties and the diversity of their application; examples include wave-guiding [69], sensing [70], catalysis [71] and electronics [72]. Moreover it has been suggested that highly periodic NP arrangements may lead to negative index materials capable of invisibility cloaking and lensing below the diffraction limit [73]. These functionalities are made possible by delicate resonant interactions between electromagnetic fields and the arrangement of the particles. Precise control over structural symmetry and the inter-particle separation distance are therefore of paramount importance. To date various types of ordered NP arrangements have been achieved by both "top-down" and "bottom up" experimental methods. The top down approach involves processes such as transfer printing, masking and templating, where structural detail is limited by instrumental precision. These methods often produce 2D arrays [74] or 3D close packed structures [75,76]. Alternatively the bottom-up approach relies on self-assembly, where molecules are used to guide the organisation of NPs [77]. In contrast to top-down methods a wide variety of 2D and 3D superlattices may be produced with structural details limited solely by the constituents.

Self organising NP superstructures are achieved by modifying the NPs with organic coatings through ligand coordination bonding. The most common ligand shells incorporate functionalised hydrocarbon chains [78], DNA proteins [79] and liquid crystal mesogens [80]. The attached molecules transform the NPs into supramolecular building blocks, enabling Van der Waals interactions, interfacial surface effects and steric anisotropy to determine the most efficient packing method. In a study by Mang *et al* [81] it has been shown that small changes in the chemical composition and surface

density of the attached molecules can have a profound impact on the structural properties of the resulting assembly. Careful design of the organic shell or "corona" can therefore lead to a variety of 2D and 3D superlattices with tuneable (temperature dependent) interparticle separation distances (see Figure 1.12). In this thesis, 3D NP arrangements are facilitated by an organic corona comprising macromolecules known as dendrons.
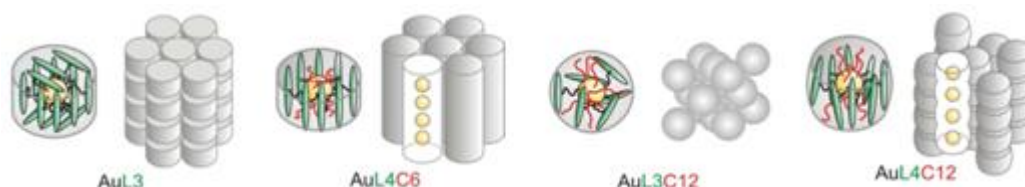
Figure 1.12 – Adapted from reference [81]. Gold NPs with laterally attached calamitic mesogens. The notation AuL(m)C(n) describes the composition of the supramolecular building blocks, where 'm' is the number of aromatic rings in the mesogens and 'n' is the number of free alkyl chains (not attached to a mesogen) in the corona.

1.7.1 – Organisational Properties of Dendritic Systems

Dendrons and dendrimers are branched, tree-like macromolecules that spread radially from a chemically addressable group known as the focal point. The focal point of a dendron has only one chemically addressable group, whereas that of a dendrimer has multiple. A dendron can therefore be thought of as a single section of a dendrimer. In the context of divergent synthesis, dendritic molecules are grown outward from the focal point by repeated cycles of coupling and activation reactions of the monomer branching units [82]. Each added layer of branching units defines the 'generation' of the dendron as shown diagrammatically in Figure 1.13. Ideally dendrons grow uniformly, but after several generations overcrowding may begin to hinder branching reactions, leading to inhomogeneity [82]; i.e. branches with blocked reaction sites will be shorter than intended. In order to avoid incomplete branching reactions and improve uniformity, a convergent synthesis method was developed in 1990 by Hawker and Fréchet [83], where the branches are grown inward from the terminal groups. The chemical compositions of the terminal groups often dictate the functional properties of the dendrons. The tailorable binding properties of dendritic macromolecules and their ability to encapsulate guest particles makes them excellent candidates for applications involving drug delivery [84], sensing [85] and nano-particle self-assembly [86].
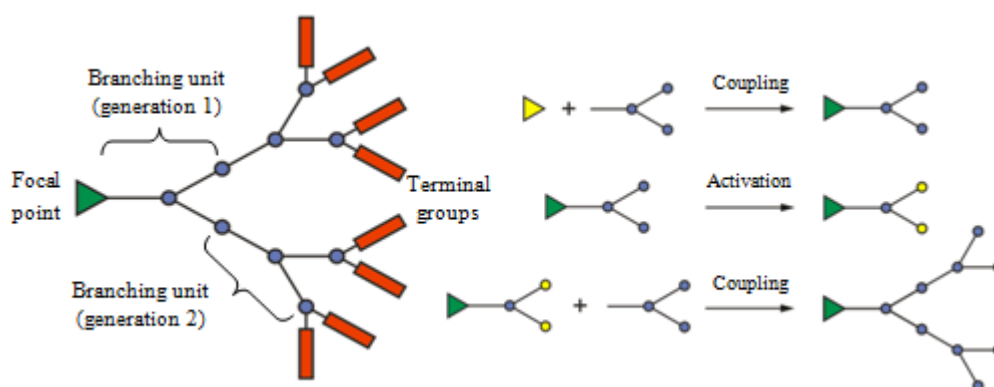
Figure 1.13 − A simplified structure of a 2nd generation dendron and the basic principle of divergent synthesis. In the convergent synthesis approach, the initial coupling reaction starts with the terminal groups rather than the focal point.

Dendrons may form several temperature dependent mesophases due to their ability to mould into building blocks of different shape. This is best demonstrated in a study by Percec *et al* [87], where the molecular conformation was found to morph from wedges to discs, and finally to spherical dendrimers with increasing temperature (see Figure 1.14). In the wedge conformation the dendrons packed into smectic phases, which transformed into square (*p2mm*), rectangular (*c2mm*) and hexagonal (*p6mm*) columnar phases when the dendrons assumed the disc-like conformation. With increased temperature, dendrimer superlattices were formed with 3D cubic ($Pm\overline{3}n$, $Im\overline{3}m$) and tetragonal ($P4_2/mnm$) symmetries.

In addition to their intrinsic organisational properties, dendrons have proven to be effective driving molecules for the self-assembly of interesting 3D ordered NP superlattices. In 2007 a study by B. Donnio *et al* [88] demonstrated that dendron encapsulated gold NPs led to 3D body centred cubic (BCC) and 2D hexagonal columnar phases with ferromagnetic properties up to 400K. In a more recent work an unexpected simple cubic ($Pm\overline{3}n$) packing arrangement was observed in a system of gold NPs coated with a two layer corona of alkyl chains (inner layer) and dendrons (outer layer) [89]. Simple cubic packing is a highly inefficient packing method for spherical objects due to the large voids that are created inside the structure. However despite the irregularity of this packing method, the self organisation of NP superlattices appears to be limited to

high symmetry structures that typically possess one or more mirror planes. The first low symmetry array of dendronised NPs is presented in Chapter 6.
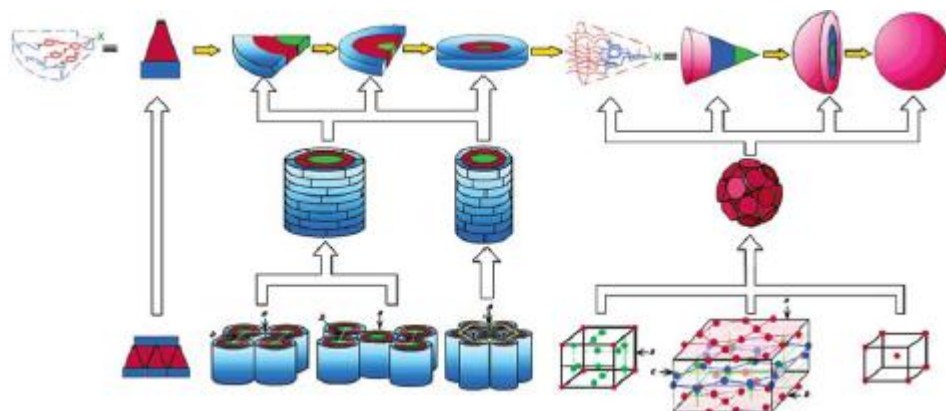
Figure 1.14 – Adapted from reference [85]. Diagrammatic representation of the wedge and cone-like conformations of dendron molecules and the various structures that can result. With increasing temperature from left to right: Smectic phases, 2D columnar and 3D superlattices.

References to Chapter 1

[1]   F. Reinitzer, *Wiener Monatscher Chemie*, 1888, **9**, 421. 2.

[2]   F. Reinitzer, *(English Translation) Liq. Cryst.*, 1989, **5**, 7.

[3]   P. J. Collings, M. Hird (1997). "*Introduction to Liquid Crystals: Chemistry and Physics*", London, Taylor and Francis.

[4]   E. B. Priestly, P. J. Wojtowicz, P. Sheng (Eds.) (1974). "*Introduction to Liquid crystals*", Princton, New Jersey, RCA Laboratories.

[5]   R. H. Chen (2011). "*Liquid Crystal Displays: Fundamental Physics and Applications*", Series: Display Technologies, Wiley-SID.

[6]   Z. Ge, S.-T. Wu (2010). "*Transflective Liquid Crystal Displays*" Series: Display Technologies, Wiley-SID.

[7]   A. M. Figueiredo Neto, S. R. A. Salinas (2005). "*The physics of Lyotropic Liquid Crystals: Phase Transitions and Structural Properties*", Oxford University Press.

[8]   S. Chandrasekhar (1992). "*Liquid Crystals*", 2nd Ed., Cambridge University Press.

[9]   E. I. Kats, *Sov. Phys. JETP*, 1976, **43**, 726.

[10]   W. M. Gibbons, P. J. Shannon, S.-T. Sun, B. J. Swetlin, *Nature*, 1991, **351**, 49.

[11] D.-K. Yang, S.-T. Wu (2014). "*Fundamentals of Liquid Crystal devices*" 2nd Ed., Chapter 4, Series: Display Technologies, Wiley-SID.

[12] I. Dierking (2003). "*Texture of Liquid Crystals*", Wiley VCH.

[13] B. I. Bleaney, B. Bleaney (1976). "*Electricity and magnetism*" Vol. 2, 3rd Ed, Oxford University Press.

[14] P. Oswald, P. Pieranski (2005). "*Smectic and Columnar Liquid Crystals: Concepts and Physical Properties Illustrated By Experiments*", Bosa Roca, U.S., Taylor and Francis.

[15] G. W. Gray, J. W. G. Goodby (1984), "*Smectic Liquid Crystals: Textures and Structures*", Leonard Hill.

[16] P. G. De Gennes, J. Prost (1995), "*The Physics of Liquid Crystals*", 2nd Ed, Oxford University Press.

[17] H. Kitzerow, C. Bahr (Eds.) (2001). "*Chirality in Liquid Crystals*", Springer-Verlag New York.

[18] M. A. Osipov, M. V. Gorkinov, *Liquis Crsytals*, 2009, **36**, 1281.

[19] H. Takezoe, K. Kondo, K. Miyasato, S. Abe, T. Tsuchiya, A. Fukunda, E. Kuze, *Ferroelectrics*, 1984, **58**, 55.

[20] I. Nishiyama, A. Yoshizawa, M. Fukumasa, T. Hirai, *Jpn. J. Appl. Phys.*, 1989, **28**, L2248.

[21] A. Fukunda, H. Hakoi, M. Sato, M. A. Osipov, *Mol. Cryst. Liq. Cryst.*, 2003, **398**, 169.

[22] I. Mušević and M. Škarabot, *Phys. Rev. E*, 2001, **64**, 051706.

[23] E. Gorecka, A. D. L. Chandani, Y. Ouchi, H. Takezoe, A. Fukunda, *Jpn. J. Appl. Phys.*, 1990, **29**, 131.

[24] A. Jákli, C. Bailey, J. Harden, Chapter 2 in "*Thermotropic Liquid Crystals: Recent Advances*", A. Ramamoorthy (Ed.) (2007), Springer Netherlands, pp. 59.

[25] E. Gorecka, N. Vaupotič, D. Pociecha, M. Čepič, J. Mieczkowski, *ChemPhysChem*, 2005, **6**, 1087.

[26] J. Watanabe, T. Niori, T. Sekine, H. Takezoe, *Jpn. J. Appl. Phys.*, 1998, **37**, L139.

[27] Y. Takanishi, M. Toshimitsu, M. Nakata, T. Izumi, K. Ishikawa, H. Takezoe, J. Watanabe, Y. Takahashi, A. Iida. *Phys. Rev. E*, 2006, **74**, 051703.

[28] J. P. Bedel, J.C. Rouillon, J. P. Marcerou, M. Laguerre, H. T. Nguyen, M. F. Archard, *J. Mater. Chem.*, 2002, **12**, 2214.

[29] W. Weissflog, C. Lischka, I. Benne, T. Scharf, G. Pelzl, S. Diele, H. Kruth, *Proc. SPIE: Int. Soc. Opt. Eng.*, 1998, **3319**, 14.

[30] S. Diele, S. Grande, H. Kruth, C. Lischka, G. Pelzl, W. Weissflog, I. Wirth, *Ferroelectrics*, 1998, **212**, 169.

[31] G. Pelzl, S. Diele, W. Weissflog, *Adv, Mater.*, 1999, **11**, 707.

[32] P. J. Le Masurier, G. R. Luckhurst, *J. Chem. Soc., Faraday Tran.*, 1998, **94**, 1593.

[33] A. E. Blatch. I. D. Fletcher, G. R. Luckhurst, *Liq. Cryst.*, 1995, **18**, 801.

[34] D. A. Coleman, J. Fernsler, N. Chattham, M. Nakata, Y. Takanishi, E. Korblova, D. R. Link, R. F. Shao, W. G. Jang, J. E. Maclennan, O. Mondainn-Monval, C. Boyer, W. Weissflog, G. Pelzl, L. C. Chien, J. Zasadzinski, J. Wantanabe, D. M. Walba, H. Takezoe, N. A. Clark, *Science*, 2003, **301**, 1204.

[35] D. A. Coleman, C. D. Jones, M. Nakata, N. A. Clarke, D. M. Walba, W. Wiessflog, K. Fodor-Csorba, J.Wantanabe, V. Novotna, V. Hamplova, *Phys. Rev. E*, 2008, **77**, 021703.

[36] R. Meyer, in *"Molecular Fluids"*, R. Balian and G. Weil, (Eds.) (1976), Gordon and Breach, New York.

[37] I. Dozov, *Europhys. Lett*. 2001, **56**, 247.

[38] R. Memmer, *Liq. Cryst.*, 2002, **29**, 483.

[39] A. Ramamoorthy (Ed.) (2007). *"Thermotropic Liquid Crystals: Recent Advances"*, Springer Netherlands, pp. 64.

[40] M. B. Ros, J. L. Serrano, M. R. de la Fuente, C. L. Folcia, *J. Mater. Chem.*, 2005, **15**, 5093.

[41] C. Meyer, G. R. Luckhurst, I. Dozov, *Phys. Rev. Lett.*, 2013, **111**, 067801.

[42] G. Ungar, V. Percec, M. Zuber. *Macromolecules*, 1992, **25**, 75.

[43] G. Ungar, V. Percec, M. Zuber, *Polymer Bulletin*, 1994, **32**, 325.

[44] V. P. Panov, R. Balachandran, M. Nagaraj, J. K. Vij, M. G. Tamba, A. Kohlmeier, G. H. Mehl, *App. Phys. Lett.*, 2011, **99**, 261903.

[45] V. P. Panov, M. Nagaraj, J. K. Vij, Yu. P. Panarin, A. Kohlmeier, M. G. Tamba, R. A. Lewis, G. H. Mehl, *Phys. Rev. Lett.*, 2010, **105**, 167801.

[46] D. Chen, J. H. Porada, J. B. Hooper, A. Klittnick, Y. Shen, M. R.Tuchband, E. Korblova, D. Bedrov, D. M.Walba, M. A. Glaser, J. E. Maclennan, and N. A. Clark, *Proc. Natl. Acad. Sci. U.S.A.*, 2013, **110**, 15931.

[47] V. Borshch,Y.-K. Kim, J. Xiang, M. Gao, A. J´akli, V. P. Panov, J. K. Vij, C. T. Imrie, M. G. Tamba, G. H. Mehl, O. D. Lavrentovich, *Nat. Commun.*, 2013, **4**, 2635.

[48] E. Gorecka, M. Salamonczyk, A. Zep, D. Pociecha, C.Welch, Z. Ahmed, G. H. Mehl, *Liq. Cryst.*, 2015, **42**, 1.

[49] L. Beguin, J. W. Emsley, M. Lelli, A. Lesage, G. R. Luckhurst, B. A. Timimi, H. Zimmermann, *J. Phys. Chem. B*, 2012, **116**, 7940.

[50] A. Hoffmann, A. G. Vanakaras, A. Kohlmeier, G. H. Mehl, D. J. Photinos, *Soft Matter*, 2015, **11**, 850.

[51] Z. Zhang, V. P. Panov, M. Nagaraj, R. J. Mandle, J. W. Goodby, G. R. Luckhurst, J. C. Jones, H. F. Gleeson. *J. Mater. Chem. C*, 2015, **3**, 10007.

[52] K. Adlem, M. Čopič, G. R. Luckhurst, A. Mertelj, O. Parri, R. M. Richardson, B. D. Snow, B. A. Timimi, R. P. Tuffin, and D. Wilkes, *Phys. Rev. E*, 2013, **88**, 022503.

[53] C. Zhu, M. R. Tuchband, A. Young, M. Shuai, A. Scarbrough, D. M. Walba, J. E. Maclennan, C.Wang, A. Hexemer, N. A. Clark, *PRL*, 2016, **116**, 147803.

[54] N. Sebastián, M. G. Tamba, R. Stannarius, M. R. de la Fuente, M. Salamonczyk, G. Cukrov, J. Gleeson, S. Sprunt, A. Jákli, C. Welch, Z. Ahmed, G. H. Mehl, A. Eremin, *Phys. Chem. Chem. Phys.*, 2016, **18**, 19299.

[55] S. A. Pardaev, S. Shamid, M. G. Tamba, C. Welch, G. H. Mehl, J. T. Gleeson, D. Allender, J. V. Selinger, B. D. Ellman, A. Jakli, S. Sprunt, *Soft Matter*, 2016, **12**, 4472.

[56] C. Meyer, G. R. Luckhurst, I. Dozov, *J. Mater. Chem. C*, 2015, **3**, 318.

[57] S. M. Salili, C. Kim, S. Sprunt, J. T. Gleeson, O. Parri, A. Jákli, *RSC Adv.*, 2014, **4**, 57423.

[58] M. G. Tamba, S. M. Salili, C. Zhang, A. Jákli, G. H. Mehl, R. Stannarius, A. Eremin, *RSC Adv.*, 2015, **5**, 11207.

[59] P. A. Henderson, C. T. Imrie, *Liq. Cryst.*, 2011, **38**, 1407.

[60] M. Cestari, E. Frezza, A. Ferrarini, G. R. Luckhurst, *J. Mater. Chem.*, 2011, **21**, 12303.

[61] P. K. Challa, V. Borshch, O. Parri, C. T. Imrie, S. N. Sprunt, J. T. Gleeson, O. D. Lavrentovich, A. Jákli, *Phys. Rev. E*, 2014, **89**, 060501.

[62] M. Cestari, S. Diez-Berart, D. A. Dunmur, A. Ferrarini, M. R. de la Fuente, D. J. B. Jackson, D. O. Lopez, G. R. Luckhurst, M. A. Perez-Jubindo, R. M. Richardson, J. Salud, B. A. Timimi, and H. Zimmermann, *Phys. Rev. E*, 2011, **84**, 031704.

[63] A. A. Dawood, M.C. Grossel, G. R. Luckhurst, R. M. Richardson, B. A. Timimi, N. J. Wells, Y. Z. Yousif, *Liq. Crsyt.*, 2016, **43**, 2.

[64] A. A. Dawood, M.C. Grossel, G. R. Luckhurst, R. M. Richardson, B. A. Timimi, N. J. Wells, Y. Z. Yousif, *Liq. Crsyt.*, 2017, **44**, 106.

[65] D. Chen, M. Nakata, R. Shao, M. R. Tuchband, M. Shuai, U. Baumeister, W. Weissflog, D. M. Walba, M. A. Glaser, J. E. Maclennan, N. A. Clarke, *Phys. Rev. E*, 2014, **89**, 022506.

[66] G. Napoli, A. Nobili, *Phys. Rev. E*, 2009, **80**, 031710.

[67] B. I. Senyuk, I. I. Smalyukh, O. D. Lavrentovich, *Phys. Rev. E*, 2006, **74**, 011712.

[68] A. Buka, N. Eber (Eds.) (2012). "*Flexoelectricity in Liquid Crystals: Theory, Experiments and Applications*", Imperial College Press, London.

[69] S. Zou, G. C. Schatz, *Phys. Rev. B*, 2006, **74**, 125111.

[70] N. S. Lynn Jr., J. Homola, *Anal., Chem.*, 2016, **88**, 12145.

[71] S. Jahn, S. J. Lechner, H. Freichels, M. Möller, J. P. Spatz, *Sci. Rep.*, 2016, **6**, 20536.

[72] M. C. Beard, G. M. Turner, J. E. Murphy, O. I. Micic, M. C. Hanna, A. J. Nozik, C. A. Schmuttenmaer, *Nano Lett.*, 2003, **3**, 1695.

[73] P. Alitalo, C. Simovski, A. Viitanen, S. Tretyakov, *Phys. Rev. B*, 2006, **74**, 235425.

[74] C. H. Lin, L. Jiang, Y. H. Chai, H. Xiao, S. J. Chen, H. L. Tsai, *Appl. Phys. A*, 2010, **98**, 855.

[75] J. Liao, X. Li, Y. Wang, C. Zhang, J. Sun, C. Duan, Q. Chen, L. Peng, *Small*, 2012, **8**, 991.

[76] Y. Wang, C. Duan, L. Peng, J. Liao, *Sci. Rep.*, 2014, **4**, 7565.

[77] X. Zeng, F. Liu, A. G. Fowler, G. Ungar, L. Cseh, G. H. Mehl, J. E. Macdonald, *Adv. Mater.*, 2009, **21**, 1746.

[78] G. H. Woehrle, L. O. Brown, J. E. Hutchison, *J. Am, Chem. Soc.*, 2005, **127**, 2172.

[79] S. Y. Park, A. K. R. Lytton-Jean, B. Lee, S. Weigand, G. C. Schatz, C. A. Mirkin, *Nat. Lett.*, 2008, **451**, 553. yguucu

[80] O. Tsutsumi, K. Yamamoto, K. Ohta, K. Fujisawa, K. Uno, T. Hashishin, *Mol. Cryst. Liq. Cryst.*, 2011, **550**, 105.

[81] X. Mang, X. Zeng, B. Tang, F. Liu, G. Ungar, R. Zhang, L. Cseh, G. H. Mehl, *J. Mater. Chem.*, 2012, **22**, 11101.

[82] G. R. NewKome, C. N. Moorefield, F. Vögtle (2001). "*Dendrimers and Dendrons: Concepts, Syntheses, Applications*", Weinheim, Wiley-VCH.

[83] C. J. Hawker, J. M. J. Frechet, J. Am. Chem. Soc., 1990, **112**, 7638.

[84] K. Madaan, S. Kumar, N. Poonia, V. Lather, D. Pandita, *J. Pharm. Bioallied Sci.*, 2014, **6**, 139.

[85] N. I. Georgiev, A. M. Asiri A. H. Qusti, K. A. Alamry, V. B. Bojinov, *Sens. Act. B: Chem.*, 2014, **190**, 185.

[86] X. Y. Ling, D. N. Reinhoudt, J. Huskens, *Pure Appl. Chem.*, 2009, **81**, 2225.

[87] V. Percec, C. M. Mitchell, W. D. Cho, S. Uchida, M. Glodde, G. Ungar, X. B. Zeng, Y. S. Liu, V. S. K. Balagurusamy, P. A. Heiney, *J. Am. Chem. Soc.,* 2004, **126**, 6078.

[88] B. Donnio, P. García-Vázquez, J.-L.Gallani, D. Guillon, E. Terazzi, *Adv. Mater.*, 2007, **19**, 3534.

[89] K. Kanie, M. Matsubara, X. Zeng, F. Liu, G. Ungar, H. Nakamura, A. Muramatsu, *J. Am. Chem. Soc*, 2012, **134**, 808.

Chapter 2 – Experimental Techniques and Analyses

2.0 – Introduction

The theoretical and analytical principles of X-ray scattering (XS), polarised optical microscopy (POM) and polarised Infrared (IR) spectroscopy are introduced, with particular emphasis on XS. Electronic circular dichroism (ECD) and differential scanning calorimetry (DSC) also featured in the project, but the data analyses presented later are basic and so the technicalities are not discussed in detail here.

2.1 – Theoretical Principles of X-ray Diffraction [1-10]

When a beam of monochromatic X-rays is incident upon a distribution of atoms, the electromagnetic field accelerates the electrons, causing them to emit radiation of the same frequency. This phenomenon is referred to as elastic or 'Thompson' scattering. Electrons scatter the radiation in all directions, effectively transforming the atoms into point source emitters of coherent X-rays. In most directions the waves destructively interfere and their amplitudes cancel due to phase mismatch. However along structure specific vectors, the waves propagate in phase leading to constructive interference and observable intensity. The 'diffracted' intensity distribution can then be used to map the electron density inside a given material, providing important information on the spatial relationship between the constituent atoms or molecules.

2.1.1 – Diffraction Conditions
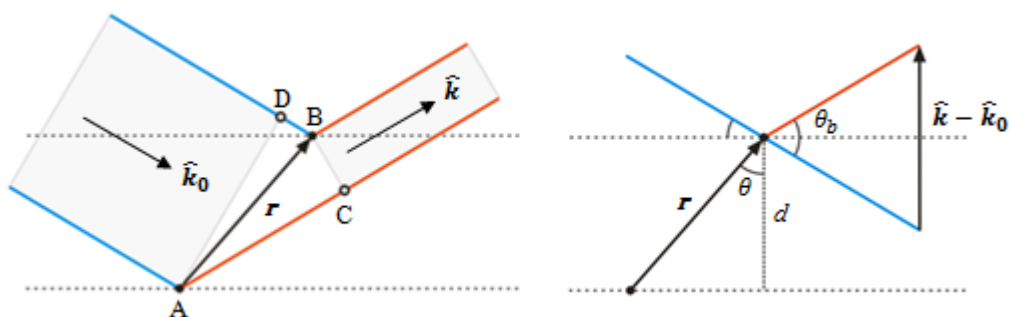
Figure 2.0 – Path difference between X-rays scattered at two different points.

The conditions for constructive interference can be determined mathematically by considering the path difference between waves scattered at points A and B, separated by a distance r (Figure 2.0). From simple geometry, the path difference between the two waves is AC + BD, which can be written in vector notation as:

$$L_p = (\mathbf{r} \cdot \mathbf{k}) - (\mathbf{r} \cdot \mathbf{k_0}) \tag{2.0}$$

If the incident and scattered wave vectors are respectively defined as $\mathbf{k_0} = \frac{2\pi}{\lambda}\widehat{\mathbf{k}}_0$ and $\mathbf{k} = \frac{2\pi}{\lambda}\widehat{\mathbf{k}}$, the phase difference between the waves is:

$$\delta_p = \frac{2\pi}{\lambda} \mathbf{r} \cdot (\widehat{\mathbf{k}} - \widehat{\mathbf{k}}_0), \tag{2.1}$$

which becomes $\mathbf{r} \cdot \mathbf{q}$ if one defines the vector $\mathbf{q}$ as:

$$\mathbf{q} = \frac{2\pi}{\lambda}(\widehat{\mathbf{k}} - \widehat{\mathbf{k}}_0) \tag{2.2}$$

In order to observe constructive interference the scattered waves must propagate in phase, which means that the phase difference between them must equal an integer multiple of 2π, I.e. $\mathbf{r} \cdot \mathbf{q} = 2\pi n$. This can equivalently be written:

$$|r||q|cos(\theta) = 2\pi n \tag{2.3}$$

where (from geometry in Figure 2.0):

$$|r|cos(\theta) = d \quad \text{and} \quad |q| = \frac{4\pi}{\lambda}sin(\theta_b) \tag{2.4}$$

Inserting these into equation 2.3 (and re-arranging) we arrive at:

$$2dsin(\theta_b) = n\lambda \tag{2.5}$$

Equation 2.5 is famously known as Bragg's law of diffraction, which explains that constructive interference can only be observed if the path difference between scattered X-rays is equal to an integer number of wavelengths. If the scattering bodies lie on a set of planes of fixed distance, d, this condition is satisfied only for a single magnitude of θ_b, referred to as the Bragg angle. It should be noted that the diffraction angle, i.e. the angle between the incident and scattered wave vectors, is $2\theta_b$.

2.1.2 – Scattered Intensity and Reciprocal Space

Scattering by a single unbound electron was first described by J. J. Thompson, where the intensity scattered through an angle 2θ, at a distance x from the electron is:

$$I = I_0 \left(\mu_0/4\pi\right)^2 \left(e^4/m^2 x^2\right) P_f \qquad (2.6)$$

$$P_f = \begin{cases} \cos^2(2\theta) & Polarised \\ \left(1 + \cos^2(2\theta)\right)/2 & Unpolarised \end{cases}$$

where I_0 is the incident intensity, μ_0 is the permeability of free space, e is the charge of an electron, m_e is the mass of an electron and P_f is the 'polarisation factor', which takes into account the polarisation state of incident radiation. The square root of equation 2.6 gives the amplitude of the wave scattered by a single electron:

$$A_s = \sqrt{I_0 P_f} \left(\mu_0/4\pi\right) \left(e^2/m_e x\right) \qquad (2.7)$$

Real materials contain a vast number of electrons and it is therefore more realistic to consider the intensity scattered by an electron distribution, taking into account interference effects. If points A and B in Figure 2.0 now represent two spherical volume elements inside a material with uniform electron density $\rho(r)$, the number of electrons in each volume element is $\rho(r)\delta r$. The amplitude of the wave scattered by a single volume element of the material is then $A_s\rho(r)\delta r$ i.e. the number of electrons in the element, multiplied by the scattering amplitude of a single electron. Recalling the phase relationship derived in 2.1.1, the amplitude contribution of the second volume element to the scattered wave is:

$$A = A_s\rho(\mathbf{r})\delta\mathbf{r} \ \exp(i\,\mathbf{r}\cdot\mathbf{q}) \qquad (2.8)$$

Integrating equation 2.8 over all space summates the amplitude contribution of all volume elements inside the material to the scattered wave. The total amplitude of the wave scattered by the material is therefore:

$$F(\mathbf{q}) = A_s \int \rho(\mathbf{r})\exp(i\,\mathbf{r}\cdot\mathbf{q})\,d\mathbf{r} \qquad (2.9)$$

with an observable intensity:

$$I(\mathbf{q}) = F(\mathbf{q})F^*(\mathbf{q}) \qquad (2.10)$$

Here $F^*(\boldsymbol{q})$ is the complex conjugate of $F(\boldsymbol{q})$. In this thesis the factor A_s is ignored because absolute intensity is irrelevant in structure determination, only relative intensity is required. For this reason, scaling factors and constants will be neglected in the future derivations.

Position and momentum are an example of Pontryagin duality, which means that the scattered wave in momentum space $F(\boldsymbol{q})$ and the electron density in position (real) space $\rho(\boldsymbol{r})$ may be related by Fourier transform: (limits are $\pm\infty$ and factors outside the integral are ignored)

$$\rho(\boldsymbol{r}) = \int F(\boldsymbol{q})\exp(-i\,\boldsymbol{r}\cdot\boldsymbol{q})\,d\boldsymbol{q}$$
$$F(\boldsymbol{q}) = \int \rho(\boldsymbol{r})\exp(i\,\boldsymbol{r}\cdot\boldsymbol{q})\,d\boldsymbol{r}$$

There are two fundamental properties of Fourier transformation that are important to later discussion: (1) if two functions are added together, the transformation of the sum is equivalent to the added transforms of the two separate functions. (2) If a function is rotated, the transform is also rotated by an equal angle (in the same direction) about a parallel axis. These properties will be recalled further on.

The link between momentum and real space can be shown geometrically using the Ewald construction (Figure 2.1). The origin of momentum space O' lies at the surface of a sphere, which is centred at the origin of real space O, with a radius equal to $|\boldsymbol{k}|$. In the remainder of this thesis, momentum space will be referred to as 'reciprocal space' due to the inverse relationship between real space length and momentum vector magnitude. The reciprocal relationship $|\boldsymbol{q}| = 2\pi/d$, can be derived by equating λ in equations 2.4 and 2.5. The Ewald sphere is an important concept for understanding X-ray diffraction patterns; only $\boldsymbol{q}$ vectors terminating on the surface of the figurative sphere satisfy the angular condition of Bragg's law and produce observable intensity.
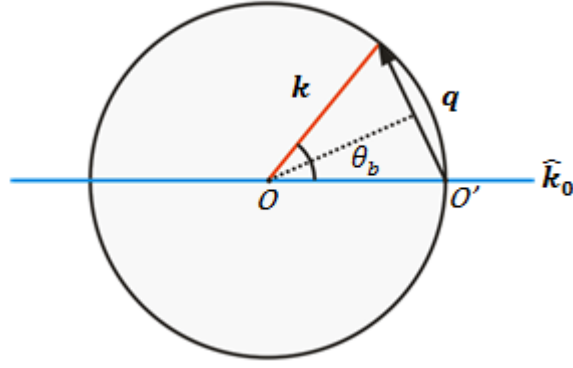
Figure 2.1 – Geometry of the Ewald sphere.

2.1.3 – X-ray Scattering from Molecular Systems and Liquid Crystals

The scattering amplitude of a single atom with a spherically averaged electron density distribution is described by the atomic form factor:

$$f(\boldsymbol{q}) = \int \rho(\boldsymbol{r})\,\text{sinc}(qr)d\boldsymbol{r} \qquad (2.11)$$

where $\text{sinc}(x) = \sin(x)/x$. Here only the modulus of $\boldsymbol{r} \cdot \boldsymbol{q}$ is necessary due to the spherical centro-symmetry of the electron density distribution. Recalling the fundamental properties of Fourier transformation, the transform of a molecule can be found by summating the transform of each constituent atom, taking into account phase differences arising from their positions:

$$F(\boldsymbol{q}) = \sum_j f_j(\boldsymbol{q})\exp{(i\,\boldsymbol{r_j} \cdot \boldsymbol{q})} \qquad (2.12)$$

Here f_j is the atomic form factor of the jth atom and r_j is its position in respect to the atom that defines the origin. From equation 2.10 it follows that the scattered intensity in reciprocal space is:

$$
\begin{aligned}
I(\boldsymbol{q}) &= \sum_j F_j(\boldsymbol{q})\exp{(i\,\boldsymbol{q} \cdot \boldsymbol{r_j})} \sum_k F_k(\boldsymbol{q})\exp(-i\,\boldsymbol{q} \cdot \boldsymbol{r_k}) \\
&= \sum_j \sum_k F_j(\boldsymbol{q})F_k(\boldsymbol{q})\exp{\left(i\,\boldsymbol{q} \cdot \boldsymbol{r_{jk}}\right)} \\
&= \sum_j F_j{}^2(\boldsymbol{q}) + \sum_j \sum_{k \neq j} F_j(\boldsymbol{q})F_k(\boldsymbol{q})\exp{\left(i\,\boldsymbol{q} \cdot \boldsymbol{r_{jk}}\right)} \\
&= |F(\boldsymbol{q})|^2\left[1 + {}^1\!/_N \sum_j \sum_{k \neq j}\exp{\left(i\,\boldsymbol{q} \cdot \boldsymbol{r_{jk}}\right)}\right] \\
&= |F(\boldsymbol{q})|^2 S(\boldsymbol{q}) \qquad (2.13)
\end{aligned}
$$

where $\boldsymbol{r_{jk}}(= \boldsymbol{r_j} - \boldsymbol{r_k})$ is the vector separation of the jth and k^{th} molecule and N is the number of molecules being considered. $S(\boldsymbol{q})$ is known as the interference function,

which accounts for interference effects between molecules. In the case of a single molecule or an ideal gas, $S(\boldsymbol{q})$ can be ignored and the scattered intensity is simply $I(\boldsymbol{q}) = |F(\boldsymbol{q})|^2$, i.e. the structure factor of the molecule. However in liquid crystals, there are many molecules and their positions influence their neighbours much more strongly. This means that intermolecular interference cannot be ignored and the entirety of equation 2.13 is required.

In the derivation of equation 2.13 $S(\boldsymbol{q})$ is written as a summation, which suffices only when the positional relationship between molecules is known, such as in a perfect crystal lattice. However in a nematic liquid crystal phase, the organisation is fluid-like, meaning that molecular density is not distributed among an ordered set of points. In this case the positional arrangement of the molecules must be treated statistically and the summation must be replaced by an integral of the form:

$$S(\boldsymbol{q}) = 1 + \int g(\boldsymbol{r})\exp\left(i\,\boldsymbol{r}\cdot\boldsymbol{q}\right)d\boldsymbol{r}$$

where $g(\boldsymbol{r})$ is the radial distribution function. The integral is over all space, meaning that $S(\boldsymbol{q})$ -1 and $g(\boldsymbol{r})$ -1 are related by Fourier transform. The radial distribution function describes the probability of finding a molecule at a distance $\boldsymbol{r} + \delta\boldsymbol{r}$ from a molecule of reference. Peaks are encountered in $g(\boldsymbol{r})$ for highly repeated intermolecular separation distances inside the volume of the material; i.e. the peak height depends on how often the corresponding distance is encountered inside the volume. In the case of nematics and amorphous materials, intermolecular correlation falls rapidly with distance from the origin, which means that the strongest peaks in $g(\boldsymbol{r})$ often correspond to the distances between a reference molecule and its closest neighbours. As the molecules do not share a strict positional relationship, intermolecular spacings are represented by small distributions around an average value. Spacing distributions produce broad peaks in $g(\boldsymbol{r})$ and $S(\boldsymbol{q})$, hence broad scattering peaks in $I(\boldsymbol{q})$. In the case of smectic liquid crystals a combination of sharp and broad scattering peaks appear in $S(\boldsymbol{q})$. This is because the layer spacing is fixed and regularly repeated (strong, sharp peak in $g(\boldsymbol{r})$), while separation distances inside the layers are nematic-like (weaker, broad peak in $g(\boldsymbol{r})$).

2.1.4 – X-ray Diffraction from Nanoparticle Superlattices

A lattice is a highly periodic series of points in space, which are related by symmetry elements such as translation, rotation and inversion. The smallest group of points that can be repeated to reproduce the entire lattice is known as the unit cell. In 3D the unit cell is described by lattice vectors a, b and c, which are defined in real space by the Cartesian coordinate system. The angles between these vectors are usually denoted α, β and γ, but only the mutually orthogonal case is encountered in this thesis and so they may be ignored. The distance from the origin to any point inside the unit cell is calculated according to:

$$r = xa + yb + zc \qquad (2.14)$$

where x, y and z are fractional coordinates (values between zero and one) along the respective lattice vectors.
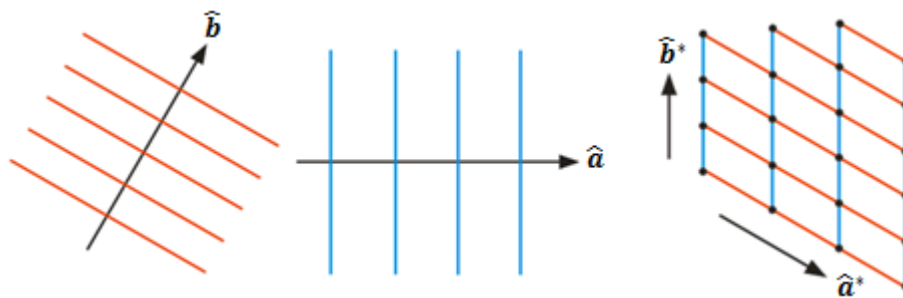
Figure 2.2 – The periodicity along each real space lattice vector gives a series of orthogonal planes in reciprocal space. The convolution of the planes gives the reciprocal lattice. The intensity in reciprocal space is non-zero only where the planes intersect (shown here in 2D). An example with angled lattice vectors was selected to better illustrate the principles.

The Fourier transform of the periodicity along each lattice vector is non-zero only on a set of perpendicular planes spaced $2\pi/a$, $2\pi/b$ and $2\pi/c$ apart, respectively (Figure 2.2). The sum of the three transforms gives the Fourier transformation of the whole 3D lattice, which is non-zero only where the three sets of planes intersect, i.e. on a set of points. The points where the transform is non-zero define the 'reciprocal lattice', which can similarly be defined by reciprocal lattice vectors a^*, b^* and c^*. The relationship between the real space and reciprocal lattice vectors are explained by the following conditions:

$$a \cdot a^* = 2\pi \quad a \cdot b^* = 0 \quad a \cdot c^* = 0$$
$$b \cdot a^* = 0 \quad b \cdot b^* = 2\pi \quad b \cdot c^* = 0$$
$$c \cdot a^* = 0 \quad c \cdot b^* = 0 \quad c \cdot c^* = 2\pi$$

By convention the reciprocal lattice is labelled by Miller indices, h, k and l, which describe the location of each reciprocal lattice point as an integer number of translations along a^*, b^* and c^* from the origin of reciprocal space. The vector q may therefore be written:

$$q_{hkl} = (ha^* + kb^* + lc^*) \tag{2.15}$$

$$= 2\pi\left(h/a + k/b + l/c\right)$$

From the reciprocal relationship described earlier one may also derive:

$$1/d_{hkl} = \left(h/a + k/b + l/c\right) \tag{2.16}$$

In the case of an atomic crystal lattice, the phase difference between scattered wave components $(r \cdot q)$ is $2\pi (hx + ky + lz)$; equation 2.12 therefore becomes:

$$F(hkl) = \sum_j f_j(hkl)\exp\left(i\,2\pi(hx_j + ky_j + lz_j)\right) \tag{2.17}$$

where $f_j(hkl)$ represents the atomic form factor of the jth atom in the unit cell and x_j, y_j and z_j are its fractional coordinates. Here the structure factor $F(hkl)$ gives the Fourier transform of the unit cell rather than the transform of a molecule as mentioned in section 2.1.3. $F(hkl)$ can be related to the observed intensity by:

$$I(hkl) = |F(hkl)|^2 \tag{2.18}$$

$$= |f(hkl)|^2\left|\sum_j \exp\left(i\,2\pi(hx_j + ky_j + lz_j)\right)\right|^2$$

Equation 2.18 describes the ideal case where all of the atoms are precisely centred in their symmetry defined positions. However in real systems, thermal fluctuations and other structural imperfections may displace the atoms from their correct locations. The impact of this displacement is accounted for by the Debye-Waller factor, which imposes an exponential dampening effect on the scattered intensity, dependent on $q^2 = |q|^2$ and the mean squared displacement of the atoms $\langle u^2 \rangle$. Equation 2.18 can therefore be modified to:

$$I(hkl) = |F(hkl)|^2\exp(-q^2\langle u^2\rangle/3) \tag{2.19}$$

The diffracted intensity from a 3D ordered nanoparticle (NP) array or 'superlattice' is very similar in principle to that described above for an atomic crystal. As the individual atoms are replaced by NPs, the atomic from factor is replaced by the scattering amplitude of a single NP. In this thesis the NPs are assumed to be perfectly spherical, which means that the Fourier transform of an NP can be written:

$$f_{NP}(q) = \rho_p \frac{4\pi}{q^2} \left(\sin qR_{np} - qR_{np} \cos qR_{np} \right) \qquad (2.20)$$

where ρ_p and R_{np} are density and radius of the NPs. A function for the scattered intensity can be found simply by expanding equation 2.19 (as shown in the bottom line of 2.18) and replacing the atomic form factor with equation 2.20 above.

2.2 – Resonant X-ray Scattering [11-15]

Resonant or 'anomalous' X-ray scattering is a technique that enables one to distinguish the chirality of structures. The principle involves tuning the energy of incident X-rays to the absorption edge of a particular atomic species in order to break the symmetry of the scattering interaction. In conventional X-ray experiments (at non-resonant energies), scattering from the diffuse electron cloud is spherically averaged (centrosymmetric) and the complex atomic form factor $f = f_0 + f'(E) + if''(E)$, reduces to f_0. Here f_0 is a scalar quantity representing the scattering amplitude of the atom, which is invariant with the polarisation direction of incident X-rays. The scattering interaction is therefore insensitive to the orientation of individual atoms/molecules. However at photon energies corresponding to the absorption edge (K-edge) of the atom, X-rays are absorbed by the inner most electron shells. In this instance the dispersive and absorptive terms of the atomic form factor ($f'(E)$ and $f''(E)$) are no longer negligible and the symmetry of bound orbitals becomes significant. Atoms residing in locally anisotropic chemical environments become dichroic to polarised X-rays and the atomic form factor becomes a complex tensor. The broken symmetry of the atomic form factor allows constructive interference to occur between waves scattered by identically oriented atoms. The presence of chiral periodicity may therefore produce additional X-ray intensity maxima that are otherwise unobservable.

Although resonant X-ray scattering is a powerful technique for structure determination, working so close to the absorption edge of the atoms introduces complications. At the

resonant energy (E_r = hv$_r$) The X-rays are more readily absorbed by the material, which means that the penetration depth of the incident beam into the material is reduced. Moreover absorbed X-rays promote electron energy transitions, from the core shells to valence levels. Relaxation of the excited atomic state may then occur in one of two ways: (1) The electron re-emits the absorbed radiation, producing a photon of the same energy (elastic scattering), or (2), an electron from a lower energy level fills the core shell, emitting a photon with a smaller frequency than the incident photon (inelastic scattering). In conventional circumstances, inelastic or 'Compton' scattering can be ignored because only a tiny percentage of incident photons are scattered in this way. However during resonance, this phenomenon occurs much more frequently and the dramatic increase of incoherently scattered X-rays can lead to a strong background on the detector, reducing the signal to noise ratio.

2.3 – Experimental X-ray Diffraction

2.3.1 – Experimental Setup

Figure 2.3 shows the basic setup of an X-ray diffraction experiment. The specifics of each numbered component (in the context of this thesis) are explained briefly below.
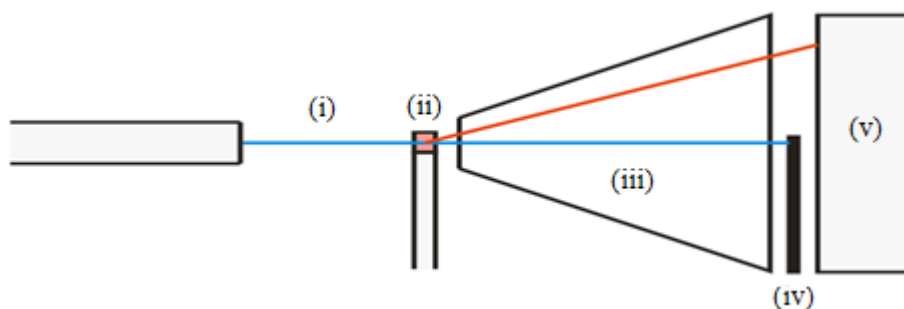
Figure 2.3 – A diagrammatic representation of an X-ray diffraction setup

(i) Incident beam: The X-ray diffraction experiments discussed in later chapters were conducted in Synchrotron radiation facilities such as the Diamond Light Source (DLS) and the European Synchrotron Radiation Facility (ESRF). Synchrotron radiation is highly collimated with low divergence and the intensity is several orders of magnitude larger than that produced by traditional copper X-ray tubes. The high intensity beam enables very short exposure times, appropriate for investigating dynamic systems such

as liquid crystals. Synchrotrons are able to produce plane polarised radiation over a wide wavelength range, which means that the incident beam is tuneable as well as highly monochromatic.

(ii) Sample position: In this project, samples were investigated using two different experimental techniques, the first is known as the transmission method. During this process the sample is held in a glass capillary and placed in the beam path with the length running perpendicular to the incident beam; X-rays are then transmitted through the bulk of the specimen. The second experimental setup is known as the grazing incidence configuration, which is a useful technique for investigating surfaces and thin film structures. An example specimen contains two interfaces (air-sample and sample-substrate), both of which have a critical angle for total external reflection. The working principle of the grazing incidence technique is to orient the specimen so that the incident beam makes a small angle θ_g with the surface of the sample. Typically the value of θ_g is below the critical angle of the sample-substrate interface, but just above that of the air-sample interface. This enables the incident X-ray beam to penetrate into the material of interest, but reflect from the substrate surface. The advantage of this technique is that a large volume of the sample is irradiated with minimal absorption from the substrate. As the sample thickness is typically very thin, the diffraction is much more sensitive to surface organisation than the traditional transmission setup.

(iii) Flight tube: X-rays scattered by a sample are easily absorbed by atoms in the air, which re-emit the radiation incoherently. This produces a non-linear background on the detector, which is strongest at small diffraction angles. In order to reduce the background noise, a helium filled flight tube or vacuum chamber may be fitted between the sample and the detector. X-rays interact very weakly with helium because of its low atomic number, which means that the signal to noise ratio of the diffraction pattern can be significantly improved.

(iv) Beam-stop: The direct beam, i.e. the un-deflected incident beam, is magnitudes more intense than the scattered beams from the sample. A metallic (usually lead) beam-stop must be fitted between the flight tube and detector to absorb the direct beam and prevent saturation of the diffraction pattern and detector damage. In the grazing incidence setup the direct beam may be partly reflected from the substrate, which

produces a vertical streak rather than a focused spot. In this case the beam-stop is tapered (arrow-shaped) to block out the reflected component of the direct beam.

(v) Detector: A variety of 2D area detectors were used throughout the project, but primarily the MAR165 CCD and Pilatus 2M dectris. The detector used will be indicated in the later experimental chapters. In this project the wide and small angle regions of each diffraction pattern were studied separately in order to maximise resolution. The small angle X-ray scattering (SAXS) region of a diffraction pattern is defined here by $0 < |q| \leq 6.3$ nm^{-1} ($d \geq 1$ nm), while the wide angle (WAXS) region is defined by $|q| > 6.3$ nm^{-1} ($d < 1$ nm). When the WAXS region is investigated, the detector is close to the sample; the detector is positioned much further away from the sample when the SAXS region is investigated.

2.3.2 – Qualitative Analyses of Diffraction Patterns

The appearance of a diffraction pattern can provide a large amount of information about the internal structure of a substance, prior to rigorous quantitative analyses. In Figures 2.4a-d the effects of positional and orientational organisation on the scattered intensity distribution are explained diagrammatically. Each window is explained in more detail in the proceeding text.
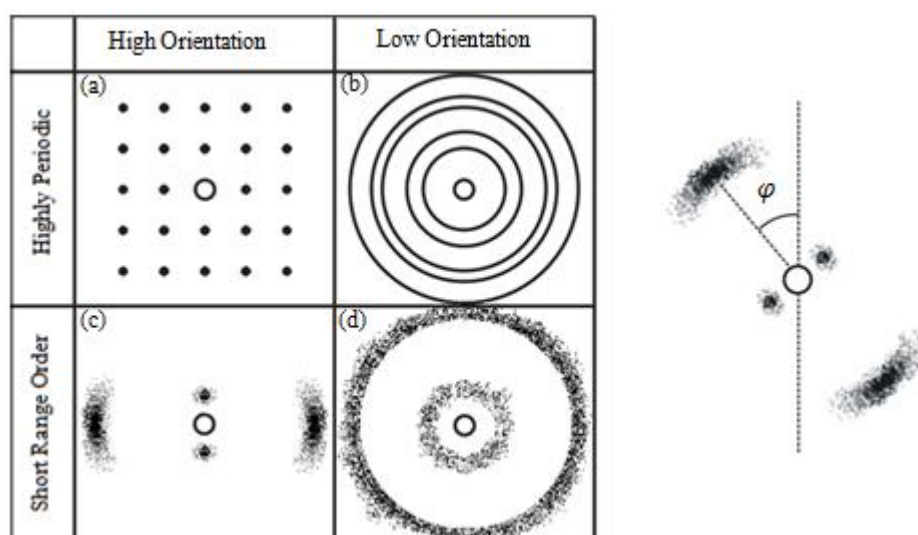
Figure 2.4 – Tabulated illustrations describing the effects of reducing structural order on the appearance of the diffraction pattern. In each square the example pattern represent the ideal situation and should not be taken literally. The azimuthal angle (φ) is also defined.

(a) High Positional order and high orientational order: This type of diffraction pattern may be expected of a single crystal sample, where the lattice can be considered infinite on the scale of the individual constituents. Each reciprocal lattice point is a sharp spot as described in section 2.1.4. In this thesis sharp diffraction peaks will be referred to as 'Bragg reflections' in line with convention.

(b) High positional order, low orientational order: When orientational order decreases inside the sample, the scattered intensity begins to spread azimuthally; diffraction spots become arcs, which become uniform rings when orientation is completely lost. The example pattern shown in (b) is referred to as a 'powder diffraction pattern'. A powder sample is effectively a large quantity of micron-sized crystallites, each of which scatters X-rays in a series of sharp points as described in (a). Because the crystallites are not fused, they may orient independently of one another. Due to the vast number of crystallites in a single sample, every possible orientation is represented, which means that the spots are diffracted spherically (in every direction) in reciprocal space. However, only q vectors that terminate at the surface of the Ewald sphere produce observable intensity, which in this circumstance gives sharp rings. (The intersection of two spherical surfaces is a ring).

(c) Low positional order, high orientational order: As the length scale of positional organisation reduces inside the sample, the peaks begin to broaden radially. In the context of crystal − liquid crystal transitions, Bragg reflections in the WAXS region of the diffraction pattern are replaced by diffuse scattering maxima, which correspond to the average side-by-side spacing between molecules. In smectic and 2D phases, the number of Bragg reflection in the SAXS region of pattern significantly reduces. In the nematic case (shown), the sharp SAXS reflections are also replaced by a series of broad scattering maxima. In all cases, the positional correlation length inside a material is inversely proportional to the full-width-half-maximum (FWHM) = Δq of the peaks.

(d) Low positional order, low orientational order: When the system possesses low positional and orientational order, a very broad diffuse halo will appear in the WAXS and SAXS regions of the diffraction pattern; however it is not uncommon for the SAXS region to be completely empty. This type of intensity distribution typically corresponds

to an isotropic liquid or an amorphous solid, where there is no definable relationship between the constituents, besides an average separation distance with immediate neighbours.

2.3.3 – Calculating Diffraction Angles and d-spacings

In order to calculate diffraction angles, one must know the wavelength of the incident X-rays and the distance between the sample and the detector. In synchrotron facilities the wavelength is always provided, but in some cases the sample to detector distance (L) must be found manually. This is done using a calibration compound, whose diffraction angles are already known; a common example is silver behenate. From geometry in Figure 2.5, the sample to detector distance is calculated by $R/\tan(2\theta_b)$, where R is the distance from the origin (defined by the direct beam) to the peak of reference. If D is known, the diffraction angles of the sample can be calculated, using the same equation, but solving for $2\theta_b$. Using Bragg's law (equation 2.5) one may use the wavelength and $2\theta_b/2$ to calculate the corresponding d-spacing and $|\boldsymbol{q}|$ of the diffraction peaks.
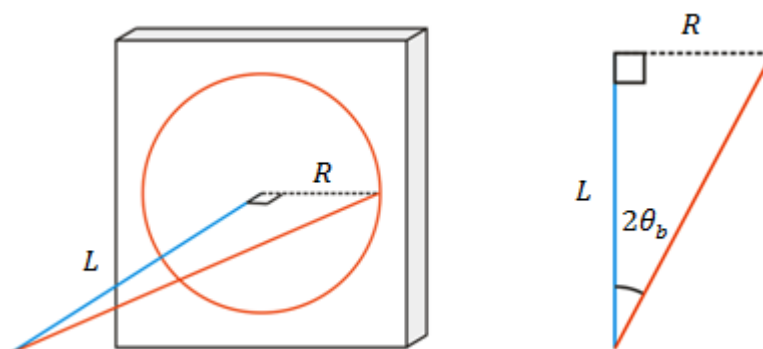
Figure 2.5 – A diagram showing the geometric relationship between the sample to detector distance, diffraction angle and the position of the peak on the 2D detector.

2.3.4 – Structure Determination in 2D and 3D

For 2D ordered materials there are five possible unit cell structures: Square, hexagonal, oblique, rectangular and centred rectangular. All of these direct lattices produce an identical lattice in reciprocal space, which are trivially identified in most circumstances. As there are only two dimensions of organisation, only the h and k indices are required to index the reciprocal lattice. In 3D ordered materials, the general structure may be described by one of seven unit cell shapes, which constitute the fourteen Bravais lattice

families. The shape of the unit cell can typically be identified by comparing the ratio between the *d*-spacings of the diffraction peaks. However the specific symmetry or 'space group' of the unit cell is determined from the 'systematic absences' of the diffraction pattern. Systematic absences are diffraction peaks that are symmetry forbidden by the arrangement of the atoms inside the unit cell. There are 230 3D space groups, which are tabulated in the International Tables of Crystallography (Volume A), along with the symmetry allowed reflection rules for each.

2.3.5 – Constructing Electron Density Maps

In this project, electron density maps were constructed using relative intensity measurements from 2D powder diffraction patterns. In each case the relative intensity ratio between the peaks was determined using the following method:

(i) The 2D powder pattern was converted into a 1D line graph. This is achieved by azimuthal integration: the intensity in each radial increment of the pattern was summed and plotted against $|\boldsymbol{q}|$ (=q).

(ii) The intensity of the 1D pattern was then multiplied by the Lorentz powder factor (q^2), which corrects for the reduced 'apparent' intensity of peaks scattered at large q values. Scattering at higher q values is less represented in the observed diffraction pattern because in reciprocal space the intensity is spread over larger spherical surfaces.

(iii) The total intensity of each Lorentz corrected peak was found by integrating the area beneath the 1D curve in the appropriate q-range. The measured intensity of each peak was then divided by its multiplicity. Multiplicity represents the number of symmetry equivalent reflections that exist in reciprocal space; for example in cubic systems (100), (010), (001), (-100), (0-10) and (00-1) all have the same q value, which means that [100] has a multiplicity of 6. Dividing the total intensity of each peak by its corresponding multiplicity gives the intensity contribution of a single diffraction spot.

(iv) The fully corrected intensity measurements were normalised in relation to the strongest peak, in order to find the relative intensity ratio. The relative intensity of each peak was then used to reconstruct the electron density map. The electron density at

every point inside the unit cell was calculated by Fourier transform of the structure factor, which for ordered phases can also be written as a summation: [1]

$$\rho(x, y, z) = |f(hkl)|^2 \sum_{hkl} F(hkl) \exp\left[-i2\pi(hx + ky + lz)\right]$$

$$|F(hkl)| = \sqrt{I(hkl)}$$

$$F(hkl) = \sqrt{I(hkl)} \exp(i\phi_{hkl})$$

$$\rho(x, y, z) = |f(hkl)|^2 \sum_{hkl} \sqrt{I(hkl)} \exp\left[-i2\pi(hx + ky + lz)\right] \exp(i\phi_{hkl}) \quad (2.21)$$

The term $\exp(i\phi_{hkl})$ arises because only the magnitude of the structure factor can be determined from a diffraction pattern. The loss of phase information is commonly referred to as the 'phase problem', which must be solved by best fit calculations or directly by resonant X-ray diffraction. In this work an electron density map is constructed for every possible phase combination of the diffracted peaks.

2.4 – Polarised Optical Microscopy (POM) [16-18]

In the context of anisotropic liquid crystal materials, POM is a process that enables one to determine the birefringence of mesophases and investigate the orientational behaviour of the molecules inside domains. During the experimental procedure the sample is placed on a heating stage between a pair of crossed polarisers as shown in Figure 2.6. As previously mentioned, liquid crystal domains are anisotropic, hence birefringent, which means that the incident plane polarised light is split into two components as it enters the material. The light is said to experience the ordinary index of refraction (n_o) or the extraordinary index of refraction (n_e) depending on the orientation of the unique axis in respect to the polarity of incident light. The optical path difference experienced by two light components imposes a phase shift is between them. The recombined light exiting the material is therefore elliptically polarised, which enables some components to pass through the second polarisation plate (analyser). Isotropic materials, with no unique axis, appear completely black between crossed polarisers. This is because the light remains linearly polarised in the direction of the first polarisation plate, which is blocked by the orthogonal orientation of the analyser.
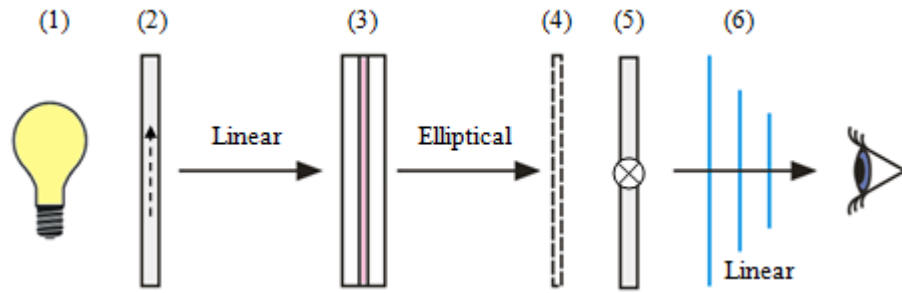
Figure 2.6 – The experimental setup of POM: (1) Source of un-polarised white light, (2) polariser, (3) thin film sample between glass slides, (4) position of retardation plates (if inserted), (5) analyser (polariser 2) and (6) magnification and focusing optics. The axis of (2) is perpendicular to that of (5).

2.4.1 – Measurement of Birefringence

Birefringence is quantified as the difference between the ordinary and extraordinary refractive indices of a material, i.e. $\Delta n = n_e - n_o$. However this quantity is not directly measurable under the microscope; instead the phase retardation (Γ) of light exiting the sample is measured, enabling the birefringence to be determined from:

$$\Gamma = \Delta n \cdot t \qquad (2.21)$$

where t is the sample thickness. Light retardation is measured by inserting a 'Berek compensator' into the optics (position (4) in Figure 2.6). The compensator contains an axial crystal, which can be pivoted to vary the angle of its unique axis in respect to the light from the sample. In practice the crystal is angled to compensate the phase difference between the two light components; if achieved, the two components recombine in phase as they exit the crystal. The correct compensation angle of the crystal is indicated visually by a dark field of view in sample regions with the same thickness and orientation. The angles that compensate the phase difference are read directly from the device and can be used to calculate the retardation using manufacturer provided information. If the sample thickness is also known, equation 2.21 can be used to find the magnitude of the birefringence.

2.4.2 – Determining the Molecular Orientation

The polarisation state of light passing through the analyser can be used to determine the direction of $\hat{n}$, i.e. the average orientation of the molecules, inside each domain. However in thin samples, the phase difference is sometimes too small to produce

noticeable differences between the domains. In order to solve this problem, a full wave retardation plate (λ-plate) may be inserted into the optics. The λ-plate consists of an anisotropic crystal, with the unique axis fixed at 45 ° (running Southwest to Northeast) in respect to the polariser and analyser. The function of a λ-plate is to exaggerate the phase difference between the two components of light as they exit the sample. Assuming that the appearance of the sample between crossed polarisers is initially white/grey, the presence of the λ-plate will introduce colour shifts that depend on the average orientation of the molecules, in respect to the optic axis of the crystal. If $\langle \hat{n} \rangle$ is parallel (/perpendicular) to the axis of the λ-plate, the light travels slower (/faster) through the plate, resulting in a blue (/yellow) colour shift.
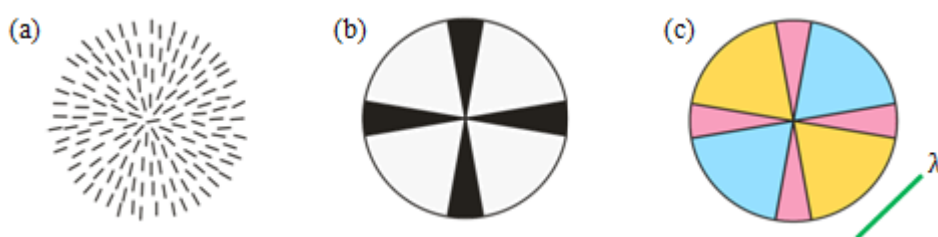
Figure 2.7 – (a) A uniformly splayed arrangement of molecules. (b) The optical texture of the arrangement in (a) observed without the λ-plate. If $\langle \hat{n} \rangle$ is parallel to the polariser or analyser, the light is unable to pass through the optics. (c) The observed texture with the λ-plate. Light that would otherwise be unable to pass through the analyser (black) is also retarded by the λ-plate and appears magenta.

2.5 – Polarised IR Spectroscopy [19-23]

Infrared (IR) spectroscopy is a process that allows one to investigate the vibrational and rotational states inside chemically bound polyatomic structures. The sample is explored over a range of IR frequencies (ν) and absorption peaks are observed in the spectrum when the associated photon energy (E=hν) matches the difference between two discrete electronic energy levels in the system. From a classical point of view, an absorbance peak is observed when the frequency of incident IR radiation resonates with the natural frequency of a particular vibrational or rotational mode inside the molecules. If a polyatomic structure is viewed as a collection of point masses joined by springs, the resonant frequency of each chemical bond depends on the 'stiffness' of the spring and the mass on each end. Using this analogy the frequency of IR absorption peaks can be predicted from:

$$\nu = (1/2\pi)\sqrt{(K/\mu)} \tag{2.22},$$

where K is a force constant analogous to the one in Hooke's law, and $\mu = m_a m_b/(m_a+m_b)$ is the reduced mass of an *a-b* pair. Conventionally IR absorption peaks are discussed in terms of reciprocal wavelength or 'wavenumber' ($\bar{\nu}$) with units of cm^{-1}, which can be accounted for by adapting equation 2.22 to $\bar{\nu} = (1/2\pi c)\sqrt{(K/\mu)}$, where *c* is the speed of light. As each type of bond has its own distinct frequency, an IR absorption (or transmittance) spectrum can reveal a large amount of information on the chemical structure of a sample. However, not all vibrational and rotational modes are visible by IR spectroscopy. Only oscillations that result in a net change in the electronic dipole moment are 'IR active' and appear in spectrum.

2.5.1 – Types of IR Active Vibrational Modes

The IR region of the electromagnetic spectrum is divided into three subdivisions: near, mid and far IR, in the order of high to low energy. Of relevance to this thesis is the mid IR band, in particular wavenumbers between 3500 and 500 cm^{-1}. This region is where the natural vibration and bending modes of chemical bonds associated with organic molecules can be found. Rotational modes are usually found at lower wavenumbers and can be disregarded onwards. For non-linear chemical structures, such as that discussed in Chapter 5, the most common modes of vibration include stretching, wagging, twisting, rocking and scissoring oscillations, which are defined in Figures 2.8a-f.
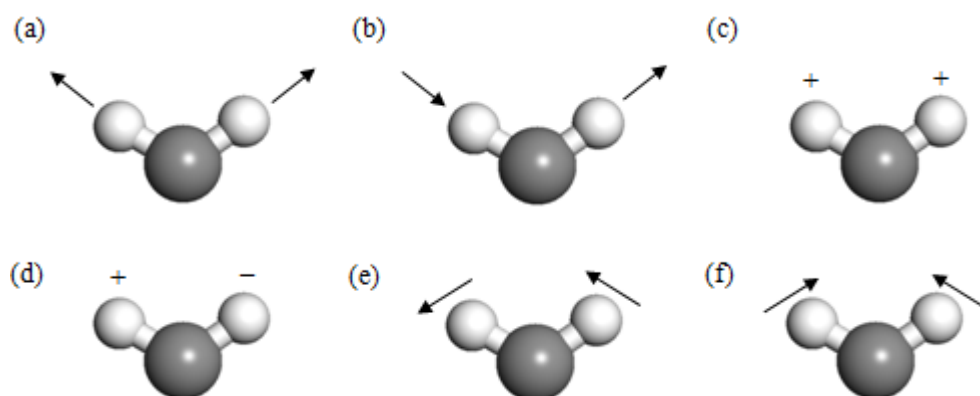
Figure 2.8 – IR active vibrational modes; CH_2 was chosen arbitrarily as an example. – and + symbols indicate movement into and out of the page, respectively. (a) Symmetric stretching, (b) Asymmetric stretching, (c) Wagging, (d) Twisting, (e) Rocking, (f) Scissoring.

2.5.2 – Calculating Orientational Order Parameters

The peak intensity (absorbance) of an IR active vibrational mode is proportional to the square magnitude of the associated transition moment (M = d$\mathbf{p}$/dr), but also its orientation in relation to the polarity of incident IR radiation, i.e. $A \propto (M \cdot \widehat{E}_p)^2 = M^2 \cos^2(\theta_v)$. Here $\mathbf{p}$ is the dipole moment, r is the charge separation and $\widehat{E}_p$ is a unit vector defining the electric vector axis of the incident electromagnetic radiation (see Figure 2.9). In instances where the sample is un-orientated or the incident beam is non-polarised, the IR spectrum represents the rotationally averaged response of the system. However, when the sample is well oriented and the incident beam is linearly polarised, the absorbance of each IR active vibrational mode becomes highly dependent on its alignment with $\widehat{E}_p$. The alignment of a vibrational mode can be quantified by the dichroic ratio $D = A_{//}/A_{\perp}$, which is found by measuring the absorbance of the sample at the corresponding wavenumber, while oriented parallel and perpendicular to the polarity of the incident IR beam. D is high (/low) when M is nearly parallel (/perpendicular) to the alignment direction and equal to 1 when M is at the 'magic angle' (54.7 °) in respect to the sample alignment direction. For nematic liquid samples the dichroic ratio of a vibrational mode can be related to the orientational order parameter by: [19]

$$S = \frac{(D-1)}{(D+2)} \cdot \frac{2}{(3\cos^2(\theta') - 1)} \qquad (2.23)$$

where θ' represents the average angle between M and the nematic director $\widehat{n}$. In the case where M is approximately parallel to the director, S can be well approximated as (D-1)/(D+2) [19].

In the work presented in later chapters, the simplified form of S is used for all vibrational modes, which is acceptable because the sample absorbance is investigated over multiple orientation angles, not just parallel and perpendicular to $\widehat{E}_p$. The need for the angular correction is eliminated by suitable fitting of a $\cos^2$ function to the data (see Appendix C). Note that the nematic director $\widehat{n}$ becomes the direction of the helical axis in the twist bend nematic (N_{tb}) phase.
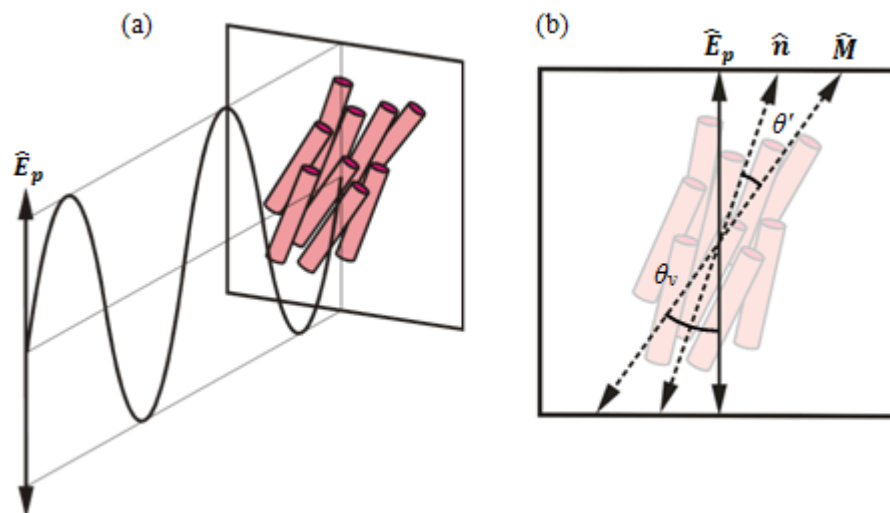
Figure 2.9 – (a) Diagram defining the oscillation plane for the electric component of linearly polarised IR radiation. In (b) the axes of the transition moment $\boldsymbol{M}$ (=$M\widehat{\boldsymbol{M}}$), the incident electric vector $\widehat{\boldsymbol{E}}_{\boldsymbol{p}}$, the nematic director $\widehat{\boldsymbol{n}}$ and the angles between them are also defined.

References to Chapter 2

[1]   D. W. L. Hukins (1983). "*X-ray Diffraction by Disordered and Ordered Systems*", Oxford, Pergamon Press.

[2]   B. E. Warren (1990). "*X-ray Diffraction*", New York, Dover Publications.

[3]   A. Guinier (1994). "*X-ray Diffraction in Crystals, Imperfect Crystals and Amorphous Bodies*", New York, Dover Publications.

[4]   N. Stribeck (2007). "*X-ray Scattering of Soft Matter*", Berlin, Heidelberg, Springer Science+Business Media.

[5]   B. B. He (2009). "*Two dimensional X-ray Diffraction*", Hoboken, New Jersey, John Wiley and Sons, Inc.

[6]   E. W. Nuffield (1966). "*X-ray Diffraction Methods*", New York, London, Wiley.

[7]   B. D. Cullity (2014). "*Elements of X-ray Diffraction*", 3rd Ed., Harlow, Essex, Pearson.

[8]   M. M. Wolfson (1997). "*An Introduction to X-ray Crystallography*", 2nd Ed., Cambridge University Press.

[9]   M. Birkholz (2006). "*Thin Film Analysis by X-ray Scattering*", Wiley-VCH.

[10]   U. Pietsch, V. Holý, T. Baumbach (2004)." *High-Resolution X-ray Scattering, From Thin Films to Lateral nanostructures*" 2nd Ed., New York, Springer Science+Business Media.

[11]   G. Materlik, C. J. Sparks (1994). "*Resonant Anomalous X-ray Scattering*", Amsterdam, North-Holland.

[12]   C. S. Nelson, J. P. Hill, D. Gibbs (2002). "Resonant X-ray Scattering as a Probe of Orbital and Charge Ordering", New York, Brookhaven National Laboratory.

[13]   D. H. Templeton, L. K. Templeton, *Acta Cryst.*, 1980, **A36**, 237- 241.

[14]   W. A. Hendrickson, *Science*, 1991, **254**, 51.

[15]   J-L. Hodeau,V. Favre-Nicolin, S. Bos, H. Renevier, E. Lorenzo, J-F. Berar, *Chem. Rev.*, 2001, **101**, 1843.

[16]   I. Dierking (2003). "*Textures of Liquid Crystals*", Wiley-VCH.

[17]   P. C. Robinson (1992). "*Qualitative Polarized-Light Microscopy*", Oxford University Press.

[18]   W. J. Patzelt (1974). "*Polarized-Light Microscopy: Principles, Instruments, Applications*", 3rd Ed., Wetzlar, Ernst Leitz.

[19]   W.-S. Park, *J. Korean Phys. Soc.*, 2000, **37**, 331.

[20]   P. Majewska, M. Rospenk, B. Czarnik-Matusewicz, L. Sobczyk, *Chemical Physics*, 2007, **334**, 117.

[21]   B. H. Stuart (2004). "*Infrared Spectroscopy: Fundamentals and Applications*", Chichester, West Sussex, John Wiley and Sons Ltd.

[22]   B. Ivanova, T. Kolev (2012). "*Linearly Polarised IR Spectroscopy, Theory and Applications for Structural Analysis*", Boca Raton, Florida, CRC Press.

[23]   C. N. R. Rao (1963). "*Chemical Applications of Infrared Spectroscopy*", New York, Academic Press.

Chapter 3 – Hard X-ray Resonant Scattering in a N_{tb} Forming Mixture of Bent Dimers

In this work the molecular arrangement inside the bulk N_{tb} phase was explored using resonant X-ray scattering in a magnetically aligned liquid crystal (LC) mixture of DTC5C7 and a novel Se-labelled dimer compound. Resonant diffraction spots were observed in the N_{tb} phase corresponding to a helix with a 9-12 nm pitch and with an unprecedentedly high helix orientation. The high helix orientation enabled deconvolution of the local and global order parameters and quantitative estimations of the helical correlation lengths. These findings, combined with simultaneously recorded non-resonant SAXS and WAXS data, enabled construction of a locally layered molecular model of the N_{tb} phase. In this model the average molecular conformation is idealised as a helical segment, which can be matched to the local heliconical director field. Furthermore, an intercalated SmC or 'tilted B6 banana phase' was observed in the pure Se-labelled dimer compound, and perhaps in the mixture on cooling from the N_{tb} phase.

3.0 – Introduction

As mentioned in Chapter 1, section 1.6.2, helical periodicity within the N_{tb} phase was recently unambiguously identified in a bulk dimer sample by resonant X-ray scattering (RXS) at the carbon absorption edge (K-edge) [1]. A resonant Bragg ring was observed in the N_{tb} phase, originating from a temperature dependant helical pitch length ranging between 8 and10 nm. Although the helical pitch was confirmed before completion of the work presented here, the preceding carbon RXS study does not elucidate any of the more widely debated properties of N_{tb} structure; these include the length scale of the helical ordering, the orientational order inside the phase and whether the structure is a nematic continuum or actually an ensemble of highly local smectic-like layers. Carbon RXS cannot provide information on such matters because the low energy 'soft' X-rays (~0.3 keV) required to establish resonance, impose severe experimental constraints; for example the beamline must be fully windowless in high vacuum and the sample must be held between thin, fragile substrates. These factors prevent sample alignment by external

fields [1]. Moreover, soft X-ray scattering allows access to a restricted range of reciprocal space and therefore excludes scattering at larger q vectors, where information on molecular conformation and packing is contained.

In this investigation, the drawbacks of carbon RXS were avoided by studying the N_{tb} phase in a LC mixture containing a newly synthesised selenoether dimer compound. The higher energy K-edge of selenium (12.658 keV) enabled the resonance effect to be established using much harder X-rays, which importantly permitted the use of an external magnetic field and simultaneous recording of the resonant (low q) and non-resonant (high q) scattering. As a result of the magnetic field, an almost perfectly aligned N_{tb} phase was achieved, which for the first time allowed the orientational distributions of the molecules and helical axis to be separately considered. Furthermore, the high sample orientation enabled quantitative estimates of the inter-mesogen correlation length and the length of the coherently diffracting helix (domain size) to be determined. From these findings, together with grazing incidence X-ray diffraction (GIXRD) measurements, the mesogen tilt angle and dimer bend angle were geometrically calculated; the latter was found to be much smaller than previously thought. Using new found information regarding molecular packing and conformation, a more detailed model of the N_{tb} phase was constructed. The construction features twisted molecular conformations matching the shape of the local heliconical director field, as well as local layering of the mesogens. This work expands on previous experimental studies concerning the N_{tb} phase and furthers our understanding of its internal structure.

The binary mixture at the focus of this investigation comprises a compound known DTC5C7 and the newly synthesised selenoether dimer (DTSe) mentioned above. Their molecular structures are shown in Figure 3.0 below. Both compounds were synthesised and provided by the organic chemistry group, led by Professor Georg Mehl, at the University of Hull, UK. The synthetic procedure of both compounds is provided in the Appendix A. The proceeding discussions will therefore be restricted to the phase behaviour and structural properties of the Se-labelled mixture and DTSe. The phase behaviour and temperature dependent internal structure of DTC5C7 is the subject of in-depth discussion in Chapter 4 and so will be partly neglected here.
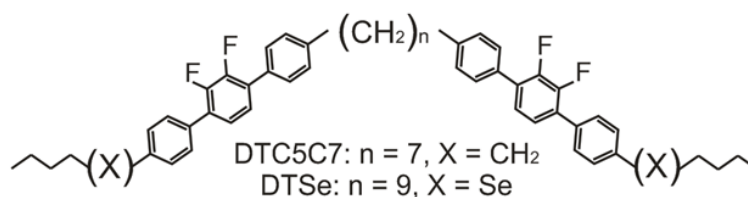
Figure 3.0 – The molecular structures of DTC5C7 (n=7, X=CH$_2$) and DTSe (n=9, X=Se).

3.1 –Phase Behaviour and Structural Analysis of Pure DTSe

3.1.1 – DSC and POM Analyses of pure DTSe
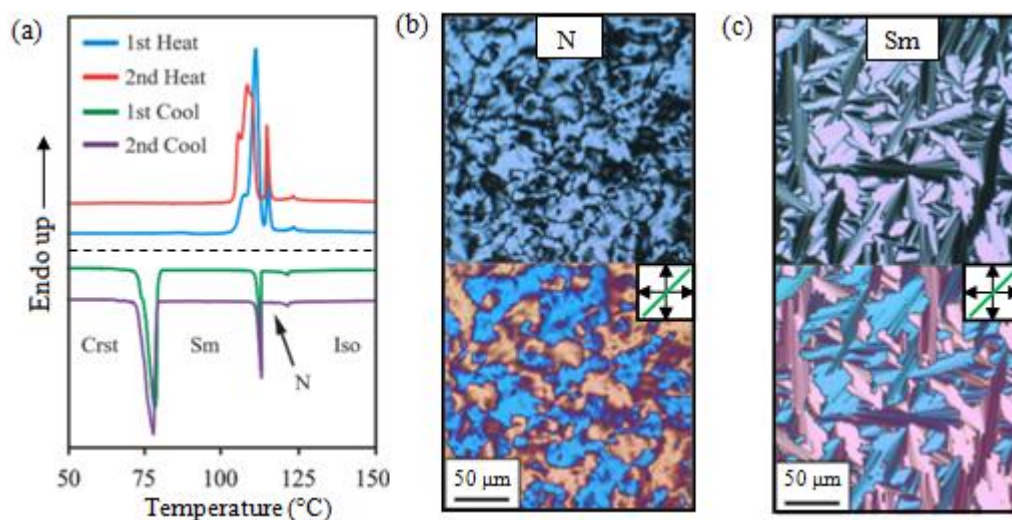
Figure 3.1 – (a) DSC thermogram of DTSe during the first and second heating and cooling cycles. The heating/cooling rate was 10 °C/min. Iso = isotropic, N = nematic, Sm = smectic and Crst = Crystal. The planar optical textures of the N phase (b) and Smectic (B6) phase (c). Top (/bottom) show the texture without (/with) a λ plate inserted into the optics; axis in green. The scale bar applies to both top and bottom.

The phase behaviour of DTSe was firstly investigated using a Perkin Elmer Diamond DSC fitted with a liquid nitrogen cooling unit. The 10 °C/min DSC traces of the sample during the first and second heating/cooling cycles are shown in Figure 3.1a; the transition temperatures on heating are provided in Table 3.0 (pp. 58). The pure compound did not exhibit the N$_{tb}$ phase, only the uniaxial N phase and a lower temperature smectic (Sm) phase. The molecular level structure of the Sm phase is discussed in section 3.1.4. The phase assignments were confirmed using conventional (non-resonant) X-ray diffraction techniques and polarised optical microscopy (POM);

the latter studies were conducted using an Olympus BX50 Microscope fitted with a Mettler FP82 HT hotstage. The Schlieren and fan-like optical textures of the N and Sm phases are respectively shown in Figures 3.1b and c.

3.1.2 – Conventional X-ray diffraction of pure DTSe

The non-resonant small and wide angle scattering (SAXS and WAXS) patterns of pure DTSe were investigated on station BM28 of the ESRF. The sample was investigated in both transmission and grazing incidence setups. In the transmission setup the sample was sealed in a 1.0 mm diameter glass capillary and placed in a custom built heating cell. The cell was in turn placed between the poles of a superconducting solenoid, which produced a magnetic field of 3 T. In the grazing incidence setup the sample was deposited as a thin film (via melting) onto a silicon substrate, which rested on the temperature controlled surface of a custom six-circle goniometer. The sample was aligned by shearing force in the N_{tb} phase. In both setups the WAXS and SAXS regions of the diffraction pattern were investigated separately using a Mar165 CCD detector. The detector was positioned ~30 cm from the sample when collecting WAXS data and ~1 m when collecting SAXS data. In all instances a helium flushed flight tube was positioned between the sample and detector to reduce air scattering.

Upon cooling pure DTSe from the isotropic phase to 119 °C (N phase), a broad WAXS peak was observed at $q = 13.8$ nm^{-1} ($d = 0.46$ nm), arising from an average side-to-side (lateral) intermolecular spacing of 0.51 nm ($1.117d$) [2] (Figure 3.2a). A broad SAXS peak was also observed at $q = 3.01$ nm^{-1}, corresponding to an average d-spacing of 2.1 nm. The origin of this peak is believed to be localised smectic-like layering, usually driven by π-π-interactions between aromatic mesogens, and often referred to as cybotactic nematic correlations [2]. Supporting evidence of local layering is presented throughout the chapter, particularly in sections 3.3 and 3.4, but is perhaps indicated here by the higher intensity of the SAXS in comparison to the WAXS (in the well oriented case). As DTSe was cooled further to 100 °C, the broad SAXS peak of the N phase was replaced by two sharp Bragg reflections at $q = 2.94$ and 5.90 nm^{-1}, indicating transition to the lamellar phase (Figure 3.2b). The 1:2 ratio between the q-values of the two Bragg reflections is consistent with a layer spacing of 2.13 nm. The q-value of the WAXS peak was almost unchanged over the transition, $q = 14.1$ nm^{-1} ($d = 0.45$ nm), indicating that the average lateral intermolecular spacing altered very little (0.50 nm).
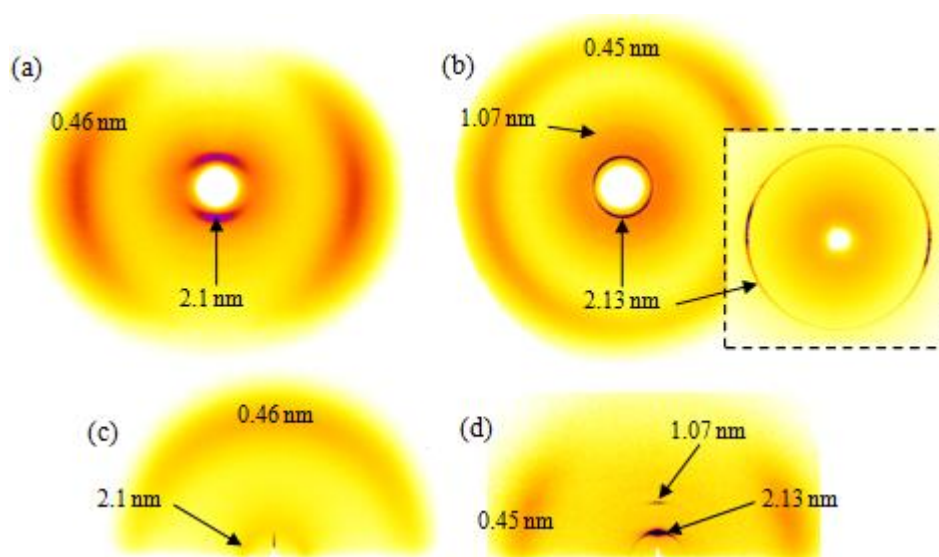
Figure 3.2 – (a) Magnetically aligned (**B** vertical) WAXS patterns of the (a) N phase (119 °C) and (b) Sm phase (100 °C) of DTSe. The inset in (b) shows the SAXS pattern in more detail, illustrating that no additional features are hidden behind the large beam-stop. GIWAXS patterns of the (c) N phase and (d) Sm phase of DTSe. In (c) the alignment is planar and was obtained on cooling from isotropic. In (d) the film was sheared to obtain homeotropic molecular alignment. This is indicated by the centring of the sharp reflections on the axis perpendicular to the substrate.

In the N phase the SAXS intensity maxima were centred on the meridian: the axis running through the beam centre, parallel to the magnetic field. Meridional centring in the N phase signifies director alignment in the magnetic field direction. The azimuthal distribution of the broad peak suggests that the local layers were not all oriented perpendicular to the director. On transition to the Sm phase, the SAXS and WAXS intensity distributions spread over larger azimuthal angles, suggesting that the sample orientation was much less influenced by the magnetic field at lower temperatures.

3.1.3 – 1D Electron Density Map of the Smectic Phase

The energy minimised length of a single DTSe dimer, i.e. the distance between the last carbon on each of the two terminal chains, was estimated using molecular simulation (materials studio) as 4.6 nm. The layer spacing of the lamellar phase (2.13 nm) is less than half the estimated dimer length, and can therefore be attributed to the separation distance between mesogens along the layer normal (tilt angle $\simeq$ 22 °). This notion was further investigated by reconstructing the one-dimensional electron density map of the

Sm phase using relative intensities determined from the azimuthally integrated and Lorentz–corrected SAXS pattern (see Chapter 2, section 2.3.5). The relative intensity ratio of the two Bragg reflections was 100:3.7, referenced from lowest to highest q. There are four possible phase combinations of the two Bragg reflections, hence four possible 1D electron density maps. However each of the four maps shows one of two electron density distributions, which differ only by the stripe thicknesses (Figure 3.3). Of the two options, the electron density map shown in Figure 3.3a was selected as the most plausible, due to the larger thickness of the high electron density stripes (purple/blue). Thicker high electron density stripes are more realistic considering that thermal fluctuations broaden the layers and that X-rays are more sensitive to the heavy Se-labelled mesogens than the alkyl chains.
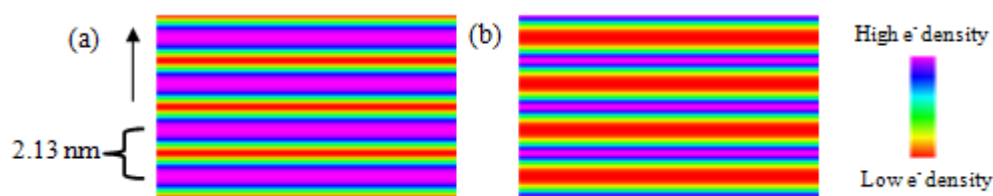
Figure 3.3 – The two possible electron density distributions in the lamellar phase of DTSe. In (a) the phase angles of the two reflections are both π, in (b) they are both 0. The arrow indicates the direction of the layer normal and applies to both figures.

3.1.4 – Molecular-level Model of the Smectic Phase

In DTSe the length of the $(CH_2)_9$ spacer and the added length of the two C_4H_9Se terminal chains are very similar in length (i.e. 9 carbons compared with 8). In this special case, one may assume that each mesogen inside the structure is equally spaced along the layer normal, regardless of how the dimers are layered. This means that the electron density distribution of the smectic phase can be equivalent described by two molecular-level arrangements. The first is the tilted B6 banana phase (also known as SmC_{int}), where the molecules are intercalated, i.e. may randomly half-step along the tilt direction in respect to their neighbours [3]. The alternative packing arrangement is the ordinary SmC phase. These two layering styles are shown overlapping the electron density map in Figure 3.4.
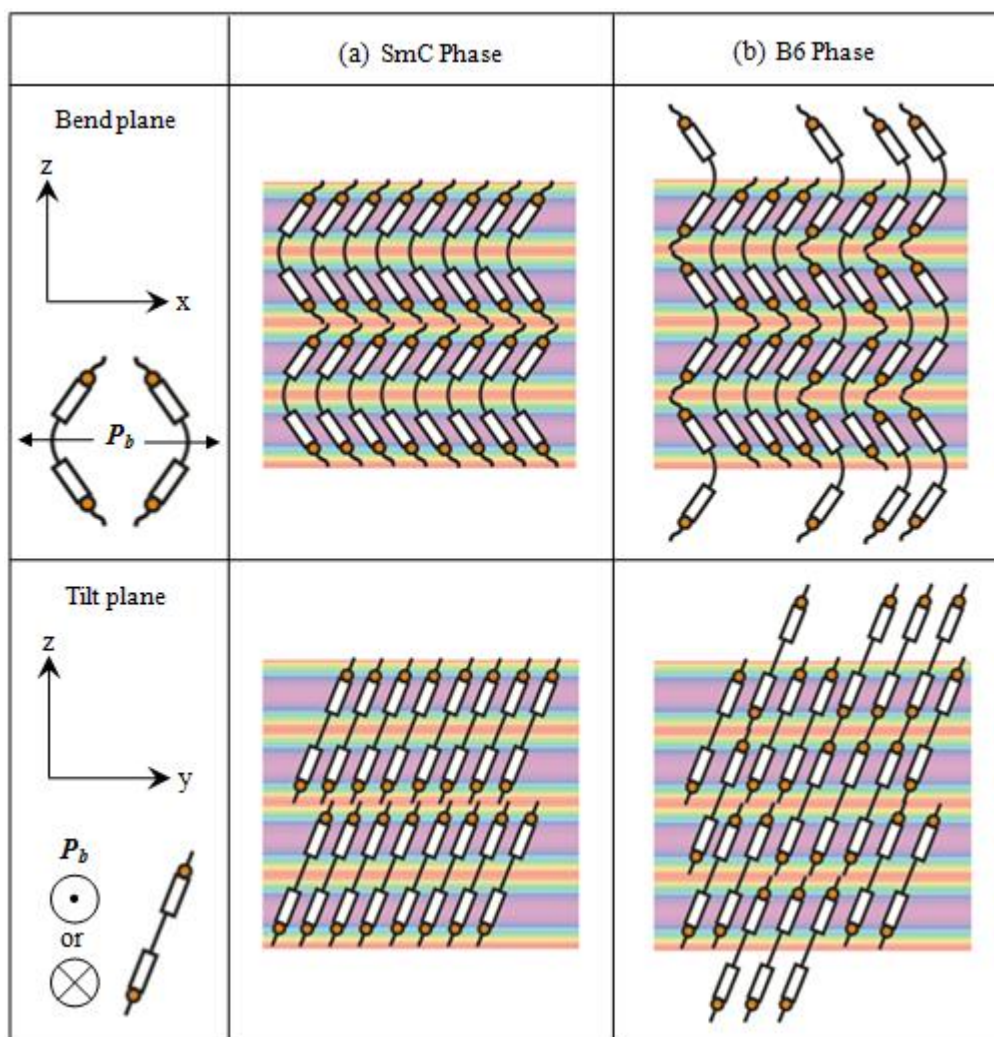
Figure 3.4 – Simplified diagrams of the two possible molecular-level structures of the lamellar phase. The orange circles are an exaggeration of the selenium atoms, illustrating the difference between the two structures. Wavy lines are terminal chains, while the continuous bent lines correspond to the spacers. P_b denotes the polar direction of the molecular bend as defined in Chapter 1, section 1.5. (a) SmC phase, the dimers are layered along the layer normal (z direction) in both the bend plane (xz) and the tilt plane (yz); this structure is polar, at least locally. (b) B6 phase, the dimers are randomly intercalated in the bend plane, or the tilt plane, or both. The dimer shifting eliminates local polarity, but does not disrupt the mesogen layering.

The two models differ only by the arrangement of selenium inside the layers. In the dimer SmC model, the Se atoms are quasi-long-range ordered and are as densely packed as the mesogens. In the dimer B6 model, the randomly inverted orientation of the mesogens along the layer direction effectively reduces positional order and packing density of the Se atoms; the mesogens may therefore be able to pack more closely in the B6 arrangement due to reduced polar repulsion. However on inspection of Figure 3.4,

both models are effectively SmC phases from the perspective of the individual mesogens. As such, the free-energies of two models are unlikely to differ by a significant amount and the dimers should have little preference for either of the two layering structures. Statistically, this means that the B6 dimer model is still the most likely phase assignment, due to the unlikelihood that the dimers will choose to segregate without an energetic incentive. Furthermore, the average d-spacing of the N phase (2.1 nm) and the B6 layer spacing (2.13 nm) are very similar, which suggest that the two phases share the same highly local structure. This perhaps indirectly supports the hypothesis of local cybotactic layering in the nematic phases of bent dimer molecules. A B6 phase was very recently reported in a bent dimer system by Dawood et. al. [4].

3.2 – Preparation and Phase Behaviour of the Se45 Mixture

As the pure Se-labelled sample (DTSe) did not form the N_{tb} phase, its suitability as a dopant in the N_{tb} phase of the previously studied compound 'DTC5C7' [5-7] was investigated. It was hypothesised that the Se-labelled dimers would serve as resonant X-ray scattering markers inside the helical structure, providing that the two samples did not phase separate. Experiments were therefore conducted to investigate the miscibility of the two compounds and also the allowed concentrations of DTSe in the mixture that enable the N_{tb} phase to form.

3.2.1 – Miscibility of DTC5C7 and DTSe

The miscibility of DTC5C7 and DTSe was examined qualitatively under crossed polarisers. A small amount of both compounds was sandwiched between a pair of glass plates and heated to 160 °C, where both samples became isotropic. The glass plates were then compressed slightly in order to create a region of contact. The optical textures within the sandwich cell were recorded on cooling until the contents became crystalline. Throughout the cooling process, the regions of the sample dominated by DTC5C7 or DTSe adhered to the phase sequence of the respective compound. However in the region of contact, a composition gradient was formed, which was most evident at 114 °C. Figure 3.5c shows a central N phase separating the N_{tb} phase of the DTC5C7-rich region (left) and the B6 phase of the DTSe-rich region (right).
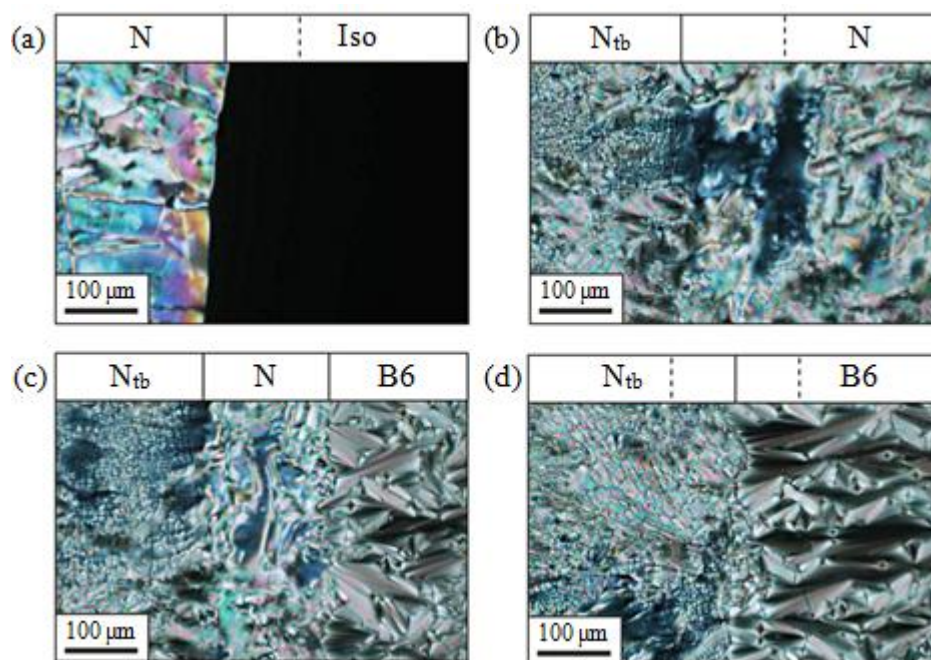
Figure 3.5 – The optical textures observed between crossed polarisers in a sandwich cell containing both DTC5C7 and DTSe. In all four images DTSe is on the right and DTC5C7 is on the left. The central region is a mixture of the two. Solid lines indicate phase boundaries and dashed lines indicate the approximate edge of the mixed region when it is in the same phase as one (or more) of the pure compounds. The images were taken at (a) 130 °C, (b) 120 °C, (c) 114 °C and (d) 110 °C. Iso = Isotropic, N = nematic, N_{tb} = Twist bend nematic, B6 = SmC_{int}.

3.2.2 – Construction of the Binary Phase Diagram

Following the miscibility testing, several mixtures of DTSe and DTC5C7 were created, each with an increased concentration of DTSe. The mixtures were then investigated using DSC (Figure 3.6a) in order to construct a binary phase diagram (Figure 3.6b). The mixtures are referred to using the notation 'Se00', where the last two digits correspond to the mol% of DTSe. The normalised (by sample mass) DSC peaks observed on the first heating are tabulated in Table 3.0. The binary phase diagram shows a stable N_{tb} region between 0 and ca 60 mol% DTSe. For resonant X-ray Scattering experiments, a mixture containing 45 mol% DTSe was selected as the optimum balance between high selenium content and workable N_{tb} temperature range.
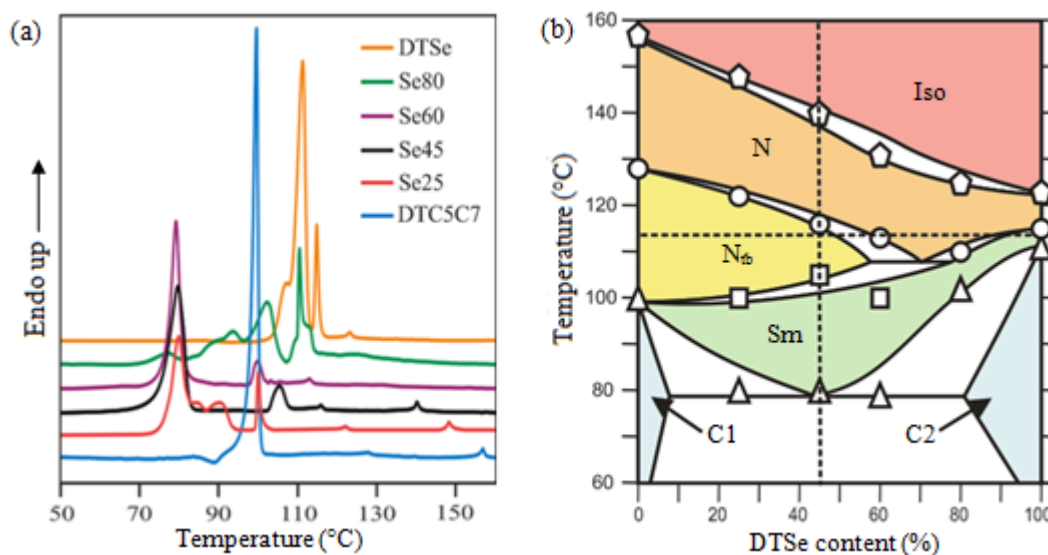
Figure 3.6 – (a) First heating DSC curves of DTC5C7, DTSe and mixtures of the two compounds. The heating rate was 10 °C/min in all cases. (b) Phase diagram of DTC5C7 and DTSe. The data points correspond to the DSC peak temperatures in (a). Note: a meta-stable smectic forms in pure DTC5C7 on cooling [5-7]. The dashed lines respectively correspond to 45% DTSe and 114 °C.

Table 3.0 – Transition Temperatures in DTSe, DTC5C7 and Se00 Mixtures

Sample	$C \rightarrow Sm$ (°C)	$C \rightarrow N_{tb}$ (°C)	$Sm \rightarrow N_{tb}$ (°C)	$Sm \rightarrow N$ (°C)	$N_{tb} \rightarrow N$ (°C)	$N \rightarrow Iso$ (°C)
DTC5C7	---	99.5	---	---	127.8	156.8
Se25	80.0	---	99.8	---	122.3	148.5
Se45	79.5	---	105.3	---	115.8	140.0
Se60	79.0	---	99.8	---	112.8	131.0
Se80	102.1	---	---	110.3	---	125.3
DTSe	111.2	---	---	114.8	---	123.1

The temperatures correspond to the DSC peak positions during the first heating of DTC5C7, DTSe and mixtures of both compounds. C = Crystal, Sm = Smectic, N_{tb} = Twist bend nematic, N = Nematic, Iso = Isotropic.

3.2.3 – Conventional X-ray Diffraction of Se45

Conventional (non-resonant) X-ray scattering investigations of Se45 were conducted on beam-line BM28 of the ESRF using the same experimental practices and equipment as described in section 3.1.2. In both transmission and grazing incidence setups, the sample was heated into the isotropic phase and cooled incrementally until crystallisation. In the N phase (120 °C), two broad SAXS peaks were observed at q = 1.41 and 3.10 nm^{-1}, which respectively correspond to average spacings $d1$ =4.5 nm and $d2$ =2.0 nm. A

diffuse WAXS maximum at $q = 13.7$ nm^{-1} was also observed, corresponding to $d3 =$ 0.46 nm, hence an average lateral intermolecular distance of 0.51 nm [2] (Figure 3.7a). On cooling to the N$_{tb}$ phase (105 °C) the q-values of the broad SAXS and WAXS peaks were virtually unchanged, giving $d1 = 4.4$ nm, $d2 = 2.0$ nm and $d3 = 0.46$ nm (Figures 3.7b,d). The temperature dependent values of $d1$, $d2$ and $d3$ are tabulated in Table 3.1 (pp. 62). As mentioned in section 3.1, the SAXS peaks are believed to arise from π-π driven cybotactic nematic correlations. This is supported by the fact that the measured values of $d1$ and $d2$ are comparable to the average dimer length (4.5nm) and centre-to-centre mesogen separation distance (2.1nm) within Se45 – The averages are weighted by the molar ratio of DTSe and DTC5C7 in Se45.

In the smectic phase (90 °C), the q-value of the diffuse WAXS peak was measured as 13.9 nm^{-1} ($d3 = 0.45$ nm) suggesting that the lateral intermolecular spacing altered very little on transition from the N$_{tb}$ phase. However, at 90 °C the broad SAXS peaks of the N$_{tb}$ phase were replaced by three sharp Bragg reflections at $q = 1.53$, 3.05 and 6.10 nm^{-1}, corresponding to spacings of 4.12, 2.06 and 1.03 nm, respectively (Figures 3.7c,e). Although the 1:2:4 ratio of the Bragg reflections would ordinarily suggest a layer spacing of 4.12nm, the structure of this lamellar phase may be explained by the same B6 dimer model proposed for DTSe. Assuming that the DTC5C7 molecules are randomly distributed throughout the structure shown in Figure 3.4b, the smaller length of the molecules and lower electron density of the mesogens, may create additional X-ray contrast, giving rise to the weak Bragg reflection at $q = 1.53$ nm^{-1} (4.12nm). The B6 dimer model is further supported by the relative intensity ratio between the three reflections, 2.3:100:0.3, referenced from lowest to highest q, which shows that the highly dominant reflection corresponds to a spacing of 2.06 nm, i.e. half of the average tilted dimer length in Se45 (tilt angle $\simeq$ 24 °). A 24 ° tilt angle in the B6 phase is also observed elsewhere [3]. Interestingly the additional smectic Bragg reflection (absent in pure DTSe) is also observed as a broad peak at slightly smaller q in the N and N$_{tb}$ phases of Se45. This suggests that the highly local positional relationship between molecules is similar in all three phases of Se45, and again indirectly supports localised layering in the nematic phases of bent dimer molecules. As shown in Figures 3.7a-c the sample orientation was much less affected by the magnetic field at lower temperatures, in-line with the observations made in pure DTSe.
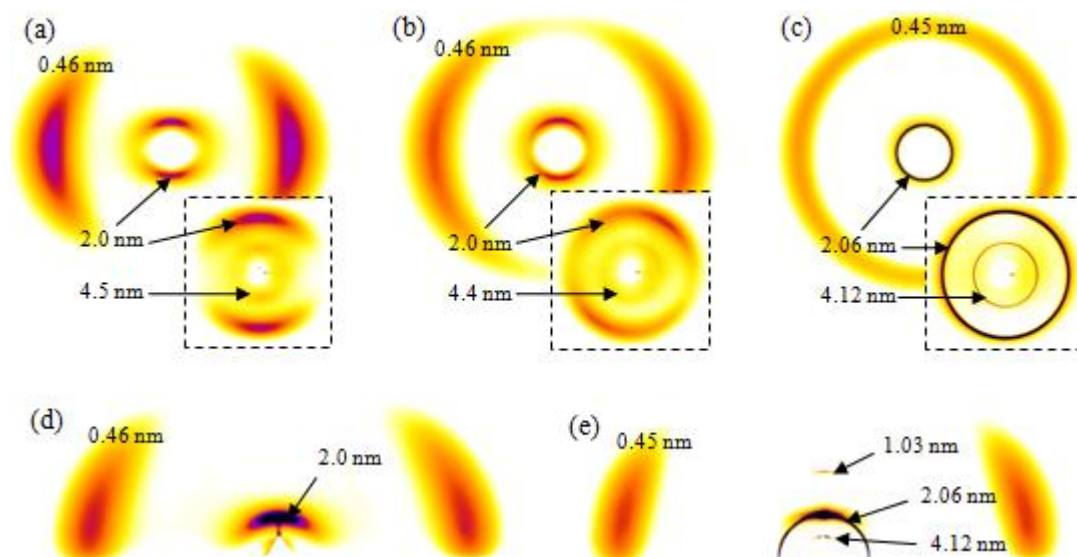
Figure 3.7 – Magnetically aligned (**B** vertical) WAXS patterns of the (a) N (120 °C), (b) N_{tb} (105 °C) and (c) Sm (90 °C) phases of Se45. The insets show the SAXS in more detail. Sheared thin film GIWAXS patterns of the (d) N_{tb} and (e) Sm phases of Se45. In both images the SAXS is centred on the axis perpendicular to the substrate, indicating homeotropic molecular alignment (local layers/layers parallel to substrate surface).

3.3 – Resonant X-ray Scattering in Se45

The resonant X-ray scattering (RXS) investigation of Se45 was performed on beam-line I22 of the DLS. The sample was held in a 1 mm glass capillary, the length of which ran perpendicular to a 1 T magnetic field. The sample was heated and cooled using thermostated nitrogen gas. Se45 was investigated in each of its LC phases using X-ray energies above and below the Se K-edge (E_r = 12.658 keV). Two Pilatus 2M detectors were simultaneously employed to cover the range of ~ 0.3 nm$^{-1} \leq q \leq 15$ nm^{-1}. The sample was first cooled from the isotropic to the N_{tb} phase (105 °C) where the incident energy (E_i) was increased in increments of 5 eV from 12.608 to 12.708 keV. Throughout this energy range, the non-resonant SAXS and WAXS peaks were observed as described in section 3.2.3. However at X-ray energies satisfying the condition $|E_i - E_r| \leq 5$ eV, an additional Bragg peak was observed at $q = 0.62$ nm^{-1}, attributed to resonant diffraction from a helical pitch p of 10.1 nm. The resonant peak was strongest at $E_i = E_r$ (Figure 3.8a). At X-ray energies close to E_r, background scattering increased by a factor of ~ 2 as a result of increased inelastic scattering/sample fluorescence (Figure 3.8b).
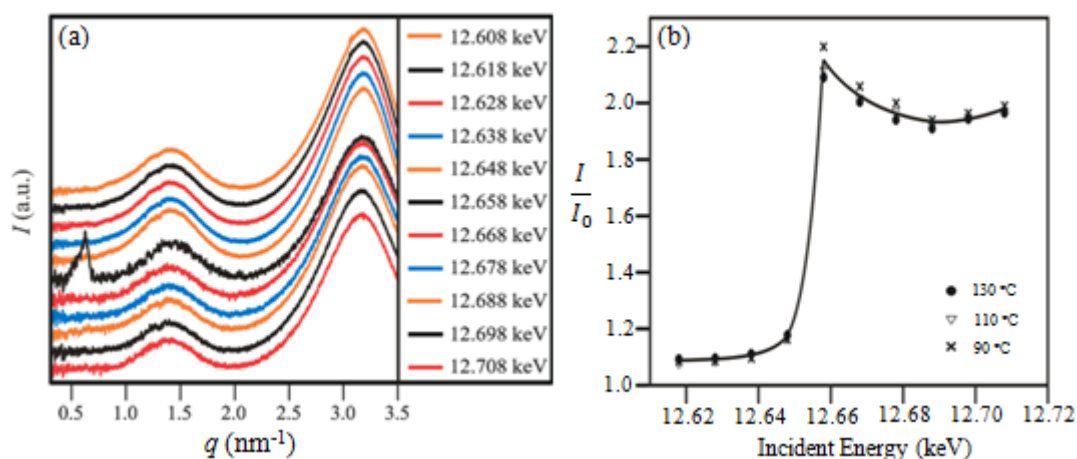
Figure 3.8 – (a) 1D (base-line shifted) diffractograms of Se45 recorded at 105 °C, with incident beam energy changing from 12.608 – 12.708 keV. The resonant diffraction peak was observed at $E_i = 12.658 \pm 0.005$ keV. The curves have been corrected for background scattering. (b) The energy dependent background intensity created by fluorescent (inelastically scattered) photons in the range of $q = 0.3 - 3.7$ nm^{-1}. The quantity I/I_0 represents the scaling factor between the initial background intensity (I_0), measured at 12.608 keV, and the background intensity measured in at each 0.01 keV increment up to 12.708 keV.

The temperature dependence of the resonance effect was investigated by incrementally cooling Se45 from the isotropic to the crystal phase with $E_i = E_r$. The resonant peak was observed exclusively in the N$_{tb}$ phase and at the biphasic boundaries with the neighbouring N and Sm phases. As shown in Figure 3.9a, the resonant peak appeared at the onset of the N$_{tb}$ phase (115 °C), reaching maximum intensity at 112 °C, with $p = 12.1$ nm. With decreasing temperature the resonant peak shifted to larger q, indicating a reducing pitch length (Figure 3.9b). The radial full width at half maximum (FWHM) of the resonant peak initially increased, indicating a broadening distribution of p, before decreasing again at the onset of the Sm phase. The resonance effect was lost with further cooling into the Sm phase. These findings are also summarised in Table 3.1.

At 112 °C the sharp resonant peaks were exactly on the meridian (Figures 3.9c,d), indicating that the helical axis of the bulk sample was highly oriented with the field. The two diffuse SAXS peaks were also centred on the meridian, but were azimuthally spread (arc-like), despite the very high orientation of the helical axis. The azimuthal arcing of the SAXS maxima indicates that the short-range cybotactic layers were not all perpendicular to the helical axis. On cooling from 112 °C the intensity maxima of all

three SAXS peaks simultaneously shifted away from the meridian; the lower the temperature, the larger the shift – see Figures 3.9d-f. The resonant peak began to broaden azimuthally, indicating decreasing orientational order of the N_{tb} phase. Phase orientation was lost entirely in the Sm phase, indicated by the sharp Bragg rings in Figure 3.9f. The WAXS maxima similarly rotated and spread azimuthally on cooling, before becoming a diffuse halo in the Sm phase (Figures 3.7a-c). Temperature dependency of the pitch length has been similarly reported by Zhu *et al* [1], who measured *p* of the compound 'CB7CB' to vary between 8 and 10 nm. However in their work the sample was unoriented and the resonant intensity was usually split over a wider *q*-range, possibly due to a surface confinement effect. The increased *p* of Se45 (9 – 12 nm) is attributed to the larger molecular lengths of DTC5C7 and DTSe.

Table 3.1 - RXS Data Summary of Se45 on Cooling

T (°C)	*p* (nm)	*d1* (nm)	*d2* (nm)	*d3* (nm)	$\Delta q_{//p}$ (nm^{-1})	$\Delta q_{//d2}$ (nm^{-1})
120	-	4.46	2.03	0.46	-	1.28
115	12.2	4.46	2.03	0.46	0.050	1.10
112	12.1	4.41	2.03	0.46	0.060	1.18
110	10.8	4.38	2.01	0.46	0.090	1.22
107	10.4	4.36	1.99	0.46	0.075	1.18
105	10.1	4.36	1.99	0.46	0.055	1.08
102	9.8	4.35	1.98/2.07*	0.45	0.050	0.015
100	9.3	4.14	2.06	0.45	0.050	0.015
95	-	4.12	2.06	0.45	-	0.015
90	-	4.12	2.06	0.45	-	0.015

Sm phase brackets rows 102, 100, 95, 90.

p = helical pitch length, *d1* and *d2* respectively correspond to the average inter- and intra- molecular spacings determined from the non-resonant SAXS peaks. *d3* is the *d*-spacing of the WAXS peak maximum; this is related to the lateral distance between molecules, which equals to 1.117 *d3* [2]. The FWHM along the helical axis ($\Delta q_{//}$) of the peaks associated with *p* and *d2* are also provided. *Here the scattering maximum of the N_{tb} phase, and the Bragg reflection of the Sm phase, are simultaneously observed. The larger of the two spacings corresponds to the SmC Bragg reflection.
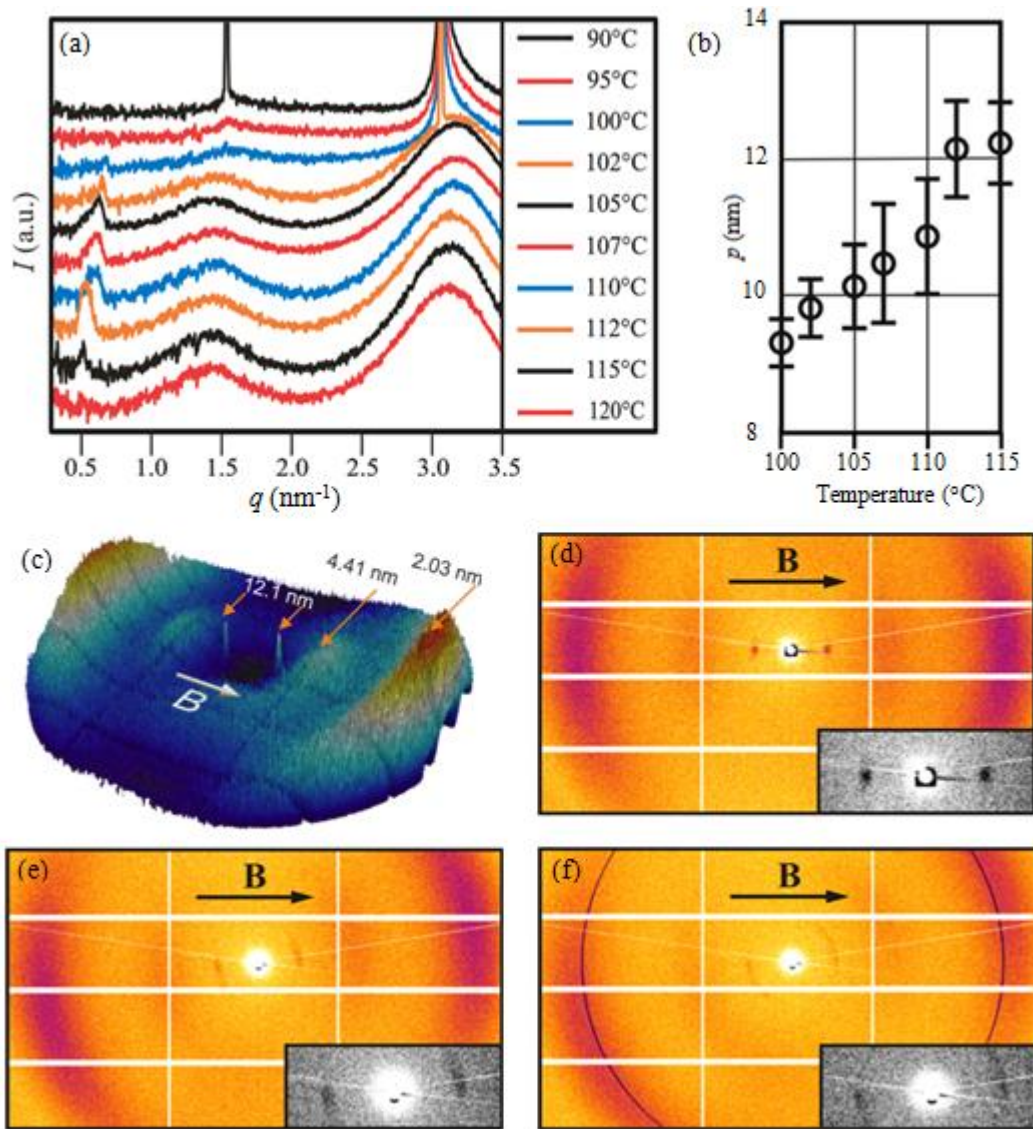
Figure 3.9 – (a) The 1D (baseline shifted) SAXS patterns of Se45 illustrating the temperature dependence of the resonant and SAXS peaks. The resonant diffraction peak is only observed in the N_{tb} phase of Se45. (b) The helical pitch p of N_{tb} phase decreases with cooling. (c) The surface plot SAXS pattern of the magnetically aligned N_{tb} phase (in Se45) at 112 °C, $E_i = 12.658$ keV. (d)(e)(f) 2D SAXS patterns of the N_{tb} phase at 112 °C, 107 °C and 102 °C, with zoom-in of the sharp resonant SAXS peaks (inset).

3.4 – Structural Correlation and Orientational Order inside Se45

At 112 °C the azimuthal FWHM of the resonant peak was measured as ~12 °, indicating that the orientational order parameter of the global helical axis (S_0) must be close to 1, i.e. $(3\cos^2 6-1)/2 = 0.98$. Here $(12/2 =) 6$ ° is the approximate mean deviation angle between the helical axes of the domains and the magnetic field direction. 0.98 is in fact an underestimate as structural correlation also contributes to peak broadening; the azimuthal FWHM would be smaller than 12 ° if this factor could be corrected for. Inside the helical domains, each mesogen is tilted by an angle θ_t in respect to the helical axis, which gives rise to second angular distribution described by $S_1 = \langle 3\cos^2\theta_t - 1\rangle/2$. The overall orientational order parameter of the N_{tb} phase, measureable by classical means, is therefore $S = S_0 \cdot S_1$, which quantifies the orientational distribution of the helical domains and the tilt angle distribution of the mesogens inside each domain. It has been shown here that S_0 of the N_{tb} phase can be close to 1 and that it decreases with temperature, but even in the case of perfect helical alignment, the classically measured orientational order parameter will be small because $S_1 \ll 1$, due to $\theta_t \gg 0$ ° (see section 3.5). The fundamental limitation imposed by S_1 may account for the low orientational order parameter ($\langle P2 \rangle \sim 0.4 - 0.6$) often reported within the N_{tb} phase of bent dimers [8-13].

Assuming perfect orientational order of the helical axis (reasonable at 112 °C where $S_0 \simeq 1$), the radial and lateral intensity distribution of the resonant peak can be attributed to structural correlations parallel and perpendicular to the helical axis, respectively. In a nematic LC one may assume that correlation decays exponentially with distance r, i.e. $\propto \exp(-r/\xi)$. Under this assumption the scattered intensity in reciprocal space is well reproduced by Lorentzian profiles of the form $I_{max}/(1 + \Delta q_{//}^2\xi_{//}^2 + \Delta q_{\perp}^2\xi_{\perp}^2)$ [14-16], where $\xi_{//}$ and $\xi_{\perp}$ are the correlation lengths parallel and perpendicular to the helical axis. By least squares fit of a Lorentzian profile to the intensity around the resonant peak at 112 °C (I vs $\Delta q_{//}$ and I vs $\Delta q_{\perp}$), and after corrections for instrumental broadening (Figure 3.10), we obtain $\xi_{//} = 33$ nm and $\xi_{\perp} = 18$ nm. Alternatively, using the FWHM of the Lorentzian fit ($\Delta q = 2/\xi$), the Scherrer equation $\tau = 2\pi T/\Delta q$ can be used to estimate the size of the coherent heliconical domain. If the shape factor (T) is set to unity, then $\tau = \pi\xi$ and the longitudinal and transverse helical domain sizes are estimated to be 104 nm (24 molecular lengths) and 57 nm (112 molecular widths). Note that both values are underestimates: The calculations assumed that the breadth of the resonant peak arose

entirely from structural correlation. However, the distribution of p and orientational imperfection also contribute to the peak breadth, as discussed previously. At temperatures below 112 °C, $\xi_\perp$ can no longer be determined due to the increased contribution of $S_0 \ll 1$ to azimuthal peak broadening. Similarly the increasing distribution of p with reducing temperature prevents accurate measurement of $\xi_{//}$. However from $\Delta q_{//p}$ (Table 3.1, pp. 62) it would appear that $\xi_{//}$ reduces as the N_{tb} phase progresses, until reaching the onset of the Sm phase, where the quasi-long-range positional order sets in [16].
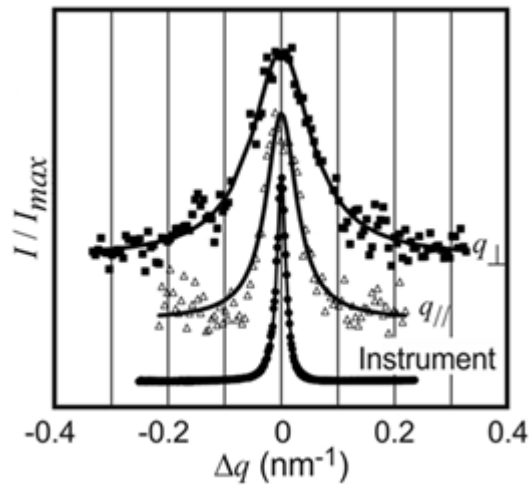
Figure 3.10 – Lorentzian fits to the resonant intensity parallel and perpendicular to the meridian of the N_{tb} diffraction pattern at 112 °C. The instrumental line shape is also shown and was used to correct the fitted FWHM of the experimentally observed data in both directions.

As mentioned in section 3.2.3, the two broad SAXS peaks of the N and N_{tb} phases correspond to average spacings *d1* and *d2*, which are respectively linked to short range inter-dimer and inter-mesogen correlations. In the N_{tb} phase This correlation must be (on average) in the direction of the helical axis because the two broad SAXS peaks remain aligned with the resonant peak at all times, despite the reducing influence of the magnetic field on cooling. At temperatures close to the N-N_{tb} boundary, the inter-mesogen correlation length along the helical axis can be estimated from $2/\Delta q_{//d2}$ (Table 3.1) as ~1.7 nm. For the Sm phase, measurement of $\Delta q_{//d2}$ is limited by the instrumental resolution (0.005 nm^{-1}), indicating a correlation length > 400 nm.

3.5 – Molecular-level Model of the N_{tb} Phase

Existing models of the N_{tb} phase describe an average helical director field inside a nematic continuum, but lack consideration for local molecular packing. Here the molecular-level model of the N_{tb} phase is extended to include local layering of the mesogens, in-line with the newly presented information, which suggests that the mesogens and alkyl chains are partially segregated along the helical axis. In this model, the ideal average conformation of the molecules resembles the shape of a helical segment, which enables each component of the dimer to match the heliconical path of the N_{tb} director field. In real dynamic systems there are a multitude of conformations; however in the following geometric construction the idealised helical average is assumed for simplicity. The energetic feasibility of this conformation is also discussed.

The local director field along the helical axis can be defined mathematically as:

$$\mathbf{n}(z) = \sin(\theta_t)\cos(-2\pi z/p)\, \boldsymbol{i} + \sin(\theta_t)\sin(-2\pi z/p)\, \boldsymbol{j} + \cos(\theta_t)\, \boldsymbol{k} \tag{1}$$

Here z is the height along the helical axis $\boldsymbol{\hat{n}_0}$, θ_t is the tilt angle of the mesogens in respect to the helical axis and p the pitch length of the resulting helix. On progression along $\boldsymbol{\hat{n}_0}$, the dimers can be imagined to wrap around a cylinder such that each successive mesogen is rotated about the helical axis by $\alpha = 2\pi h_l/p$. h_l denotes the cybotactic layer height, i.e. the projected inter-mesogen separation distance along the helical axis, which is approximately equal to the value of $d2$ in Table 3.1, pp. 62. A visual definition of these parameters and the relationships between them is provided in Figure 3.11. Furthermore, the radius of curvature (helical radius) R_c can be derived from $2\pi R_c = p\tan(\theta_t)$, which if re-arranged for p can be inserted into the rotation angle equation, giving $\alpha = (h_l/R_c)\tan(\theta_t)$, showing the dependency of α on θ_t.

From Figure 3.11, the tilt angle of the mesogens can be calculated from the experimental X-ray scattering results using the relation:

$$h_l = l <\cos(\theta_t)> \tag{2}$$

where l is the centre-to-centre mesogen separation distance, which becomes a contour length when the dimer is wrapped around the imaginary cylinder in Figure 3.11b. The averaging accounts for the distribution of mesogen tilt angles described by S_1 in the previous section. Equation 2 also applies to the N phase, but in this case θ_t represents the

tilt angle of the mesogens in respect to the nematic director, rather than the helical axis. At temperatures close to the N-N_{tb} boundary θ_t is almost unchanged, evidenced by the similar values of *d2* in Table 3.1. For simplicity the distribution of θ_t will be ignored in the remaining discussion and a constant value of *l* will be assumed.
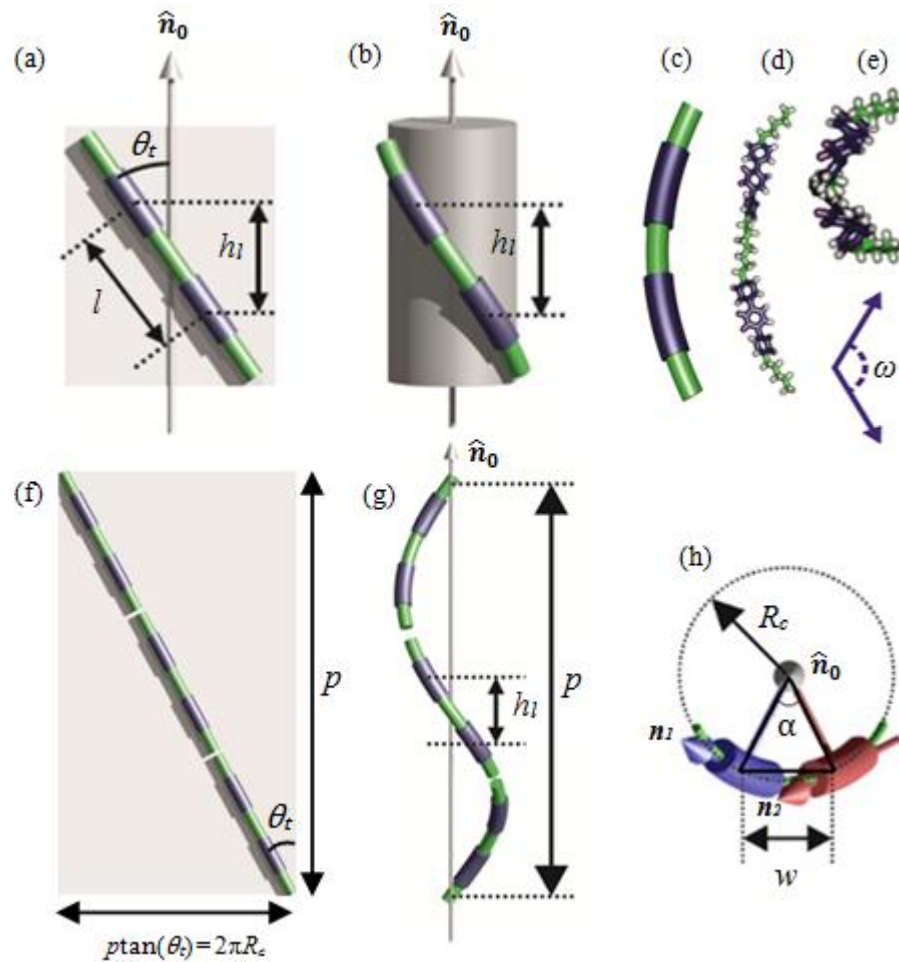
Figure 3.11 – (a) A straight dimer (bend angle = 0) resting on a 2D plane (b) the plane is wrapped cylindrically to create the bent dimer conformation, resembling a helical segment. (c) Simplified view of the idealised average molecular conformation, which is shown in more detail in (d) and (e). (e) shows the view along the axis of the spacer. (f) Derivation of the helical radius. If the plane is wrapped cylindrically, one arrives at (g). The distance between dimers has been exaggerated; in reality the local inter-mesogen separation should be almost invariant along $\hat{n}_0$. (h) View of the structure along $\hat{n}_0$; *w* is the transverse separation between mesogens projected onto the plane perpendicular to $\hat{n}_0$. The unit vectors n_1 and n_2 denote the direction of each mesogen of the dimer.

The value of l can be estimated from the known molecular structures of DTC5C7 and DTSe. From Figure 3.12, the average spacer and mesogen lengths, weighted by the molar ratio of the two compounds, are 0.88 and 1.46 nm, respectively. The value of l is therefore $0.88 + (2(1.46/2)) \simeq 2.3$ nm. The terminal chains were ignored in this calculation as they tend to be conformationally more disordered and are likely to partially interdigitate. As shown in Table 3.1, the value of h_l is almost invariant with temperature (~2 nm), suggesting a near constant tilt angle of ~29 ° in the N_{tb} phase. This tilt angle is larger than that obtained from birefringence measurements on DTC5C7 [6], but broadly in line with those discussed for 'CBCnCB' systems [18]; it is also slightly larger than the dimer tilt angle estimated for the Sm phase of Se45 (24 °). A smaller tilt angle in the Sm phase is in fact suggested by GIXRD experiments on oriented thin films of Se45: Comparison of Figures 3.7d and e shows that the Sm diffraction pattern has a smaller azimuthal spread in the WAXS region and larger d-spacing in the SAXS region, evidencing a smaller tilt angle.
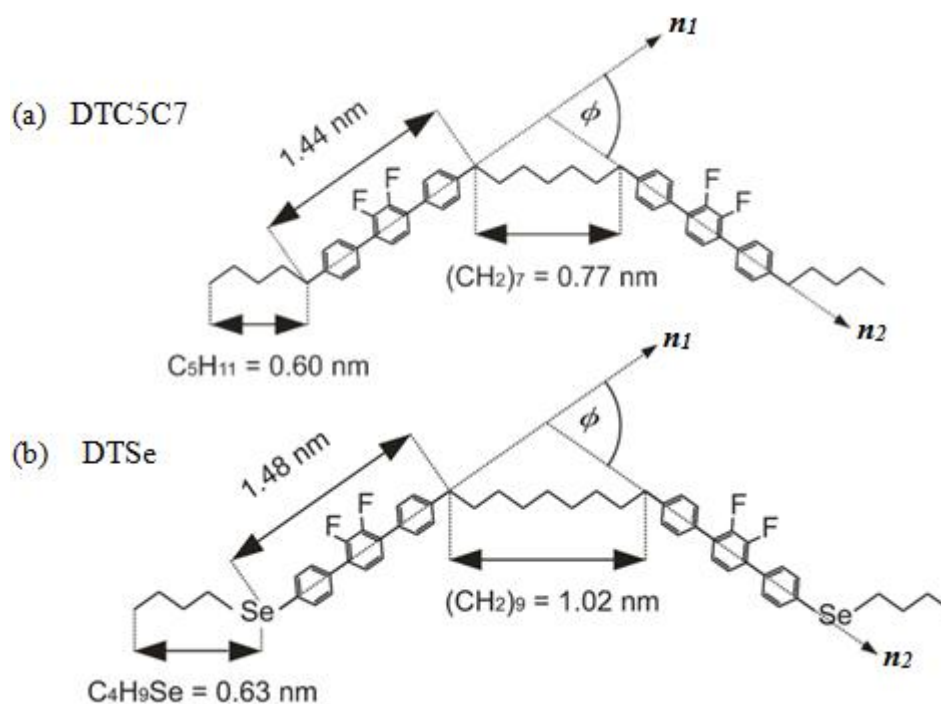
Figure 3.12 – The molecular structures of (a) DTC5C7 and (b) DTSe. The vectors n_1 and n_2 define the direction of each of the two mesogens in the dimer and ϕ is the angle between them, i.e. the molecular bend angle.

Using the experimental values of the rotation angle α and tilt angle θ_t, one may also calculate the bend angle between the two mesogens of a dimer. If one respectively defines the directions of the two rod-like mesogens by unit vectors $\boldsymbol{n_1}$ and $\boldsymbol{n_2}$ (see Figure 3.11h), it can be derived geometrically that:

$$\sin(\phi/2) = \sin(\theta_t)\cdot\sin(\alpha/2) \qquad\qquad (3)$$

where ϕ is the exterior bend angle between them (for a linear dimer $\phi = 0$). At 115 °C ϕ is calculated to be 28 °, which increases to 35 ° on cooling to 105 °C. In both instances ϕ is surprisingly low and much smaller than the bend angle imposed by an all-trans spacer (>60 °). Another important parameter is its twist angle ω, i.e. the angle between the two mesogens when projected along the spacer axis (Figure 3.11e). Using our model it can be calculated that the twist angle is 128 ° at 115 °C, and 125 ° at 105 °C (Appendix A). These values are far from the 0 ° twist angle for an all-trans conformation of the spacer.

In comparison to our model, a molecular dynamic simulation of the N_{tb} phase formed by the cyano-biphenyl dimer CB7CB has been carried out by D. Chen *et al* [19] in a periodic bounding box of size 5.6 × 5.6 × 8.0 nm. According to their computational model the average external bend angle ϕ of the dimer should be ~47 °, which is significantly larger than proposed by our model of Se45. On the other hand, Vanakaras and Photinos [20] have performed a simpler computer simulation where the molecules are represented by two rod-like units (representing the two mesogens in the dimer) with a fixed core-core distance between them. This simpler model predicted that an exterior bend angle of bend angle of ~30 ° and a twist angle also of ~120 °, similar to the values suggested by our model.

The results presented here (low bending angle and high twist angle of the dimer) suggest that in order to follow the heliconical path of the N_{tb} phase, the molecules must adopt a higher energy conformation in which the arms are twisted about the spacer axis, and closer to parallel than in the minimum energy conformation. Molecular modelling (Appendix A) has shown that this can be achieved by changing the torsion angles of the C-C bonds in the spacer, as shown in Figure 3.11e. In the N_{tb} phase (Figure 3.13) it is likely that this distortion energy is compensated by the entropy associated with the retained positional freedom of the dimers. Furthermore, the higher energy molecular conformation can explain several of the temperature dependant experimental

observations. For example, equation (3) shows that $p \propto 1/\phi$. The reducing pitch length in Se45 can therefore be attributed to an increasing bend angle on cooling. Lower energy conformations, i.e. a larger bend angles, are preferred at lower temperatures. On further cooling to the N_{tb}-Sm phase boundary, the translational entropy gain inside the N_{tb} phase must become insufficient to outweigh the energy cost of the twist-bend molecular distortion; the system must then adopt a long range layered structure. At the N-N_{tb} boundary, the value of ϕ is small and the dimers are close to straight. Here the helix unwinds as longitudinal motion no longer requires the molecules to follow the helical path. A smaller ϕ in the N phase is indicated by the reduced azimuthal spread of the WAXS arcs in Figure 3.7a, in comparison to 3.7b. The establishment of long-range homochirality in the N_{tb} phase appears to be a unique example of entropy-driven chirality synchronisation in achiral systems. Chirality synchronisation occurs where cooperativity in the choice of same-sense conformation in many molecules lowers the free energy - see recent reviews [21,22]. In all other reported cases the reduction in free energy means lowering the interaction energy through closer packing.
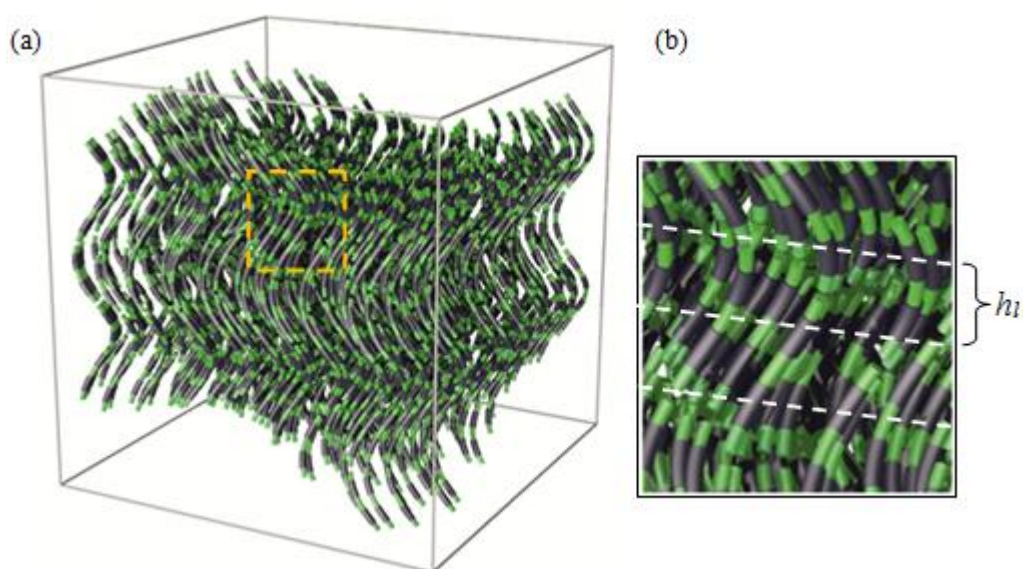
Figure 3.13 – (a) The molecular-level model of the N_{tb} phase with locally layered mesogens. The local layering is more visible in the magnified region shown in (b). The layering is only local and so positional fluctuation along the layer normal is expected to be much higher than in smectics. h_l is the average inter-mesogen separation distance, which is also the cybotactic layer height. Layers appear slanted due to the perspective view in (a).

3.6 – Summary

In summary, a selenium-containing dimer compound was specially synthesised, which exhibited the uniaxial nematic and B6 banana phases; however when mixed with a second dimer compound known as 'DTC5C7', the N_{tb} phase was observed. Using the Se-labelled dimer mixture, the first resonant hard X-ray scattering experiment on the N_{tb} phase was presented, which enabled magnetic sample alignment. A Resonant Bragg reflection at the Se absorption edge revealed a temperature dependent helical pitch between 9 and 12 nm. The high magnetic alignment of the sample in the N_{tb} phase, allowed the two components of the orientational order parameter, S_0 and S_1, to be deconvoluted. Consequently, it has been shown here for the first time that the order parameter of the global helical axis (S_0) can reach an unprecedentedly high value between 0.98 and 1.00. Simultaneous recording of the resonant Bragg reflection and the non-resonant scattering at higher q, revealed that the SAXS peaks are azimuthally broad even with near perfect alignment of the helical axis. The combined resonant and non-resonant data allowed the tilt angle of the mesogens, as well as the bend angle of the dimers, to be calculated. From these calculations the previous model of N_{tb} phase was expanded to consider the molecular-level arrangement, which is believed to be locally layered. Moreover, the mesogenic arms of the dimers must be twisted about the spacer axis and closer to parallel than suggested by the minimum energy conformation. Furthermore the first quantitative estimates of the helical correlation lengths were made, which suggest coherently diffracting N_{tb} domain sizes of approximately 0.1 μm.

References to Chapter 3

[1]   C. Zhu, M. R. Tuchband, A. Young, M. Shuai, A. Scarbrough, D. M. Walba, J. E. Maclennan, C.Wang, A. Hexemer, N. A. Clark, *PRL*, 2016, **116**, 147803.

[2]   A. de Vries, *Mol. Cryst. Liq. Cryst*, 1970, **10**, 219.

[3]   G. Pelzl, S. Diele, W. Weissflog, *Adv, Mater.*, 1999, **11**, 707.

[4]   A. A. Dawood, M.C. Grossel, G. R. Luckhurst, R. M. Richardson, B. A. Timimi, N. J. Wells, Y. Z. Yousif, *Liq. Crsyt.*, 2017, **44**, 106.

[5]   M. G. Tamba, S. M. Salili, C. Zhang, A. Jákli, G. H. Mehl, R. Stannarius, A. Eremin. *RCS Adv.*, 2015, **5**, 11207.

[6]   N. Sebastián, M. G. Tamba, R. Stannarius, M. R. de la Fuente, M. Salamonczyk, G. Cukrov, J. Gleeson, S. Sprunt, A. Jákli, C. Welch, Z. Ahmed, G. H. Mehl, A. Eremin, *Phys. Chem. Chem Phys.*, 2016, **18**, 19299.

[7]   S. A. Pardaev, S. Shamid, M. G. Tamba, C. Welch, G. H. Mehl, J. T. Gleeson, D. Allender, J. V. Selinger, B. D. Ellman, A. Jakli, S. Sprunt, *Soft Matter*, 2016, **12**, 4472.

[8]   Z. Zhang, V. P. Panov, M. Nagaraj, R. J. Mandle, J. W. Goodby, G. R. Luckhurst, J. C. Jones, H. F. Gleeson. *J. Mater. Chem. C*, 2015, **3**, 10007.

[9]   C.Meyer, G. R. Luckhurst, I. Dozov, *J. Mater. Chem. C*, 2015, **3**, 318.

[10] K. Adlem, M. Čopič, G. R. Luckhurst, A. Mertelj, O. Parri, R. M. Richardson, B. D. Snow, B. A. Timimi, R. P. Tuffin, D. Wilkes. *Phys. Rev. E*, 2013, **88**, 022503.

[11] V. P. Panov, M. Nagaraj, J. K. Vij, Yu. P. Panarin, A. Kohlmeier, M. G. Tamba, R. A. Lewis, G. H. Mehl, *Phys. Rev. Lett.*, 2010, **105**, 167801.

[12] L. Beguin, J. W. Emsley, M. Lelli, A. Lesage, G. R. Luckhurst, B. A. Timimi, H. Zimmermann, *J. Phys. Chem. B*, 2012, **116**, 7940.

[13] A. Hoffmann, A. G. Vanakaras, A. Kohlmeier, G. H. Mehl, D. J. Photinos, *Soft Matter*, 2015, **11**, 850.

[14] G. J. Brownsey, A. J. Leadbetter, *Phys. Rev. Lett.*, 1980, **44**, 24.

[15] K. K. Chan, P. S. Pershan, L. B. Sorensen, *Phys. Rev. A*, 1986, **34**, 2.

[16] S. H. Hong, R.Verduzco, J. C. Williams, R. J. Twieg, E. DiMasi, R. Pindak, A. Jákli, J**.** T. Gleeson, S. Sprunt, *Soft Matter*, 2010, **6**, 4819.

[17] P. S. Pershan, (1988). *"Structure of Liquid Crystal Phases"*. World Scientific Publishing Ltd.

[18] C.Meyer, G. R. Luckhurst, I. Dozov, *J. Mater. Chem. C*, 2015, **3**, 318.

[19] D. Chen, J. H. Porada, J. B. Hooper, A. Klittnick, Y. Shen, M. R.Tuchband, E. Korblova, D. Bedrov, D. M.Walba, M. A. Glaser, J. E. Maclennan, and N. A. Clark, *Proc. Natl. Acad. Sci. U.S.A.*, 2013, **110**, 15931.

[20] A. G. Vanakaras, D. J. Photinos, *Soft Matter*, 2016, **12**, 2208.

[21] C. Tschierske and G. Ungar, *ChemPhysChem*, 2016, **17**, 9.

[22] E. Yashima, N. Ousaka, D. Taura, K. Shimomura, T. Ikai, K. Maeda, *Chem. Rev*., 2016, **116**, 13752.

Chapter 4 – Circular Dichroism in the N_{tb} Phase and Characterisation of the Lower Temperature Phases

The first circular dichroism experiments were performed on the N_{tb} phase in a series of bent, di-flouro-terphenyl-based, dimer homologues, abbreviated as DTC5Cn. This enabled direct identification of chirality in the bulk sample without complicated resonant X-ray diffraction methods. In molecules with shorter spacers (DTC5C5 and DTC5C7) a 2D modulated smectic, known as the 'X phase' was observed on cooling from the N_{tb} phase. This structure is currently believed to be oblique, but the evidence presented here supports a centred rectangular unit cell with a unique, optically biaxial, intercalated double-layering style that may be exclusive to systems of bent dimers. Based on the similarities of the X phase and the B1 banana phase, it is proposed here that the in-layer modulation likewise arises from polarisation splay of the molecular bend. Moreover circular dichroism suggests that the X phase is chiral, which may be explained by the interplay between molecular tilting and splay. Bent achiral dimers may therefore create in-layer (transverse) chirality, as well as the heliconical (longitudinal) type observed in the N_{tb} phase. In longer spacer molecules (DTC9C5) a different 1D, or perhaps 2D, smectic phase was observed, with a currently unknown layering structure.

4.0 – Introduction

Due to the ambiguity of topological characterisation techniques (Chapter 1, section 1.6.2), methods of identifying chirality in the bulk N_{tb} phase are more advantageous. To date, bulk phase chirality has been identified by ^{1}H-NMR spectroscopy [1,2] and more recently by resonant X-ray scattering (RXS) [3]; however, electronic circular dichroism (ECD) experiments on the N_{tb} phase have not yet been performed. In contrast to RXS experiments, ECD is very simple in practice: the UV/Visible absorbance of the sample is measured while being sequentially exposed to left and right handed circularly polarised light. If the two polarisation types are absorbed unequally, the sample must be handed and therefore comprise chiral molecular bonds, chiral molecular conformations or a locally chiral structure [4]. Although ECD can be used to directly identify chirality in the bulk sample, there are two primary drawbacks associated with this method: (i) Like NMR, the CD signal does not allow any specific structural features to be determined.

(ii) CD spectra are impacted heavily by unwanted linear dichroism and birefringence effects [5,6].

In this study the CD signal of the N_{tb} phase was measured in a series of bent di-flouro-terphenyl based, symmetric dimer compounds, labelled according to 'DTC5Cn', where 'n' (= 5, 7, 9, 11) is the number of CH_2 linkers in the adjoining oligomethylene spacer (see Figure 4.0). The drawbacks mentioned above were addressed by aligning the N_{tb} phase homeotropically, such that the helical axis ran parallel to the propagation direction of the incident beam. When homeotropically aligned the N_{tb} phase is non-birefringent which drastically reduces the contributions of linear optical effects to the CD spectra, allowing phase chirality to be determined. Although the origin of the chiral signal cannot be directly determined, the N_{tb} phase is known to possess a helical structure with a pitch length between 9 and 12 nm (Chapter 3, section 3.3). Moreover the molecules are chemically achiral, which means that CD can only be attributed to the helical structure or to chiral molecular conformations inside the helical structure (see Chapter 3, section 3.5).
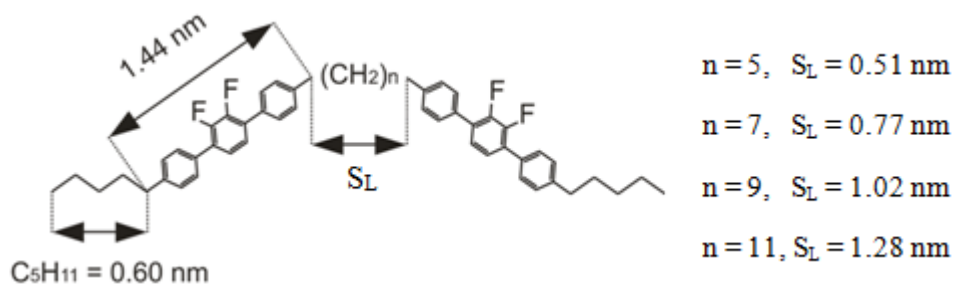
Figure 4.0 – Molecular structure of DTC5Cn homologues. 'n' denotes the number of CH_2 linkers in the central spacer chain; S_L = Spacer length. The lengths of each component were determined using geometry optimisation calculations in Materials Studio (version 6).

In addition to the first CD measurements, the effects of increasing spacer length, hence molecular flexibility, on the temperature range and local structure of the N_{tb} phase, and lower temperature smectic (Sm) phases, are discussed. Varying the spacer length was found to result in one of two lower temperature Sm phases: 'X' type (DTC5C5/DTC5C7), or 'Y' type (DTC5C9). The X phase was first reported in DTC5C7 [7] and is currently believed to have a 2D modulated structure described by an oblique unit cell [8]. However this assignment is challenged here by the results of a

more in-depth grazing incidence X-ray scattering (GIXS) study, which supports a centred rectangular unit cell, analogous to the B1 banana phase of bent core mesogens (see Chapter 1, section 1.5.1). Based on the new experimental findings, a modified model is constructed based the work of Coleman *et al* [9,10], featuring local polarisation splay of the molecular bend direction. Furthermore this study is believed to be the first observation of the Y phase, which possesses a complex 1D or 2D modulated structure that is yet to be identified.

All compounds featured in this study were synthesised and provided by the organic chemistry group, led by Professor Georg Mehl, at the University of Hull, UK. As the molecular homologues differ only by the spacer chain length, the synthetic procedure of each compound need not be discussed. However, as mentioned in the previous chapter, the synthetic procedure of DTC5C7 is provided in Appendix A.

4.1 – DSC Analysis of DTC5Cn Dimer Compounds

The phase behaviour of the DTC5Cn (n = 5, 7, 9, 11) compounds was firstly investigated via DSC using a Perkin Elmer Diamond DSC fitted with a liquid nitrogen cooling unit. The normalised 10 °C/min DSC traces of the samples during the first heating and second cooling are shown in Figure 4.1a. Peak temperatures and measured transition enthalpies are tabulated in Tables 4.0 and 4.1. The phase assignments were confirmed using supporting evidence from polarised optical microscopy (POM) and conventional (non-resonant) X-ray scattering experiments, which are discussed later.

With increasing spacer length, the isotropisation transition is pushed to higher temperatures and the N-N_{tb} transition is simultaneously shifted to lower temperatures. This creates a much wider temperature range for the uniaxial N phase. This may be because the increased flexibility of long spacer molecules allows the two mesogen arms to be more parallel than in the shorter spacer compounds. With the mesogen arms closer to parallel the N phase would be preferential. The enthalpy (peak area) associated with the first order N-N_{tb} transition decreases with increasing spacer length. There is no sharp N-N_{tb} peak in the DSC of DTC5C11, and it is still unclear whether the transition is second order or weakly first order. The reducing enthalpy with spacer length can perhaps be explained by a varying local layering structure in the N_{tb} phase (see section

4.4). The spacer length was also found to affect the N_{tb}-Sm transition: the longer the spacer, the lower the transition temperature to the lamellar phase; in DTC5C11, there is no smectic phase at all. In DTC5C7 and DTC5C9 the temperature of the smectic phase transition is below the crystal melting point, which means that their Sm phases are monotropic (observed only on cooling) and meta-stable. Short spacer molecules may choose to adopt lamellar phases more easily due to the increased rigidity and molecular curvature. Dependency of the phase transition temperatures on the chemical structure of bent LC dimers is discussed in detail in ref [11].
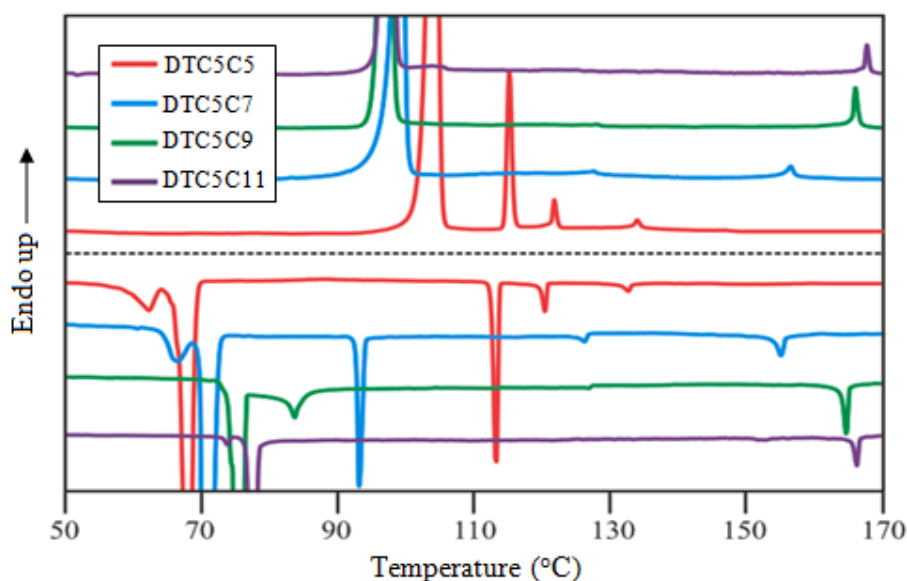
Figure 4.1 – DSC curves recorded during the first heating and second cooling of each DTC5Cn compound. The heating/cooling rate was 10 °C/min in all cases.

Table 4.0 – Transition Temperatures and Enthalpies of DTC5Cn Compounds on Heating

Heating	$C{\rightarrow}Sm$ (°C)[Jg^{-1}]	$Sm{\rightarrow}N_{tb}$ (°C)[Jg^{-1}]	$C{\rightarrow}N_{tb}$ (°C)[Jg^{-1}]	$N_{tb}{\rightarrow}N$ (°C)[Jg^{-1}]	$N{\rightarrow}Iso$ (°C)[Jg^{-1}]
DTC5C5	104.3 [45.96]	115.4 [5.41]	-	122.0 [0.68]	134.3 [0.29]
DTC5C7	-	-	99.5 [39.39]	127.8 [0.26]	156.8 [0.78]
DTC5C9	-	-	97.4 [54.03]	128.3 [0.24]	166.1 [2.00]
DTC5C11	-	-	98.0 [54.64]	Unknown	167.8 [1.13]

Numbers in square brackets correspond to the transition enthalpy. Iso = isotropic, N = Nematic, N_{tb} = Twist bend nematic, Sm = Smectic and C = Crystal.

Table 4.1 – Transition Temperatures and Enthalpies of DTC5Cn Compounds on Cooling

Cooling	Iso→N (°C)[Jg^{-1}]	N→N$_{tb}$ (°C)[Jg^{-1}]	N$_{tb}$→C (°C)[Jg^{-1}]	N$_{tb}$→Sm (°C)[Jg^{-1}]	Sm→C (°C)[Jg^{-1}]
DTC5C5	132.8 [-0.26]	120.5 [-0.78]	-	113.5 [-5.61]	68.2 [-29.88]
DTC5C7	155.0 [-0.94]	126.3 [-0.32]	-	93.4 [-3.00]	71.4 [-30.62]
DTC5C9	164.7 [-1.56]	126.9 [-0.26]	-	83.8 [-1.26]	75.8 [-44.66]
DTC5C11	166.5 [-1.17]	Unknown	77.7 [-48.25]	-	-

Numbers in square brackets correspond to the transition enthalpy. Iso = isotropic, N = Nematic, N$_{tb}$ = Twist bend nematic, Sm = Smectic and C = Crystal.

4.2 – Optical Textures of DTC5Cn Dimer Compounds

The Optical textures of the DTC5Cn compounds were investigated using an Olympus BX50 Microscope fitted with a Mettler FP82 HT hotstage. Each compound was placed between two glass plates and heated until isotropic. The samples were then cooled stepwise through their respective phase sequences until reaching the crystal phase. It should be noted that the DTC5Cn compounds are reported to possess negative dielectric anisotropy [8,12,13], meaning that the slowest axis of the domains is perpendicular to the average alignment direction of the molecules.

4.2.1 – Optical Textures of Short Spacer Molecules

The compounds of short spacer molecules, DTC5C5 and DTC5C7, were found to exhibit the same phase sequence, but with differing transition temperatures and associated enthalpies (see above). On cooling from the isotropic to the N phase, large domains of uniaxial alignment or schlieren disclinations were observed (Figure 4.2a), which upon further cooling to the N$_{tb}$ phase, transformed into the rope-like texture (Figure 4.2b). After even further cooling, the rope-like texture of the N$_{tb}$ phase was replaced by a wavy block-like texture with increased birefringence; this signified the transition to the X phase (Figure 4.2c). The optical textures of DTC5C5 and DTC5C7 were further explored by applying shearing force. Shearing in the N phase altered the optical texture very little; the sample was liquid-like between the plates and flowed easily. However when cooled into the N$_{tb}$ phase the viscosity of the sample increased significantly, as reported elsewhere [2]. With shearing force (applied at 118 °C in both

samples), the N_{tb} phase aligned homeotropically, evidenced by an almost perfect black field of view on the scale of millimetres (Figure 4.2d). The field of view remained black in all sample orientations. The black field of view indicates that the helical axis of the N_{tb} phase was oriented perpendicular to the glass substrates and parallel to the viewing direction.

On cooling the sheared N_{tb} phase into the X phase, regions of very fine striping were observed (Figure 4.2e). In contrast to the planar block-like texture, the striping was very weakly birefringent, suggesting that the sample remained homeotropically aligned in the X phase, i.e. with the layer normal oriented perpendicular to the glass plates and parallel to the viewing direction. The X phase is therefore biaxial, arising from long range orientational order of the second anisotropic axes of the molecules. The striping is believed to be another example of the Helfrich-Hurault effect, where the layers are periodically undulated in response to mechanical stress [14,15]. The transition between the N_{tb} dark-field and the X phase stripes was found to be highly reversible on repeated heating and cooling. It should be noted that X phase was found to be even more viscous than the N_{tb} phase (comparable to crystal) and any attempt to directly shear the phase induced crystallisation. In DTC5C7 crystallisation was also found to occur after long standing in the X phase (~15 min).
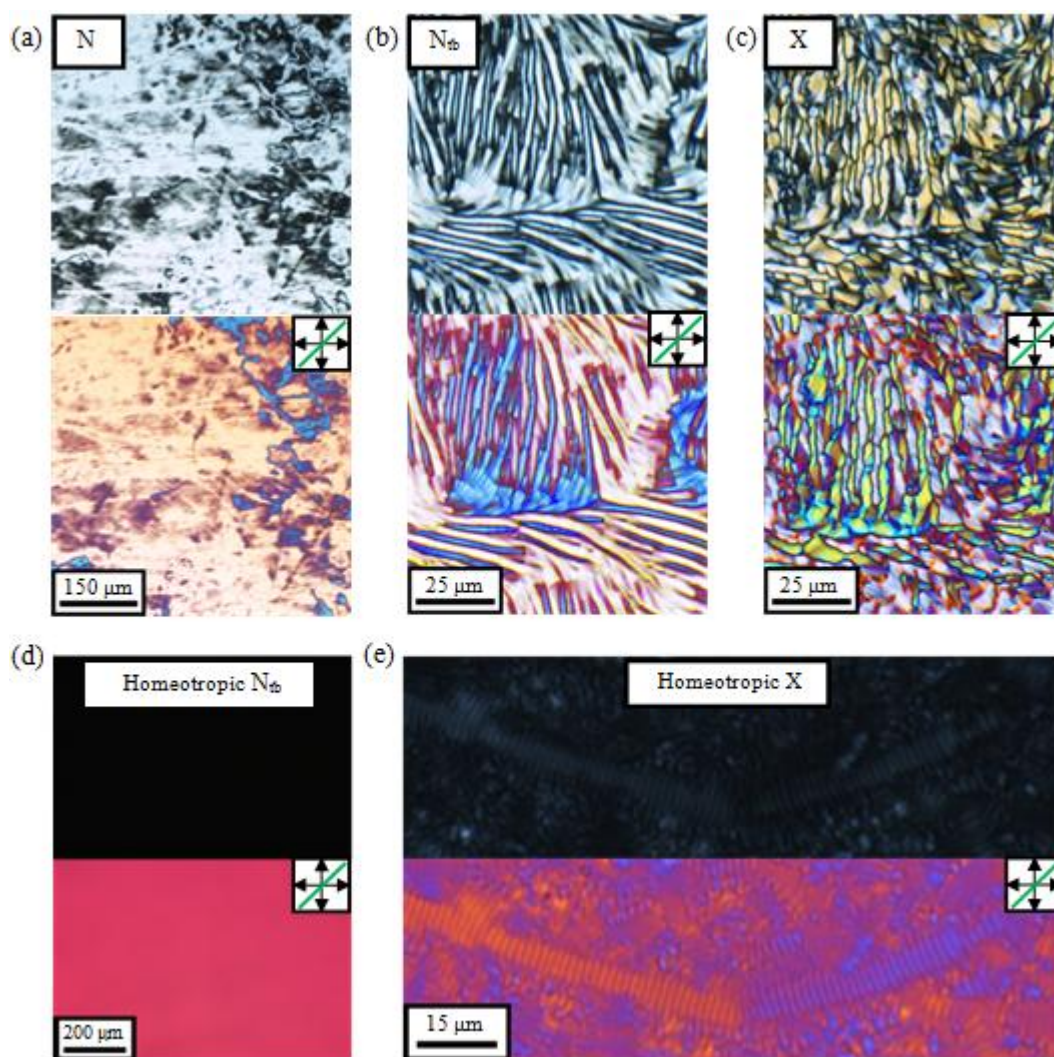
Figure 4.2 – The planar optical textures of DTC5C7 in the N phase (130 °C) (a), N_{tb} phase (115 °C) (b) and X phase (90 °C) (c). (d) Sheared (homeotropically aligned) N_{tb} phase (118 °C) with helical axis perpendicular to the glass plates. Shearing direction horizontal. (e) Homeotropically aligned X phase (90 °C), achieved on cooling from (d). The layer normal is perpendicular to the glass plates. Similar textures were also observed in DTC5C5 (Appendix B). In all cases top (/bottom) show the textures without (/with) a λ-plate inserted into the optics with axis direction indicated in green. The scale bar applies to both.

4.2.2 – Optical Textures of Long Spacer Molecules

The optical textures of the longer spacer molecules, DTC5C9 and DTC5C11, were very similar to those described in section 4.2.1 above. In the planar oriented sample the schlieren and rope-like textures of the N and N_{tb} phases were respectively observed (Appendix B). Shearing the N_{tb} phases of DTC5C9 and DTC5C11 at 118 °C produced near perfect homeotropic sample alignment as observed in the shorter spacer samples.

On cooling DTC5C9 from the homeotropically aligned N_{tb} phase to the Y phase (80 °C), no optical changes were observed; the field of view was completely black until crystallisation, which began after standing for ~5 minutes. Furthermore, there were no observable differences between the textures of the planar N_{tb} and Y phases; the texture of the sample was rope-like from the N-N_{tb} transition through to crystallisation. Although there are no optical changes, the N_{tb}-Y transition is obvious when investigated via X-ray diffraction (see section 4.4).

4.3 – ECD Analysis of DTC5Cn Dimer Compounds

ECD experiments were conducted on station B23 of the DLS using a custom made instrument featuring an ultra high vacuum Olis DSM20 monochromator and a photomultiplier tube (detector) with an MgF_2 window. The cross-sectional area of the incident beam was approximately 0.5 mm^2 at the sample position. Inside the optical chamber, the sample was held in a quartz glass sandwich cell, which rested on a custom made rotatable stage, featuring a Linkam heating element. In this configuration the incident beam ran perpendicular to the surfaces of the glass plates (see Figure 4.3). The CD spectra of the LC phases were recorded in the wavelength range of 250–450 nm. The intensity was integrated for 1 second in each 1 nm increment. Due the angular dependence of unwanted linear optical effects, the CD spectra of the LC phases were recorded in various sample orientations. The rotatable stage ensured that the same region of the sample was illuminated in each case, enabling birefringent contributions to the CD spectra to be identified [5,6]. In this work CD is given as the absorption difference between left and right handed circularly polarised light ($\Delta A = A_{Left} - A_{right}$) [16,17]. This is related to ellipticity (Ω, measured in millidegrees) by $\Delta A = \Omega/32.98$ [16,17]. However the cell gap was different for each sample (preventing normalisation) and so an arbitrary scale is used.
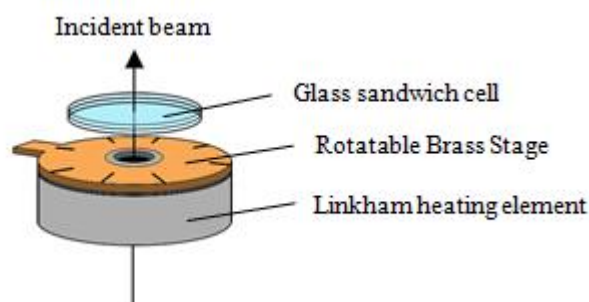
Figure 4.3 – The custom rotatable stage used during ECD experiments.

<u>4.3.1 – ECD in the N_{tb} phase</u>

The DTC5Cn (n = 5, 7, 9) samples were cooled from the isotropic phase to the N_{tb} phase (118 °C) and consequently sheared to obtain homeotropic alignment. Sample shearing was performed directly inside the optical chamber of the CD instrument, while resting on the heated stage. When homeotropically aligned, large regions of all three samples were found to be non-birefringent due to parallel alignment of the helical axis with the direction of light propagation (Figure 4.2d). The CD spectra of the homeotropically aligned N_{tb} phase are shown in Figures 4.4a-c. The spectra of the planar N phase in DTC5C7 are also shown to illustrate the dominance of birefringence (Figure 4.4d). For DTC5C7 and DTC5C9 samples, the cell thickness was determinable due to a resonance effect between the incident wavelength and the cell gap. Resonance of longitudinal cavities requires a cell gap equal to an integer number of half wavelengths [18], allowing the sample thickness to be determined as 3.4 μm in DTC5C7 and 8.3 μm in DTC5C9. The cell gap was found to be temperature dependent and was determined as 4.1 μm in the N phase of DTC5C7. With the known cell gaps, the average ellipticity per micron in the N_{tb} phase was calculated as 13.5 m°/μm in DTC5C7 and 9.3 m°/μm in DTC5C9. This suggests that the N_{tb} phase is more strongly chiral in shorter spacer molecules, but further work on DTC5C5 and DTC5C11 is needed to support this hypothesis.

In all three compounds, the CD spectra of the homeotropically aligned N_{tb} phase exhibited a singular negative peak with a maximum amplitude between 315 and 326 nm. The absorption peak is attributed to electron energy transitions in the fluorinated terphenyl mesogens. In the N_{tb} phase, the sign of the peak was invariant with rotation angle, indicating that the signal arises primarily from phase chirality rather than linear optical effects. However, the varying amplitude of the CD peak in the N_{tb} phase suggests that birefringence was not entirely eliminated by homeotropic alignment. In the planar N phase the sign of the CD peak did not remain constant and was much larger in amplitude, indicating strong birefringent contributions. Other N_{tb} sample regions were investigated, but in all cases the peak was persistently negative and similar in amplitude. This suggests that a single handedness (right handedness) dominates the sample, but does not necessarily rule out the existence of oppositely handed domains.

The precise origin of the chiral signal cannot be directly determined from the CD spectra, but the N_{tb} phase of DTC5C7 is known to possess a helical structure with a pitch length between 9 and 12 nm. This was confirmed in the previous chapter by RXS in a 55/45 mol% mixture of DTC5C7/DTSe. Pure DTSe does not form the N_{tb} phase, which means that the N_{tb} helix must be a feature of DTC5C7. In this sample the CD peak must therefore correspond to the helical structure of the N_{tb} phase, or alternatively to the presence of chiral molecular conformations. However, as the molecules are chemically achiral, this explanation also supports the helical structure of the N_{tb} phase. In fact chiral conformations are expected according to the molecular-level model presented in Chapter 3, section 3.5. The CD signal of the N_{tb} phase appears almost identical in each compound, which strongly suggests that the helical structure is present in all three cases.
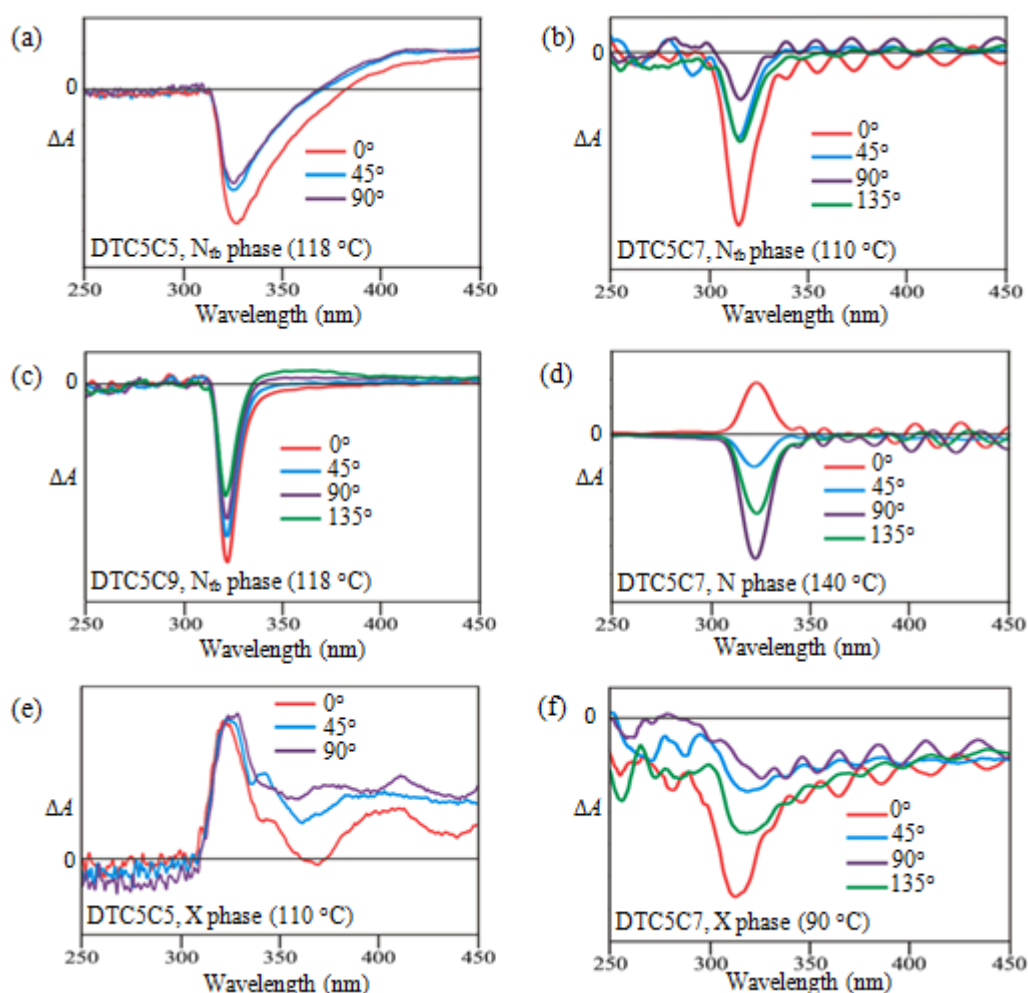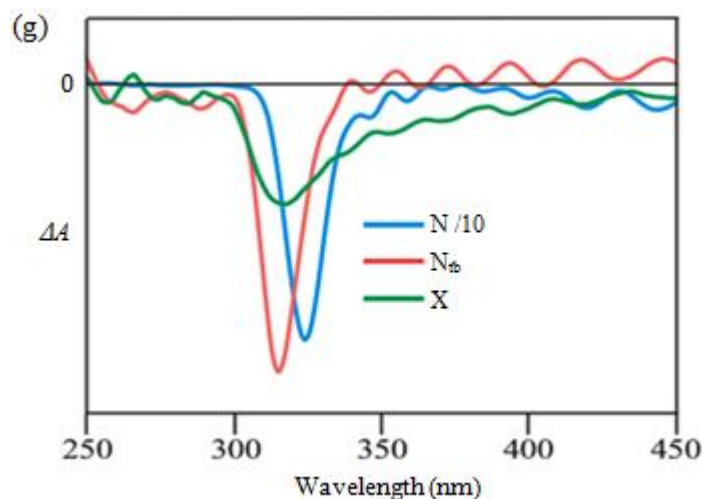
Figure 4.4 – The CD spectra of the homeotropically aligned N_{tb} phase (sheared at 118 °C) in DTC5C5 (a), DTC5C7 (b) and DTC5C9 (c). (d) The CD spectra of the N phase in DTC5C7. The CD spectra of the X phase in DTC5C5 (e) and DTC5C7 (f). (g) Comparison of the average CD signal recorded in the N, N_{tb} and X phases of DTC5C7. The CD signal of the N phase has been divided by a factor of ten to compensate the huge contribution of linear effects (birefringence) to the peak amplitude. Oscillation between 450 and 350 nm is believed to arise from a resonance effect between the incident wavelength and the cell gap. $\Delta A = A_{Left} - A_{Right}$ shown on an arbitrary scale.

4.3.2 – CD in the X phase

The X phase of short spacer molecules, DTC5C5 and DTC5C7, was investigated on cooling from the sheared N_{tb} phase. Homeotropic sample alignment is preserved over the N_{tb}-X transition as discussed in section 4.2.1. Unlike the sheared N_{tb} phase, the X phase is weakly birefringent even when homeotropically aligned due to phase biaxiality. The CD spectra of the X phase in DTC5C5 and DTC5C7 are shown in Figures 4.4e and f, respectively. In both cases the dominant peak is positioned between 312 and 329 μm, and is similarly associated with electronic transitions in the fluorinated terphenyl group. The sign of the peak is invariant with rotation angle suggesting that the peak arises from phase chirality rather than linear optical effects. The amplitude of the peak fluctuates more in the X phase than previously observed in the N_{tb} phase, but this is probably a result of increased linear contributions in the X phase. Interestingly, in DTC5C5 the handedness of the sample changes on transition from the N_{tb} to the X phase. The reason for this is not yet understood. In DTC5C7 the thickness of the X phase was directly determined from cell gap resonance as 3.1 μm, enabling the average ellipticity per micron to be calculated as 6.0 m°/μm. The CD signal of the X phase is therefore weaker

than that of the N_{tb} phase and the shape of the peak is also different. The peak shift, modified line-shape and reduced CD amplitude are consistent with a change in molecular arrangement on transition from the N_{tb} to the X phase, which is discussed further in section 4.5. For comparison, the relative CD spectra of the N, N_{tb} and X phases (in DTC5C7) are shown in Figure 4.4g. Despite being only meta-stable in DTC5C7, the CD spectra of the X phase look very similar in the two compounds (ignoring opposing handedness), suggesting that DTC5C7 did not re-crystallise during the timeframe of the measurements.

Note: The Y phase of DTC5C9 could not be investigated because it crystallises much more quickly than the X phase of DTC5C7. The results cannot be trusted without in situ POM.

4.4 – X-ray Scattering by DTC5Cn Dimer Compounds

The small and wide angle X-ray scattering (SAXS and WAXS) patterns of the DTC5Cn (n = 5, 7, 9, 11) compounds were investigated on station BM28 of the ESRF and station I22 of the DLS. Each sample was investigated in both transmission and grazing incidence setups. In the transmission setup the samples were sealed in 1.0 mm diameter glass capillaries. On station BM28 the capillaries were held in a custom heating cell, positioned between the poles of a superconducting solenoid (magnetic field = 3 T). On station I22 the capillaries were held in a permanently magnetised cell (magnetic field = 1 T) and were heated/cooled using temperature controlled nitrogen gas. In the grazing incidence setup the samples were deposited as a thin film (via melting) onto silicon substrates, which rested on the temperature controlled surface of a custom six-circle goniometer. Each sample was aligned by shearing force in the N_{tb} phase. In both setups the WAXS and SAXS regions of the diffraction pattern were investigated separately using a Mar165 CCD (BM28) or two Pilatus 2M area detectors (I22). To reduce air scattering, a helium flushed flight tube (BM28) or a vacuum chamber (I22) was positioned between the sample and detector.
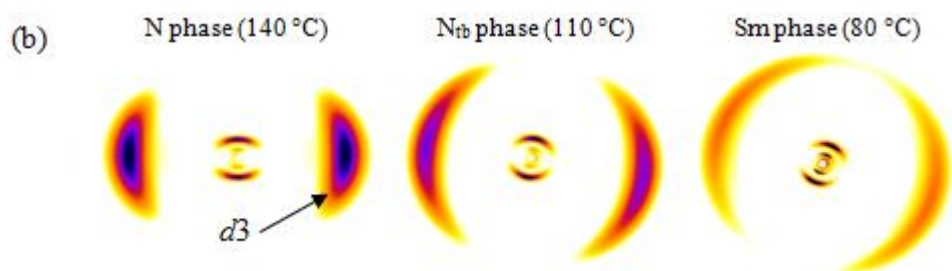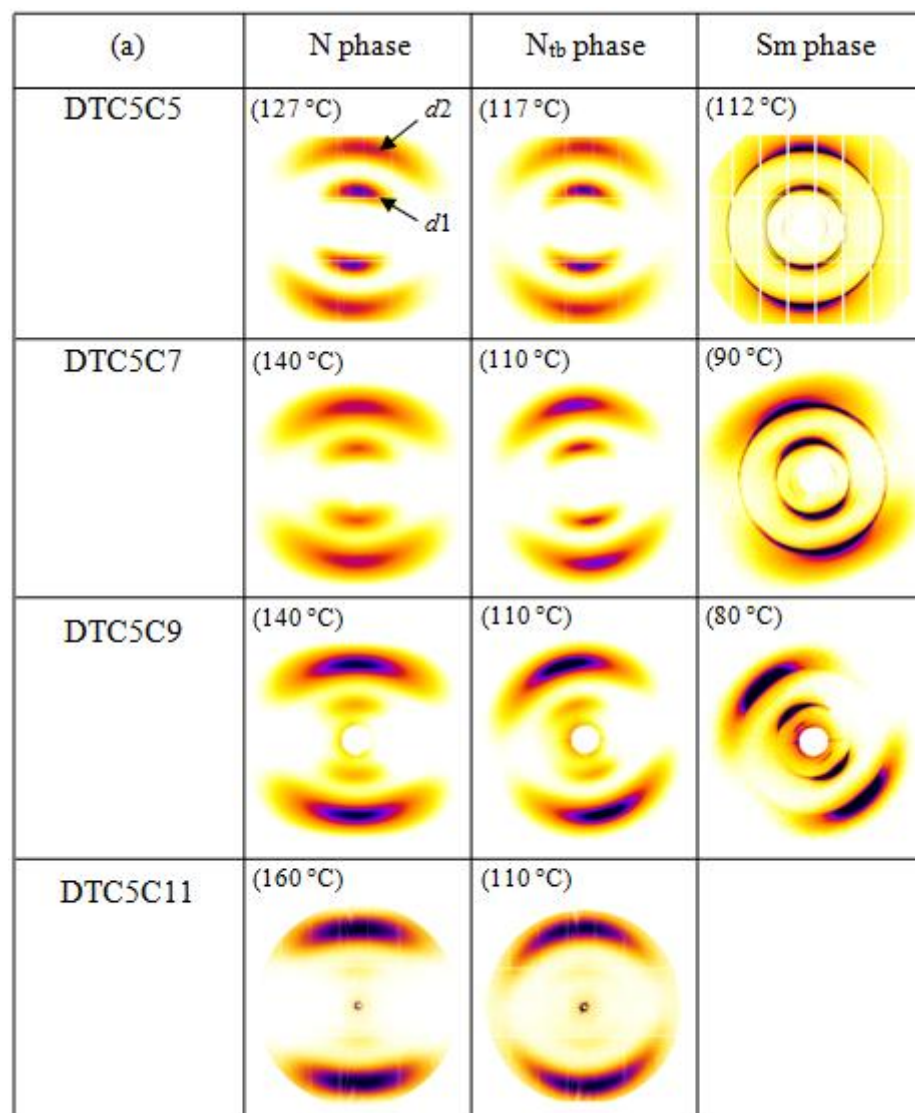
Figure 4.5 – (a) Magnetically aligned 2D SAXS patterns of the LC phases observed in each DTC5Cn compound. The field **B** is vertical in all cases. The measured values of $d1$ and $d2$, as well as the measured spacing of the diffuse WAXS peak ($d3$), are provided in Table 4.2. (b) Magnetically aligned 2D WAXS patterns of DTC5C9, with field **B** vertical. The wide angle region appears very similar in all four compounds (in the respective phases).

During investigation, each of the DTC5Cn compounds was heated to the isotropic phase and cooled through each of its LC phases until crystalline. In the N and N_{tb} phases, two broad SAXS peaks were observed arising from local nematic correlation (cybotactic layering), as discussed in Chapter 3. The two broad peaks are labelled $d1$ and $d2$, where $d1$ corresponds to the peak at lower q (~4 nm), associated with inter-dimer separation, and $d2$ corresponds to the peak at higher q (~2 nm), associated with inter-mesogen separation. A broad WAXS peak ($d3 \simeq 0.45$ nm) was also observed in both phases, attributed to the average side-by-side inter-molecular spacing ($1.117d3 \simeq 0.5$ nm [19]). In the X and Y phases, the broad SAXS peaks were replaced by sharp Bragg reflections; however the WAXS peak remained broad, confirming that the X and Y phases are LCs and not crystals (see sections 4.5 and 4.6). The SAXS patterns of the DTC5Cn compounds are shown in Figures 4.5a. The measured d-spacings are tabulated in Table 4.2.

Table 4.2 – XRD Data Summary of DTC5Cn Compounds on Cooling

		N phase	N_{tb} phase	X phase	Y phase
DTC5C5	$d1$ (nm)	3.9	3.8	3.78	-
	$d2$ (nm)	1.8	1.8	1.91	-
	$d3$ (nm)	0.45	0.44	0.44	-
DTC5C7	$d1$ (nm)	4.0	4.0	4.13	-
	$d2$ (nm)	1.9	1.9	2.09	-
	$d3$ (nm)	0.46	0.46	0.45	-
DTC5C9	$d1$ (nm)	4.5	4.3	-	4.35
	$d2$ (nm)	2.1	2.0	-	2.18
	$d3$ (nm)	0.46	0.45	-	0.45
DTC5C11	$d1$ (nm)	*4.8	*4.8	-	-
	$d2$ (nm)	2.3	2.2	-	-
	$d3$ (nm)	0.47	0.46	-	-

The measurements correspond to the diffraction patterns shown in Figure 4.5. In the X phase, $d1$ and $d2$ respectively correspond to (11) and (02) reflections; in the Y phase, $d1$ and $d2$ respectively correspond to (70) and (14 0) reflections (see Figures 4.6 and 4.9). *Difficult to accurately measure.

The measured *d*-spacings of the peaks increase almost linearly with the length of the spacer. This was expected due to the increasing length of the molecules with 'n'. *d*3 alters very little, ranging between 0.47 and 0.44 nm depending on the temperature and compound. More interestingly, the intensity ratio between *d*1 and *d*2 changes progressively with spacer length. In DTC5C5 the inter-dimer peak (*d*1) is strongest, but weakens in comparison to the inter-mesogen peak (*d*2) in compounds with longer spacer molecules; *d*1 is almost unobservable in DTC5C11. The intensity redistribution between *d*1 and *d*2 with increasing spacer length suggests that local layering structure in the N_{tb} phase changes from SmC-type dimer layering (shorter spacers) to intercalated dimer layering (longer spacers). When the dimers are intercalated i.e. randomly half-stepped along the helix axis, only the mesogens are locally layered, which may explain why the *d*1 peak is weak in comparison to *d*2 in compounds featuring longer spacers. In both local layering styles the molecules are assumed to be tilted due to fundamental requirement of the N_{tb} helix.

Locally intercalated dimer layering must be energetically allowed only when the spacer length is similar to the combined length of the two $(CH_2)_5$ terminal chains. In instances where the spacer is much shorter than the combined length of the terminal chains, the dimer must behave more like rigid molecules. This is indirectly supported by DSC measurements, which show that shorter spacer molecules form banana phases (see section 4.5) at higher temperatures than longer spacer molecules. The two different layering styles can also be used to explain why the N-N_{tb} transition enthalpy decreases with increasing spacer length: In all compounds, one may assume that the dimers are intercalated/randomly positioned in the uniaxial N phase. In systems of long spacer molecules, the dimers remain intercalated on transition to the N_{tb} phase, but twist into the helix. However in systems of shorter spacer molecules, the dimers must locally segregate into local SmC layers, as well as twist into the helix. The lower entropy of the N_{tb} phase in short spacer systems means that more energy must be released during the N-N_{tb} transition in short spacer compounds.

4.5 – Structural Analysis of the X phase

4.5.1 – Identification of the 2D Unit Cell

The X phase of short spacer molecules, DTC5C5 and DTC5C7, was examined via transmission and grazing incidence X-ray diffraction techniques, using the same instruments and experimental setups described in section 4.4. However non-magnetically aligned (powder) SAXS patterns were also recorded for the purpose of relative intensity measurements. The powder SAXS patterns were recorded after cooling each sample from the isotropic phase to 110 °C in DTC5C5 and 90 °C in DTC5C7 (Figure 4.6a). The indexing procedure was facilitated by orientational information obtained by GISAXS of sheared thin films (Figure 4.6b). The samples were sheared in the N_{tb} phase (118 °C) and cooled into the X phase. The shearing produced homeotropic alignment of the helical axis/layer normal, which was confirmed optically (section 4.2.1) and by symmetry of the GIWAXS patterns (Figures 4.6c,d). The diffuse WAXS peaks are centred on the axis parallel to the substrate (equator), while the SAXS peaks are centred on a perpendicular axis (meridian).

The intensity distribution and d-spacings of the X phase (Table 4.3) agree with a centred rectangular ($c2mm$) unit cell. In DTC5C5 the lattice parameters are $a = 27.29 \pm 0.02$ nm and $b = 3.81 \pm 0.02$ nm, while in DTC5C7 $a = 27.39 \pm 0.01$ nm and $b = 4.17 \pm 0.01$ nm. The lattice parameters a and b respectively correspond to the in-layer modulation wavelength and the layer height. In both compounds the layer height of the X phase is smaller than the estimated length of the molecules, suggesting a tilt angle of 22 ° in DTC5C5 and 14 ° in DTC5C7. In the latter compound, $d1$ of the N_{tb} phase is smaller than the layer height of the X phase, suggesting a larger tilt angle in the N_{tb} phase (22 °). This is also supported by Figures 4.6c and d; the increased azimuthal spread of intensity in the WAXS region infers a larger tilt angle in the N_{tb} phase. Moreover, the diffuse WAXS peak, corresponding to an average side-to-side molecular separation of ~0.5 nm, confirms that the X phase is an LC. The FWHM of the Bragg reflections are comparable to the resolution limit of the experimental setup, indicating crystal-like molecular correlation lengths along both axes of the unit cell. These findings are contrary to previous studies of the X phase, which propose an oblique unit cell [8] and correlation lengths shorter than the 'a' parameter determined here [7].
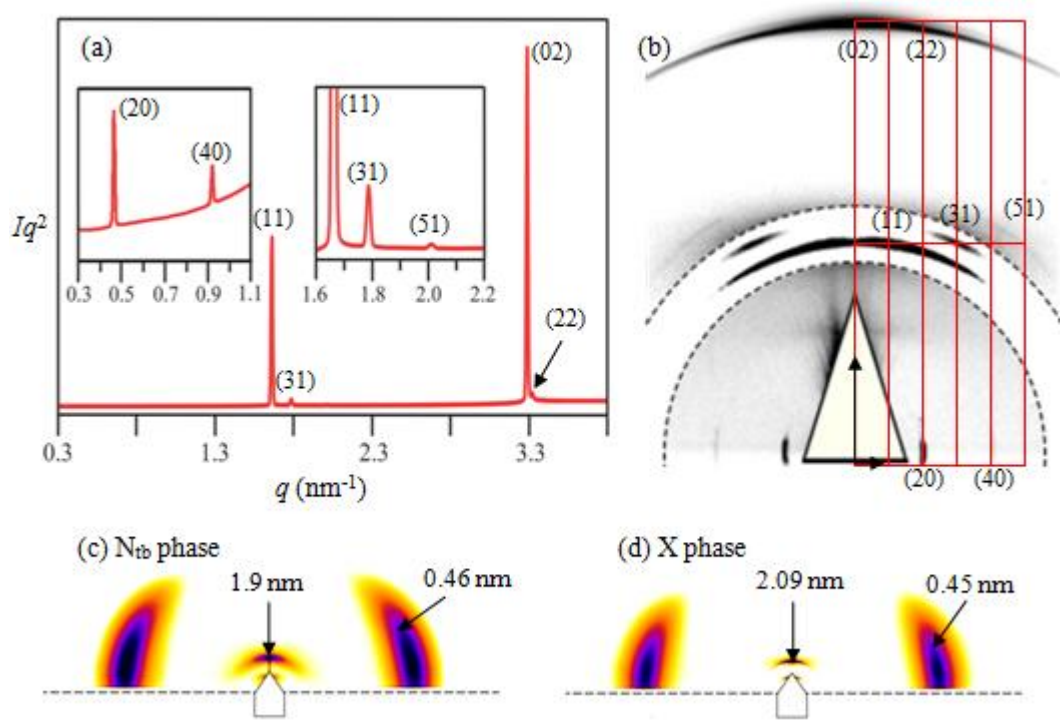
Figure 4.6 – (a) The 1D powder SAXS pattern of the X phase in DTC5C7. (b) A 2D composite GISAXS pattern of the homeotropically aligned X phase in DTC5C7. (c)(d) GIWAXS patterns of the homeotropically aligned N_{tb} and X phase in DTC5C7, respectively. In both images the WAXS intensity has been increased by a factor of two compared to the SAXS. The diffuse lobes in the WAXS region appear shifted from the equator (dashed line) due to absorption from the substrate.

Table 4.3 – Measured *d*-spacings in the X phase of DTC5C5 and DTC5C7

hk	DTC5C5		DTC5C7	
	d Observed (nm)	*d* Calculated (nm)	*d* Observed (nm)	*d* Calculated (nm)
(20)	13.67	13.65	13.69	13.69
(40)	6.82	6.82	6.85	6.85
(11)	3.78	3.78	4.13	4.13
(31)	3.52	3.52	3.79	3.80
(51)	3.12	3.13	3.32	3.32
(02)	1.91	1.91	2.09	2.09
(22)	1.90	1.89	2.06	2.06

The calculated *d*-spacings are the expected values using the unit cell parameters $a = 27.29$ nm, $b = 3.81$ nm (DTC5C5) and $a = 27.39$ nm, $b = 4.17$ nm (DTC5C7).

Table 4.4 – Relative Intensities of the Bragg Reflections in the X phase of DTC5C7

hk	Multiplicity	Iq^2/M Relative to (02) (%)	Phase Angle (Rads)
(20)	2	0.21	π
(40)	2	0.07	π
(11)	4	14.77	0
(31)	4	0.77	π
(51)	4	0.12	π
(02)	2	100.00	π
(22)	4	5.12	π

The phase angles correspond to the electron density

map shown in Figure 4.7.

4.5.2 – Construction of the Electron Density Map

The electron density map of the X phase was reconstructed by Fourier transform of the diffraction structure factors using the method described in Chapter 2, section 2.3.5. The multiplicity and relative intensity of the Lorentz-corrected peaks (in DTC5C7) are provided in Table 4.4. As the phase information of each Bragg reflection could not be directly determined, an electron density map was created for every possible phase combination of the seven peaks. Due to the dominance of the (11) and (02) reflections, all maps exhibited one of eight electron density distributions (Appendix B). Four of these distributions were unrealistic as they suggested low mesogen density; the remaining four possibilities were found to differ very little. The electron density map shown in Figure 4.7 was selected as the most likely representation of the molecular arrangement as the stripes appear slightly smoother in comparison to the alternatives. The relative peak intensities of the X phase in DTC5C5 were very similar to those shown in Table 4.4 and so the same map applies to both samples. In Figure 4.7 the high electron density, corresponding to the aromatic mesogens, is arranged in paired layers (double layers) which mirror one another along the 'a' axis of the unit cell. The regions of lower electron density must therefore correspond to the locations of the $(CH_2)_{5,7}$ spacers and the $(CH_2)_5$ terminal chains. The least electron dense regions (red) are attributed to the terminal chains, based on the assumption that they will behave almost liquid-like within the structure.
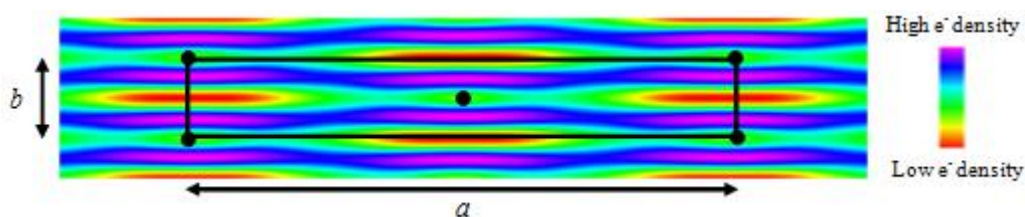
Figure 4.7 – The electron density map of the X phase, constructed using the contents of Table 4.4. The $c2mm$ unit cell is outlined in black. The regions of high and low electron density respectively correspond to the aromatic mesogens and aliphatic chains of the dimers.

4.5.3 – Molecular-level Model

The *c2mm* symmetry of the 2D unit cell arises from a highly periodic double layer half-step (*b*/2) which occurs in intervals of *a*/2. The local arrangement of the molecules must therefore prevent, or at least disfavour, continuous side-by-side dimer packing within the layers. A similarly modulated structure is observed in the B1 banana phase, which is known to form within systems of bent core mesogens [20-22]. As mentioned in Chapter 1, section 1.5.5, the lamellar phases within such systems can be explained by the tendency of the molecules to form small bundles, or "blocks", of locally splayed polarisation within the layers [9,10, 22-24]. The local polarisation splay of the molecular bend creates defect regions inside the layers which typically results in an undulated smectic phase. In some instances, such as the B1 phase, the layers are unable to accommodate the frustration and choose to dislocate [22]. As the X and B1 phases are similarly modulated, we propose that the *c2mm* unit cell is likewise formed by small bundles of locally splayed molecules. Local splay in the X phase may arise as a requirement for efficient space-filling and as a result of the lateral electro-negative C-F bonds.

The figurative splay block shown in Figure 4.8a was constructed using the lattice parameters of the *c2mm* unit cell. The height of the block, equal to the '*b*' parameter, corresponds to the double layer spacing and the height of the tilted dimers along the layer normal. The number of molecules within each block was deduced from the modulation wavelength ('*a*' parameter) and *d*3. The effective width of the each dimer is approximately 0.5 nm, indicating that the unit cell is 50-55 molecules in width (*a*/0.5). As the layering structure shifts in periods of *a*/2, each block must therefore enclose approximately 25-28 splaying dimers. Remembering that P_b is the polar direction of the molecular bend, the splay direction of the enclosed molecular bundle is assumed to be convergent ($\nabla \cdot P_b < 0$), in line with the previous assumption that the $(CH_2)_5$ terminal chains are packed less densely than the $(CH_2)_{5,7}$ spacers. Convergent splay reduces the separation distance between the spacers and simultaneously fans the end tails. One could equally assume divergent splay ($\nabla \cdot P_b > 0$), in which case the least electron dense regions in Figure 4.7 would correspond to the spacers rather than the terminal chains.

If the molecular bundle (Figure 4.8a) is stacked analogous to the B1 phase, we arrive at the structure displayed in Figure 4.8b. A similar dimer layering structure has been

proposed by Takanishi *et al* [25]; however in their model the molecules are not splayed and consequently the blocks do not interlock, and pockets of low mesogen density are formed within the layers. The splayed model proposed here does not lead to intermittent mesogen packing; instead the mesogens progress inside the layers almost continuously, but with frustration at the block boundaries. The frustration arises from the varying layer height, created by the unequal lengths of the spacer and the two combined end tails. This frustration may be compensated by layer undulation, or alternatively by the flexibility of the dimer conformation. If the layers are indeed undulated, this *c2mm* structure is the first experimental observation of the SmCPU$_{A'}$ phase (Chapter 1, Figure 1.8) theoretically predicted by Coleman *et al* [10] in 2008. Helfrich-Hurault type undulation in the X phase is suggested by POM, but with a period much larger than the '*a*' parameter. Further investigation by FF-TEM is required to confirm the presence or absence of nano-scale layer undulation.

According to the ECD results presented in section 4.3.2, the X phase is chiral, meaning that a single handedness must be preserved from one block to the next along the '***a***' axis of the unit cell. The *c2mm* assignment is not strictly accurate due to the absence of mirror planes in the molecular arrangement. As shown in Figures 4.8f and g, there are two possible chiral arrangements of the blocks. In the first, Figure 4.8f, the polar direction of molecular bend is also preserved meaning that the structure is locally ferroelectric and chiral. In the second version, Figure 4.8g, the polar direction alternates on progression along the '***a***' direction, similar to the B1 banana phase. Electronic studies are required to identify the correct orientation of the central block; however preliminary studies on the X phase of DTC5C7 show that application of voltage induces crystallisation. In future electronic studies will be performed on the stable X phase of DTC5C5 to see if crystallisation can be avoided. Although the orientation of the central block is currently unknown, this work has shown that N$_{tb}$ forming systems of achiral bent dimer molecules may also form structures with transverse chirality, as well as longitudinal N$_{tb}$ helices. Furthermore, the continuity of the mesogen layers over the block boundaries in the X phase may significantly reduce the energy cost of the periodic half-step in comparison to other dislocated LC phases.
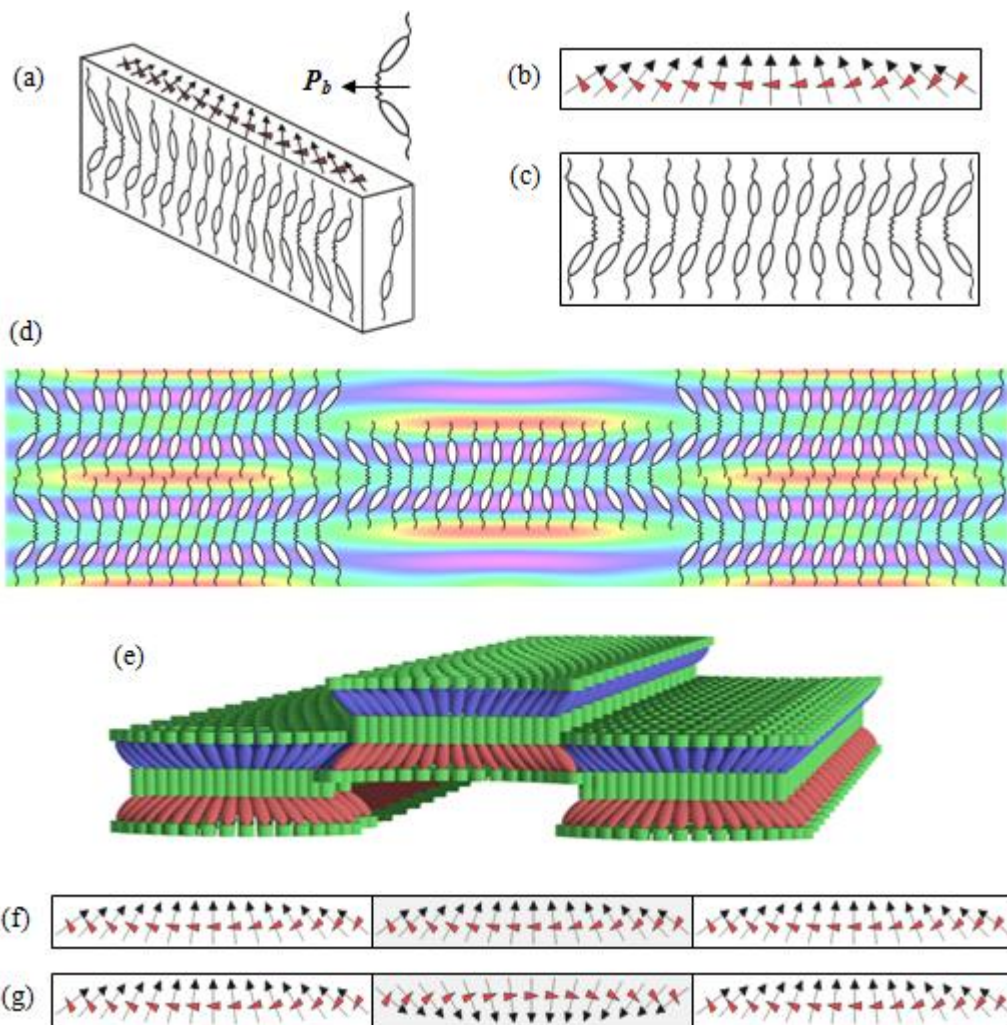
Figure 4.8 – (a) Figurative splay block used to construct the molecular-level model of the X phase. The number of molecules shown should not be taken literally. P_b denotes the direction of the molecular bend. (b) Top view of the splay block. Arrows correspond to the direction of the molecular bend and red triangles indicate the tilt direction of the molecules. The pointed tip of the triangle represents the bottom end of the molecule. (c) Front view of the splay block. If the blocks are arranged analogous to the B1 phase, one arrives at the molecular-level model of the X phase (d) shown overlapping the electron density map. (e) 3D molecular level-model of the X phase. (f,g) Top views of the molecular-level model showing the two possible orientations of the central (shifted) block. In (g) the central block has been rotated by 180 ° compared to (f), but the chiral handedness of the block is unchanged. The orientation shown in (f) has been assumed in (d).

4.6 – X-ray Diffraction Analysis of the Y phase

The meta-stable (monotropic) Y phase of DTC5C9 was investigated using the same methods already discussed in sections 4.4 and 4.5. The powder SAXS pattern of the Y phase (Figure 4.9a) was recorded at 80 °C after continuous cooling from the isotropic phase. Additional information regarding peak orientation was obtained by GISAXS of a homeotropically aligned thin film (Figure 4.9b). Homeotropic alignment was achieved by shearing the sample in the N_{tb} phase (118 °C) and was preserved on cooling into the Y phase (80 °C). This was confirmed optically (section 4.2.1) and by symmetry of the GIWAXS patterns (Figures 4.9c,d). The diffuse WAXS peaks are centred on the axis parallel to the substrate (equator), while the SAXS peaks are centred on a perpendicular axis (meridian). The diffuse WAXS peaks in the Y phase confirm that it is an LC phase. Further evidence is also provided in Figure 4.9e, which illustrates a significant change in the SAXS and WAXS intensity distribution, when crystallisation begins (after standing for ∼5 minutes).

The *d*-spacings of the Y phase (Table 4.5) are relatable by integer divisions (orders) of a single spacing equal to 30.38 nm. This is much larger than anything directly linked to the molecules themselves, indicating the existence of a modulated structure. All of the observed Bragg reflections appear to be centred along one axis, suggesting a 1D lamellar Phase. However layering alone cannot explain why the 4th, 7th, 8th and 11th reflections are split, i.e. appear as a pair of spots/streaks on either side of the meridian. Peak splitting was similarly observed in the X phase (Figure 4.6b) and suggests at least 2D order. It is possible that the structure of the Y phase is described by a rectangular or oblique unit cell, but in this case '*a*' must be much larger than that of the X phase. On the other hand, the optical texture of the Y phase appears identical to the N_{tb} phase in both planar (rope-like) and homeotropic (dark field) alignment conditions. The lack of any optical differences between the N_{tb} and Y phases opposes the existence of long range 2D modulation.

Table 4.5 – XRD Summary of the Y phase in DTC5C9

Peak	d Observed (nm)	d Calculated (nm)	Iq^2 Relative to (70) (%)
(30)	10.13	10.13	0.01
(40)	7.59	7.60	0.81
(60)	5.06	5.06	---
(70)	4.35	4.34	100
(80)	3.82	3.80	---
(10 0)	3.05	3.04	0.48
(11 0)	2.77	2.76	0.77
(13 0)	2.36	2.34	---
(14 0)	2.18	2.17	58.91

The calculated d spacings were calculated assuming a first order (10) of 30.38 nm. The dashed lines in the intensity column indicate reflections too weak to accurately measure in 1D.

The relative intensities of the Lorrentz-corrected Bragg reflections (where measureable) are shown in Table 4.5. The strongest reflection corresponds to a spacing of 2.18 nm suggesting layers of tilted dimers (tilt angle $\simeq$ 19 °). $d1$ of the N_{tb} phase is slightly smaller than the layer height of the Y phase suggesting a larger tilt angle in the N_{tb} phase (21 °). Figures 4.9c and d, show that the N_{tb} and Y phases have similar WAXS distribution in agreement with the similar tilting angles. At this stage the precise structure of the Y phase is unknown and further analysis is required.
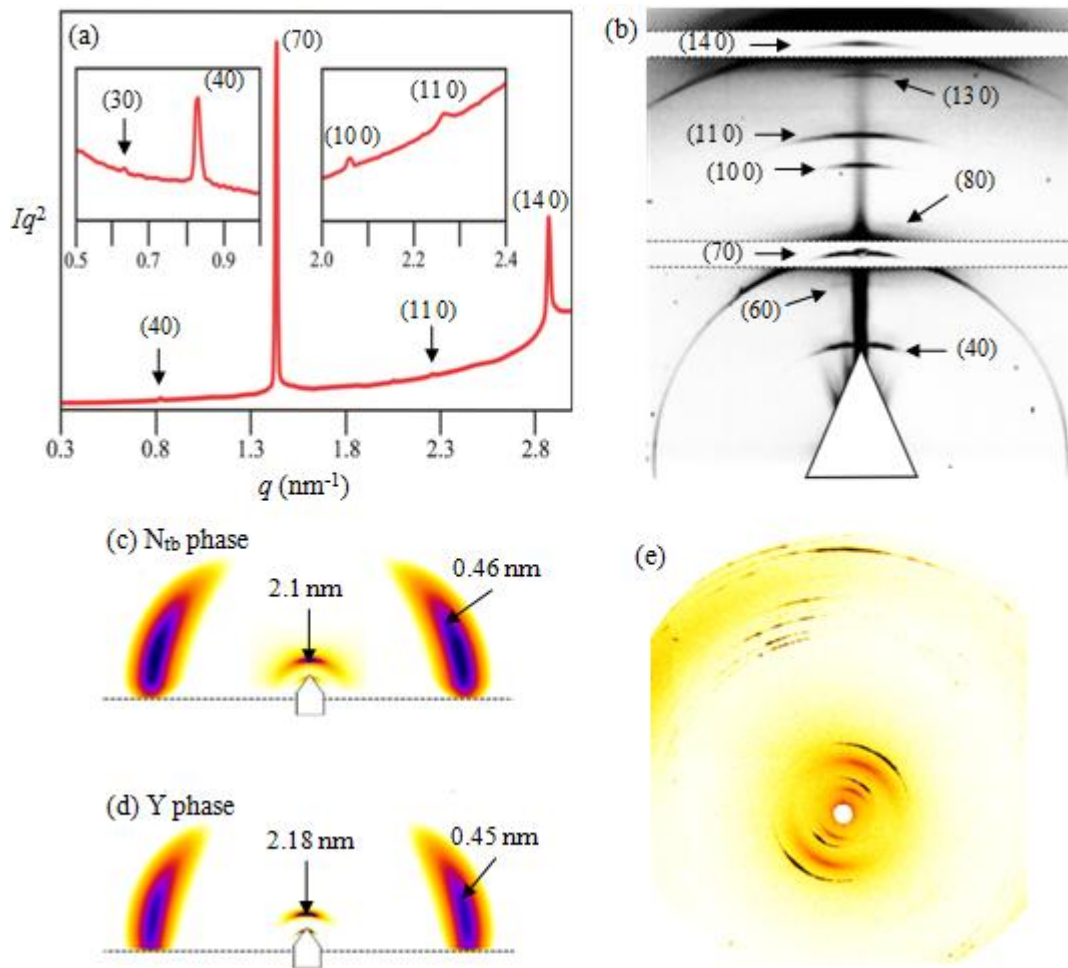
Figure 4.9 – (a) The 1D powder SAXS pattern of the Y phase in DTC5C9. (b) A 2D composite GISAXS pattern of the homeotropically aligned Y phase in DTC5C9. (c)(d) GIWAXS patterns of the homeotropically aligned N_{tb} and Y phases, respectively. In both images the WAXS intensity has been increased by a factor of two compared to the SAXS. The diffuse lobes in the WAXS region appear shifted from the equator (dashed line) due to absorption from the substrate. (e) At the onset of crystallisation the strong peaks of the crystal can be seen on top of the remnants of the Y phase. The SAXS and WAXS intensity distributions change significantly during crystallisation.

4.7 – Summary

In summary, the liquid crystal phases of bent dimer homologues have been investigated with varying spacer chain length. The temperature range of the uniaxial nematic (N) phase was found to be wider in compounds with longer spacers. Molecules with shorter spacers were found to adopt lamellar banana phases at higher temperatures. These observations may be explained in terms of molecular flexibility: In long spacer dimers, the high flexibility enables the two mesogens to be almost parallel, stabilising the nematic phase. Dimers with shorter spacers are more rigid and bent, meaning that banana phases are more comfortable. X-ray scattering studies were performed, which suggest that the highly local structure of the twist bend nematic (N_{tb}) phase is also dependent on the molecular composition. In compounds of short spacer molecules the dominant scattering peak is associated with inter-dimer separation, but when the spacer length becomes comparable to added length of the terminal chains, the inter-dimer peak is smeared out. This suggests that the local dimer layering structure in the N_{tb} phase changes from smectic C (SmC) type, to intercalated dimers in longer spacer molecules. Furthermore, the first CD measurements in the N_{tb} phase were presented, showing that chirality and the dominant handedness of the sample can be directly determined. One may also determine the rotational strength of the N_{tb} phase, provided that the sample thickness is known. CD may therefore serve as a quick and easy alternative to complicated resonant X-ray scattering experiments. However, CD is limited by the fact that near perfect homeotropic sample alignment is required and that it does not allow one to determine the helical pitch length.

In three of the four compounds studied, lower temperature smectic phases (X and Y) were observed with complex modulated structures. The structure of the 'X phase' in short spacer molecules was found to possess a centred rectangular unit cell, where the dimers periodically shift in a similar fashion to that observed in the B1 banana phase. However in contrast to the B1 phase, the shifted structure does not break the mesogen layers, instead a unique double layering style is created that is both chiral and optically biaxial. The shifting structure and phase chirality are thought to arise from interplay of molecular tilting and polarisation splay along the layering direction. This demonstrates that systems of bent achiral dimers are capable of producing transversely chiral structures in addition to longitudinal N_{tb} helices. Furthermore, the X phase may be the

first experimental example of the SmCPU$_{A'}$ phase, theoretically predicted by Coleman *et al* in 2008 [10]. These findings also contradict current work [8], which claim that the X phase possesses an oblique unit cell. The precise structure of the 'Y phase' in longer spacer molecules is currently unknown. The findings of X-ray diffraction studies show an intensity distribution suggestive of at least 2D modulation, but the Bragg reflections correspond to integer multiples of a single spacing, suggesting only 1D SmC-type order. Further investigation of the Y phase is required.

References to Chapter 4

[1]   L. Beguin, J. W. Emsley, M. Lelli, A. Lesage, G. R. Luckhurst, B. A. Timimi, H. Zimmermann, *J. Phys. Chem. B*, 2012, **116**, 7940.

[2]   A. Hoffmann, A. G. Vanakaras, A. Kohlmeier, G. H. Mehl, D. J. Photinos, *Soft Matter*, 2015, **11**, 850.

[3]   C. Zhu, M. R. Tuchband, A. Young, M. Shuai, A. Scarbrough, D. M. Walba, J. E. Maclennan, C.Wang, A. Hexemer, N. A. Clark, *PRL*, 2016, **116**, 147803.

[4]   S. M. Kelly, T. J. Jess, N. C. Price, *Biochemica et Biophysica Acta*, 2005, **1751**, 119.

[5]   J. Altschuh, T. Karstens, H.-G. Kuball, *J. Phys. E: Sci. Instrum.*, 1981, **14**, 43.

[6]   H. Nagayama, S. K. Varshney, M. Goto, F. Araoka, K. Ishikawa, V. Prasad, H. Takezoe, *Angew. Chem. Int. Ed.*, 2010, **49**, 445.

[7]   M. G. Tamba, S. M. Salili, C. Zhang, A. Jákli, G. H. Mehl, R. Stannarius, A. Eremin. *RCS Adv.*, 2015, **5**, 11207.

[8]   N. Sebastián, M. G. Tamba, R. Stannarius, M. R. de la Fuente, M. Salamonczyk, G. Cukrov, J. Gleeson, S. Sprunt, A. Jákli, C. Welch, Z. Ahmed, G. H. Mehl, A. Eremin, *Phys. Chem. Chem Phys.*, 2016, **18**, 19299.

[9]   D. A. Coleman, J. Fernsler, N. Chattham, M. Nakata, Y. Takanishi, E. Korblova, D. R. Link, R. F. Shao, W. G. Jang, J. E. Maclennan, O. Mondainn-Monval, C. Boyer, W. Weissflog, G. Pelzl, L. C. Chien, J. Zasadzinski, J. Wantanabe, D. M. Walba, H. Takezoe, N. A. Clark, *Science*, 2003, **301**, 1204.

[10]   D. A. Coleman, C. D. Jones, M. Nakata, N. A. Clarke, D. M. Walba, W. Wiessflog, K. Fodor-Csorba, J.Wantanabe, V. Novotna, V. Hamplova, *Phys. Rev. E*, 2008, **77**, 021703.

[11]   A. A. Dawood, M.C. Grossel, G. R. Luckhurst, R. M. Richardson, B. A. Timimi, N. J. Wells, Y. Z. Yousif, *Liq. Crsyt.*, 2017, **44**, 106.

[12]   V. P. Panov, M. Nagaraj, J. K. Vij, Yu. P. Panarin, A. Kohlmeier, M. G. Tamba, R. A. Lewis, G. H. Mehl, *Phys. Rev. Lett.*, 2010, **105**, 167801.

[13] V. P. Panov, R. Balachandran, M. Nagaraj, J. K. Vij, M. G. Tamba, A. Kohlmeier, G. H. Mehl. *App. Phys. Lett.*, 2011, **99**, 261903.

[14] G. Napoli, A. Nobili, *Phys. Rev. E*, 2009, **80**, 031710.

[15] B. I. Senyuk, I. I. Smalyukh, O. D. Lavrentovich, *Phys. Rev. E*, 2006, **74**, 011712.

[16] N. Berova, K. Nakanishi, R. Woody (Eds.), (2000). "*Circular Dichroism: Principles and Applications*". 2nd Ed., Wiley VCH, pp. 29-30.

[17] G. D. Fasman (Ed.), (1996). "*Circular Dichroism and the Conformational Analysis of Biomolecules*". Springer Science + Business Media New York, pp. 26-28.

[18] K. F. Renk, (2012). "*Basics of Laser Physics: For Students of Science and Engineering*". Springer Science + Business Media.

[19] A. de Vries, *Mol. Cryst. Liq. Cryst*, 1970, **10**, 219.

[20] J. P. Bedel, J. C. Rouillon, J. P. Marcerou, M. Laguerre, M. F. Achard, H. T. Nguyen, *Liq. Cryst.*, 2000, **27**, 1, 103.

[21] E. Gorecka, N. Vaupotič, D. Pociecha, M. Čepič, J. Mieczkowski, *ChemPhysChem*, 2005, **6**, 1087.

[22] J. Martinez-Perdiguero, J. Etxebarria, C. L. Folcia, J. Ortega, N. Gimeno, M. B. Ros, *Phys. Rev. E*, 2010, **82**, 041706.

[23] N. Vaupotič, M. Čopič, *Phys. Rev. E*, 2005, **72**, 031701.

[24] D. K. Yoon, R. Deb, D. Chen, E. K. Orblova, R. Shao, K. Ishikawa, N. V. S. Rao, D. M. Walba, I. I. Smalyukh, N. A. Clark. *PNAS*, 2010, **107**, 50, 21311.

[25] Y. Takanishi, M. Toshimitsu, M. Nakata, T. Izumi, K. Ishikawa, H. Takezoe, J. Watanabe, Y. Takahashi, A. Iida. *Phys. Rev. E*, 2006, **74**, 051703.

Chapter 5 – Study of Orientational Order in the N_{tb} phase of Diphenylethane-based Copolyethers

In light of recent developments in the field, the main-chain liquid crystal (LC) copolyethers in which the N_{tb} phase was first experimentally observed were revisited and re-characterised. Grazing incidence X-ray scattering (GIXS) revealed that the sample could be highly aligned by shearing force, even more so than the previously studied LC dimers. This was evidenced by a four-point wide angle X-ray scattering (WAXS) distribution. It is proposed here that the four-point WAXS pattern originates from orientational modulation of the tilt direction along the helical axis of the N_{tb} phase. Orientational order in the N_{tb} phase was further explored using polarised infrared (IR) spectroscopy, allowing additional information regarding the polymer chain conformation to be obtained. The findings suggest that the average conformation of the polymer chains is that of helix and that the bend angle between mesogenic units is inversely proportional to temperature. These findings are in line with a similar model proposed for bent LC dimers in a previous chapter. All experimental evidence, including a jump in birefringence at the N_{tb}-N phase boundary, shows that the copolyether mirrors the behaviour of bent LC dimers over the nematic-nematic transition. This confirms that previously reported "n_1-n_2" transition [1] is in fact the N-N_{tb}.

5.0 – Introduction

The nematic-nematic phase transition was first confirmed in 1992 in a series of main chain liquid crystal "RBPE" copolymers, featuring semi-flexible diphenylethane-based mesogens [1-3]. Originally, the partial flexibility of the diphenylethane segments was thought to be the key property for observing the transition, but since then it has been witnessed frequently in systems of LC dimers with rigid aromatic mesogens [4-18]. The common factor between these two sample types is the inclusion of flexible oligomethylene spacers, which pair the mesogens at an angle to each other (bent conformation) and comprise an odd number of CH_2 linkers. At the time of first report very little was known about the nematic-nematic transition or the structure of the lower temperature phase, but in the last decade in particular, knowledge of the subject has significantly developed. The lower temperature nematic phase, previously labelled "n_2"

[1], but more commonly referred to as the twist bend nematic (N_{tb}) phase, is now known to exhibit spontaneous symmetry breaking despite being made of chemically achiral constituents. A nano-scale helical pitch length ranging between 8 and 10 nm was confirmed by resonant X-ray scattering [4] and coexistence of oppositely handed domains has been suggested by NMR [5-7] and optical microscopy [8-10]. Topological studies have also suggested a pitch length of 8-10nm [11,12]. In view of recent advances, the purpose of this study is to provide an up to date characterisation of the nematic-nematic phase transition in LC copolyethers and to further explore some of the least understood features of the N_{tb} structure; these involve the local packing and orientational order inside the bulk phase.

To date, orientational order inside the bulk N_{tb} phase has been investigated by Raman scattering [19], X-ray scattering [20] and NMR spectroscopy [21]. In such studies the orientational order is quantified by the Haller function or by a second-rank tensor, which for nematics is approximated by the second Legendre polynomial in $\cos(\theta)$: $S = <P_2 (\cos(\theta))> = <(3 \cos^2(\theta)-1)/2>$. Treatments such as this typically result in S=0.4-0.6 in well aligned N_{tb} phases [5-9,19]. In Chapter 3, section 3.5, it was proposed that such values unfairly represent orientational order in the N_{tb} phase and are fundamentally limited to values <1 due to preferential tilting of the mesogens in respect to the helical axis. As a solution, it was also proposed in Chapter 3 that a two part order parameter $S=S_0 \cdot S_1$ should be used, where S_0 describes the orientational distribution of helical domains and S_1 describes the tilt distribution inside each domain. We note that the tilt of the mesogens has been taken into account in previous work [19,21], but in these instances the helical axis was assumed constant in the direction of alignment, which is not strictly true. This is acknowledged by Zhang *et al* [19]. It has been shown in Chapter 3, section 3.4, that helical domains have dimensions on the scale of 0.1 μm, much smaller than the cross-sectional area of any instrumental sampling size. If experimental measurements sample several domains, a distribution of helical axis directions (centred on the alignment direction) must be accounted for; this is the purpose of S_0.

In this work the nematic (N)-N_{tb} phase transition was re-investigated in an RBPE-type copolyether, comprising Cl/CH$_3$ substituted diphenylethane mesogens and $[CH_2]_{5/7/9}$ spacers in molar ratios of 50/50 and 33/33/33, respectively (Figure 5.0). This compound

is referred to as CLMBPE henceforth. Such variation of spacer length and phenyl substitution unit has been shown to suppress or even prevent crystallisation, producing a wide N_{tb} temperature range [1,2]. Examination of an aligned CLMBPE thin film by grazing incidence X-ray scattering (GIXS) revealed that high orientational order was achieved within the sample. A four-point wide angle X-ray scattering (WAXS) pattern was observed, which enabled direct determination of the average tilt or 'conical angle' of the chains in respect to the helical axis. Orientational order was further investigated by performing the first polarised IR spectroscopy measurements on the N_{tb} phase. The high sample alignment enabled determination of S_0 of the N_{tb} phase to be determined and S_1 for each vibrational mode. Furthermore, conformational details suggest that the average chain conformation is that of a helix, in-line with a similar model proposed for LC dimers in Chapter 3, section 3.5. All experimental evidence suggests that the nematic-nematic phase transition is identical in both sample types.

This work represents collaboration between the University of Sheffield and Zhejiang Sci-Tech University, Hangzhou, China. The synthesis of CLMBPE was carried out by collaborators (Jianggen An), as well as the collection of IR spectra. The author is responsible for (or took part in) all other aspects of the investigation. A brief description of the synthesis of CLMBPE is provided in Appendix C, but the discussion here will focus on the phase behaviour and structural properties of the sample.
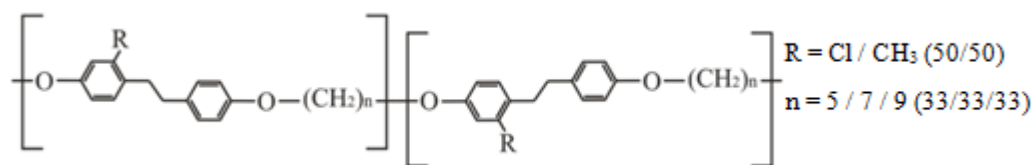
Figure 5.0 – Chemical structure of CLMBPE copolymer.

5.1 – Phase Behaviour of CLMBPE

5.1.1 – DSC Analysis
The phase behaviour of CLMBPE was firstly investigated via DSC using a Perkin Elmer Diamond DSC fitted with a liquid nitrogen cooling unit. The normalised 10 °C/min DSC traces of the sample are shown in Figure 5.1. The phase assignments were confirmed by

supporting evidence from Grazing Incidence X-ray Scattering (GIXS) experiments, which are discussed later. During the first heating scan, the crystal melted into N phase, which then melted into the high temperature amorphous state. This is analogous to the isotropic phase of the LC dimers discussed in previous chapters. Upon cooling from the 'isotropic' (Iso) phase, CLMBPE exhibited the N and N_{tb} phases, but did not re-crystallise. This is evident from the second heating scan, which shows only the glass, N_{tb}-N and N-Iso transitions. The second cooling scan appeared identical to the first and so has been omitted. The sample was further investigated to see if it would re-crystallise after long standing at room temperature. After leaving for 5 hours at 23 °C and then heating, no significant change in the DSC thermogram was observed (Appendix C), suggesting that the sample did not re-crystallise during this time. It was also found that the sample did not re-crystallise during slow cooling runs (0.1 °C/min).
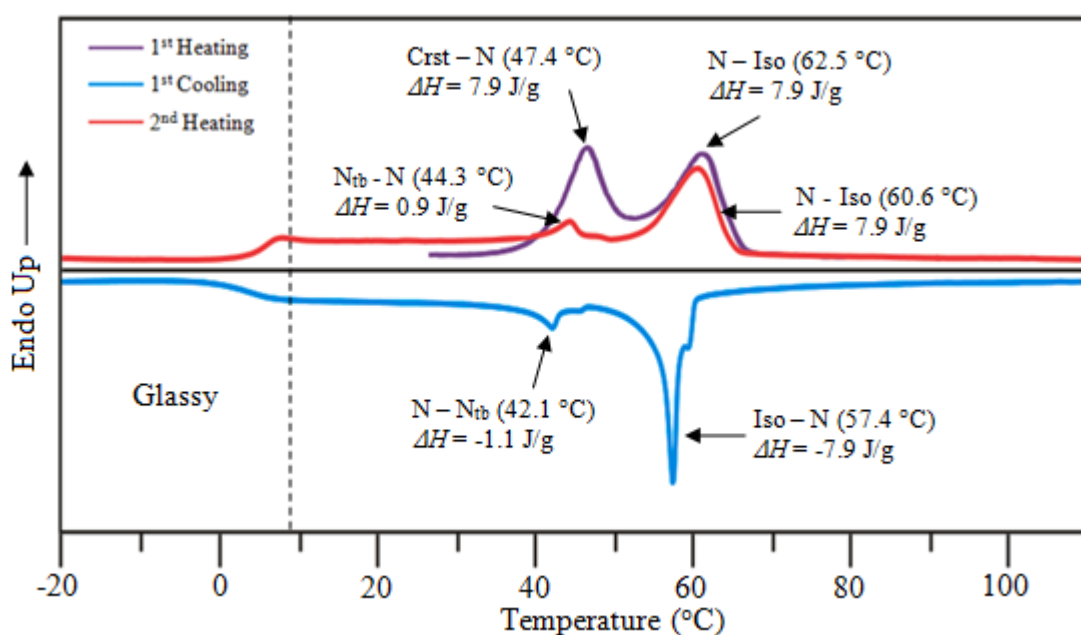
Figure 5.1 – DSC traces of CLMBPE. The scanning rate was 10 °C/min in all cases. The sample did not re-crystallise for at least 5 hours after the first melt. Crst = Crystal, N_{tb} = Twist bend nematic, N = Nematic, Iso = Isotropic.

5.1.2 – Optical Properties

The optical textures of CLMBPE were investigated by polarised optical microscopy (POM) using an Olympus BX50 Microscope fitted with a Mettler FP82 HT hotstage. The sample was dissolved in dichloromethane and drop-cast at room temperature onto a glass plate. After removing the solvent, the sample was heated to isotropic temperatures

to melt the residual crystal. Covering glass was then applied, resulting in an almost uniform thin film of CLMBPE. In the isotropic phase, only a dark field of view was observed between crossed polarisers; however upon slow cooling (0.1 °C/min) into the N phase, a grainy first order birefringent texture developed (Figure 5.2a). This texture is common in both nematic and smectic LC polymers [22]. With continuous cooling into the N_{tb} phase, the texture did not change, but after shearing the film between the two glass plates, a striped texture was observed (Figure 5.2b). The stripes ran mostly perpendicular to the shearing direction and fibre axis, suggestive of the "banded texture" [22,23]. The banded texture has been observed in a wide range of thermotropic LC polymers and is explained by relaxation (elastic contraction) of the chains in response to rapid flow (shearing). This produces a periodically undulating director along the direction of flow [22,23]. Much smaller regions of banding were also observed after shearing the higher temperature N phase, implying that the stripes do not correspond to the rope-like N_{tb} texture observed in LC dimers.
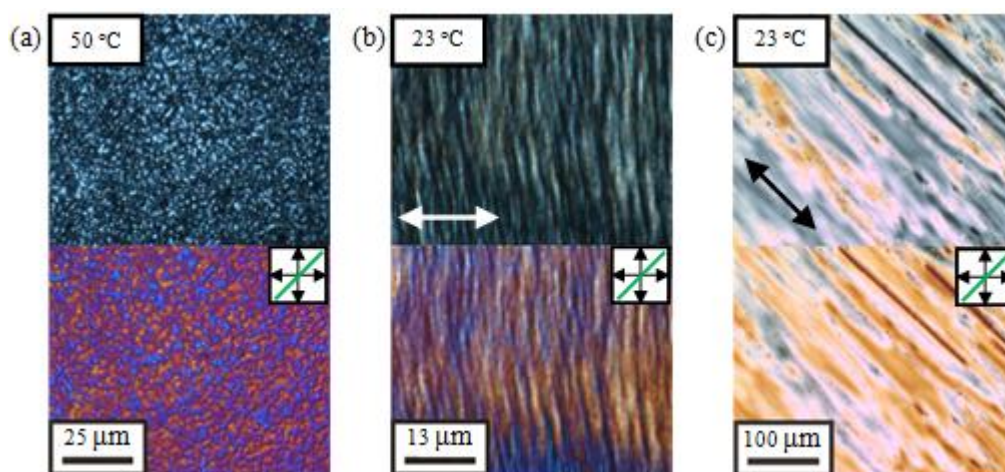
Figure 5.2 – Optical textures of CLMBPE between crossed polarisers. (a) Drop cast onto glass, sandwiched and then cooled from the isotropic phase at a rate of 0.1 °C/min into the N phase. The grainy texture did not change upon entering the N_{tb} phase. (b) The banded texture of CLMBPE obtained after shearing the N_{tb} phase between two glass plates at room temperature (shearing direction horizontal). (c) The texture of the N_{tb} phase after shearing CLMBPE across a glass surface at room temperature using a scalpel blade (knife edge) (shear direction and chain axis 45 ° to polariser and analyser). Top (/bottom) show the texture without (/with) a λ plate inserted into the optics with axis direction indicated in green.

When sheared between glass plates the N_{tb} phase of CLMBPE was birefringent even with the chain axis in parallel alignment with the analyser. One would expect a well oriented sample to be brought to extinction in this orientation. In an attempt to improve alignment in the N_{tb} phase, a new sample was prepared by directly melting a small amount of CLMBPE onto a glass plate. The molten lump of material was then cooled from the isotropic phase to room temperature and sheared repeatedly using the blade of a scalpel (knife edge). High sample alignment was achieved using this method, evidenced by the region of uniform planar alignment shown in Figure 5.2c. When the shear direction and average chain axis was aligned parallel to the polariser or analyser, the field of view was almost perfectly dark. In Figure 5.2c the chain axis (slow axis) is perpendicular to that of the λ-plate and the texture appears mainly first order yellow. CLMBPE must therefore possess a positive dielectric anisotropy.

The birefringence of the well aligned (sheared by knife edge) CLMBPE film was investigated by inserting an Olympus U-CBE Berek compensator into the microscope optics. The retardation of the film was found by tilting the axis of the compensator until the centre of the sample was brought to extinction. The retardation (Γ) was then used to calculate birefringence (Δn) using $\Gamma = \Delta n \cdot t$, taking the film thickness (t) as 4.5 μm. The film thickness in the region of retardation measurements was determined from the findings of 3D sample mapping (see Appendix C). At room temperature the birefringence of CLMBPE was determined to be 0.027 ± 0.003. The uncertainty is associated with the angular range of the compensator over which the centre of the sample remained extinct. The sheared CLMBPE film was then heated at a rate of 0.5 °C/min until isotropic. Retardation measurements were recorded throughout the temperature range, but in smaller increments around the phase transition temperatures. The birefringence of CLMBPE during this process is plotted as a function of temperature in Figure 5.3. In the N_{tb} phase the birefringence was found to slowly increase linearly with temperature. At the transition to the N phase a small jump was observed, but was followed by a slow linear decrease in birefringence as the temperature progressed. At the isotropisation transition a sudden drop in birefringence was observed; Δn fell more rapidly with temperature, until the birefringence could no longer be measured. Similar behaviour has also been reported in bent LC dimers [8,13]. These results will be recalled in later discussions.
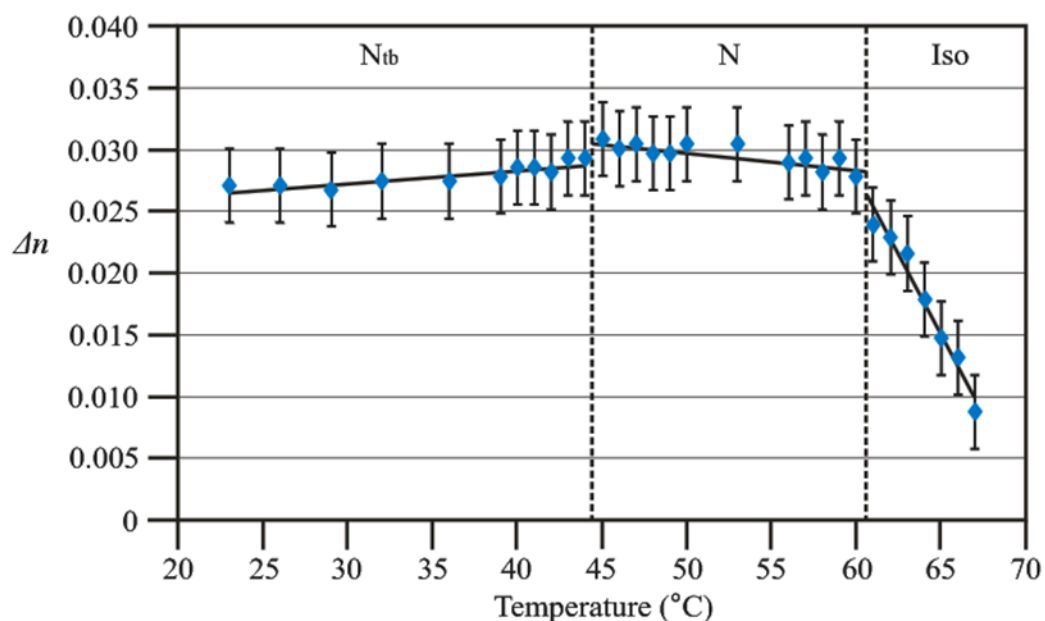
Figure 5.3 – Temperature dependence of Δn in CLMBPE. The vertical dashed lines correspond to the phase transition temperatures according to the second heating, provided by DSC. N_{tb} = Twist bend nematic, N = Nematic, Iso = Isotropic.

5.2 – GIXS Analyses of CLMBPE

CLMBPE was studied by GIXS on beamline BM28 of the ESRF. The sample was placed on a silicon substrate and heated, using a Mettler FP82 HT hot stage, to 100 °C. This ensured proper melting of the crystal. The sample was then cooled to room temperature (N_{tb} phase) and sheared on the silicon substrate by knife edge. The sheared N_{tb} phase was then placed on the temperature controlled surface of a custom six-circle goniometer with the shearing direction perpendicular to the incident beam. A helium-filled flight tube was positioned between the sample and a Mar165 CCD detector to reduce background scattering due to air.

At room temperature (23 °C) the GIXS pattern of the sheared N_{tb} phase (Figure 5.4a) did not exhibit any small angle features, only broad wide angle X-ray scattering (WAXS) at q = 14.6 nm^{-1} (d = 0.43 nm), arising from lateral (side-by-side) packing of the polymer chains. Unlike previous observations in LC dimer compounds, the WAXS had four intensity maxima rather than just two. Note that only half of the scattering pattern is visible in Figure 5.4a-d due to the grazing incidence setup. The appearance of a four-point WAXS distribution signifies that higher order was achieved in the N_{tb}

phase of CLMBPE compared to that obtained previously in bent LC dimers. Four WAXS maxima in the N_{tb} phase were observed in earlier work on oriented RBPE polymer fibres [2]. In the present case, azimuthal measurements at 23 °C (see Appendix C for details) suggest that each maximum is angled 18.5 ° in respect to the equator. In planar alignment conditions, the equator is the axis running through the beam centre, perpendicular to the substrate surface/horizon and shear direction (vertical in Figure 5.4a-d). This represents a separation angle of 37 ° between each pair of maxima. The origin of the four-point WAXS distribution is discussed in section 5.2.2.

5.2.1 – Temperature Dependency of the Azimuthal WAXS Distribution

As the temperature was incrementally raised from room temperature to 65 °C, the WAXS intensity distribution progressively changed from four maxima in the N_{tb} phase, to two equatorial maxima ($d = 0.45$ nm) in the N phase (Figure 5.4b). With further heating into the isotropic phase, sample orientation was lost, evidenced by the diffuse WAXS ring ($d = 0.46$ nm) in Figure 5.4c. To test the reversibility of the azimuthal intensity shifts, CLMBPE was re-sheared (by knife edge) at room temperature and incrementally heated into the N phase (50 °C); the sample was then cooled back into the N_{tb} phase (Figure 5.4d). The sample was not cooled from the isotropic phase because alignment did not recover in the LC phases once orientation had been lost. The progressive changes in the 1D azimuthal WAXS intensity distribution during straight heating to the Iso phase and cooling from the N phase are shown in Figures 5.4e and f, respectively. 0 ° corresponds to the equator axis, while -90 and 90 ° correspond to the meridian axis.

At 23 °C, the 1D azimuthal distribution closely resembles the line-shape of the double peak or "sugar loaf" orientational distribution function calculated elsewhere [20], which was reproduced suitably by two Gaussian profiles. Here the WAXS azimuthal intensity could not be fitted by Gaussian, Lorentzian, Voigt or pseudo-Voigt peaks. Instead two anisotropic peaks were required to obtain a satisfactory fit to the data (Figure 5.4g). An explanation for such an anisotropic intensity distribution will be the subject of future investigation. The data fit suggests that the separation angle between the WAXS maxima of the doublet peak is 58 °, which is significantly larger than the value obtained by direct measurement (37 °). Immediately after the transition to the N phase (45 °C)

the WAXS azimuthal intensity distribution could be fitted using a single symmetric Voigt peak (Figure 5.4h).

On cooling from the N phase to the N_{tb} phase, the radial position of the peak shifted back to higher q (d = 0.43 nm), consistent with previous reports [1]. Although the intensity maximum remained centred on the equator after the N-N_{tb} transition, the intensity was found to spread to wider azimuthal angles. An increasing azimuthal spread after the N-N_{tb} transition is similarly observed by X-ray scattering in magnetically aligned samples of bent LC dimers [5,13,20]. This further supports that the transition is the same in both sample types. The absence of the four-point WAXS pattern in the N_{tb} phase of LC dimers may be explained by the much higher mobility of the molecules in comparison to the polymer chains. Polymers take much more time to relax in response to the mechanical strain, particularly at lower temperatures, whereas the dimers behave fluidly and are able to reorganise easily. It should be noted that after cooling CLMBPE back into the N_{tb} phase, the azimuthal intensity could not be fitted by a single symmetric peak of any kind.
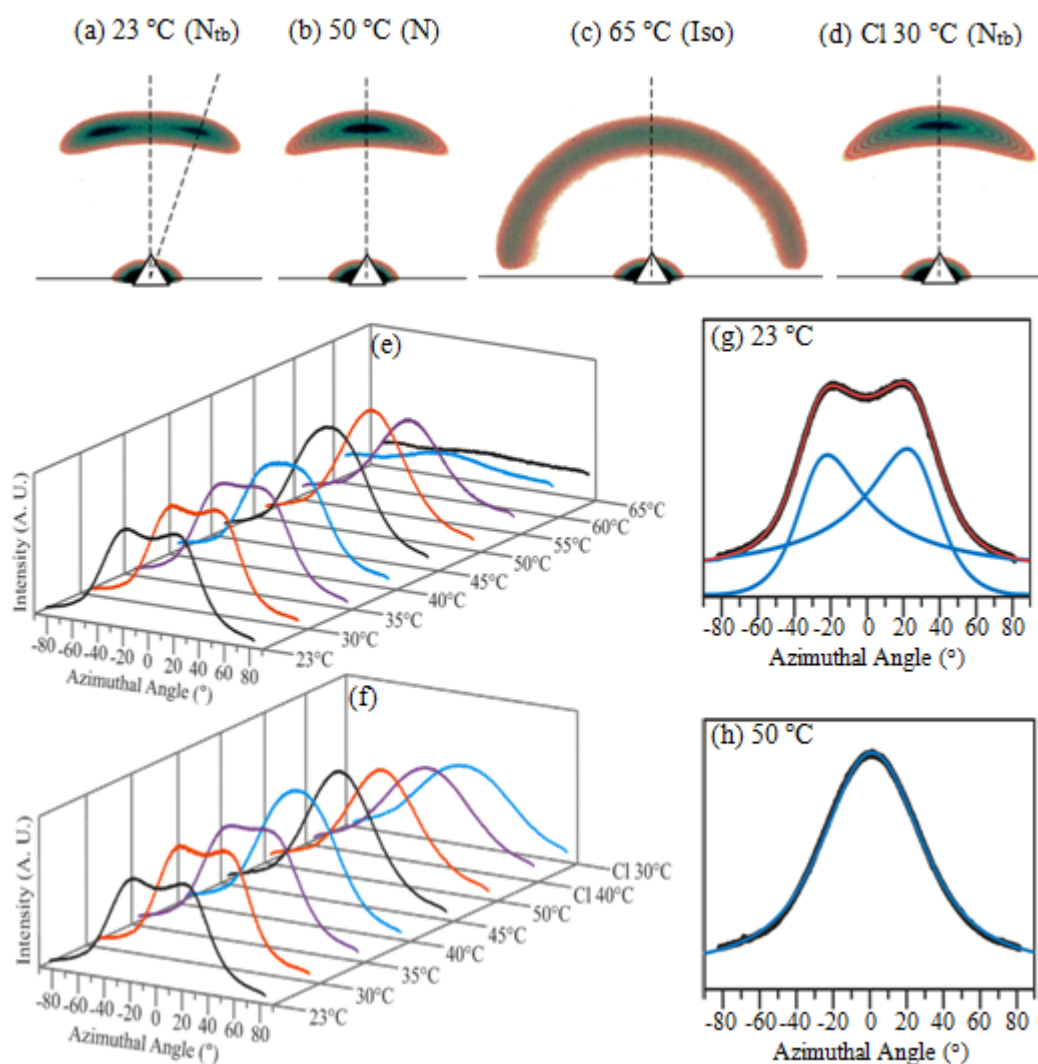
Figure 5.4 – GIXS patterns of CLMBPE. (a) The N_{tb} phase, sheared by knife edge at room temperature. The sheared sample was then heated into the N (b) and Isotropic (c) phases. (d) The WAXS distribution of the N_{tb} phase after cooling from the N phase. The vertical dashed line and solid horizontal line indicate the equator and meridian, respectively. (e)(f) Series of Intensity vs. Azimuthal angle plots at different temperatures starting from 23 °C. 'Cl' indicates cooling. (g) At 23 °C (N_{tb} phase) the azimuthal intensity can be well fitted (red) using a pair of asymmetric 'Fano' peaks (blue) and a constant background. (h) At 50 °C (N Phase), the WAXS intensity can be well reproduced by a single Voigt profile (blue) and the same constant background used in (g). The 50 °C profile was taken from (e).

5.2.2 – Origin of the Four-point WAXS Distribution

A diffuse four-point small angle X-ray scattering (SAXS) distribution is well documented in work relating to biaxial and cybotactic nematic phases of bent mesogens [24-27]. Such phases are said to contain short range clusters of smectic C (SmC) type ordering. Under magnetic alignment conditions the mesogens prefer to align their long axes with the field, which as a consequence, causes the local layer normals to angle away from the field direction; this is shown diagrammatically in Figure 5.5a. The tilt of the layer planes results in off-meridional centring of the corresponding SAXS peaks. The WAXS azimuthal intensity distribution in the N_{tb} phase of CLMBPE can be explained using a similar principle, but adjusted to account for preference of tilted local director in respect to the helical axis and alignment direction. If the tilt direction of the chains was restricted to the plane of the page, an X-ray scattering pattern such as that in Figure 5.5b would be observed. However, in the N_{tb} phase the tilt direction is not restricted and the average orientation changes progressively along the helical axis. The WAXS pattern therefore represents a superposition of all possible tilt orientations about the helical axis (Figure 5.5c). In CLMBPE the resolved separation angle of the doublet was determined to be 58 °. As such the tilt or 'conical angle' of the polymer chain axis in the N_{tb} phase is approximately 29 °. This value is equal to the conical angle obtained by SAXS analysis in Chapter 3, section 3.5, in a LC dimer mixture known as Se45. This is also broadly in-line with ^{2}H NMR measurements on CBC7CB-d_4 [21].

SAXS was not observed in the GIXS pattern of CLMBPE. This may be because the aromatic rings of the diphenylethane segments are not directly linked. The ethane spacer between the aromatic rings introduces conformational flexibility, but could also increase the steric compatibility of the mesogens with the longer oligomethylene spacers. This would weaken the preference of the mesogens to locally layer, which based on the findings of Chapters 3 and 4, is thought to be the origin of SAXS in the N_{tb} phase. The fact that SAXS is strong with rigid triphenyl groups (Chapter 4), weaker with rigid biphenyl groups [20] and unobserved with flexible diphenyethane groups, suggests that the extent of local layering is dependent on the chemical composition of the mesogens.
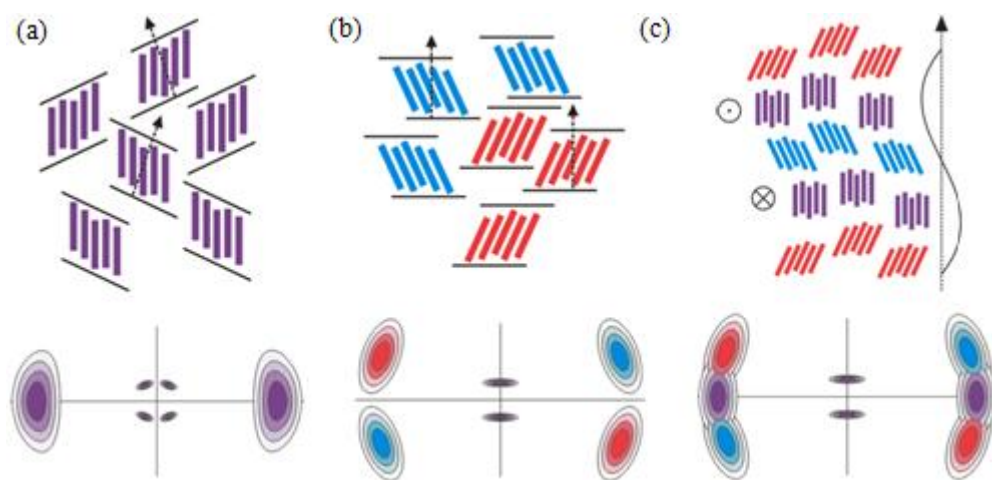
Figure 5.5 – Visual explanation of four-point WAXS distribution in the N_{tb} phase. Top is the local layer arrangement of the mesogens and below, the expected X-ray scattering pattern. Here the meridian is vertical and equator horizontal. (a) Cybotactic SmC cluster model used to explain four-point SAXS distributions in N phases [24-27]. (b) Re-orientation of the clusters on account of preference for tilted mesogens in the N_{tb} phase. (c) In the N_{tb} phase the tilt direction rotates progressively along the helical axis. Purple mesogens tilt into and out of the page, but lateral separation is effectively non-tilted, giving rise to equatorial intensity. The arrow indicates the direction of the helical axis.

5.3 – Polarised IR Analyses of CLMBPE

CLMBPE was deposited directly onto a KBr substrate and heated into the isotropic phase. The sample was then cooled to room temperature and sheared across the surface by knife edge. CLMBPE was then analysed by linearly polarised infrared (IR) spectroscopy using a Nicolet iS50 FTIR spectrometer with a temperature controlled cell and a ZnSe polariser. An IR spectrum was recorded with the polarity of incident radiation running parallel to the shear direction and also after rotating the sample in 15 ° increments, until the shear direction was perpendicular to the beam polarity. This process was initially carried out at 25 °C, but was repeated in 5 °C increments up to 65 °C, where the sample became isotropic. Representative IR spectra of CLMBPE at 25 °C, with the shear direction parallel, perpendicular and at 45 ° degrees to the incident wave polarity, are shown in Figure 5.6a. The wavenumbers of prominent peaks are tabulated in Table 5.0 along with the proposed assignments. The peak assignments follow from a previous IR study by Koenig *et al* [28] on an almost identical series of copolymers. However, in their study the IR beam was not polarised and orientational behaviour was not explored.

5.3.1 – Calculation of Orientational Order Parameters

The orientational order parameter (S) of each vibrational mode was estimated using $S=(D-1)/(D+2)$, where $D=A_{//}/A_{\perp}$ is the dichroic ratio (see Chapter 2, section 2.5). To improve the accuracy of 'D' values, the amplitude of each peak was plotted against the sample orientation angle and then a $\cos^2$ curve was fitted to the data (example provided in Appendix C). The peak and trough of the fitted sinusoid were taken as the values of $A_{//}$ and $A_{\perp}$. This data reduction process was repeated for spectra in each 5 °C increment, enabling S of each vibrational mode to be plotted as a function temperature. The vibrational modes relevant to later discussions are provided in Figure 5.6b. In the N_{tb} phase, the value of S is almost constant for all IR modes, but on transition to the N phase, an abrupt bump or dip appears in the line shape of several bands. A sudden post-transitional change was similarly observed in birefringence measurements, although IR suggests that orientational order decreases more rapidly with temperature in the N phase. The highest S values are in line with other measurements in the N_{tb} phase, $S = 0.4$-0.6 [5-8,19]. Positive S indicates vibrational modes oscillating below the 'magic angle' ($\simeq 55$ °), while negative S indicates modes which oscillate at larger angles (in reference to the shear direction).

As discussed in Chapter 3, section 3.4, the measurable order parameter S of the N_{tb} phase consists of at least two components, i.e. $S = S_0 \cdot S_1$, where S_0 describes the orientational alignment of local helical axes (domains), and S_1 describes the tilt distribution inside each domain. In the N_{tb} phase of CLMBPE the polymer chains in each domain can be imagined to wind around the helical axis at an angle of ~ 29 °. An average tilt or 'conical angle' of 29 ° was suggested by the GIXS azimuthal separation angle. The vibrational mode with the highest value of S corresponds to CH_2 wagging in the oligomethylene (OM) spacer (1392 cm^{-1}). Although one may expect various spacer conformations, hence spacer disorder in the real N_{tb} phase, the averaged wagging direction should always be along the spacer axis. This means that high S for CH_2 wagging can be achieved, even with conformational variety, so long as the overall axes of the spacers are well aligned. Assuming that this is the case in the sheared (by knife edge) CLMBPE sample, the average angle between the helical axis and the CH_2 wagging mode is taken to be 29 °, giving: $S_1 = ((3\cos^2(29)-1)/2 = 0.65$. From this, S_0 may also be estimated as 0.82 using $S_0 = S/S_1$ and the measured value of S (0.53 at 23 °C). The same value of S_0 applies to all other modes at 25 °C, which enables the angle

of vibration (θ_v) to be calculated for each mode using: $S_1 = S/S_0 = S/0.82 = ((3\cos^2(\theta_v)-1)/2$ (see Table 5.0). Note only the magnitude of θ_v can be determined due to the $\cos^2$ function. After heating beyond 25 °C S_1 and S_0 cannot be separated, meaning that the temperature dependence of θ_v cannot be discussed.
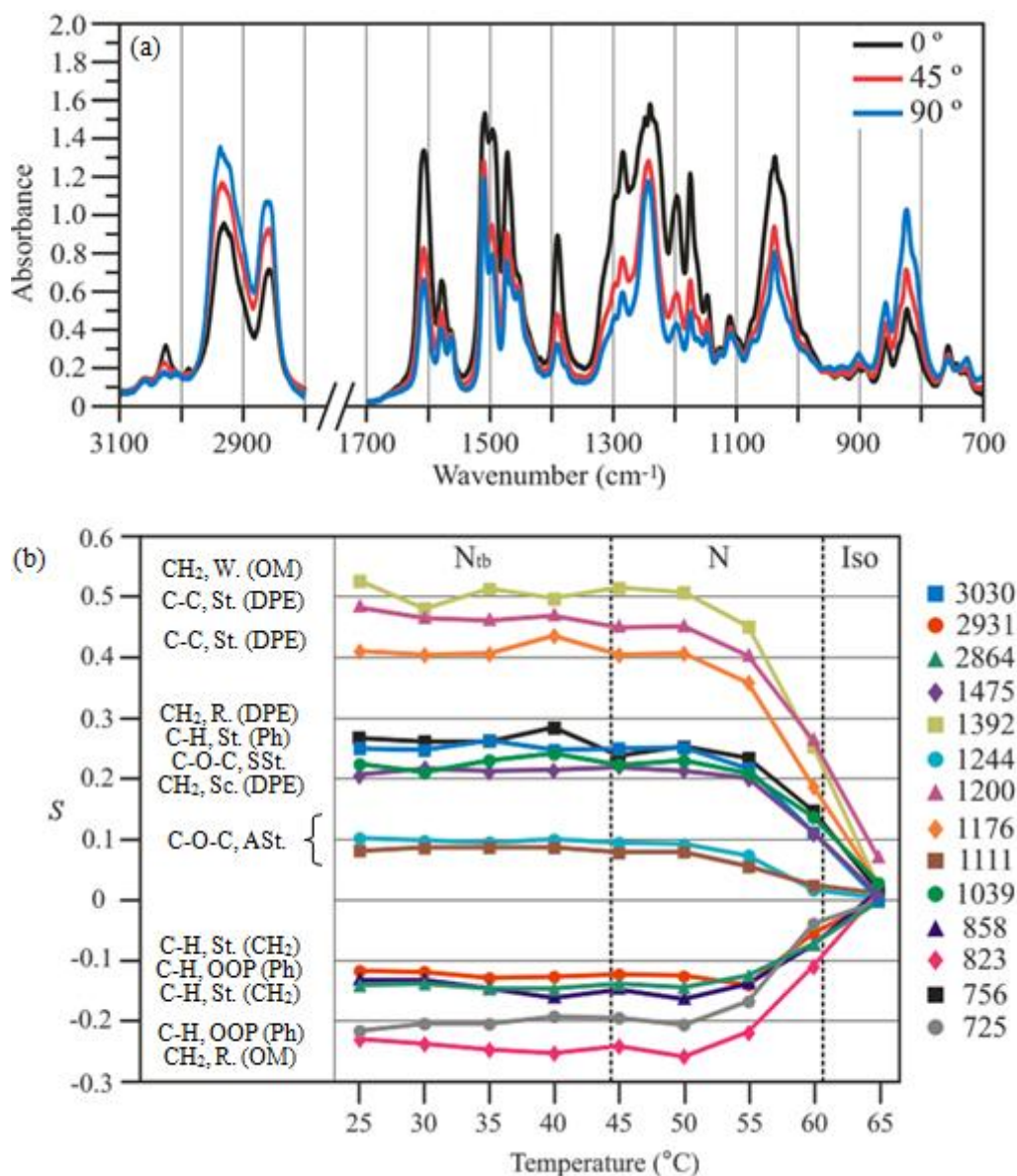
Figure 5.6 – (a) Polarised IR spectra of CLMBPE after shearing in the N_{tb} phase at room temperature. Spectra are shown with the polarisation direction of incident IR radiation parallel (0 °), perpendicular (90 °) and at 45 ° to the shearing direction. (b) Calculated orientational order parameters (S) against temperature. ASt./SSt.=Stretch (asymmetric or symmetric), W.=Wag, R.=Rock, Sc.=Scissor, OOP=Out of plane, Ph=Phenyl, OM=Oligomethylene spacer. In this context DPE refers to the ethane spacer in the mesogen rather than the mesogen as whole.

Table 5.0 – IR Peaks, Corresponding Assignments and Estimated Bond Angles

IR Peak (cm^{-1})	Sign of $\langle S \rangle$	Peak Assignment	Estimated Angle of Vibration (°)
3030	+	C-H stretching phenyl	42
2931	-	C-H stretching alkyl chains	62
2864	-	C-H stretching alkyl chains	62
1610	+	C-C stretching in Phenyl rings	41
1581	+	C-C stretching in Phenyl rings	-
1566	+	C-C stretching in Phenyl rings	-
1512	+	C-C stretching in Phenyl rings	51
1498	+	C-C stretching in Phenyl rings	-
1475	+	CH$_2$ scissoring in DPE spacer	44
1456	+	C-C stretching in Phenyl rings	-
1392	+	Wagging of CH$_2$ in OM spacer	29
1286	+	Wagging of CH$_2$-O in OM spacer	44
1244	+	Phenyl-Oxygen (C-O-C) asymmetrical stretching	50
1200	+	C-C stretching in DPE spacer	31
1176	+	C-C stretching in DPE spacer	34
1149	+	Unknown	-
1128	+	Unknown	-
1111	+	CH$_2$-O (C-O-C) asymmetrical stretching	51
1039	+	Phenyl-Oxygen (C-O-C) symmetrical stretching	43
903	+	Unknown	-
858	-	C-H out of plane deformation (1,2,4 phenyl)	63
823	-	C-H out of plane deformation (para phenyl)	69
756	+	Rocking of CH$_2$ groups in DPE spacer	42
725	-	Rocking of CH$_2$ groups in OM spacer	66

OM=Oligomethylene spacer, DPE=Ethane spacer in mesogen. Calculated vibration angles (θ_v) were calculated from $S_1 = S/S_0 = (3\cos^2(\theta_v)-1)/2$, where $S_0 = 0.82$ at 25 °C.

5.3.2 – CLMBPE Chain Conformation

The calculated bond angles were compared with a simulated section of an MBPE chain, where the positions of the oxygen atoms define the axes of each moiety (Figure 5.7). As mentioned previously, the average OM spacer axis tilts at an angle of 29 ° to the (vertical) helical axis. The alkyl C-H stretching modes (2931, 2864 cm^{-1}) and the OM CH$_2$ rocking mode (725 cm^{-1}) oscillate perpendicular to this axis, which is corroborated by the calculated values of θ_v (|29-90|=61 °).

The second and third highest values of S in the N$_{tb}$ phase correspond to CH$_2$-CH$_2$ stretching modes in the short ethane-like spacers of the diphenylethane (DPE) mesogens. These IR modes (1200, 1176 cm^{-1}) were tentatively assigned in previous work [28], but have been accepted here because high mesogen alignment and low conformational disorder in the short DPE spacer, hence high S, are sensible. Rotational freedom about the phenyl-CH$_2$ bond means that the exterior bend angle ϕ between mesogens is variable between 36 and 62 ° (assuming that the short ethane spacer is fixed in a '*trans*' conformation). The angle between the axes of the OM spacers and mesogens ($\phi/2$) can then vary between 18 and 31 °. In Figure 5.7 the diphenylethane segments are presented to be symmetric about the central CH$_2$ unit of the OM spacer. However, when the chain is tilted by 29 ° in respect to the helical axis, the bend angle brings one of the mesogens much closer to parallel with the helical axis than the other. In order to obtain high order parameters for DPE CH$_2$-CH$_2$ stretching modes, the angle between the helical axis and that of the mesogens should be similar in all cases. This can only be achieved if the MBPE chain is twisted about the OM spacer axis in a chiral conformation. Twisting about the spacer axis was proposed for LC dimers in Chapter 3, section 3.5 and its energetic feasibility was discussed in Appendix A. In CLMBPE rotational freedom about the oxygen bond and the Phenyl-CH$_2$ bond may significantly reduce the size of the twisting angle that each CH$_2$ linker of the OM spacer must contribute. The value of the twisting angle cannot be calculated without knowing either the pitch length or radius of the helix.

The oxygen related vibrational modes were found to have high value of θ_v, which on inspection of Figure 5.7, can be explained by the fact that some C-O bonds lie nearly parallel to the helical axis, while some are nearly perpendicular to it. The average should therefore be around 45 °. θ_v of the CH$_2$ rocking (756 cm^{-1}) and scissoring (1475

cm^{-1}) modes in the DPE ethane spacer were found to be very similar to those of the oxygen modes, which cannot be explained. The rocking and scissoring modes should be almost perpendicular to the axis of the mesogens, which should therefore produce a negative value of S and therefore much larger angles.
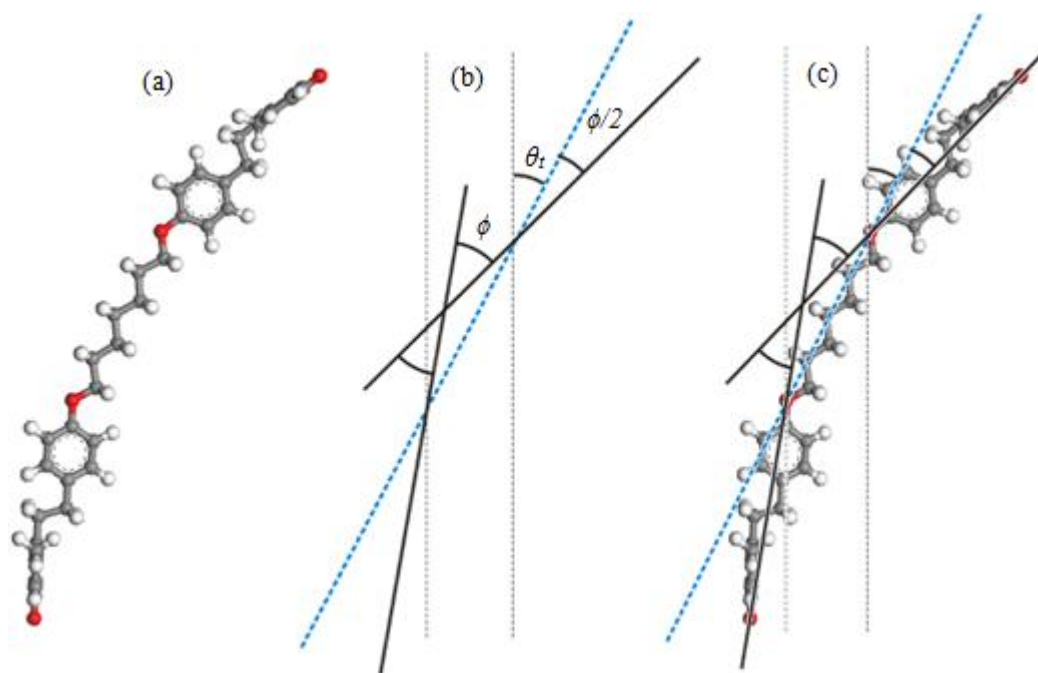
Figure 5.7 – (a) Simulated MBPE homopolymer chain segment (methyl group sub unit) with OM spacer axis tilted at $\theta_t = 29$ °. (b) Geometric construction showing the axes of the OM spacer (blue dashed) and DPE mesogens (solid black), which are defined by the positions of the oxygen atoms (red). The bend angle ϕ and the angle between the mesogen and spacer axes (ϕ /2) are also defined. (c) Overlap of the chain segment and the geometric construction. Shear direction/helical axis is vertical. In order to obtain high order parameters of DPE C-C stretching modes, the chain must adopt a chiral twisted conformation rather than this co-planar mirror symmetric one suggested by energy minimisation calculations of a single chain section.

5.4 – Discussion of Findings

The findings of polarised IR spectroscopy in the N_{tb} phase of CLMBPE suggest a twisted chain conformation, where the spacers and mesogens are tilted at almost the same angle in respect to the helical axis. This infers that the chains select an average conformation resembling a short range continuous helix, in-line with a previous model (Chapter 3, section 3.5) proposed for bent LC dimers. Peak fitting of the GIXS azimuthal intensity profile indicates that the average tilt or 'conical angle' of the helix is 29 °, again in-line with the LC dimer model in Chapter 3 and close to values reported

elsewhere [21]. The WAXS doublet was found to merge into a singular equatorial peak at temperatures close to the N phase. At the same time birefringence of the sample steadily increased until reaching the N phase where a significant jump occurred. These findings are consistent with straightening of the chain conformation, i.e. a progressively reducing bend angle with increasing temperature. In the N phase the chain must be close to straight, increasing the packing symmetry and length to breadth ratio (conformational anisotropy). The tilt angle of the chains in respect to the shear direction may also change slightly with temperature, but the calculated orientational order parameters of all IR vibrational modes do not significantly differ until the centre of the N phase temperature range is reached. This is also where the GIXS peak begins to azimuthally broaden (lose orientation) in Figure 5.4e. If the orientational distribution of the chains does not significantly change until the middle of the N phase, a reducing bend angle must be the explanation for the observed birefringence and GIXS findings. The small jump in the orientational order parameters of the alkyl CH_2 stretching modes and dip in the DPE C-C stretching modes also support a straighter chain conformation. One can imagine the OM spacers becoming slightly more parallel and at high temperatures the short ethane spacers may abandon the '*trans*' state to straighten the chain, introducing conformational variety and lowering *S*. On cooling CLMBPE back from the N phase into the N_{tb} phase the four point GIXS pattern was not recovered, but this is likely because the effects of shearing are permanently reduced as the chains relax at higher temperatures.

5.5 – Summary

CLMBPE copolymers were revisited and re-characterised by grazing incidence X-ray scattering (GIXS), polarised optical microscopy (POM) and polarised infrared (IR) spectroscopy. Analysis of vibrational modes in the sample revealed that the mesogens and oligomethylene spacers curve around the helical axis at approximately the same angle. This suggests that the conformational average of the polymer chains is that of a helix, in agreement with the model first proposed in Chapter 3, section 3.5. Similar to previous work on the CLMBPE copolymers a four-point wide angle X-ray scattering (WAXS) pattern was observed, which is now known to arise from the conical angle of the helical axis. Loss of the four point WAXS pattern and the jump in sample birefringence on transition to the N phase is believed to arise from straightening of the

chain conformation. This is also indirectly supported by the near constant orientational order parameters, which suggests that changes in the orientational distribution are not responsible for the GIXS and birefringence observations. On cooling CLMBPE from the N phase into the N_{tb} phase, the four-point WAXS distribution was not recovered, but the intensity did spread over a wider range of azimuthal angles. Azimuthal spreading of the WAXS arcs, increased birefringence at the N_{tb}-N transition and decreasing orientational order in the N phase have all been previously reported in systems of bent LC dimers. All experimental evidence indicates that the nematic-nematic transition is identical in both copolyether and LC dimer sample types.

References to Chapter 5

[1]   G. Ungar, J. L. Feijoo, A. Keller, R. Yourd, V. Percec, *Macromolecules*, 1990, **23**, 3411.

[2]   G. Ungar, V. Percec, M. Zuber, *Macromolecules*, 1992, **25**, 75.

[3]   G. Ungar, V. Percec, M. Zuber, *Polym. Bull.*, 1994, **32**, 1325.

[4]   C. Zhu, M. R. Tuchband, A. Young, M. Shuai, A. Scarbrough, D. M. Walba, J. E. Maclennan, C.Wang, A. Hexemer, N. A. Clark, *PRL*, 2016, **116**, 147803.

[5]   K. Adlem, M. Čopič, G. R. Luckhurst, A. Mertelj, O. Parri, R. M. Richardson, B. D. Snow, B. A. Timimi, R. P. Tuffin, D. Wilkes. *Phys. Rev. E*, 2013, **88**, 022503.

[6]   L. Beguin, J. W. Emsley, M. Lelli, A. Lesage, G. R. Luckhurst, B. A. Timimi, H. Zimmermann, *J. Phys. Chem. B*, 2012, **116**, 7940.

[7]   A. Hoffmann, A. G. Vanakaras, A. Kohlmeier, G. H. Mehl, D. J. Photinos, *Soft Matter*, 2015, **11**, 850.

[8]   C.Meyer, G. R. Luckhurst, I. Dozov, *J. Mater. Chem. C*, 2015, **3**, 318.

[9]   V. P. Panov, M. Nagaraj, J. K. Vij, Yu. P. Panarin, A. Kohlmeier, M. G. Tamba, R. A. Lewis, G. H. Mehl, *Phys. Rev. Lett.*, 2010, **105**, 167801.

[10]   V. P. Panov, R. Balachandran, M. Nagaraj, J. K. Vij, M. G. Tamba, A. Kohlmeier, G. H. Mehl, *App. Phys. Lett.*, 2011, **99**, 261903.

[11]   D. Chen, J. H. Porada, J. B. Hooper, A. Klittnick, Y. Shen, M. R.Tuchband, E. Korblova, D. Bedrov, D. M.Walba, M. A. Glaser, J. E. Maclennan, and N. A. Clark, *Proc. Natl. Acad. Sci. U.S.A.*, 2013, **110**, 15931.

[12]   E. Gorecka, M. Salamonczyk, A. Zep, D. Pociecha, C.Welch, Z. Ahmed, G. H. Mehl, *Liq. Cryst.*, 2015, **42**, 1.

[13]   V. Borshch,Y.-K. Kim, J. Xiang, M. Gao, A. J´akli, V. P. Panov, J. K. Vij, C. T. Imrie, M. G. Tamba, G. H. Mehl, O. D. Lavrentovich, *Nat. Commun.*, 2013, **4**, 2635.

[14]   P. K. Challa, V. Borshch, O. Parri, C. T. Imrie, S. N. Sprunt, J. T. Gleeson, O. D. Lavrentovich, A. Jákli, *Phys. Rev. E*, 2014, **89**, 060501.

[15]   M. Cestari, S. Diez-Berart, D. A. Dunmur, A. Ferrarini, M. R. de la Fuente, D. J. B. Jackson, D. O. Lopez, G. R. Luckhurst, M. A. Perez-Jubindo, R. M. Richardson, J. Salud, B. A. Timimi, and H. Zimmermann, *Phys. Rev. E*, 2011, **84**, 031704.

[16]   N. Sebastián, M. G. Tamba, R. Stannarius, M. R. de la Fuente, M. Salamonczyk, G. Cukrov, J. Gleeson, S. Sprunt, A. Jákli, C. Welch, Z. Ahmed, G. H. Mehl, A. Eremin, *Phys. Chem. Chem. Phys.*, 2016, **18**, 19299.

[17]   S. M. Salili, C. Kim, S. Sprunt, J. T. Gleeson, O. Parri, A. Jákli, *RSC Adv.*, 2014, **4**, 57423.

[18]   P. A. Henderson, C. T. Imrie, Liq. Cryst., 2011, **38**, 1407.

[19]   Z. Zhang, V. P. Panov, M. Nagaraj, R. J. Mandle, J. W. Goodby, G. R. Luckhurst, J. C. Jones, H. F. Gleeson, *J. Mater. Chem. C*, 2015, **3**, 10007.

[20]   G. Singh, D. M. Agra-Kooijman, M. R. Fisch, M. R. Vengatesan, J.-K. Song, S. Kumar, arXiv:**1510.08362v1 [cond-mat.soft]**, 2015.

[21]   J. P. Jokisaari, G. R. Luckhurst, B. A. Timmi, J. Zhu, H. Zimmermann, *Liq. Crsyt.*, 2015, **42**, 708.

[22]   A. M. Donald, A. H. Windle (1992). "*Liquid Crystalline Polymers*", Cambridge University Press, pp. 223-224.

[23]   A. J. Guenthner, T. Kyu, *Macromolecules*, 2000, **33**, 4463.

[24]   A. De Vries, *Mol. Cryst. Liq. Cryst.*, 1970, **10**, 219.

[25]   C. Tschierske, D. J. Photinos, *J. Mater. Chem.*, 2010, **20**, 4263.

[26]   O. Francescangeli, E. T. Samulski, *Soft Matter*, 2010, **6**, 2413.

[27]   O. Francescangeli, V. Stanic, S. I. Torgova, A. Strigazzi, N. Scaramuzza, C. Ferrero, I. P. Dolbnya, T. M. Weiss, R. Berardi, S. Orlandi, C. Zannoni, *Adv. Funct. Mater.*, 2009, **19**, 2592.

[28]   R. L. Silvestri, J. L. Koenig, *Polymer*, 1994, **35**, 2528.

Chapter 6 – A Low Symmetry Cubic Mesophase of Dendronised CdS Quantum Dots

In this chapter, A new liquid crystal (LC) phase with $P2_13$ symmetry, the lowest possible cubic symmetry, is presented in a system of CdS quantum dots (QDs) modified with a two-layer corona of aliphatic thiols (inner) and LC aromatic dendrons (outer). It is proposed that the unusual low symmetry of this cubic mesophase is a result of the multi-layered corona, which prefers to adopt an anisotropic radial profile due to the combination of long and short 'bristles'. The anisotropic distribution of dendrons (long bristles) in the $P2_13$ phase is thought to facilitate π-π interaction among the aromatic moieties. The interaction gives rise to non-radiative exciton energy transfer pathways, which induce photoluminescence quenching of the CdS QDs. This is believed to be the first example of structure-dependent emission-quenching behaviour within QD arrays.

6.0 – Introduction

Semiconductor nanoparticles (NPs), sometimes referred to as quantum dots (QDs), have attracted a great deal of scientific attention due to their size-dependent and tuneable light absorption/emission properties [1,2]. Moreover, periodic arrays of QDs have considerable potential in photovoltaics [3-5] and opto-electronics, where interactions of electronic charge and spin are expected between QDs [6,7]. QD arrays may also function as efficient thermoelectric devices where high electronic − low phonon conduction is required [8]. As these future devices rely on quantum phenomena, such as tunnelling of charge and spin, the arrangement of the QDs, as well as their separation lengths, are of prime importance. To date two or three dimensional QD organisations have been created by various processes including epitaxial growth on substrates [9,10], dispersion in anisotropic LC media [11-16] and by synthesis of QDs in dendrimer templates [17-19]. However 2D and 3D arrays of QDs with interparticle distances on the scale of nanometres to tens of nanometres, were yet to be achieved by any bottom-up or top-down method prior to the work soon to be discussed.

As mentioned in Chapter 1, section 1.7, self-organisation is a powerful means of forming NP-based periodic structures, where the ordered arrangement is precisely controlled by the constituents themselves. In this work, Cadmium Sulphide (CdS) QDs were self-organised by a two layered shell of aliphatic thiols (inner) and dendrons (outer). The system of organic-semiconductor dendrimers was investigated using GISAXS and a variety of UV/Visible spectroscopic methods. In a previous study, the same two layered 'corona' resulted in hexagonal columnar and 3D simple cubic (*SC*) packing of gold NPs [20]. However, by changing the core material and optimising the ligand surface density and ratio, a novel NP cubic superlattice was achieved in this work (space-group $P2_13$), which represents a new cubic mesophase of unprecedented low symmetry. The specific ordered arrangement of the dendritic ligands within the structure is believed to be responsible for the observed photoluminescence (PL) quenching within the material. The tailorable self-organisation and the 'high absorption, low re-emission' properties of the ordered 3D phase may prove to be a promising advance towards more efficient solar cells and dye-sensitised up-conversion emission enhancement.

The following text describes the results of a joint project between the University of Sheffield, UK, Tohoku University, Japan and Kyushu University, Japan. The author of this thesis was involved in the GISAXS structure determination, construction of the molecular model and consequent explanation of the PL quenching mechanism. Sample synthesis, sample analysis and PL measurements were contributed entirely by collaborators. A detailed synthetic procedure will not be provided here, but is reported elsewhere for the interested reader [20].

6.1 – Synthesis and Characterisation of Dendronised CdS QDs

6.1.1 – Joint Synthesis of CdS QDs and the Inner Corona.

The CO_2H-modified CdS QDs, abbreviated '**C**', were synthesised by the method of Kanehara *et al* [21], but modified slightly with 12-dodecanethiol (DT) and 16-mercapto hexadecanoic acid (MHA) as thiol ligands. The basic synthetic procedure is as follows: Initially, cadmium stearate (204 mg, 0.30 mmol), 1,1,3,3-tetramethyl-2-thiourea (20 mg, 0.15 mmol), DT (15.2 mg, 0.075 mmol), and MHA (21.6 mg, 0.075 mmol) were

dissolved into 10 mL of dioctyl ether. The solution was heated at 150 °C for 2 hours and then at 230 °C for 3 hours under an N_2 atmosphere. The resulting solution was centrifuged and washed with $CHCl_3$/EtOH three times to remove excess amount of thiols. The residue was dried under reduced pressure, producing **C** (Figure 6.0c).
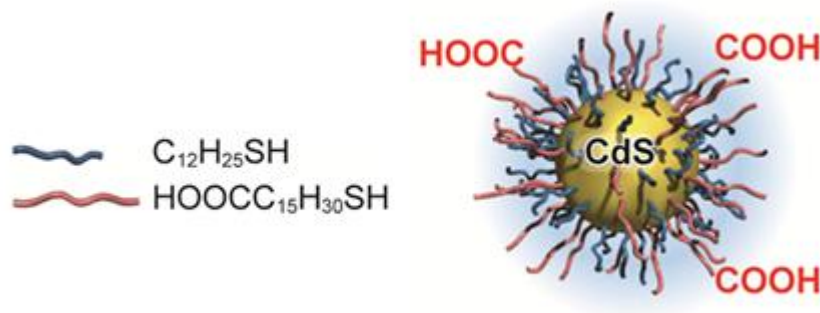

Figure 6.0 − Visual representation of **C**, comprising a CdS QD an inner corona (shell) of thiols.

6.1.2 − Characterisation of C (CdS QDs + Inner Corona)

From transmission electron microscopy (TEM) the mean diameter of the CdS cores was estimated to be 3.9 nm; the standard deviation of the particle size distribution was approximately 0.4 nm. As shown in Figure 6.1a, the shape of **C** is close to spherical.

In the previous study it was shown that a well-ordered NP arrangement can be obtained if the outer corona contains an optimum number of dendrons [20]. This is reliant on the number of MHA ligands (potential binding sites) on the NP surface. In this investigation the number of dendrons in the outer corona was controlled by optimising the molar ratio of the DT/MHA mixture during the synthesis of **C**. A 1:1 DT/MHA molar mixture was used in the preparation of **C**, but the ratio of DT to MHA on the surface of the NPs was found to differ. The molar ratio of DT/MHA on the surface of NPs was found by isolating the thiols from the CdS cores by I_2-decomposition [22]: A dispersion of **C** (50 mg) in CH_2Cl_2 (10 mL) was stirred with iodine (5 mg) for 1 hour to make a disulfide bond between thiol ligands. After stirring, the insoluble brown residue was removed by filtration, and the resulting solution was dried under reduced pressure. The residue was then dissolved in $CDCl_3$ and investigated by ^{1}H-NMR. In Figure 6.1b the peak at δ = 0.9 ppm is attributed to the terminal methyl group of DT, and peaks around δ = 1.2 ppm to methylene groups of both DT and MHA. By comparing the

integral peak intensities, the DT/MHA modification ratios (mol/mol) on the surfaces of **C** was determined as 10/3.2. The lower MHA fraction may be due to the lower solubility of MHA compared to that of DT in dioctyl ether.
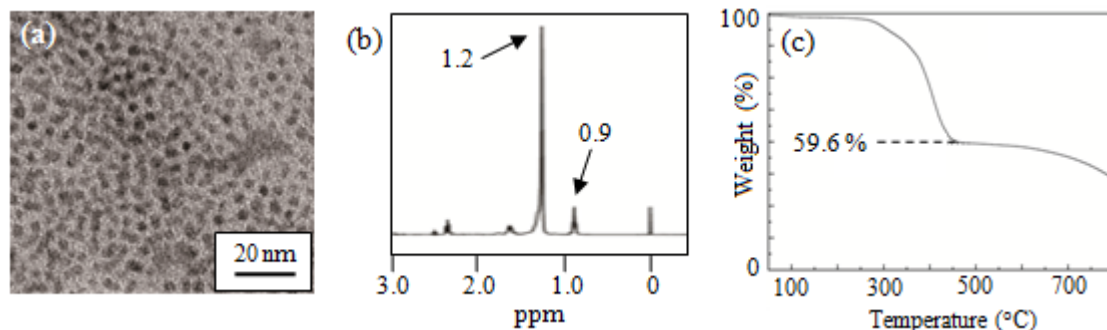

Figure 6.1 – (a) TEM image of **C**, CdS particle size = 3.9$\pm$ 0.4nm. (b) ^{1}H-NMR spectrum of **C**. peaks at 0.9 and 1.2 ppm respectively correspond to the terminal group of DT and the methylene group of both DT and MHA. (c) TG profile of **C**, reveals 40.4 wt% of organic material.

The number of molecules on the surface of the CdS NPs was determined using the molar ratio determined by ^{1}H-NMR and additional results from Thermogravimetric (TG) analysis. TG analysis showed that the weight loss of **C** (W_L) was 40.4% (Figure 6.1c). This value is attributed to the burning off of DT and MHA. The weight of one CdS NP (M_p) was calculated by the following equation: $M_p = 4\pi\rho_p (D_p \times 10^{-7}/2)^3/3$. Here, ρ_p is bulk density of CdS (= 4.82 g cm^{-3}), and D_p is the particle mean size determined by TEM. As a result, M_p of CdS was 1.50 x 10^{-19} g. Following this, the number of CdS NPs per gram (N_p) was 4.4 x 10^{18} calculated from $N_p = (1 - W_L)/M_p$. The number of thiols per CdS NP (N_T) was calculated as 273 from $N_T = W_L N_A/(N_p M_{ave})$. In this equation, M_{ave} is the average molecular weight of thiols and N_A is Avogadro's constant. The number of DT (N_{DT}) and MHA (N_{MHA}) molecules on one CdS NP was therefore 207 and 66 molecules, respectively (273 split in a ratio of 10/3.2).

6.1.3 – Attachment of the 2nd Generation Dendrons (Outer Corona)

A phenethyl ether-type dendron, abbreviated '**D**', was synthesised by convergent methods with an amino group at the apex (Figure 6.2a). In the pure **D** compound, the molecules spontaneously assemble into spherical dendrimer aggregates 9.8 nm in diameter, which above 55 °C, arrange in a dodecagonal quasi-crystal phase that fully

melts at 80°C (Figure 6.2b). The dendrons were attached to **C** as the outer corona through amidation reactions with the carboxylic groups at the surface of the inner corona (tips of the MHA ligands), encapsulating the QDs. The dendronised sample, i.e. CdS core + thiols + dendrons, will be referred to as **D/C**.
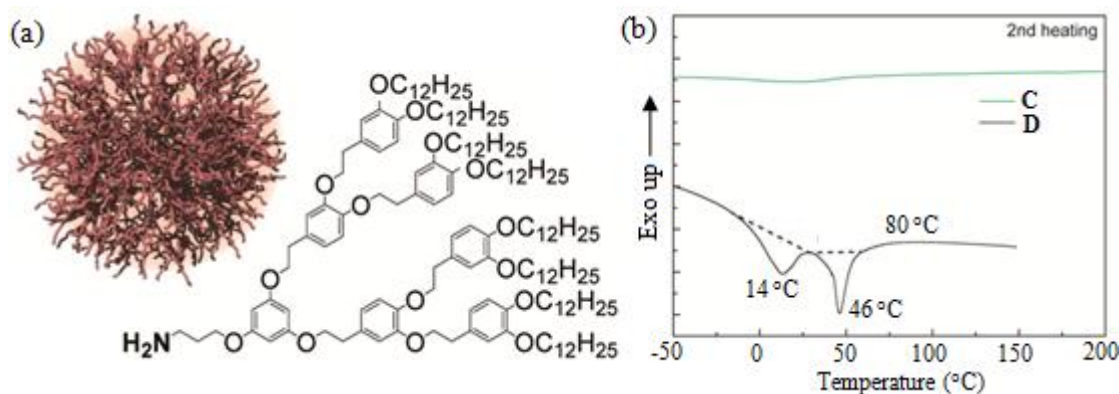

Figure 6.2 – (a) The chemical structure of the 2nd generation dendron, abbreviated as 'D', and a visual representation of the 9.8nm spherical aggregate observed in the pure compound. (b) DSC traces of pure **D** and pure **C**.

6.1.4 – Characterisation of D/C (CdS QDs + Inner Corona + Outer Corona)

In this section, many of the values defined in the last paragraph of section 6.1.2 are recalled. Figure 6.3a shows the TG result of **D/C**; the weight loss (W_D) during the experiment was 64.3%. This loss is attributed to burning off DT, MHA and **D**. Here, the wt% of thiols on the surface of **D/C** was calculated as $(1-W_D) W_L/(1-W_L) = 24.2\%$. Thus, the wt% of **D** in **D/C**, determined by subtracting the thiol component from the total weight loss, is calculated as 40.1%. This indicates that 1.03×10^{20} molecules per gram of **D** were attached to the surfaces of **C** to form **D/C**. Using the value of N_p, the number of **D** molecules per **C** (N_D) was 69 molecules; the N_D/N_{MHA} ratio in **D/C** was therefore 1.05. The fact that the N_D/N_{MHA} ratio was close to 1 meant that the optimised amidation reaction with **D** proceeded almost stoichiometrically. The high yield of amidation is partly due to the choice of alkyl chain lengths in the inner corona. The longer MHA chains allow the CO_2H groups to protrude from the surface of the inner corona, making them more accessible to the reaction. After **D** modification, dispersion-cast NPs tend to form ordered hexagonal monolayers with an interparticle spacing of *ca.* 9 nm (Figure 6.3b). Figure 6.3c exhibits Fourier Transform Infrared (FT-IR) spectra of **C**, **D**, and **D/C**. A C=O absorption at 1,740 cm^{-1} due to CO_2H moieties on **C** was replaced by

another C=O peak at 1,722 cm^{-1}, attributed to the CONH groups of **D/C**. This confirms successful amidation reactions.

The DSC thermograms of **D/C** are shown in Figure 6.3d. The second heating trace shows three endotherms, a large one at 7 °C, and two very small ones at 133, and 216 °C. The material is rigid below the first endotherm and is subject to degradation above the third endotherm. This thermal behaviour is similar to that observed previously in systems of gold NPs [20,23]. The endotherms at 7 °C and 216 °C are attributed to melting of the alkyl chains and isotropisation, respectively.
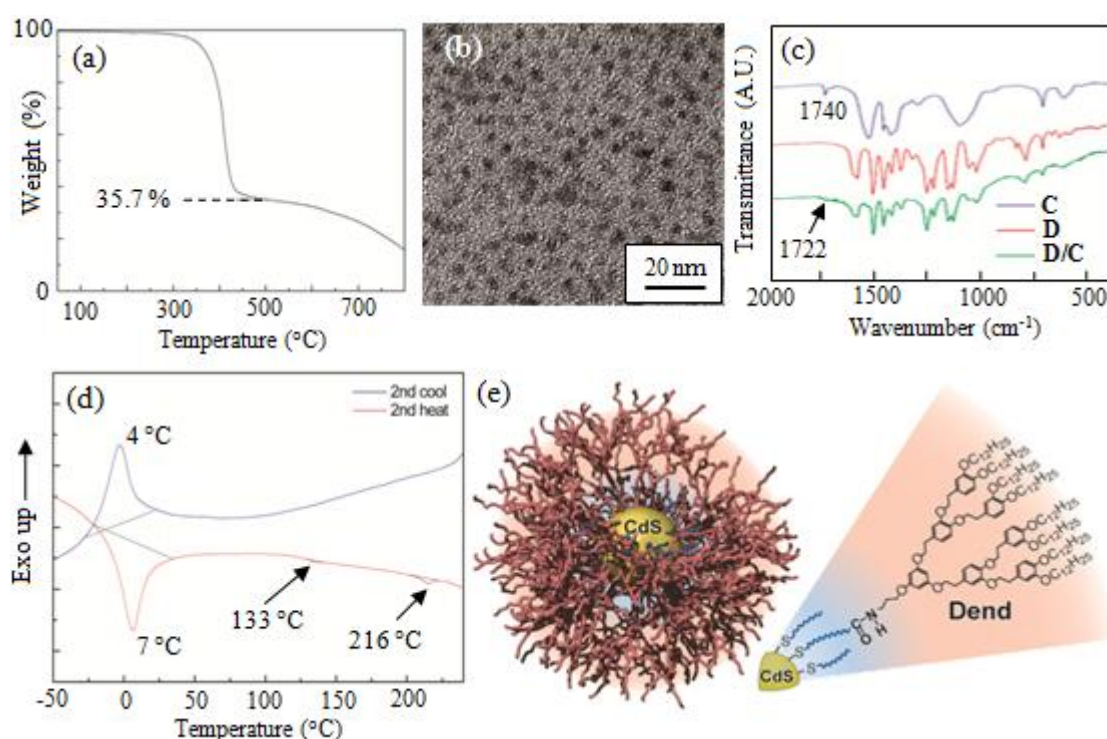
Figure 6.3 – (a) TG profile of **D/C** reveals that the sample contains 64.3 wt% organic material. (b) TEM image of **D/C**, CdS particle size is still = 3.9± 0.4nm. (c) IR spectra showing before and after amidation of **C**. The peak at 1722 (not present in **C**) indicates successful amidation. (d) DSC trace of **D/C** during the 2nd heating and cooling cycle. (e) Visualisation of **D/C**, featuring a CdS QD and a two layer corona of DT and MHA ligands (inner) and dendrons (outer). Dendrons are exclusively connected to MHA via amidation.

6.2 – Structural Analysis of the Thin-film Self-assembly

6.2.1 – GISAXS Analysis of D/C

Thin film samples of **D/C** were prepared by casting from $CHCl_3$ dispersion on silicon substrates. GISAXS experiments were then carried out on station I16 of the DLS. The sample was mounted on a 6-circle Goniometer, which enabled control of the angle and position of the incident beam on the sample. A Dectris Pilatus-2M area detector was used for collection of GISAXS patterns. A flight tube flushed with flowing helium was inserted between the sample and the detector, in order to cut down the background noise due to air scattering from the main beam. An adjustable tapered beam-stop was positioned inside the flight tube near the detector end. The annealing of the sample was carried out using a programmable vacuum oven. The GISAXS patterns used in this study were recorded at room temperature, but it was ascertained, using high-temperature GISAXS, that the patterns before and after cooling from the annealing temperature did not change.

To investigate the 3D self-organisation of **D/C**, transmission SAXS patterns were recorded from the bulk sample at different temperatures. At 50 °C **D/C** showed only broad scattering peaks, resulting from the form factor of the nanoparticles in a disordered (amorphous) spatial arrangement. This situation persisted at higher temperatures, although at 150 °C some weak Bragg reflections began to emerge. In order to refine the Bragg reflections and encourage orientational order, thin films of **D/C** were prepared and consequently annealed at 150 °C. Throughout the high temperature annealing process the films were examined using GISAXS. Initially, a strong diffuse peak was observed, indicating the absence of a well ordered structure (Figure 6.4a). However after 12 hours annealing, three Bragg reflections were detected signifying the development of long-range order (Figure 6.4b). After 19 hours, additional reflections appeared, indicating further perfection of the ordered structure (Figure 6.4c,d). Similar annealing behaviour has been observed previously with **D**-coated gold NPs [20].

The ratio between the q vector magnitudes of the Bragg reflections observed in the present **D/C** sample was $\sqrt{2}:\sqrt{3}:\sqrt{4}:\sqrt{5}:\sqrt{8}:\sqrt{9}:\sqrt{11}$, suggesting a cubic unit cell with lattice parameter $a = 11.86 \pm 0.05$ nm. The d-spacings of the observed peaks are presented in Table 6.0. Furthermore, the sole systematic absence of (h00) Bragg reflections, h = odd, rules out all but two possible space groups: $P2_13$ (spacegroup No. 198) or $P4_232$ (spacegroup No. 208) [24]. The choice between the two space groups was made using the weight-to-volume fraction conversions of the TG results, approximating the density of the CdS and organics as 4.82 g/cm^3 and 0.9 g/cm^3 respectively. According to the calculation, CdS occupies 9.4% of the unit cell (157 nm^3) which, if divided by the volume of a 3.9 nm spherical particle (as determined by TEM), suggests that each contains five CdS NPs; however, a site multiplicity of five is absent in the above space groups. In the case of $P4_232$, special positions with multiplicities of four and six, as well as two (4 + 2 = 6), all introduce additional systematic extinctions that are disobeyed by the GISAXS pattern. For space group $P2_13$, a site multiplicity of four is the only solution that agrees with the observed systematic absences. If the CdS volume is divided amongst only four NPs, they must have a slightly larger diameter of 4.2 nm, which is in reasonable agreement with the value of 3.9 nm suggested by TEM.

Table 6.0 – Observed and Calculated diffraction peak d-spacings of the $P2_13$ phase

(hkl)	Observed d-spacing (nm)	Calculated d-spacing (nm)
(110)	8.38	8.39
(111)	6.85	6.85
(200)	5.92	5.93
(210)	5.35	5.30
(220)	4.19	4.19
(221)	3.93	3.95
(311)	3.58	3.58

The calculated d-spacings were determined using equation 2.16, Chapter 2, setting $a = b = c = 11.86$nm.
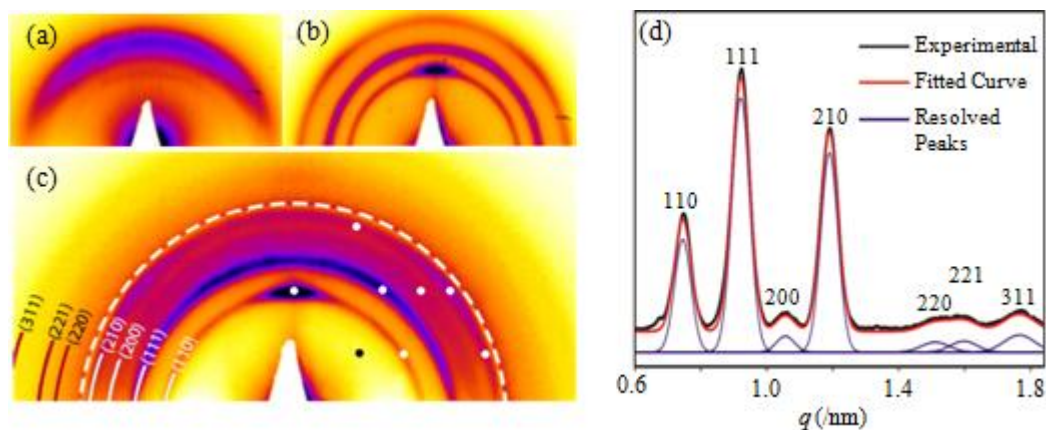
Figure 6.4 – X-ray diffraction patterns of **D/C** after (a) 6 hours (b) 12 hours and (c) 19 hours of annealing at 150 °C. The region outside the dashed line in (c) was recorded with a longer exposure. The white spots are the expected positions of the Bragg maxima of the observed reflections assuming a cubic structure with [110] oriented vertical. The black spot shows the expected position of the missing (100) peak, indicating the reflection condition $h00 = 2n$. (d) 1-D azimuthally averaged and Lorentz-corrected diffractogram of (c), showing numerically resolved peaks; the experimental data and fitted curve are superimposed and vertically displaced for clarity.

6.2.2 – Reconstruction of Electron Density Map

In order to confirm our hypothesis of the spacegroup, a simulated diffraction pattern of the system was calculated to see if a match with the observed relative intensities could be found. The observed relative intensity of the four most prominent Bragg reflections was found using the method described in Chapter 2, section 2.3.5 and Figure 6.4d. The relative intensity of each simulated Bragg reflection was calculated using equations 2.19 and 2.20 for perfect 4.2 nm spheres centred at special positions: (x, x, x), ($-x+\frac{1}{2}$, $-x$, $x+\frac{1}{2}$), ($-x$, $x+\frac{1}{2}$, $-x+\frac{1}{2}$), and ($x+\frac{1}{2}$, $-x+\frac{1}{2}$, $-x$). The simulated relative intensities were then matched to the observed measurements by trial and error, varying the 'x' value of the particle positions and $\sqrt{\langle u^2 \rangle}$, their root mean squared (RMS) displacement from the ideal locations. As shown in Table 6.1 an excellent fit was achieved between the simulated and observed relative intensities, with exception to (200) Bragg reflection. However it is likely that the observed intensity of the (200) peak is underestimated in Table 6.1. This is because the q-value of the (200) peak overlaps that the scattering maximum of the amorphous background, which means that some of the (200) intensity may have been unavoidably subtracted with the background. In light of the excellent fit with the remaining peaks and the reflection criteria discussed previously, the structure

must possess $P2_13$ symmetry. Moreover, the fitted simulation enabled the phase information of this non-centrosymmetric spacegroup to be determined and the electron density map to be reconstructed.

Table 6.1 – The Integrated and Calculated Intensities and Calculated Phase Angles of the Diffraction Peaks.

(hkl)	q (nm^{-1})	Multiplicity	Integrated intensity $I_{(hkl)}/I_{(111)}$	Calculated Intensity $I_{(hkl)}/I_{(111)}$	Phase Angle (Rad)
(110)	0.750	12	0.288	0.290	$\pi/2$
(111)	0.917	8	1.000	1.000	-1.515
(200)	1.061	6	0.078	0.424	π
(210)	1.174	24	0.607	0.609	π

The best fit was achieved for $x = 0.198$ and $\sqrt{\langle u^2 \rangle} = 1.22$ nm.
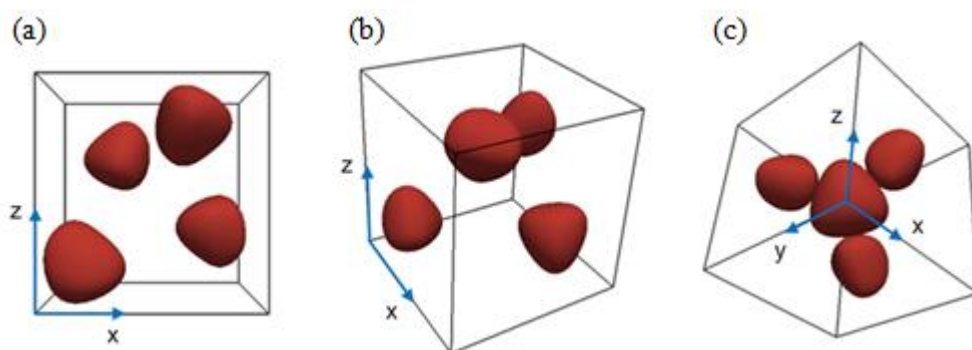
Figure 6.5 – (a)-(c) The single isosurface presentation of the electron density map reconstructed using the integrated intensities and phase angles shown in Table 6.1; views along [100] (a), an arbitrary axis (b), and [111] (c). The surfaces each enclose a high-density volume equal to that of a 4.2 nm sphere.

The reconstruction shows that the unit cell contains four points of high electron density in the configuration described by space group $P2_13$ ($x = 0.198$) – see Figure 6.5a-c. We attribute the non-spherical shape of these points to the anisotropic Debye-Waller factor (or "temperature factor") associated with a large RMS displacement (1.22 nm). The non-spherical displacement is consistent with the attached organic ligands restricting movement towards the closest neighbouring particles. The $\sqrt{\langle u^2 \rangle} = 1.22$ nm value

should be compared with the standard deviation of 0.4 nm in CdS core size distribution determined from TEM to realise how the thick soft corona cushions the effect of core non-uniformity and allows nanoparticles to form LC arrays with 3D long-range order in spite of their polydispersity.

6.3 – Supramolecular Model

The $P2_13$ arrangement of the dendronised quantum dots is closely related to the face centred cubic (*FCC*) structure; the two structures are in fact identical in the special case when $x = 0$ (see Figures 6.6a-d). An *FCC* LC structure has recently been reported for gold NPs coated with side-on attached rod-like mesogens [25], however it has been noted that neither of the "close packed" structures, i.e. *FCC* or hexagonal close packing (*HCP*), have been observed in dendrimers [26]. This has been attributed [27,28] to the supramolecular spheres being soft rather than hard balls, enabling them to pack more efficiently in structures known as Frank-Kasper (FK) phases [29,30]. FK phases contain only the smallest, i.e. tetrahedral [31], interstices in contrast to *FCC* and *HCP*, which both possess large octahedral vacancies whose centres are hard to reach by the ends of the dendron tails. While it is unsurprising that **D/C** did not form a *FCC* structure, it is unusual for mesophases to adopt such low-symmetry and "inefficient" packing modes as $P2_13$. The previous study on gold NPs coated with the same two-layer corona of DT+MHA (inner) and dendron **D** (outer) also had unexpected outcomes: a simple cubic (*SC*) structure was obtained, which contains interstices even larger than those of *FCC* and *HCP* [20]. Body centred cubic (*BCC*) structures have also been reported in dendrimers [26], as well as in dendronised gold NPs [32], but *BCC* is similar to FK phases.
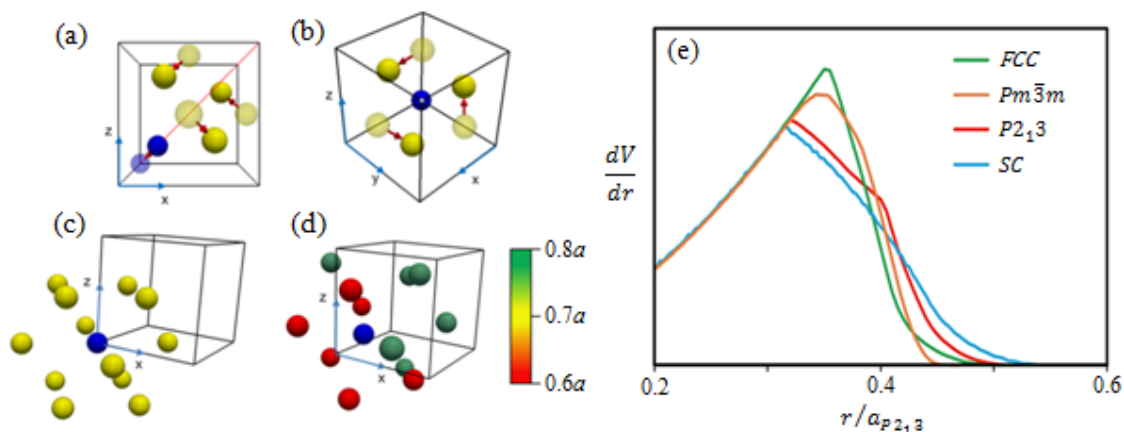
Figure 6.6 – (a,b) The unit cell transformation from *FCC* (hollow spheres) to $P2_13$ (solid spheres); views along the [100] and [111], respectively. The displacement is by *x* along one of the [111] directions. Particles which lie outside the cell after the displacement are not shown. (c,d) The 12 nearest neighbours of a reference particle within a *FCC* and a $P2_13$ lattice, respectively. The particles are coloured here according to their closeness to the reference particle (Particles have been reduced in size for clarity). (e) Calculated volume increase of an average spherical particle upon radial growth from its centre for four cubic packings: $P2_13$, *FCC*, *SC* and $Pm\overline{3}n$. The *dV/dr* functions were scaled so that final volume enclosed by each of the expanding spheres is equal to the total volume of a single particle. The curves of *SC* and $Pm\overline{3}n$ were then normalised according to the ratio $1:\sqrt[3]{4}:\sqrt[3]{8}$, as the number of spheres in a *SC*, $P2_13$, *FCC* and $Pm\overline{3}n$ unit cell is 1, 4, 4 and 8, respectively. The radius is given as a fraction of the $P2_13$ unit cell parameter.

In order to relate the properties of the organic corona to the packing mode of the spheres, or "spherical brushes", *dV/dr* functions were calculated and compared in Figure 6.6e for four packing modes: *FCC*, $Pm\overline{3}n$ or A15 (typical in dendrimers), $P2_13$, and *SC*. The *dV/dr* function [20,33] describes the average volume increase of the spheres as their radius *r* increases from 0. Initially all *dV/dr* functions follow a parabola as $dV/dr \propto r^2$, but once the spheres clash the gradient of each function drops and becomes negative; *dV/dr* reaches zero when all space is filled. The length of the decay after the first point of collision therefore describes the degree of anisotropy that must be adopted by the brushes in order to fill the remaining space. As illustrated in Figure 6.6e, the packing modes differ by the decay of their *dV/dr* curves. For dendrimers with tails of equal length, packing modes with *dV/dr* rapidly decaying to zero are preferred. $Pm\overline{3}n$ is therefore more favorable than *FCC* as the large octahedral vacancies of the latter lengthen the decay of its *dV/dr* function. By contrast, it appears that particles possessing

132

our two-layered corona prefer modes with slowly decaying *dV/dr*, featuring large interparticle voids. A multi-layered corona appears to prefer an anisotropic radial profile due to the combination of long and short bristles.
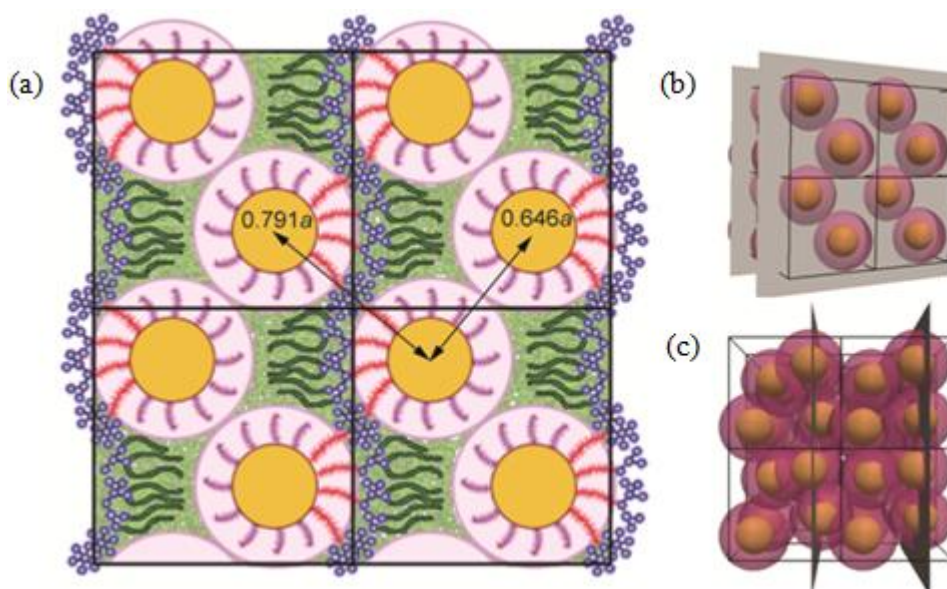

Figure 6.7 – Schematic illustrations of dendronised CdS QDs in the $P2_13$ phase. (a) A single plane slice at $x = 0.75$ parallel to (100) illustrating schematically the general principles of the proposed molecular arrangement within the $P2_13$ structure. Yellow = CdS, pink = DT, red = MHA, blue = aromatic and green = dendron tails. (b,c) Perspective views of the 3D quantum dot array showing the (100) Miller planes depicted in (a).

In our $P2_13$ structure ($x = 0.198$), the twelve nearest neighbours of a reference particle are separated into two shells of six (Figure 6.6d), with respective centre-to-centre distances ($2r_0$) of $0.646a$ and $0.791a$. For *FCC* and $P2_13$, the values of r_0 can be read directly from the gradient drops in Figure 6.6e. Converting r_0 to nanometres, we find that the spheres within the $P2_13$ structure expand without obstruction up to $r = 3.83$ nm. The CdS cores and the alkylthiol ligands combined occupy 43.5% of the unit cell volume (757 nm^3), which if divided amongst four spheres, suggests that **C** reaches a radius of 3.51 nm. The closeness of this approximation to r_0 infers that the minimum interparticle separation within the sample is in this case governed by the thickness of the dense inner corona. Furthermore, the lack of space between nearest neighbour NPs suggests that the dendrons, hence the MHA ligands, are indeed distributed anisotropically around the CdS surface, aggregating in regions that allow them to fill the

open interparticle channels (see Figure 6.7). The proposed reorganisation of MHA–**D** ligands on the NP surface during annealing is in line with a similar idea proposed previously for gold NPs [25,32,34]. The re-distribution of the dendrons will be recalled in later discussions.

6.4 – Fluorescence Spectroscopy

6.4.1 – Emission and Absorption Properties of D/C

To investigate the PL behaviour of **D/C**, a **D/C** film was prepared on hydrophobic quartz glass by casting from a CHCl$_3$ dispersion followed by drying. Figures 6.8a and b show photographs of the **D/C** film without and with UV irradiation at 365 nm. The film shows strong fluorescence when excited by UV irradiation. After annealing the film at 150 °C for 20 hours the brightness of the PL is drastically reduced and almost completely quenched, despite UV excitation (Figure 6.8c). TEM revealed that there is no change in the size and shape of CdS cores before and after annealing (Figure 6.8d). However, under these conditions **D/C** forms the $P2_13$ superlattice.
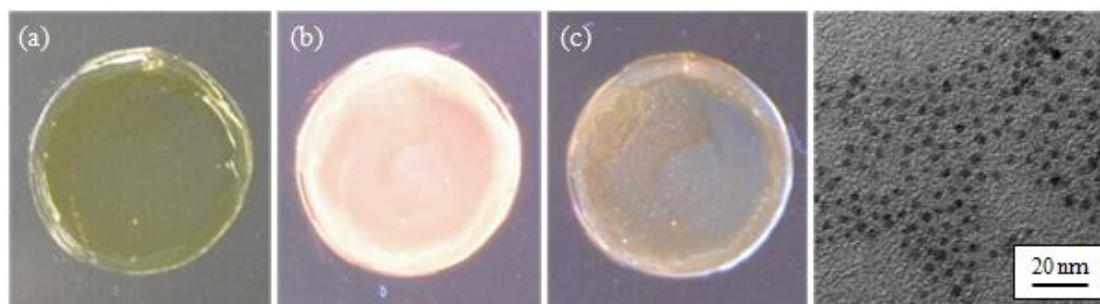
Figure 6.8 – Photographs of **D/C** on a hydrophobic, circular cover glass. (a) As prepared, without UV irradiation, (b) As prepared, under UV irradiation (λ_{ex} = 365 nm) and (c) Annealed at 150 °C for 20 h, then photographed at room temperature under UV irradiation (λ_{ex} = 365 nm). PL of **D/C** was almost completely quenched after annealing. (d) A TEM image of annealed **D/C**. The CdS cores were unaffected by the long annealing process.

To investigate such unusual quenching behaviour, UV/Visible absorption and PL spectra of the **D/C** film were recorded as a function of annealing temperature (T_a). The sample was annealed for one hour at each T_a, followed by rapid cooling to room temperature under an N$_2$ positive pressure in the dark. Thereafter the emission and absorption spectra were recorded in air at room temperature using a Hitachi F-2700

fluorescence spectrometer and a Hitachi U-3900 spectrometer (equipped with an integrating sphere), respectively. Performing the measurements at room temperature eliminated the possibility of thermal fluorescence quenching, which is regarded as electron trapping in temporary trapping sites generated at elevated temperatures. An initial T_a of 50 °C was chosen and was increased to 150 °C in 20 °C increments. The LC structures formed during annealing were preserved on cooling due to the high viscosity of the system. The resulting PL and absorption spectra are shown in Figures 6.9a and b, respectively. The spectra of the $P2_13$ structure, obtained after the long annealing at 150 °C, are also shown. The absorption spectra are normalised at 442 nm.
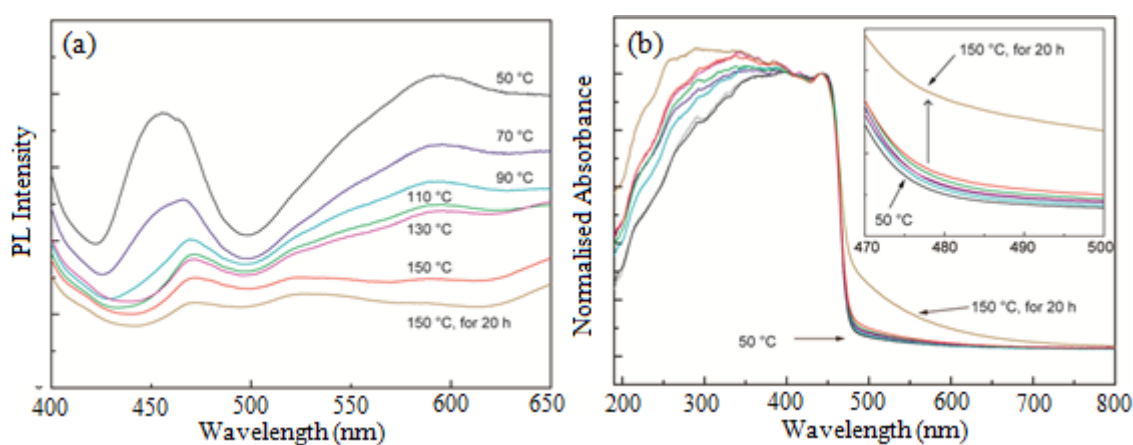

Figure 6.9 – (a) Annealing-temperature dependence of PL profiles of **D/C**. PL measurements were carried out after cooling to room temperature. (b) Normalised UV/Visible absorption spectra of annealed **D/C**. Inset: magnified between 470 to 500 nm. The line colours in (a), denoting annealing temperature, also apply in (b). The UV/Visible spectra are normalised at 442 nm because the absorption is derived from the CdS cores.

After annealing at 50 °C, **D/C** exhibited two strong emission peaks: the first corresponds to band-edge emission from two close energy levels at $\lambda = 450$ and 470 nm, the second is attributed to broad defect-trapped emissions ($\lambda \simeq 600$ nm). In the case of pure **C**, only band-edge emission at $\lambda = 450$ nm and broad defect-trapped ($\lambda \simeq 600$ nm) emission were observed, which is typical of CdS QDs [35] (see Appendix D). This suggests that the band-edge emission of **D/C** at $\lambda = 450$ nm arose solely from the CdS-QD cores. The band-edge emission at $\lambda = 470$ nm, only observed in **D/C**, may therefore be attributed to the formation of a new lower energy state, which will be referred to as the dendron-mediated extended state (DMES), henceforth. The exact origin of the

DMES is difficult to directly determine; however the 470nm peak is not observed before or after annealing when **D/C** is dispersed in CHCl$_3$ (see Appendix D). This suggests that the DMES arises from near-field interactions between neighbouring CdS cores, which are inherently dependent on the inter-QD spacing. In solution the QDs are mobile, hence no DMES, but in the film, the QDs are closely situated, with inter-particle distances controlled by the dendrons.

With increasing T_a, the peak intensity of the 450 nm band-edge emission of the **D/C** film significantly decreased; the peaks at 470 and 600 nm were also quenched but to a lesser extent (Figure 6.9a). Reduced PL intensity of defect-trapped emission can arise from quenching of band-edge emissions [36,37]. In contrast to the decreased emission, the absorbance of the **D/C** film was found to gradually increase with T_a, between λ=450-800 nm and < 350 nm (Figure 6.9b). Interestingly, the most drastic changes to both the absorption and emission spectra of **D/C** were observed after annealing the film at 150 °C for 20 hours; here the λ=450 nm band-edge emission is almost completely quenched and absorption between λ=450-800 nm increases considerably. It is under these conditions that the $P2_13$ LC structure is formed, suggesting that the new arrangement of the QD cores increases sample absorption, but simultaneously encourages non-radiative mechanisms of exciton de-excitation.

6.4.2 – Time-resolved PL Spectroscopy of D/C

To further investigate the exciton de-excitation mechanism, the emission lifetimes of the **D/C** film were measured by time-resolved PL spectroscopy using a frequency-doubled femto-pulse Al$_2$O$_3$:Ti laser source (384 nm, 125 nJ/cm^2 a pulse) and a streak camera detector. The lifetimes of the band-edge emission at 450 and 470 nm were determined by collecting the time-resolved PL decay of the **D/C** film (before and after annealing) in the spectral range between 445 to 455 nm and 465 to 475 nm, respectively (Figure 6.10). The decay curves were well fitted to a double exponential model, provided in Appendix D. According to these analyses [38,39], the initial lifetimes of the fast dominant component of the emissions were 43 ps for the 450 nm peak and 65 ps for the 470 nm peak. The lifetimes were virtually unchanged after 20 hours annealing at 150 °C and were calculated as 41 and 63 ps, respectively. The emission lifetimes of the **D/C** film were also examined after dissolving the long annealed film in CHCl$_3$ and re-casting the solution back onto glass, re-obtaining the amorphous film. After re-casting

the emission lifetimes were shorter: 32 ps for the 450 nm peak and 41 ps for the 470 nm peak.

To date, PL emission and quenching phenomena have been explained by a variety of mechanisms, such as energy transfer [40,41], thermal quenching [42], electron tunnelling [43], and charge transfer [44]. Emission lifetimes of several tens of pico-seconds in CdS QDs are recognised as recombination towards non-radiative centres, i.e. non-radiative relaxation, through energy transfer [39]. Thus, the lifetimes observed in the present system suggest that energy transfer is the predominant de-excitation mechanism in **D/C** films. The shorter emission lifetimes of the re-cast film, compared to those of the original film, indicate reduced efficiency of the ET process; the cause of this is currently unknown. The PL behaviour of the re-cast film will be revisited in later discussions.
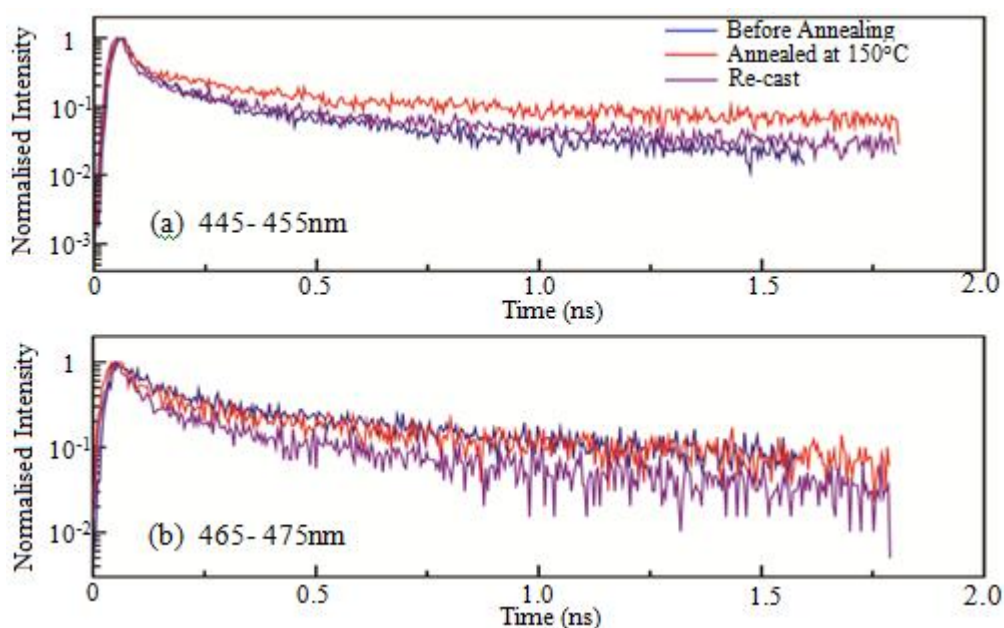

Figure 6.10 – Normalised time resolved PL decays of untreated, annealed, and re-cast **D/C** films in two spectral ranges: (a) 445-455 nm and (b) 465-475 nm. The decay curves can be well fitted to a double exponential model (see Appendix D). The line colour legend in (a) also applies to (b).

<u>6.4.3 – Proposed PL Quenching Mechanism of the $P2_13$ Structure</u>

In the previous sections is has been shown that PL emission is progressively quenched as the $P2_13$ structure becomes progressively more ordered; it has also been shown that the most likely de-exciton method of excitons in the **D/C** film is energy transfer (both before and after annealing). To explain this behaviour, we propose that the anisotropic distribution of the two ligand types, required to fill the inter-particle space in the $P2_13$ structure, enables the formation of long-range aromatic networks as depicted schematically (blue colour) in Figure 6.7a. As the $P2_13$ superlattice gradually forms, the dendrons begin to cluster in the interparticle voids, leading to increased aromatic π-stacking in the local environment of the QDs. The modified electronic state of the π-stacked aromatic moieties provides a non-radiative pathway for QD carrier de-excitation via energy transfer. The probability of PL emission from the sample is then proportional to the concentration of π-stacked moieties in the local vicinity of the QDs, which is in turn dependent on the degree of $P2_13$ order in the **D/C** film. Even when the film is initially cast (before annealing), the sample is likely to contain a base concentration of π- stacked moieties, hence the similar emission lifetimes before and after annealing. Amrutha *et al* [45] reports decreased PL intensity due to π-stacking in oligophenylenevinylene films. In their study, an increase in absorption intensity around 250 nm and > 500 nm was observed. This, in combination with our presents findings and other reports [46,47], strongly supports the hypothesis that the development of a π-stacked aromatic network, associated with formation of the $P2_13$ structure, plays a key role in the PL behaviour of **D/C**. This is discussed more quantitatively below.

Before annealing the **D/C** film, the band-gap energies (E_g's) resulting in PL emission at λ=450 nm and 470 nm were respectively calculated as 2.76 eV and 2.64 eV, using $E_g = 1240/\lambda$ (eV). The associated band structure before annealing (assuming no π-stacked moieties) can then be illustrated as shown in Figure 6.11a. The E_g of **D** was calculated as ~ 4 eV from the absorption spectra of pure **D** (Appendix D). In the absence of π-stacking, the much higher E_g of **D** restricts exciton recombination to radiative processes associated with the CdS cores (2.76 eV) and the dendron mediated extended state - DMES (2.64 eV). However, when a large concentration of π-stacked aromatic moieties inhabits the local environment of the QDs, as is proposed after annealing at 150 °C for 20 hours, the modified electronic state of the organic composition introduces a new E_g, with lower energy than that of the DMES. The E_g after long annealing, corresponding to

the π-stacked state, was calculated as 2.61 eV from the absorption edge in Figure 6.9b (see Appendix D for details). The band-edge structure in the presence of π-stacked moieties (i.e. after long annealing) is shown diagrammatically in Figure 6.11b. Here, the excitons transfer to energy levels permitted by the π-stacked moieties and recombine non-radiatively due to the narrower band gap.
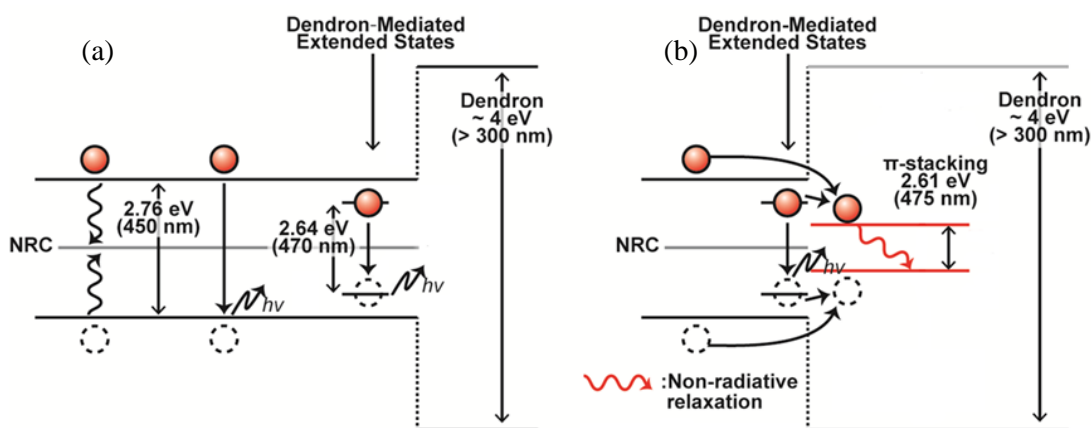

Figure 6.11 – Band gap diagrams of **D/C**. (a) Before annealing, the excitons recombine predominantly through radiative processes associated with the intrinsic QD band gap and the DMES. (b) After long annealing, an increased concentration of π-stacked aromatic moieties surrounds the QDs, increasing the likelihood of non-radiative recombination via energy transfer.

To confirm the above hypotheses regarding the quenching mechanism, the PL properties of **D/C** were explored after re-dissolving the long annealed film in $CHCl_3$. When in solution the previously quenched emission peak at $\simeq$450 nm returned and appeared similar to that observed in the initial solution of **D/C** (Appendix D). The reduced absolute peak intensity is likely a consequence of the re-dissolving process, i.e. it is probable that the initial dispersion contained a higher concentration of **D/C** than the solution containing the re-dissolved film. Following this result, the PL properties of the re-cast **D/C** film were investigated. First the **D/C** film was cast from solution onto quartz glass and annealed at 50 °C for one hour; the film was then annealed at 150 °C for 20 hours. Following this, the long annealed film was re-dissolved in $CHCl_3$ and re-applied to the substrate. As shown in Figures 6.12a and b the long annealing process quenched the PL emission and drastically increased the sample absorbance. However, when re-cast, the initial PL/absorbance properties were recovered. The film was annealed and re-cast three times and in all cases the PL/absorbance properties were

quenched by the long annealing process and recovered by re-casting (Appendix D). This result can only be explained as structure dependent PL/ absorbance behaviour: In all instances where the CdS cores are dispersed in solution, or deposited as an amorphous film, strong PL emission is observed. When the **D/C** film is annealed, its PL signal progressively reduces and is quenched almost entirely when the $P2_13$ structure is fully formed. Furthermore, the PL/absorbance properties of the **D/C** film return close to their original starting points when the $P2_13$ superlattice is destroyed. It should be noted however that after re-casting, the emission lifetimes became slightly shorter (450 nm: 32 ps, 470 nm: 41 ps) than those of the original un-annealed and annealed **D/C** film, indicating decreased ET efficiency.
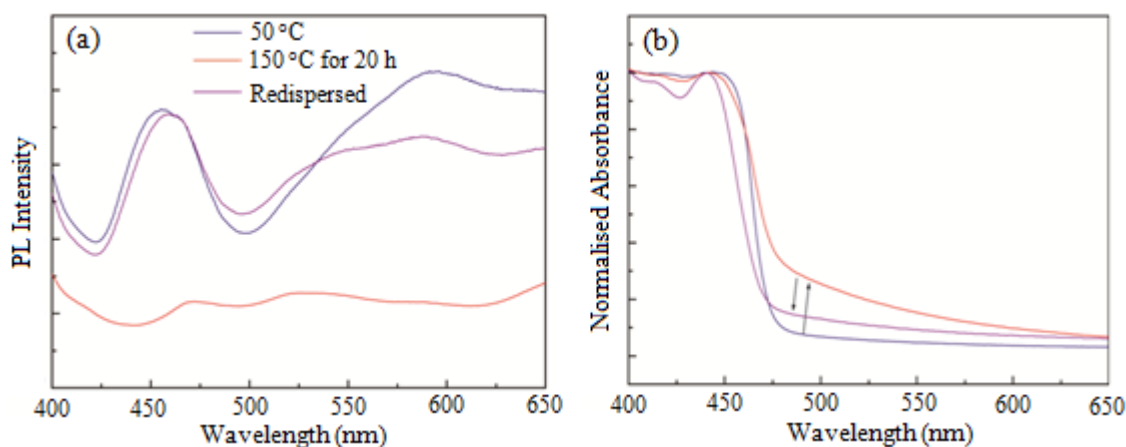
Figure 6.12 – Reversibility of PL and the corresponding absorbance spectra. (a) PL and (b) Normalised absorbance spectra of annealed and re-dispersed **D/C**. After re-dispersing into $CHCl_3$ and re-casting on glass substrate, the quenched PL intensity was recovered; the absorption spectra also became similar to that observed before annealing. The line colour legend in (a) also applies in (b).

6.5 – Summary

In summary, CdS quantum dots (QDs) encapsulated by a two-layer shell of thiols (layer 1) and dendrons (layer 2) were found to self-assemble into a new low-symmetry cubic liquid crystal (LC) phase. The annealing-induced transition from disorder to the cubic superlattice was accompanied by strong quenching of photoluminescence (PL). The most likely explanation of PL quenching inside the sample is exciton recombination via non-radiative energy transference with π-stacked aromatic moieties. π-stacking interactions are encouraged by the formation of the cubic structure, which requires an anisotropic surface organisation of ligands, hence dendron aggregation, to fill the large

inter-particle voids of the unit cell. To the author's knowledge, this is the first example of PL quenching of quantum dots, induced by supramolecular self-assembly. Incidentally, this work is the first report of a $P2_1 3$ cubic LC phase and is believed to be the first record of a nano-particle (NP) superlattice of such low symmetry. The principle applied here, i.e. embedding NPs in double-shell soft coronas, may enable creation of other novel NP and QD arrays. Furthermore, the radial *dV/dr* based model has been shown to provide a rational, semi-quantitative relationship between the density profile across the soft corona and the resulting superlattice. The observed PL behaviour offers the possibility of developing QD-based energy-conversion materials for application in emission enhanced photovoltaic cells, heat induced conduction and light emitting diodes.

References to Chapter 6

[1]   J. Y. Kim, O. Voznyy, D. Zhitomirsky, E. H. Sargent, *Adv. Mater.*, 2013, **25**, 4986.

[2]   T. Trindade, P. O'Brien, N. L. Pickett, *Chem. Mater.*, 2001, **13**, 3843.

[3]   M. L. Brongersma, Y. Cui, S. Fan, Nat. Mater., 2014, **13**, 451.

[4]   A. Kongkanand, K. Tvrdy, K. Takechi, M. Kuno, P. V. Kamat, (2008), J. Am. Chem. Soc., 2008, **130**, 4007.

[5]   S. Ren, L.-Y. Chang, S.-K. Lim , M. Smith, N. Zhao, V. Bulović, M. Bawendi, S. Gradecak, *Nano Lett.,* 2011, **11**, 3998.

[6]   D. A. Hines, P. V. Kamat, *ACS Appl. Mater. Interfaces*, 2014, **6**, 3041.

[7]   E. A. Chekhovich, M. N. Makhonin, A. I. Tartakovskii, A. Yacoby, H. Bluhm, K. C. Nowack, L. M. K. Vandersypen, *Nat. Mater.*, 2013, **12**, 494.

[8]   J. J. Urban, *Nat. Nanotechnol.*, 2015, **10**, 997.

[9]   R. Hull, J. Floro, J. Graham, J. Gray, M. Gherasimova, A. Portavoce, F. M. Ross, (2008). *Mater. Sci. Semicond. Process.*, 2008, **11**, 160.

[10]   G. Springholz, V. Holy, M. Pinczolits, G. Bauer, *Science*, 1998, **282**, 734.

[11]   J. Mirzaei, M. Reznikov, T. Hegmann, J. Mater. Chem., 2012, **22**, 22350.

[12]   A. L. Rodarte, Z. S. Nuno, B. H. Cao, R. J. Pandolfi, M. T. Quint, S. Ghosh, J. E. Hein, L. S. Hirst, *ChemPhysChem*, 2014, **15**, 1413.

[13]   A. L. Rodarte, R. J. Pandolfi, S. Ghosh, L. S. Hirst, *J. Mater. Chem. C*, (2013), *1*, 5527.

[14]   A. L. Rodarte, G. V. Shcherbatyuk, L. Shcherbatyuk, L. S. Hirst, S. Ghosh, *RSC Adv.*, 2012, **2**, 12759.

[15]   M. F. Prodanov, N. V. Pogorelova, A. P. Kryshtal, A. S. Klymchenko, Y. Mely, V. P. Semynozhenko, A. I. Krivoshey, Y. A. Reznikov, S. N. Yarmolenko, J. W. Goodby, V. V. Vashchenko, *Langmuir*, 2013, **29**, 9301.

[16]   M. Kumar, S. Kumar, *RSC Adv.*, 2015, **5**, 1262.

[17]   D. Yamamoto, T. Koshiyama, S. Watanabe, M. T. Miyahara, *Colloids and Surfaces A: Physicochem. Eng. Aspects*, 2015, **411**, 12.

[18]   B. I. Lemon, R. M. Crooks, *J. Am. Chem. Soc.*, 2000, **122**, 12886.

[19]   J. R. Lakowicz, I. Gryczynski, Z. Gryczynski, C. J. Murphy, *J. Phys. Chem. B*, 1999, **103**, 7613.

[20]   K. Kanie, M. Matsubara, X. B. Zeng, F. Liu, G. Ungar, H. Nakamura, A. Muramatsu, *J. Am. Chem. Soc*., 2012, **134**, 808.

[21]   M. Kanehara, H. Arakawa, T. Honda, M. Saruyama, T. Teranishi, (2012). *Chem. Eur. J.*, 2012, **18**, 9230.

[22]   A. C. Templeton, M. J. Hostetler, E. K. Warmoth, S. Chen, C. M. Hartshorn, V. M. Krishnamurthy, M. D. E. Forbes, R. W. Murray, *J. Am. Chem. Soc.*, 1998, **120**, 484.

[23]   M. Matsubara, A. Miyazaki, X. Zeng, A. Muramatsu, G. Ungar, K. Kanie, *Mol. Cryst. Liq. Cryst.*, 2015, **617**, 50.

[24]   T. Hahn (1996). International Tables of Crystallography Vol. A: Spacegroup Symmetry 4th ed. (Netherlands: Kluwer Academic).

[25]   X. Mang, X. B. Zeng, B. Tang, F. Liu, G. Ungar, R. Zhang, L. Cseh, G. H. Mehl, (2012). *J. Mater. Chem*., 2012, **22**, 11101.

[26]   G. Ungar, F. Liu, X. B. Zeng (2014). Thermotropic Cubic Liquid Crystal Phases, Other 3D Phases and Quasicrystals, Chap. 7 in "*Handbook of Liquid Crystals*", 2nd ed., Vol. 5, Goodby, J. W., Collings, P. J., Kato, T., Tschierske, C., Gleeson, H. F., Raynes, P., eds., Weinheim, Germany, Wiley-VCH Verlag GmbH) pp. 363-436.

[27]   G. Ungar, X. B. Zeng, *Soft Matter*, 2005, **1**, 95.

[28]   Y. Y. Li, S. T. Lin, W. A. Goddard III, *J. Am. Chem. Soc.*, 2004, **126**, 1872.

[29]   Frank, F. C., Kasper, J. S. (1959). Acta Crystallogr. *12*, 483.

[30]   S. Hajiw, B. Pansu, J. F. Sadoc, *ACS Nano*, **8**, 2015, 8116.

[31]   A. K. Sinha (1972). "*Topologically Closed Packed Structures in Transition Metal Alloys*". Oxford, Pergamon Press.

[32]   M. Wojcik, M. Kolpaczynska, D. Pociecha, J. Mieczkowski, E. Gorecka, *Soft Matter*, 2010, **6**, 5397.

[33] G. Ungar, Y. Liu, X. B. Zeng, V. Percec, W.-D. Cho, *Science*, 2003, **299**, 1208.

[34] X. Liu, M. Yu, H. Kim, M. Mameli, F. Stellacci, *Nat. Commun.*, 2012, **3**, 1182.

[35] J. Ouyang, J. Kuijper, S. Brot, D. Kingston, X. Wu, D. M. Leek, M. Z. Hu, J. A. Ripmeester, K. Yu, *J. Phys. Chem. C*, 2009, **113**, 7579.

[36] M. O'Neil, J. Marohn, G. McLendon, *Chem. Phys. Lett.*, 1990, **168**, 208.

[37] A. Veamatahau, B. Jiang, T. Seifert, S. Makuta, K. Latham, M. Kanehara, T. Teranishi, Y. Tachibana, *Phys. Chem. Chem. Phys.*, 2015, **17**, 2850.

[38] J. Z. Zhang, R. H. O'Neil, T. W. Roberti, *Appl. Phys. Lett.*, 1994, **64**, 1989.

[39] D. A. Wheeler, J. Z. Zhang, *Adv. Mater.*, 2013, **25**, 2878.

[40] I. Medintz, N. Hildebrandt (2013). "*FRET - Förster Resonance Energy Transfer From Theory to Applications*". Weinheim, Germany:Wiley-VCH Verlag GmbH.

[41] K. E. Sapsford, L. Berti, I. L. Medintz, *Angew. Chem. Int. Ed.*, 2006, **45**, 4562.

[42] D. Valerini, A. Cretí, M. Lomascolo, *Phys. Rev. B*, 2005, **71**, 235409.

[43] E. I. Zen'kevich, Th. Blaudeck, M. Heidernätsch, F. Cichos, C. von Borczyskowski, *Theor. Exp. Chem.*, 2009, **45**, 23-34.

[44] W. R. Algar, M. H. Stewart, A. M. Scott, W. J. Moon, I. L. Medintz, *J. Mater. Chem. B*, 2014, **2**, 7816.

[45] S. R. Amrutha, M. Jayakannan, *J. Phys. Chem. B*, 2008, **112**, 1119.

[46] B. Valeur, M. N. Berberan-Santos, (2012). "*Molecular Fluorescence: Principles and Applications*", 2nd ed., Wiley-VCH.

[47] Y. Hong, J. W. Y. Lama, B. Z. Tang, *Chem. Commun.*, 2009, **29**, 4332.

Conclusions and Future Work

The primary aim of this project was to investigate the internal structure of the bulk N_{tb} phase and provide empirical evidence relating to phase chirality, the intermolecular packing behaviour and the order parameters of the phase. At the outset of the project this information was missing in current work; however during the closing stages, phase chirality was unambiguously identified elsewhere by resonant X-ray scattering (RXS) at the carbon absorption edge. Nevertheless, the RXS investigation presented in this thesis, on a selenium-labelled mixture of bent dimer molecules, allowed a much deeper exploration of the N_{tb} structure. In addition to sharp resonant Bragg reflections, arising from a temperature dependent helical pitch length between 9 and 12 nm, the broad peaks at higher q, relating to intermolecular packing, were simultaneously investigated. With the aid of magnetic sample alignment, this enabled the first oriented and complete diffraction pattern of the N_{tb} phase to be obtained. Using the new information, inaccessible to carbon RXS, the first estimations of the coherent helical domain sizes were made and it was also shown that two order parameters are required to quantify the orientational order in the N_{tb} phase. Moreover it was shown here for the first time that the orientational order parameter of the global helical axis can reach a value close to 1. Based on these new findings, the current model of the N_{tb} phase was quantitatively reconstructed and has now been adapted to consider the local-packing arrangement of the molecules.

Small angle X-ray investigations of the N_{tb} phase in a series of dimer homologues with varying spacer chain length, have suggested that there are two different local layering styles in the N_{tb} phase. It was also hypothesised that the layering style is selected depending on the molecular composition. In compounds with short spacer molecules, the dimers are locally layered, but when the spacer chain becomes comparable to the added length of the two terminal chains, there is no energetic incentive for the dimers to separate and they form intercalated local layers. This hypothesis can also explain the reducing enthalpy of the nematic (N)-N_{tb} transition with increasing spacer length. These are the first findings to suggest varying N_{tb} local structure, but at the present time the evidence is only qualitative. In future this hypothesis should be explored using dynamic simulation, starting from an intercalated state and performing energy minimisation

calculations. If the simulation is performed for both short and long spacer molecules, one could see how the dimers choose to re-organise in each case.

The first circular dichroism experiments on the N_{tb} phase were performed in the same dimer series mentioned above. The findings confirm chirality in the N_{tb} phase, but also enable one to quantify the rotational strength of the phase, providing that the sample thickness is known. The findings also suggest that a single handedness is dominant in each sample. CD may therefore be a much simpler and time effective alternative to cumbersome RXS investigations of the bulk N_{tb} phase, but at the cost of losing information about the pitch length. The method reported here is also limited by the fact that near perfect homeotropic sample alignment is required, which may not be achievable in all sample types. In future this process should be refined with in situ microscopy studies and also a method of directly determining the cell gap thickness, without lucky resonant effects. In the context of this work, further CD experiments will be performed in the near future on DTC5C5 and DTC5C11. The cell gaps will be determined and compared with DTC5C7 and DTC5C9 so that the rotational strength of the N_{tb} phase can be found as a function of spacer length. It would also be beneficial to perform carbon RXS experiments on each of the four compounds, to see how the rotational strength can be related to the pitch length in the N_{tb} phase.

Orientational order in the N_{tb} phase was further investigated in a re-synthesised copolyether. The first polarised IR experiments on the N_{tb} phase were conducted, which suggested a helical chain conformation, in-line with the N_{tb} model proposed in Chapter 3 for liquid crystal dimers. Orientational modulation along the helical axis in a highly aligned thin film led to observation of a four-point wide angle X-ray scattering pattern. From the azimuthal peak separation, the average tilt angle of the polymer chain axis, in respect to the helical axis could be directly determined. Using the known average conical angle, each component of the two part order parameter (suggested in Chapter 3) could be separated. Furthermore the N-N_{tb} transition in the copolymer appeared almost identical to that observed in liquid crystal dimers. In future the copolymer should be investigated by resonance X-ray scattering so that the pitch length can be determined. This would then enable other key parameters of the chain conformation to be calculated, namely the average bend and twist angles between mesogens.

Over the course of the project the lower temperature lamellar phases of the N_{tb} phase were investigated in systems of bent dimer molecules. In the Se-labelled mixture, a B6 type banana phase was observed with an intercalated dimer layering style. However from the perspective of the individual mesogens, the phase is effectively a smectic C (SmC). In the dimer homologue series, two different modulated smectic phases were observed: 'X' and 'Y' type. The X phase was found to possess a centred rectangular structure analogous to the B1 banana phase, with an optically biaxial, interlocking double layering style. The shifting structure is believed to arise from polarisation splay of the molecular bend as described by Coleman *et al* [1,2]. This is contrary to current work on the X phase, which claims that the phase possesses an oblique unit cell [3]. Furthermore, the X phase may in fact be the first experimental example of the $SmCPU_{A'}$ phase, theoretically predicted by Coleman *et al* [2] in 2008. In order to confirm this hypothesis, freeze fracture TEM measurements are required to see if the phase is locally undulated as expected. Moreover the orientation of the shifted block in the centred rectangular unit cell is currently unknown. In future electronic studies will be performed on the DTC5C5 sample, as it is the only compound to exhibit a stable X phase. Such studies will enable the presence or absence of ferroelectricity, which will in turn allow the orientation of the shifted block to be determined. The structure of the Y phase is yet to be identified, but this investigation is still ongoing.

The secondary objective of this project was to identify and characterise the unknown structure of an annealed dendronised quantum dot material and explain the strange fluorescence quenching properties observed by collaborators. The structure was found to possess a low symmetry cubic unit cell, representing the first $P2_13$ LC phase and also the lowest symmetry 3D self-assembled NP array reported to date. Formation of this structure can be explained using a semi-quantitative radial density model of the QD and the two layer shell of organic molecules. According to this model, a two layer shell of long and short 'bristles' prefers to adopt an anisotropic radial profile, enabling the long dendrons to fill large inter-particle voids of the unit cell. This provides strong evidence of ligand re-organisation/dendron aggregation on functionalised NP surfaces. Moreover the progressive dendron aggregation with annealing time is believed to be the root of the fluorescence quenching phenomenon. Prior to annealing the dendrons are randomly distributed in the amorphous material; however, with annealing the dendrons being to redistribute and cluster into the inter particle voids of the self-assembling structure. The

increased concentration of dendrons in the highly local vicinity of the QDs encourages pi-stacking interactions among the aromatic moieties. The altered electronic state of the organic molecules then enables exciton de-excitations via non-radiative energy transfer. This is supported by fluorescence lifetime measurements, which show that the most likely method of de-excitation is energy transfer. This work is the first known example of self-assembly induced emission quenching and is an important advance towards photovoltaic applications which favour 'high light absorption, low re-emission' properties, such as solar cells. In future it would be interesting to synthesise more double shelled NPs to see if altering the ligand density and composition would enable more unusual 3D arrays to be created.

[1]   D. A. Coleman, J. Fernsler, N. Chattham, M. Nakata, Y. Takanishi, E. KOrblova, D. R. Link, R. F. Shao, W. G. Jang, J. E. Maclennan, O. Mondainn-Monval, C. Boyer, W. Weissflog, G. Pelzl, L. C. Chien, J. Zasadzinski, J. Wantanabe, D. M. Walba, H. Takezoe, N. A. Clark, *Science*, 2003, **301**, 1204.

[2]   D. A. Coleman, C. D. Jones, M. Nakata, N. A. Clarke, D. M. Walba, W. Wiessflog, K. Fodor-Csorba, J.Wantanabe, V. Novotna, V. Hamplova, *Phys. Rev. E*, 2008, **77**, 021703.

[3]   N. Sebastián, M. G. Tamba, R. Stannarius, M. R. de la Fuente, M. Salamonczyk, G. Cukrov, J. Gleeson, S. Sprunt, A. Jákli, C. Welch, Z. Ahmed, G. H. Mehl, A. Eremin, *Phys. Chem. Chem Phys.*, 2016, **18**, 19299.

Publications and Conferences

Publications:

[1]   W. D. Stevenson, Z. Ahmed, X. B. Zeng, C. Welch, G. Ungar, G. H. Mehl: "*Molecular organization in the twist-bend nematic phase by resonant X-ray scattering at the Se K edge and by SAXS, WAXS and GIXRD*". *Phys. Chem. Chem. Phys*., 2017, **19**, 13449.

[2]   M. Matsubara, W. Stevenson, J. Yabuki, X. B. Zeng, H. Dong, K. Kojima, S. F. Chichibu, K. Tamada, A. Muramatsu, G. Ungar, K. Kanie: "*A Low Symmetry Cubic Mesophase of Dendronized CdS Nanoparticles and their Structure Dependent Photoluminescence*". *Chem*, 2017, **2**, 860.

Conferences:

[1]   W. Stevenson, X. B. Zeng, G. Ungar, K. Kanie, M. Matsubara: "*Dendronized CdS Quantum Dots: Cubic with a Twist!*", British Liquid Crystal Society Annual Conference, University of Durham, 2014.

[**2**]   W. Stevenson, X. B. Zeng, G. Ungar, K. Kanie, M. Matsubara: "*A P2$_1$3 Arrangement of Dendronized CdS Quantum Dots*", British Liquid Crystal Society Annual Conference, University of Sheffield, 2015.

[3]   W. Stevenson, Z. Ahmed, X. B. Zeng, G. Ungar, Georg Mehl: "*A c2mm Liquid Crystal Phase Formed by Dimer Molecules*", British Liquid Crystal Society Annual Conference, University of Edinburgh, 2016.

[4]   W. Stevenson, J. An, X. Mie, X. B. Zeng, G. Ungar: "*Nx Phase in Polyethers based on Diphenylethane*", Twist-Bend Nematic Workshop, University of Southampton, 2016.

Appendix A

A1 – Synthesis of DTSe

The Se-labelled compound DTSe was synthesised entirely by the organic chemistry group at the University of Hull, UK, led by Professor Georg Mehl. The four step synthetic process is shown diagrammatically in Figure A1 below. The details of each step are provided in the appropriate sub-section. Spectroscopic information is also listed.

Starting reagents and solvents were purchased from Fischer, Sigma Aldrich, Acros Organics and Fluorochem and used without further purification. Boronic acids were purchased from Kingston chemicals and were also used without further purification.

The structures after purification were confirmed by ^{1}H and ^{13}C nuclear magnetic resonance spectroscopy. The experiments were performed with a Joel JNM-ECP 400 MHz FT-NMR. The chemical shifts reported in this section are relative to tetramethylsilane used as an internal standard and coupling constants J are reported in Hertz (Hz). ^{1}H experiments were performed at 400 MHz, ^{13}C at 100 MHz and ^{19}F 376 MHz.

Low resolution electron ionisation (EI), electro-spray (ES), chemical ionisation (CI), matrix assisted laser deposition ionisation (MALDI) and high resolution mass spectrometry (HRMS) were obtained via the EPSRC National Mass Spectrometry Service Centre at Swansea University, Wales.

The purity of the final compounds was confirmed by high performance liquid chromatography. The HPLC setup consisted of Gilson 321 pump, Agilent/HP1100 detector with a Phenomex LUNA 18(2) reverse phase C18 column. The column dimensions are 250 mm x 4.6 mm, 5 μm particles and 100 Å pore size.
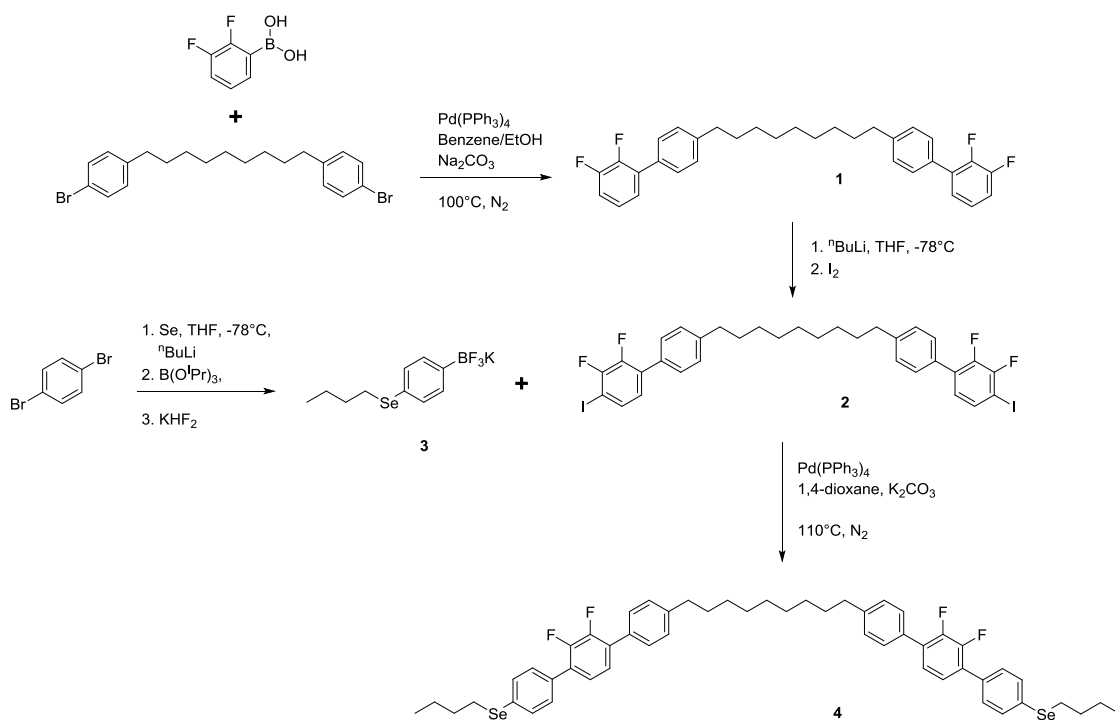
Figure A1 – The Four step Synthesis of the Se-labelled compound DTSe (compound 4).

Compound (1): 1,9-bis(2',3'-difluoro-[1,1'-biphenyl]-4-yl)nonane

A stirred solution of 1,9-bis(4-bromophenyl)nonane (0.82 g, 1.9 mmol) and Pd(PPh$_3$)$_4$ (79 mg, 0.07 mmol, 4 mol%) in benzene (15 mL) were added to a solution of sodium carbonate (2M, 15mL) under nitrogen atmosphere. Nitrogen gas was bubbled through the resulting two-phase mixture for 10 minutes and then a solution of (2,3-difluorophenyl) boronic acid (0.77 g, 4.9 mmol) in ethanol (15 mL) was added. The reaction was heated under reflux conditions to 100 °C for 15 hours. After cooling to ambient temperature, diethyl ether (150 mL) and water (100 mL) were added to the mixture. The separated organics were then washed with water (2x100 mL) and dried over MgSO$_4$(s). After removal of the dessicant by filtration, the solvent was concentrated in vacuo and the product isolated by column chromatography (Silica gel, eluent: hexane/CH$_2$Cl$_2$, 9:1). Yield 0.79 g, 84%.

δ_H(400MHz; CD$_2$Cl$_2$) δ 7.48-7.40 (m, 4H), 7.27 (d, ^3J=8.4Hz, 4H), 7.23-7.06 (m, 6H), 2.64 (t, ^3J=7.8Hz, 4H), 1.63 (q, J = 7.4 Hz, 4H), 1.43-1.25 (m, 10H)

δ_C(100MHz; CD_2Cl_2) δ 151.58 (dd, ^1J(C-F) = 247 Hz, ^2J(C-F) = 13.8 Hz), 148.41 (dd, ^1J(C-F) = 248 Hz, ^2J(C-F) = 13.1 Hz), 143.75 (s), 132.31 (d, J(C-F) = 2.3 Hz), 131.69 (d, J(C-F) = 10.0 Hz), 129.16 (d, J(C-F) = 3.1 Hz), 129.06 (s), 125.78-125.72 (m), 124.54 (dd, J(C-F) = 7.7 Hz, 4.6 Hz), 116.07 (d, J(C-F) = 17.7 Hz), 36.05 (s), 31.88 (s), 29.94 (s), 29.91 (s), 29.76 (s)

δ_F(376MHz; CD_2Cl_2) -139.09 (dt, ^3J(F-F) = 20.8 Hz, ^4J(F-H) = 6.9 Hz), -144.75 (dd, ^3J(F-F) = 20.8 Hz, ^4J(F-H) = 4.6 Hz)

Compound (2): 1,9-bis(2',3'-difluoro-4'-iodo-[1,1'-biphenyl]-4-yl)nonane
Compound (1) (0.67 g, 1.3 mmol) was dissolved in anhydrous THF (15 mL) under a dry N_2 atmosphere and the solution was cooled to -78°C. ^{n}BuLi (1.6 M, 1.83 mL, 2.9 mmol) was added dropwise and (after the addition) the reaction was left to stir for 1 hour at -78 °C. A solution of iodine (0.74 g, 2.9 mmol) in anhydrous THF (15 mL) was then added. The reaction was stirred for 16 hours, slowly rising to ambient temperature. Water (100 mL) and diethyl ether (100 mL) were added to separate the organics, which were then washed successively with brine (50 mL) and $Na_2S_2O_3$(aq) (saturated solution, 100 mL). The organic layer was separated and dried over $MgSO_4$(s). After removal of the dessicant by filtration the solvents were concentrated to leave a yellow residue which quickly solidified. The pure product was obtained by re-crystallisation from ethanol.

δ_H(400MHz; CD_2Cl_2) 7.54 (ddd, ^3J = 8.4 Hz, ^4J(H-F) = 5.7 Hz, ^5J(H-F) = 2.0 Hz, 2H), 7.42 (dd, ^3J = 8.3 Hz, ^4J =1.8 Hz, 4H), 7.26 (d, ^3J = 8.4 Hz, 4H), 7.03-6.96 (m, 2H), 2.63 (t, J = 7.8 Hz, 4H), 1.69-1.57 (m, 4H), 1.39-1.27 (m, 10H)

δ_C(100MHz; CD_2Cl_2) 151.47 (dd, ^1J(C-F) = 244.5 Hz, ^2J(C-F) = 14.6 Hz), 147.84 (dd, ^1J(C-F) = 252.9 Hz, ^2J(C-F) = 14.6 Hz), 144.12 (s), 133.72 (d, J(C-F) = 3.8 Hz), 131.97 (d, J(C-F) = 10.8 Hz), 131.53 (br s), 129.12 (s), 128.96 (d, J(C-F) = 3.1 Hz), 126.89 (m), 80.23 (d, ^2J(C-F) = 23.1 Hz), 35.69 (s), 31.77 (s), 29.83 (s), 29.80 (s), 29.65 (s)

δ_F(376MHz; CD_2Cl_2) -117.92 (dd, ^3J(F-F) = 20.8 Hz, ^4J(F-H) = 4.6 Hz), -140.06 (dd, ^3J(F-F) = 20.8 Hz, ^4J(F-H) = 6.9 Hz)

MS (EI) *m/z* 756.0 (M)[+]

HRMS : calculated for $C_{33}H_{30}F_4I_2$: 756.0373, found 756.0373

Compound (3): Potassium 4-(Butylselanyl)phenyltrifluoroborate

A solution of 1,4-dibromobenzene (2.36 g, 10 mmol) and selenium powder (0.79 g, 10 mmol) in anhydrous THF (60 mL) was cooled to -78 °C in a nitrogen atmosphere. [n]BuLi (2.2 M in cyclohexane, 4.5 mL, 10 mmol) was added dropwise and the reaction was warmed to 0°C over a period of 30 minutes. After the reaction mixture was clear, triisopropyl borate (1.88 g, 2.31 mL, 10 mmol) was added (at 0 °C) and the reaction mixture was re-cooled to -78 °C. [n]BuLi (2.2 M in cyclohexane, 4.5 mL, 10 mmol) was then slowly added. After 10 minutes at -78 °C the temperature was raised to -10 °C and the reaction was stirred at this temperature for 40 minutes. The reaction mixture was quenched with KHF_2(aq) (1N, 25 mL, 25 mmol) and then warmed to room temperature. After stirring for 15 minutes, the suspension was concentrated and the residual solid was dissolved in dry acetone (80 mL). The insoluble salts were filtered off and the resulting organic solution was concentrated to leave a solid. This was dissolved in acetone (70 mL) and diethyl ether (70 mL) and precipitated to produce an off-white solid, 1.64g, 51%

δ_H(400MHz; $(CD_3)_2CO$) 7.41 (d, ^3J = 7.7 Hz, 2H), 7.26 (d, ^3J = 7.6 Hz, 2H), 2.82 (t, ^3J = 7.3 Hz, 2H), 1.62 (m, 2H), 1.40 (m, 2H), 0.87 (t, ^3J = 7.3 Hz, 3H)

δ_C(100MHz; $(CD_3)_2CO$) 133.42, 132.07, 126.78, 33.17, 27.88, 23.46, 13.82

δ_F(376MHz; $(CD_3)_2CO$) -142.54

δ_B(128 MHz; $(CD_3)_2CO$) 2.69

MS (NSI) *m/z* 274.03 (M-K)[-]

HRMS : calculated for $C_{10}H_{13}{}^{10}BF_3{}^{74}Se$: 274.0329, found 274.0335

Compound (4): 1,9-bis(4''-(butylselanyl)-2',3'-difluoro-[1,1':4',1''-terphenyl]-4-yl)nonane

Pd(PPh$_3$)$_4$ (28 mg, 0.02 mmol, 6 mol%) and K$_2$CO$_3$ (0.33 g, 2.4 mmol) were added to a mixture of (**2**) (0.3 g, 0.4 mmol) and (3) (0.25 g, 0.8 mmol) dissolved in 1,4-dioxane (32 mL) and water (8 mL). Nitrogen gas was bubbled through the mixture for 10 minutes and the reaction was subsequently heated to 110 °C for 15 hours under an N$_2$ atmosphere. After cooling to ambient temperature, the organics were separated by adding diethyl ether (150 mL) and water (100 mL). The organics were washed with water (2x100 mL) and dried over MgSO$_4$(s). After removal of the dessicant by filtration, the solvent was concentrated in vacuo and the product isolated by column chromatography (Silica gel, eluent: hexane/CH$_2$Cl$_2$, 8:2). Yield 0.25 g, 68%.

δ_H(400MHz; CD$_2$Cl$_2$) 7.58-7.54 (m, 4H), 7.52-7.46 (m, 8H), 7.30 (d, ^{3}J = 8.2 Hz, 4H), 7.28-7.26 (m, 4H), 2.99 (t, ^{3}J = 7.3 Hz, 4H), 2.67 (t, ^{3}J = 7.6 Hz, 4H), 1.77-1.61 (m, 8H), 1.51-1.29 (m, 14H), 0.93 (t, ^{3}J = 7.3 Hz, 6H)

δ_C(100MHz; CD$_2$Cl$_2$) 148.93 (dd, ^{1}J = 249.8Hz, ^{2}J = 15.4Hz), 148.75 (dd, ^{1}J = 249.8 Hz, ^{2}J = 15.4 Hz), 143.85 (s), 133.04 (s), 132.20 (s), 132.00 (s), 130.22 (dd, J(C-F) = 8.5 Hz, 2.3 Hz), 129.68 (s), 129.30-129.19 (m), 129.12 (s), 129.04 (br s), 125.24-125.17 (m), 124.97-124.90 (m), 36.03 (s), 32.64 (s), 31.85 (s), 29.86 (s), 29.83 (s), 29.69 (s), 27.67 (s), 23.39 (s), 13.73 (s)

δ_F(376MHz; CD$_2$Cl$_2$) -143.92 (s)

MS (EI) *m/z* 928.1 (M)$^+$

A2 – Synthesis of DTC5C7

The compound DTC5C7 was synthesised entirely by the organic chemistry group at the University of Hull, UK, led by Professor Georg Mehl. The four step synthetic process is shown diagrammatically in Figure A2 below. The details of each step are provided in the appropriate sub-section. Spectroscopic information is also listed.
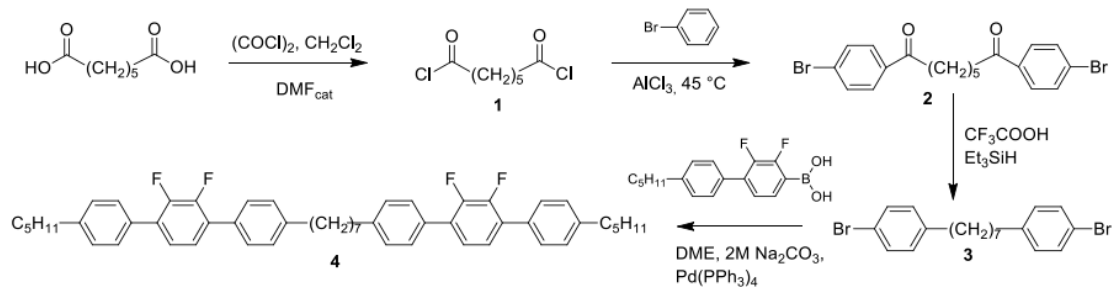
Figure A2 – Four step synthesis of DTC5C7 (compound 4).

Compound (1): Heptanedioyl dichloride (1)

Heptanedioic acid (14.4 g, 0.09 mol) was dissolved in dry dichloromethane (200 ml) under nitrogen. Oxalyl chloride (30 ml, 44.3 g, 0.35 mol) was added followed by dry N, N'-dimethylformamide (1 drop) and gentle stirring. The nitrogen supply was turned off and the reaction was monitored by the evolution of gas. The reaction was stirred overnight and then refluxed for 2 hours until gas evolution had ceased. The solution was evaporated by vacuum distillation to yield crude nonanedioyl dichloride which was used immediately in the Friedel-Crafts acylation described below. Due to the instability of acyl chlorides the crude product was used immediately; no NMR spectra were recorded.

Compound (2): 1,7 -bis(4-bromophenyl)heptane-1,5-dione

Bromobenzene (50 ml, 37.4. g, 0.24 mol) was added to powdered aluminium chloride (12.5 g, 0.094 mol) and rapidly stirred under nitrogen for 1 hour. The crude heptanedioyl dichloride was dissolved in bromobenzene (15ml, 22.4. g, 0. 143 mol) and was added dropwise over a period of one hour. The temperature of the reaction was maintained below 45 °C during the addition. The reaction mixture was maintained at 40 °C and stirred overnight. The reaction was allowed to cool to ambient temperature and poured into a solution of concentrated hydrochloric acid (150 ml) in ice water (600 ml). A small portion of dichloromethane was added to dissolve the suspended solids. The aqueous layer was extracted with dichloromethane several times and the organic extracts were dried over magnesium sulphate with rapid stirring overnight. The dichloromethane was evaporated under reduced pressure. The crude solid was re-crystallised from ethanol four times to yield 1,5-bis-(4-bromophenyl)heptane-1,7-dione. The yield was found to be 9.2 g, 42 %. 1 H NMR (400 MHz ,CDCl3, J/Hz): δ 7.81 (4H, d, J = 8.6); 7.59 (4H, d, J = 8.6); 2.92 (4H, t, J = 7.3); 1.69-1.76 (4H, m); 1.42-1.35 (2H, m).

Compound (3): 1,7-bis-(4-bromophenyl)nonane

1,5-Bis-(4-bromophenyl)heptane-1,5- dione (4.4 g , 0.01 mol) was dissolved in trifluoroacetic acid (30.75 ml , 45.79 g , 0.40 mol). Triethylsilane (8.3 ml, 6.05 g, 0.05 mol) was added dropwise over a period of one hour with rapid stirring and cooling in a water bath. The reaction mixture became turbid white after 1 hour. The reaction was stirred at ambient temperature for 48 hours. The reaction mixture was poured into a mixture of ice and water. Hexane was added and the aqueous layer was extracted in hexane four times. The organic extracts were combined and were dried over magnesium sulphate overnight. The solvent was then evaporated. The crude product was separated by column (silica) chromatography and yielded 1,5-bis-(4-bromophenyl)heptane. The mobile phase was a hexane/dichloromethane gradient starting with pure hexane finishing at 35% dichloromethane. The yield was found to be 1.56 g, 38.1% 1 H NMR (400 MHz, CDCl3, J/Hz): δ 7.38 (4H, d, J = 8.4); 7.04 (4H, d, J = 8.6); 2.55 (4H, t, J = 7.7); 1.53-1.61 (4H, m); 1.24-1.35 (6H, m).

Compound (4): 1,7-bis(2',3'-difluoro-4''-pentyl-[1,1':4',1''-terphenyl]-4-yl)heptanes

A solution of 1,5-bis-(4-bromophenyl)heptane (0.5 g, 0.012 mol) and (2,3-difluoro-4'-pentyl- [1,1'-biphenyl]-4-yl)boronic acid (1.0 g, 0.03 mol) in a mixture of 1,2-dimethoxyethane (12 ml) and saturated aqueous solution of sodium hydrogen carbonate (18 ml) was thoroughly degassed with argon for 1 hour. Tetrakis(triphenylphosphine)palladium(0) 50 mg was added. The reaction was refluxed at 125 °C for 12 hours under stirring. The reaction was allowed to cool to room temperature. Water was added to the reaction. The aqueous solution was extracted with dichloromethane four times and dried over magnesium sulphate overnight. The solvent was evaporated and the crude product was separated by column chromatography and yielded 1,5-bis(2',3'-difluoro-4''-pentyl-[1,1':4',1''-terphenyl]-4-yl)nonane. The mobile phase was a hexane/dichloromethane gradient starting with pure hexane, finishing at 50% dichloromethane. The yield was found to be 0.60 g, 68 %. 1 H NMR (400 MHz ,CDCl3, J/Hz,); δ: 7.50 (8H, d, J = 8.0); 7.28 (4H, d, J = 8.0); 7.22 (4H, m); 2.64 (8H, t, J = 8.0); 1.62-1.70 (8H, m); 1.39-1.38 (14H, m); 0.91 (6H, t, J = 7.1). 13C NMR (100 MHz, CDCl3);δC: 148.5 , 143.1, 143.0, 132.0, 131.9, 129.5, 128.71, 128,68, 124.6, 35.7, 31.6, 31.3, 31.1, 29.3, 29.2, 22.6, 14.0.

A3 – Spacer Torsion Simulations

Molecular modelling was carried out to show how a smaller bend angle (ϕ), between the two mesogenic arms of a dimer molecule, can be achieved by changing the C-C torsion angles in the spacer. The energy costs associated with such changes of torsion angles in the spacer were also explored. The simulation was performed by Dr Xiangbing Zeng, University of Sheffield.

The modelling of the molecules was carried out using Materials Studio (BIOVIA). The conformations of the ($-C_7H_{14}-$) spacer were studied, starting from the all-trans conformation where all six torsion angles in the spacer are $\gamma = 180$ °. Assuming that the spacer is always helical, the six torsion angles are kept to the same value of γ, changing from 180 ° to 150 ° with 5 ° steps. The bend angle ϕ is measured for each torsion angle (Figure A3) and listed in Table A1. The energies of the spacer in different conformations were also calculated, using Universal Forcefield calculations and compared in Table A2. According to Tables A1 and A2, the ideal torsion angle should be around 160 ° as the experimentally measured bend angle ϕ from X-ray studies is around 29 °. Even though the energy involved in such a conformational change from the all-trans state seems to be high, ~9.8 kcal/mol, it is an over-estimation as the many other spacer conformations that achieve the same bend angle have not been considered. A high energy conformational state could in fact be stabilised by the high entropy of the spacer.

Table A1 – The bend angle ϕ of a dimer as a function of torsion angles γ adopted by the spacer.

γ (°)	ϕ (°)
180	56.1
175	54.0
170	48.4
165	39.3
160	29.6
155	14.9
150	1.4

Table A2 – Energy Estimation of Spacer ($-C_7H_{14}-$) with Different Torsion Angles γ.

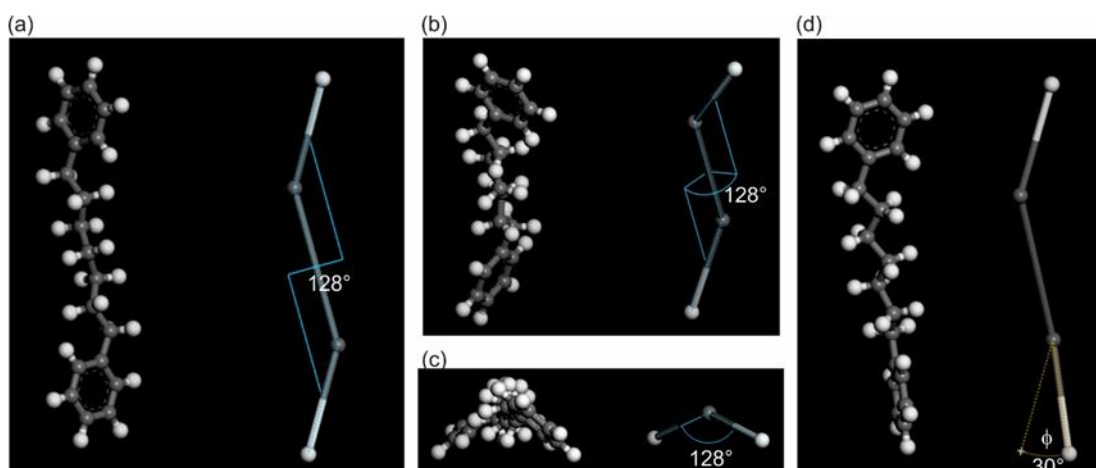| γ (°)	Total (kcal/mol)	Valence (kcal/mol)	Non-Bond (kcal/mol)
180	3.997	1.248	2.750
175	4.359	1.463	2.896
170	5.444	2.096	3.348
165	7.250	3.106	4.144
160	9.755	4.423	5.332
155	12.941	5.952	6.989
150	16.880	7.604	9.276

Figure A3 – The molecular model of DTC5C7 with torsion angles in the spacer $\gamma =$ 160 °. For simplicity only the spacer and the two phenyl rings directly connected to the spacer are shown. To show the molecular geometry more clearly a rod model of the molecule is shown on the right hand side, where the C-C bond represents the spacer, and C-H bonds the mesogens. (a-c) The dihedral angle of the two mesogens around the spacer is measured to be 128 °. (a) View when the spacer is parallel to the paper; (b) tilted view, (c) view along the spacer. (d) The bend angle ϕ of the dimer, i.e. the angle between the two mesogens, is measured to be 30 °.

Appendix B

B1 – Optical Textures of DTC5C5, DTC5C9 and DTC5C11

The Optical textures of the DTC5Cn compounds were investigated using an Olympus BX50 Microscope fitted with a Mettler FP82 HT hotstage. Each compound was placed between two glass plates and heated until isotropic. The samples were then cooled stepwise through their respective phase sequences until reaching the crystal phase. It should be noted that the DTC5Cn compounds are reported to be negatively birefringent, meaning that the slowest axis of the domains is perpendicular to the average alignment direction of the molecules. The optical textures of DTC5C7 are shown in the Chapter 4, section 4.2.1 of the main text and are not reproduced here. The texture of the homeotropically aligned N_{tb} phase is not shown for each compound because the field of view is featureless, i.e. completely black (magenta with lambda plate), in all cases. The textures of DTC5C5 are shown in Figure B1, the textures of DTC5C9 are shown in Figure B2 and the textures of DTC5C11 are shown in Figure B3.
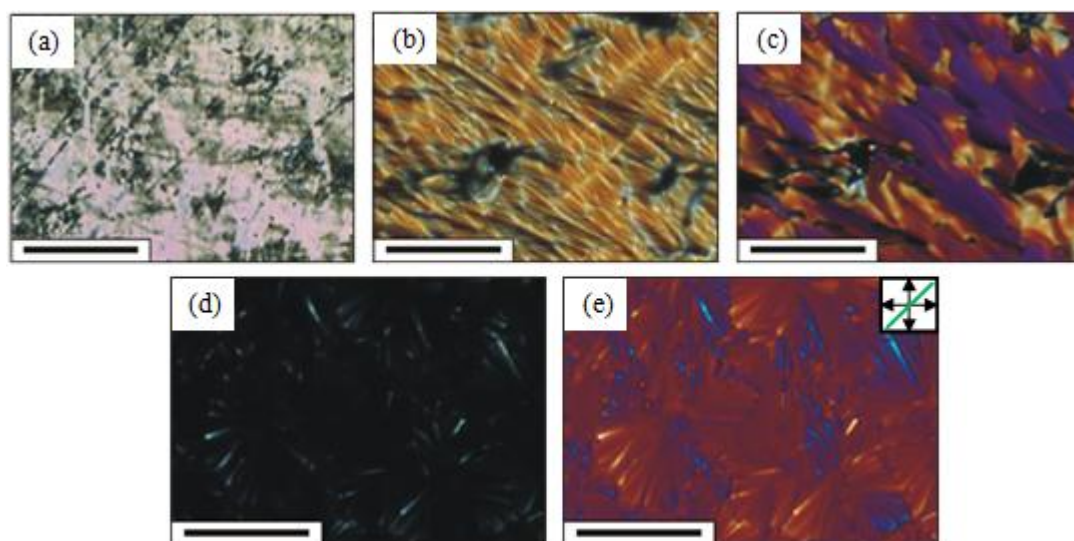

Figure B1 – Optical textures of DTC5C5. (a) Planar N phase (130 °C), scale bar = 200 μm. (b) Planar N_{tb} phase (114 °C), scale bar = 50 μm. (c) Planar X phase (110 °C), scale bar = 50 μm. In (a-c) there is no lambda plate inserted into the optics. (d,e) the homeotropically aligned X phase, scale bar = 50 μm. Left (/right) shows the texture without (/with) the lambda plate inserted; axis in green.
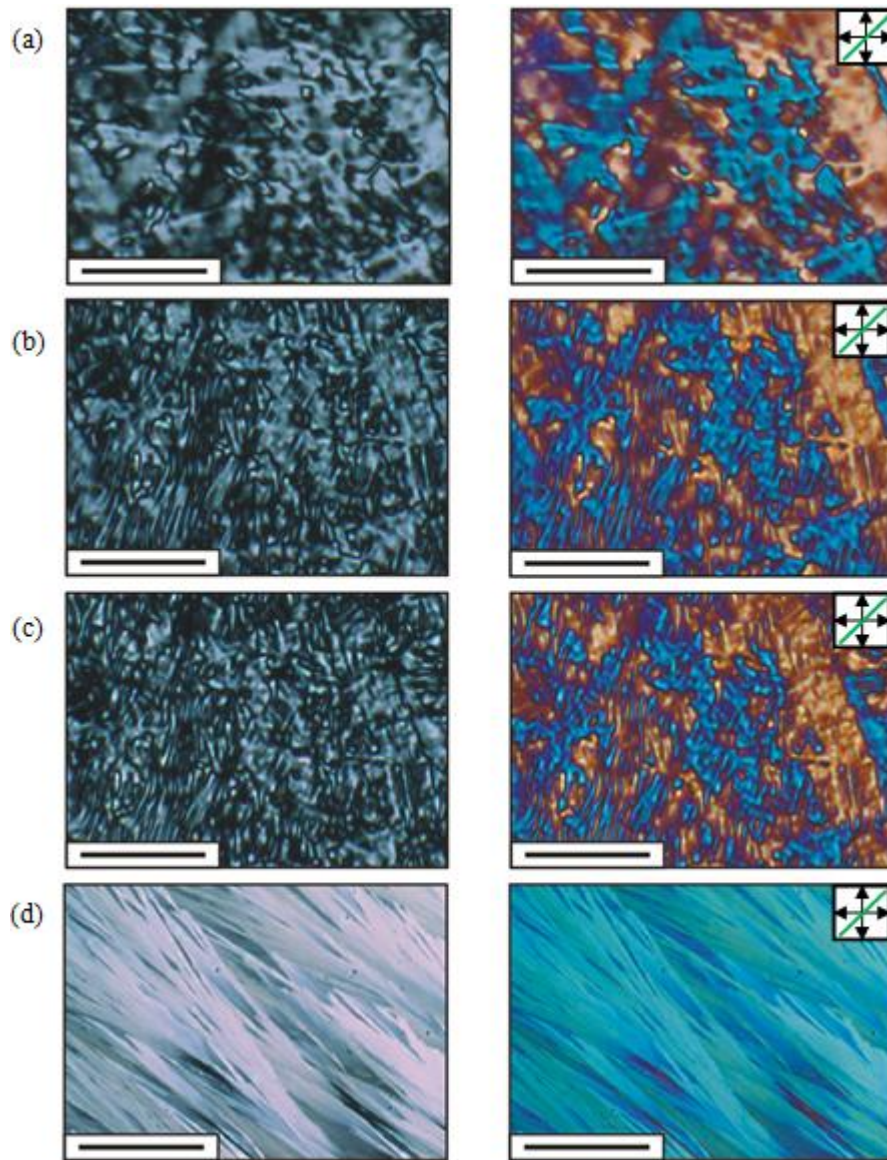
Figure B2 – Planar optical textures of DTC5C9. (a) N phase (150 °C), scale bar = 50 μm. (b) N_{tb} phase (110 °C), scale bar = 50 μm. (c) Y phase (80 °C), scale bar = 50 μm. (d) The sample temp is still 80 °C, but crystallisation begins after ~ 5 min; scale bar = 50 μm. In all cases left (/right) show the texture without (/with) the lambda plate inserted; axis in green.
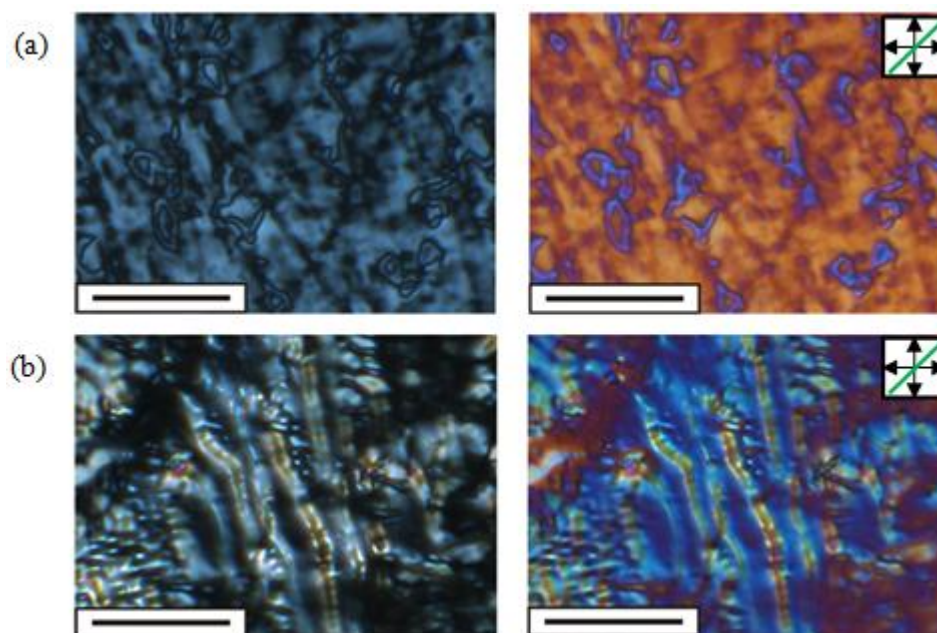
Figure B3 – Planar optical textures of DTC5C11. (a) N phase (150 °C), scale bar = 50 μm. (b) N$_{tb}$ phase (120 °C), scale bar = 50 μm. Note that (a) and (b) do not show the same sample spot. The exact transition point between the N and N$_{tb}$ phases is difficult to determine. The texture changes are more gradual than in the other DTC5Cn compounds. In all cases left (/right) show the texture without (/with) the lambda plate inserted; axis in green.

B2 – Possible Electron Density Maps of the X phase

As stated in Chapter 4, section 4.5.2, the electron density maps of the X phase were determined from the relative intensity ratio between the seven Bragg reflections and the equations provided in Chapter 2, section 2.3.5. As the phase information could not be experimentally determined, an electron density map was created for every possible phase combination of the seven peaks. Of the 128 maps created, only eight general electron density distributions were found. The eight options are shown below in Figure B4. High electron density corresponds to the aromatic mesogens and low electron density corresponds to the alkyl chains.
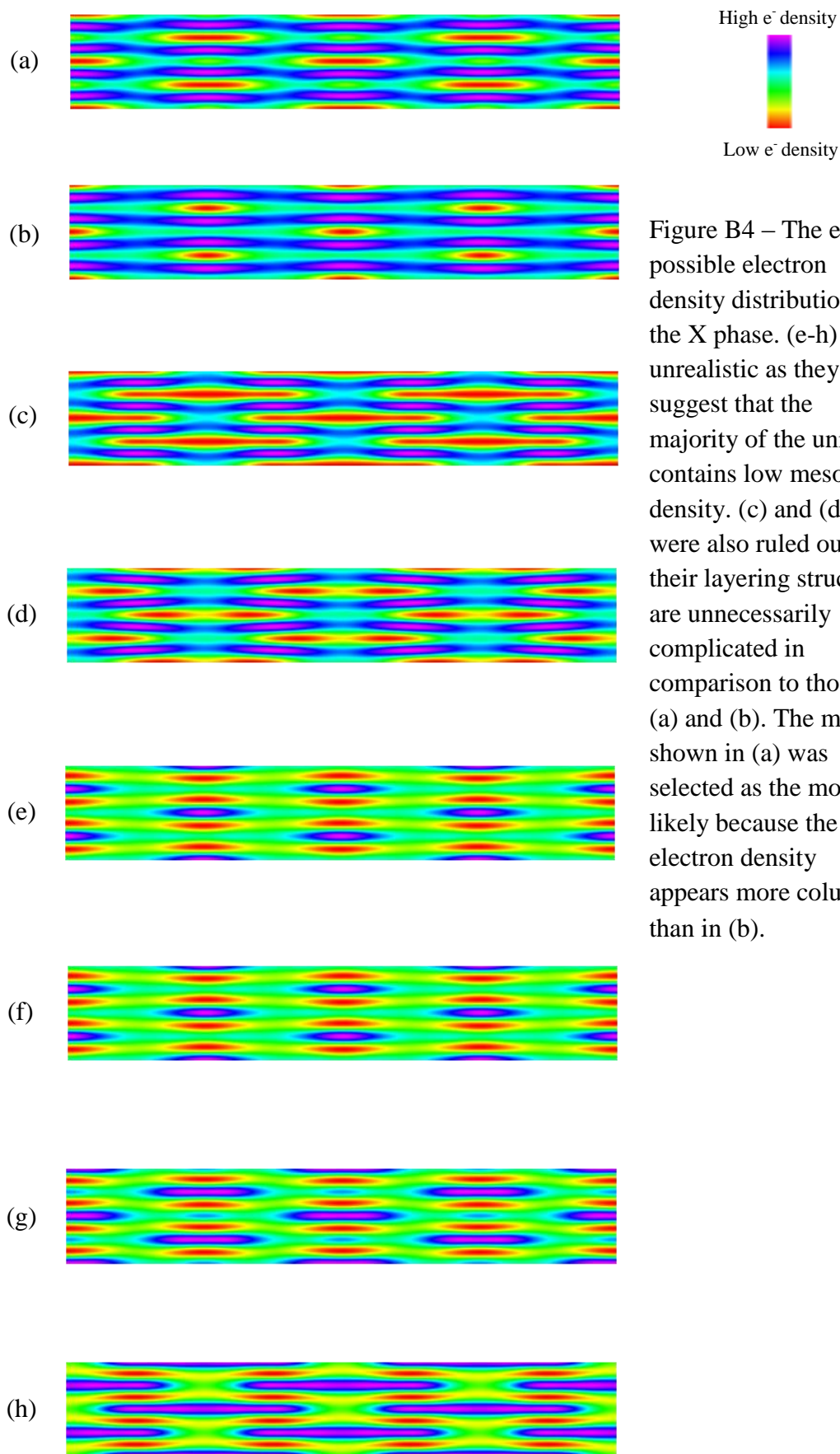
(a)

High e⁻ density

Low e⁻ density

(b)

Figure B4 – The eight possible electron density distributions of the X phase. (e-h) are unrealistic as they suggest that the majority of the unit cell contains low mesogen density. (c) and (d) were also ruled out as their layering structures are unnecessarily complicated in comparison to those in (a) and (b). The map shown in (a) was selected as the most likely because the electron density appears more columnar than in (b).

(c)

(d)

(e)

(f)

(g)
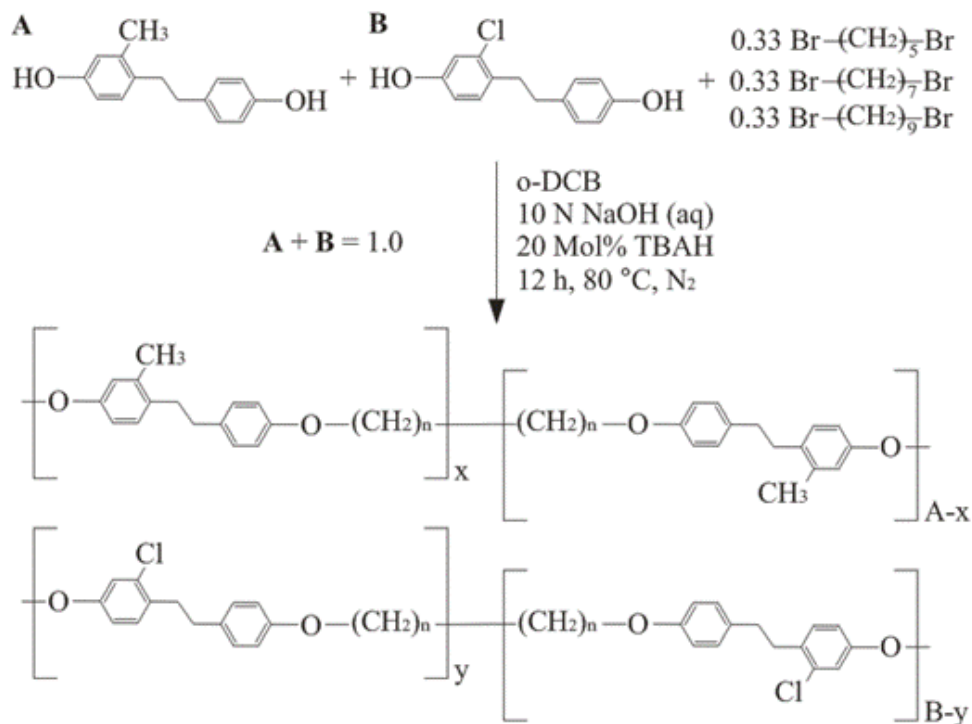

(h)

Appendix C

C1 – Synthesis of CLMBPE

Figure C1 – Schematic synthesis of CLMBPE.

The synthesis of the CLMBPE copolyether based on a 33/33/33 molar ratio of **1,5-dibromopentane**, **1,7-dibromoheptane**, and **1,9-dibromononane** and a 50/50 molar ratio of **1-(4-hydroxyphenyl)-2-(2-methyl-4-hydroxyphenyl)ethane** (MBPE) and **1-(4-hydroxyphenyl)-2-(2-chloro-4-hydroxyphenyl)ethane** (CLBPE), is shown schematically in Figure C1. The copolymer was synthesised by liquid-liquid phase transfer-catalysed polymerisation reactions. The polyetherifications were carried out under nitrogen atmosphere at 80 °C in an o-dichlorobenzene/10 N aqueous NaOH mixture (10-fold molar excess of NaOH versus phenol groups) in the presence of TBAH (20 mol% of the phenol groups) as the phase-transfer catalyst. The molar ratio of nucleophilic to electrophilic monomers was in every case 1.0/1.0. After 12 hours of reaction, the organic and aqueous layers were diluted with chloroform and water, respectively. The organic layer was separated and washed several times with water, dilute HC1, and finally with water. The polymer was separated by precipitation into methanol. The yields were always higher than 90%. The polymer was purified by

successive precipitation from chloroform solution into acetone, from tetrahydrofuran solution into water, and finally from chloroform solution into methanol, to yield a white fibrous precipitate. The non-crystallisable polymers separated as a viscous gum.

The synthesis was carried out by Jianggen An from the physics department of Zhejiang Sci-Tech University, Hangzhou, China.

C2 – Further DSC Data

In the main text (Chapter 5, section 5.1.1) the 10 C/min DSC thermograms of CLMBPE indicate that the sample did not re-crystallise after the first melting. To investigate this further the sample was cooled from isotropic and left for 5 hours at room temperature. The sample was then reheated at 10 °C/min (Figure C2). The DSC trace appeared identical to the one observed on the second heating in the main text, suggesting that the sample did not re-crystallise during this time. 5 hours is much longer than the duration of the X-ray scattering and birefringence experiments discussed in Chapter 5. The sample was also investigated on slow cooling at a rate of 0.1 °C/min. During the cooling process no significant exotherms were observed. After consequent heating, the DSC trace again appeared identical to the one shown in section 5.1.1 of the main text, suggesting that the sample did not re-crystallise.
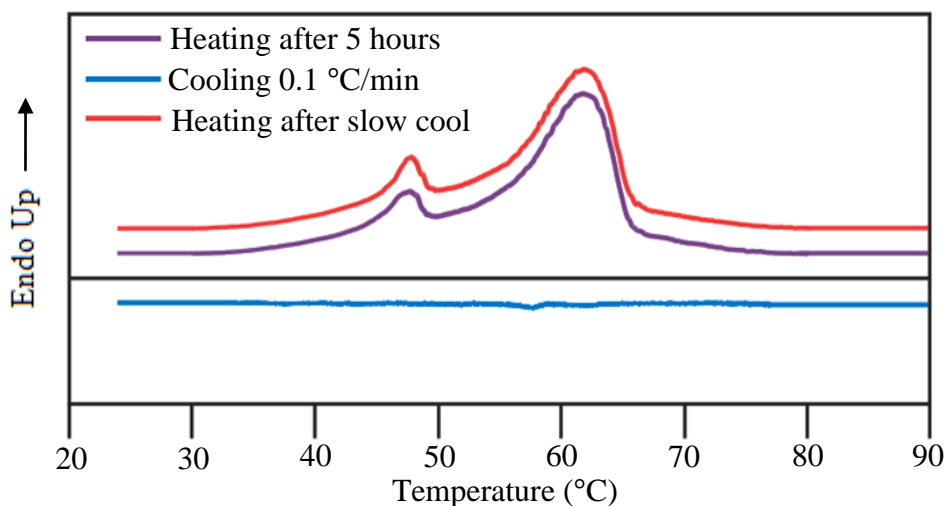

Figure C2 – Additional DSC traces showing the thermal behaviour of CLMBPE after long standing at room temperature for 5 hours and slow cooling (0.1 °C/min). The scanning rate is 10 °C/min unless otherwise specified. The baseline of the red curve has been raised artificially.

C3 – 3D Sample Mapping for Birefringence Calculations

The birefringence of a CLMBPE thin film (on glass) was investigated by determining the retardation state of linearly polarised light as it exited the material. The measurements were performed using an Olympus BX50 microscope (with crossed polarisers), fitted with a U-CBE Berek compensator, as described in Chapter 5, section 5.1.2. In order to convert from retardation (Γ) to birefringence (Δn), the sample thickness (t) must be known ($\Gamma=\Delta n \cdot t$). The thickness of the CLMBPE thin film was estimated using a self calibrating, Bruker contour GT optical microscope, which can be used to produce a 3D map of the substrate surface (see Figure C3). A groove was intentionally carved into the film to allow its thickness to be determined (relative to the glass surface) and also to mark the region investigated under the microscope. In the region that the retardation measurements were performed, the sample thickness was estimated to be 4.5 μm.
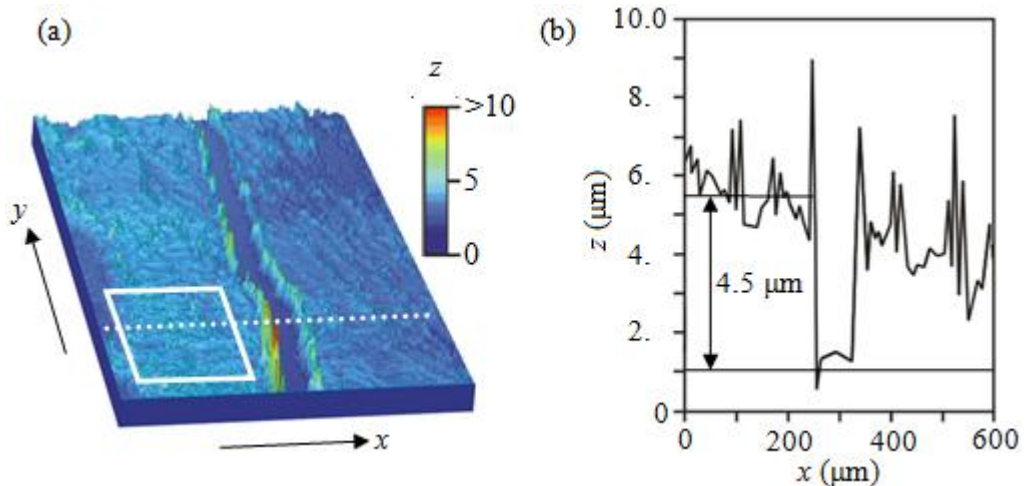

Figure C3 – Determination of sheared (by knife edge) CLMBPE film thickness. (a) 800×1800 μm section of the mapped CLMBPE film. The box indicates the approximate region where retardation measurements were performed; the dotted line indicates the position of the xz cross-sectional slice plotted in (b). *z* is referenced from the top surface of the glass.

C4 – Azimuthal measurements

Azimuthal analyses of the 2D grazing incidence X-ray scattering (GIXS) patterns of CLMBPE were conducted after converting the data into 1D plots. This was achieved by radially integrating the intensity inside a thin slice of the 2D pattern as shown in Figure C4. In all cases the slice was centred on the point of maximum peak intensity, which varied with temperature ($q \propto 1/T$). The angular range of the slice was 180 ° in all cases and progressed anticlockwise. Note that in Chapter 5, 0 ° corresponds to the equator axis, which is the 90 ° position in Figure C4.
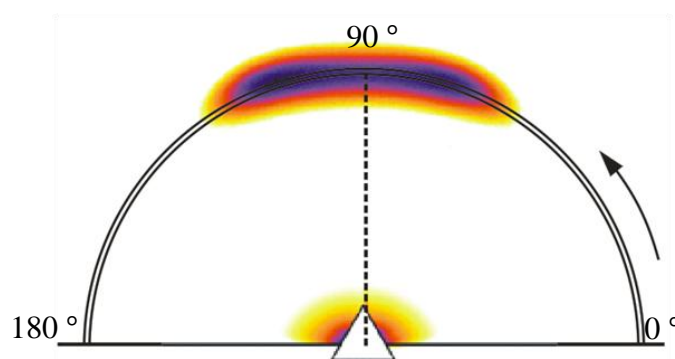

Figure C4 – An example 2D GIXS pattern of CLMBPE and the azimuthal slice used to obtain the corresponding 1D intensity plot. The intensity inside the slice was integrated radially for each azimuthal angle. Azimuthal angle increases in the anticlockwise direction. The vertical dashed line and the solid horizontal line indicate the equator and meridian, respectively.

C5 – cos^2 Fitting of IR Data

The orientational order parameter (S) of each vibrational mode was estimated using $S=(D-1)/(D+2)$, where $D=A_{//}/A_{\perp}$ is the dichroic ratio. As mentioned in Chapter 2, section 2.5.2, this form of D applies in the case that the polar direction of the IR beam runs approximately parallel to the sample alignment direction and beam polarity. However the sample was rotated incrementally through a 90 ° angle and so all modes were temporarily brought into near parallel alignment with beam polarity. To improve the accuracy of 'D' values, the amplitude of each peak was plotted against the sample orientation angle (θ_0) and then a cos^2 curve was fitted to the data (see Figure C5). The least squares fit to the data was performed using the formula: $E cos^2(\theta_0 + \delta) + c$, where '$E$' is the cos^2 amplitude, 'δ' compensates angular misalignment of the shear direction with the beam polarity, and 'c' is the baseline. The peak and trough of the

fitted curve were taken as the values of $A_{//}$ and $A_{\perp}$. The fitting was performed for all modes at each temperature. The magnitude of δ was fixed in each temperature increment.
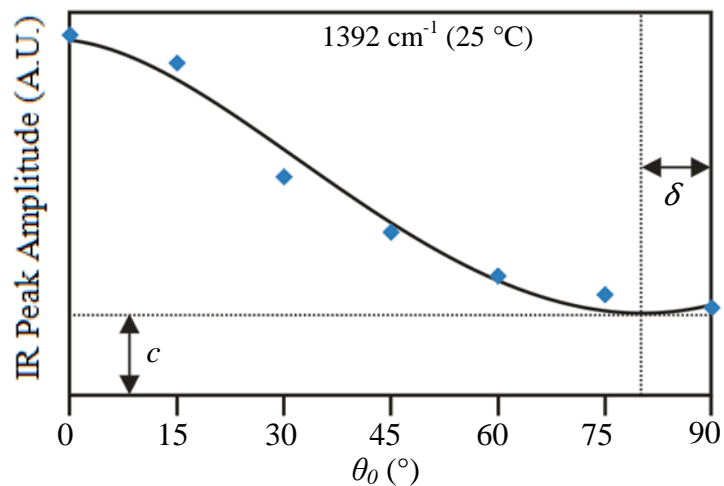

Figure C5 – Measured peak amplitude Vs sample orientation angle (θ_0) for the 1392 cm^{-1} polyethylene symmetric wagging mode (at 25 °C). Diamonds correspond to measured data points, while the solid black line corresponds to the least squares fit of a cos^2 function.

Appendix D

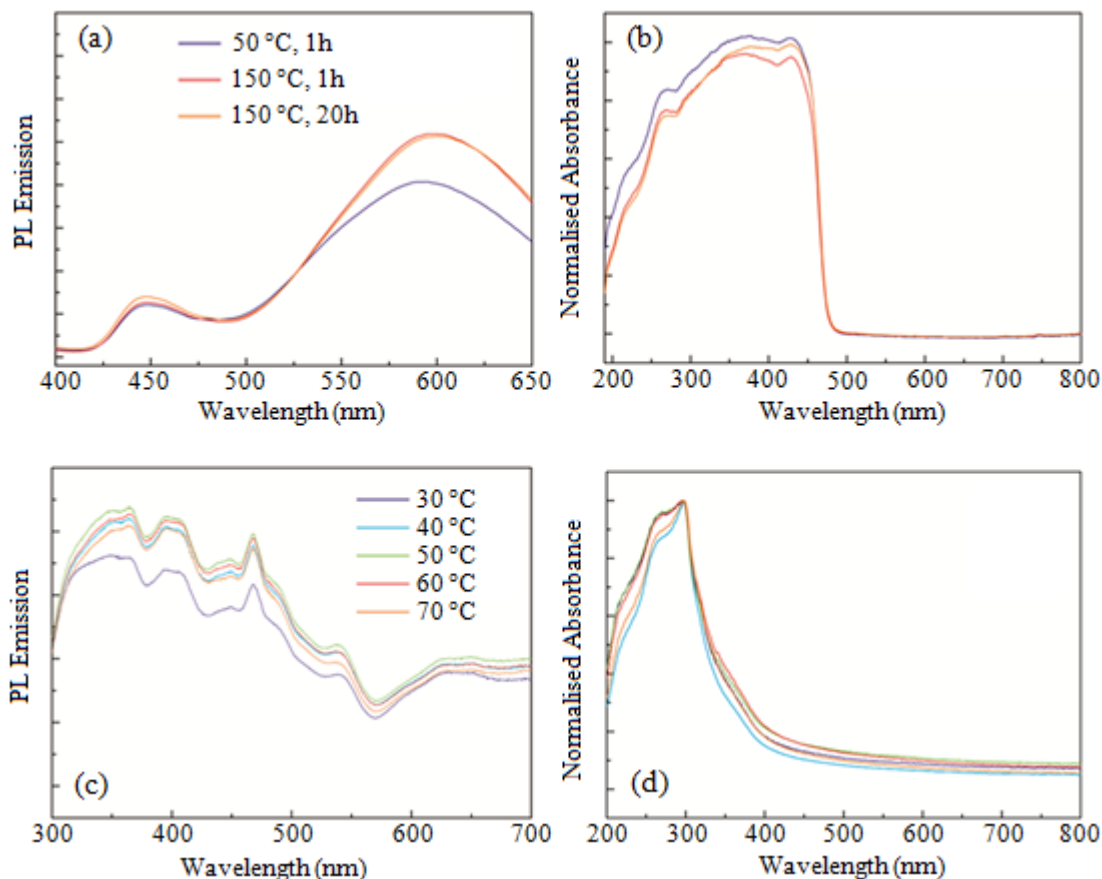## D1 – Supporting Emission and Absorption Spectra

Figure D1 – (a) PL emission spectra and (b) normalised absorption spectra of pure **C** before and after long annealing. The colour legend in (a) also applies to (b). PL emission spectra (c) and normalised absorption spectra (d) of pure **D**. The colour legend in (c) also applies in (d).

The emission and absorption spectra of pure 'C' (CdS QD + thiols) and pure 'D' (dendrons) are shown in Figure D1. The emission spectra were recorded in air at room temperature using a Hitachi F-2700 fluorescence spectrometer. The absorption spectra were collected using a Hitachi U-3900 spectrometer (equipped with an integrating sphere). The emission spectra of **C** features band edge emission at 450 nm and defect trapped emission at 600 nm. This suggests that the same peaks observed in **D/C** (CdS QD + thiols +dendrons) arise from the CdS cores. The absorbance spectra of pure **D** show a maximum absorbance around 300 nm allowing the band gap to be estimated

(using E_g = 1240/λ) as ~ 4 eV. This data was provided by the Chemistry group at Tohoku University, Japan, led by Professor Kiyoshi Kanie.

The emission spectra of **D/C** were explored before and after annealing while dissolved in CHCl$_3$. When dispersed in solvent, only 450 nm band edge emission and ~ 600 nm defect trapped emissions are observed (Figure D2a). The band gap emission at 470 nm, present in the **D/C** film, disappears. Moreover, the PL signal of the quenched **D/C** film is recovered when the material was re-dissolved in solvent. As discussed in Chapter 6, section 6.4.3, the recovered PL properties of the dissolved material remain when **D/C** is recast onto the substrate. The casting – annealing – re-dissolving – recasting process is repeatable for up to at least 3 cycles (Figure D2b).
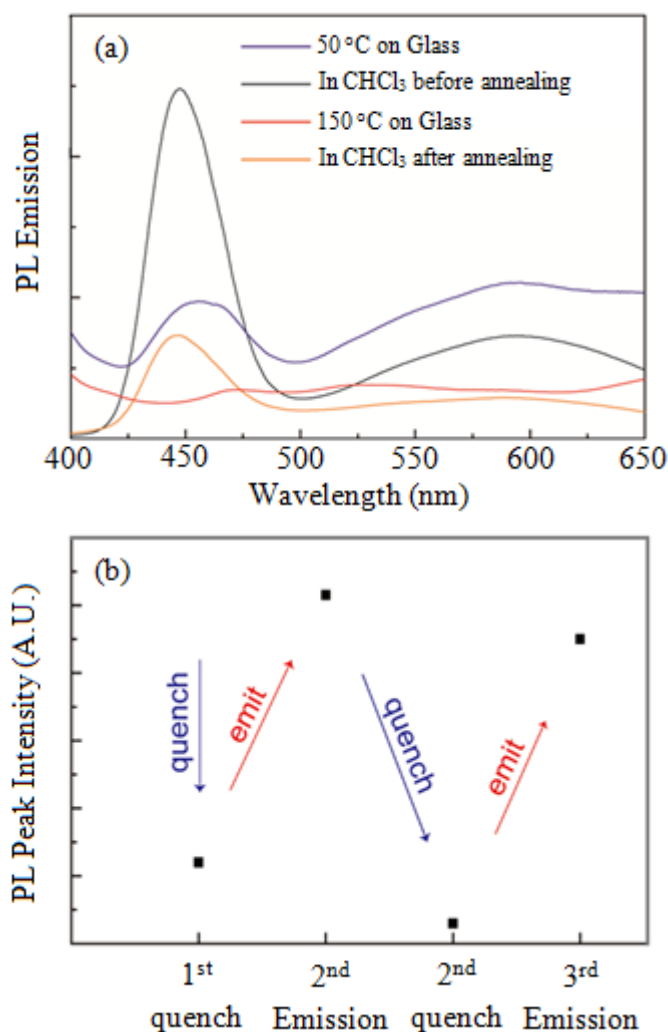

Figure D2 – (a) PL spectra of **D/C** on glass and dispersed in CHCl$_3$. (b) A graph demonstrating the reversibility of the PL quenching and recovery process, up to three emission cycles.

Figure D3 shows the $(A/\lambda)^2$ Vs photon energy plot of **D/C** with and without annealing at 150 °C; A is absorbance and λ is wavelength. In each case the band gap energy (E_g) was extrapolated from the intercept of the tangent-line of the plot with the abscissa axis [1]. Thus, E_g was determined as 2.61 and 2.64 eV before and after annealing at 150 °C, respectively.
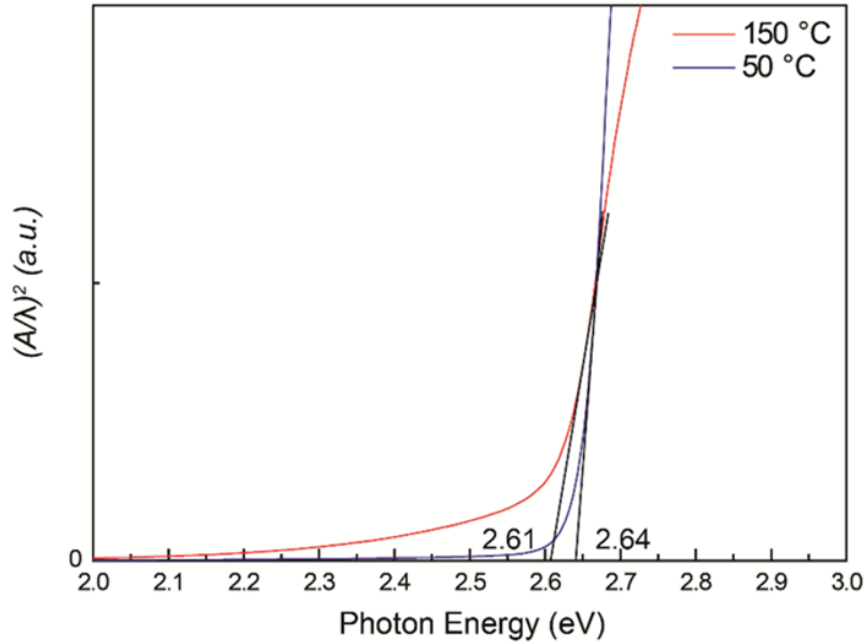

Figure D3 – $(A/\lambda)^2$ Vs photon energy plot of **D/C** with and without annealing at 150 °C.

D2 – Exponential Fitting of Fluorescence Decay

The normalised time resolved PL decays of annealed and re-dispersed **D/C** in the ranges of 445-455 and 465-475 nm are shown in Chapter 6, Figure 6.10. The decay curves can be well fitted to a double exponential model described by Equation S1, where τ_1 and τ_2 ($\tau_1 < \tau_2$) represent the time constants, and A_1 and A_2 represent the amplitudes of the fast and slow components, respectively. The fitted values of parameters are summarised in Table D1 in the range of 445-455 nm and Table D2 in the range of 465-475 nm.

$$F(t) = A_1 exp\left(-\frac{t}{\tau_1}\right) + A_2 exp\left(-\frac{t}{\tau_2}\right) \quad \text{(Equation S1)}$$

Table D1 – Time Constants τ_1 and τ_2, and Components A_1 and A_2 of the Initial, Annealed and Re-dispersed **D/C** film in the range of 445-455 nm

	A_1 / %	τ_1 / ns	A_2 / %	τ_2 / ns
Before Annealing	90.5	0.043	9.5	0.678
Annealed at 150 °C	86.2	0.041	13.8	1.114
Redispersed	91.9	0.032	8.1	0.776

Table D2 – Time Constants τ_1 and τ_2, and Components A_1 and A_2 of the Initial, Annealed and Re-dispersed **D/C** film in the range of 465-475 nm

	A_1 / %	τ_1 / ns	A_2 / %	τ_2 / ns
Before Annealing	68.2	0.065	31.8	0.773
Annealed at 150 °C	75.1	0.063	24.9	1.001
Redispersed	84.2	0.041	15.8	0.473

[1] R. Mariappan, M. Ragavendar, V. Ponnuswamy, *J. Alloys Compd.* 2011, **509**, 7337-7343.

Abbreviations and Acronyms

AFM – Atomic force microscopy.

BCC – Body centred cubic.

Bn = Banana phases; n=integer.

CBCnCB – Cyano-bi-phenyl sample variety; n=number of carbons in spacer.

C – CdS NP with thiol coating sample variety.

(E)CD – (Electronic) circular dichroism.

CLMBPE – Chlorine or methyl substituted dipheylethane copolymer sample variety.

D – Dendron sample variety.

D/C – CdS NP with thiol coating and dendron shell.

DLS – Diamond Light Source, UK.

DMES – Dendron mediated extended state.

DPE – Diphenylethane mesogen.

DSC – Differential Scanning Calorimetry.

DT – Dodecane thiol ligands.

DTC5Cn – Di-flouro-terphenyl sample variety; n=number of carbons in spacer.

DTSe – Selenium labelled di-flouro-terphenyl sample variety.

ESRF – European Synchrotron Radiation Facility, France.

FCC – Face centred cubic.

FWHM – Full width at half maximum.

HCP – Hexagonal close pack.

LC – Liquid crystal.

MHA – Mercapto hexadecanoic acid ligands.

N/N* – Uniaxial/chiral nematic phase.

N_{sb} – Splay-bend nematic phase.

N_{tb} = Nx – Twist-bend nematic phase.

NMR – Nuclear magnetic resonance spectroscopy.

NP – Nanoparticle.

OM – Oligomethylene spacer.

PL – Photoluminescence.

(E-)POM – (Electronic) polarised optical Microscopy.

QD – Quantum Dot.

RMS − Root means squared.

RXS – Resonant X-ray scattering.

(GI)SAXS – (Grazing incidence) small angle X-ray scattering.

SC – Simple cubic.

Se00 – 00% molar mixture of DTC5Cn and DTSe sample types.

Sm(A/C/C*) – Smectic (A/C/chiral C) phase.

SmC_{int} = B6 – Intercalated smectic C.

SmCxPy = B2 – Polar SmC phases; x=A/S denotes clinicity, y=F/A denotes polarity.

SmCxPyUz – Undulated polar Sm phases; z=A/S/A'/S' denotes defect type.

(FF-)TEM – (Freeze fracture -) transmission electron microscopy.

TG – Thermogravimetric analysis.

(GI)WAXS – (Grazing incidence) wide angle X-ray scattering.

(GI)XRD − (Grazing incidence) X-ray diffraction.

(GI)XS − (grazing incidence) X-ray scattering.

Mathematical Symbols and Definitions

$\Delta A = A_{\text{Left}} - A_{\text{Right}}$ − Absorption difference between left and right handed circularly polarised light.

Δn − Birefringence.

Δq − Radial FWHM of 1D X-ray scattering peaks.

$A_{//}$ /$A_\perp$ − Absorption parallel /perpendicular to sample alignment direction.

A − Amplitude

A_s − Scattering amplitude from a single electron.

a, b, c /*a*, b*, c** − Lattice parameters (lattice vectors when bold) in real/reciprocal space.

B − Magnetic field vector.

D − Dichroic ratio.

d − Distance between two planes (Bragg spacing) or layers.

D_p /M_p /R_{np} /ρ_p − Nanoparticle diameter /mass /radius /density.

E /E_i /E_r /E_g − Energy /incident energy /resonant energy /band gap energy.

e − Charge of an electron.

$\widehat{\boldsymbol{E}}_{\boldsymbol{p}}$ − Vector defining polar plane of incident linearly polarised radiation.

F_t/F_0/F_d − Free energy total / of ideal state / of elastic distortions.

f(q) /*F(q)* /*S(q)* − Atomic form factor /structure factor /interference function.

f(q)$_{np}$ − Form factor of a spherical nanoparticle.

g(r) − Radial distribution function.

h − Plank's constant.

h, k, l − Miller indices.

h_l – Cybotactic layer height

$I_0 / I = I(q)$ – Incident intensity /scattered intensity.

K – Force constant.

K_n – Frank elastic constants.

$\mathbf{k} = k\hat{\mathbf{k}}$ – Scattered wavevector.

$\mathbf{k_0} = k\hat{\mathbf{k}}_0$ – Incident wavevector.

L – Sample to detector distance.

L_p – Path difference

l – Centre-to-centre distance between mesogens (contour length in helical case).

$\mathbf{M} - M\hat{\mathbf{M}}$ – Transition dipole moment.

M_{avg} – Average molecular mass of thiols.

m_e – Mass of an electron.

$\hat{\mathbf{n}} / \hat{\mathbf{n}}(r)$ – Nematic director /director field.

$\hat{\mathbf{n}}_0 / \mathbf{n_1} / \mathbf{n_2}$ – Unit vectors defining the axis of: the helix /mesogen 1 /mesogen 2.

$n / n_o / n_e$ – Refractive index /ordinary index /extraordinary index.

N_a – Avogadro's constant.

$N_P / N_T / N_{DT} / N_{MHA} / N_D$ – Number of: NPs (g^{-1}) / thiols /DT ligands /MHA ligands /dendrons per NP.

O / O' = Origin of real space /reciprocal space.

$\mathbf{p}$ – Dipole moment.

p – Helical pitch length.

$\langle P_2 \rangle$ – Average of the second Legendre polynomial.

$\mathbf{P_b}$ – Denotes direction of molecular bend.

P_f – X-ray polarisation factor.

$\boldsymbol{q}$ – Reciprocal scattered wavevector. Magnitude = q.

q_c – Net charge.

R /R_c – Radius /radius of curvature (helical radius in N_{tb} phase).

r – Used generally as distance between two points (separation vector when in bold).

S – Orientational order parameter.

S_0/S_1 – Orientational order parameter describing alignment of helical domains /moieties inside helical domains.

S_L – Oligomethylene spacer length (nm).

T – Scherer equation shape factor.

t – Sample thickness.

T_a – Annealing Temperature.

$\sqrt{\langle u^2 \rangle}$ – Debye-Waller factor (RMS displacement).

w – Distance between dimers projected onto the plane perpendicular to the helical axis.

W_D – TG weight loss of **D/C**.

W_l – TG weight loss of **C**.

α – Rotation angle between mesogens around the helical axis.

Γ – Retardation.

γ – Torsion angle of each CH_2 linker in OM spacer.

δ_p – Phase difference.

ε_r – Dielectric constant.

θ – Arbitrary angle.

θ_0 – Sample orientation angle.

θ_b – Bragg angle.

θ_t – Tilt angle in respect to a defined axis.

θ_g – Grazing angle.

θ_v – Angle of vibration.

θ' – Angle between transition dipole moment and the nematic director.

λ / λ_{ex} – Wavelength /excitation wavelength.

μ / μ_0 – Reduced mass /permeability of free space.

$\nu / \nu_r / \bar{\nu}$ – Frequency /resonant frequency /wavenumber.

ξ – Correlation length determined by Lorentz peak fitting.

$\rho / \rho_0 / \rho(r)$ – Density /mean density /density distribution.

τ – Coherence length (estimated domain size) from Scherer equation.

τ_n – Time constants.

ϕ – Exterior bend angle between mesogens.

φ - Azimuthal angle.

ϕ_{hkl} – Phase angle of Bragg reflection.

Ψ – Smectic order parameter.

Ω – Dichroic ellipticity.

ω – Twist angle between mesogens about the spacer axis.